University of California

Los Angeles

Longitudinal Shaping of Relativistic Bunches of Electrons Generated by an RF Photoinjector

A dissertation submitted in partial satisfaction

of the requirements for the degree

Doctor of Philosophy in Physics

by

Robert Joel England

2007

The dissertation of Robert Joel England is approved.

Steven Cowley

Chandrashekhar Joshi

Claudio Pellegrini

James B. Rosenzweig, Committee Chair

University of California, Los Angeles

2007

To my parents . . .

for their continuing love and support.

Table of Contents

List of Figures

List of Tables

Acknowledgments

I am grateful to the many people who have supported, advised, assisted, and encouraged me in a multitude of ways throughout my graduate career. I will humbly attempt to acknowledge them here.

First and foremost, I must thank my advisor Jamie Rosenzweig. In my first year as a graduate student I was lured into the field of accelerator physics by Jamie's contagious enthusiasm for electron beams and for all the exciting things that can be done with them, and I have not regretted it since. Without Jamie's input, advice, and support, this thesis could not exist. Thanks also to Sergei Tochitsky for his daily help on numerous fronts, for always striving to keep everyone's spirits up in the face of a minor setback, and for loaning me his black wrench and his favorite scissors (among many other things).

I wish to thank Gil Travish for his help in numerous aspects of my research and for his continual willingness to lend a hand in the lab, proofread a paper, or offer his advice. Many thanks to Chan Joshi for fostering an atmosphere of harmony and cooperation between our two research groups, and for his excellent management of the Neptune laboratory, which has kept it at the forefront of research in lasers, plasmas, and beams. I also wish to thank Claudio Pellegrini for his interest in my work and for his numerous contributions to our research group and to the physics department.

The Neptune accelerator is a complicated system, and the successful day-to-day operation of the beamline during the commissioning and running of my experiment was made possible by the assistance of numerous people, including: Oliver Williams, Rodney Yoder, Adnan Doyuran, Rodion Tikhoplav, and Chris Clayton.

For their assistance with aspects of the deflecting cavity design and construction, I wish to thank David Alesini for his advice on HFSS, Brendan O'Shea for his diligent work on the CAD drawings, Joris Fourrier for his meticulous calibrations of the various RF components, and to Harry Lockart for his excellent management of the physics machine shop.

For their camaraderie and advice in my formative years I thank my fellow graduate students who have since graduated: Scott Anderson, Matt Thompson, Alex Murokh, Gerard Andonian, and Pietro Musumeci. I owe special thanks to Pietro for putting up with and helping me as I learned how to operate the beamline, and for transferring to me various bits of arcane knowledge about the system which were invaluable in its day-to-day operation.

Finally, I wish to thank my family who have always supported me in all things, big and small.

Vita

1975	Born, Denton, Texas, USA.
1997	B.S. (Physics), University of Texas, Austin.
1997-1999	Teaching Assistant, Physics Department, University of Texas. Taught undergraduate physics laboratory (mechanics and optics).
1999-2000	Teaching Assistant, Physics and Astronomy Department, UCLA, Los Angeles, California. Taught discussion sections for Physics 1A and 1B.
2001	M.S. (Physics), UCLA.
2001-present	Graduate Research Assistant, Physics and Astronomy Department, UCLA, Los Angeles, California. Studied under Professor James Rosenzweig. In Spring 2004 served as Teaching Assistant for Physics 150 (Physics of Charged Particle Beams).

Publications

H. Suk, N. Barov, R. J. England, E. Esarey, G. Kim, J. B. Rosenzweig, M. Thomson, "Dynamics of a driver beam propagating in an underdense plasma with a downward density transition," Proceedings of the 2001 Particle Accelerator Conference, Piscataway, NJ, p. 4011 (2001).

R. J. England, J. B. Rosenzweig, and N. Barov, "Plasma electron fluid motion and wave breaking near a density transition," Phys. Rev. E, **66**, 016501 (2002).

R. J. England, P. Musumeci, R. Yoder, and J. B. Rosenzweig, "Beam Shaping and Compression Scheme for the UCLA Neptune Laboratory," Proceedings of the 2003 Particle Accelerator Conference, 3258-3261 (2003).

P. Musumeci, SYa Tochitsky, S. Boucher, A. Doyuran, R. J. England, C. Joshi, C. Pellegrini, J. Ralph, J. B. Rosenzweig, C. Sung, S. Tolmachev, G. Travish, A. Varfolomeev, A. Varfolomeev Jr., T. Yarovoi, and R. Yoder, "Very high energy gain at the Neptune Inverse Free Electron Laser Experiment," AIP Conference Proceedings, **737**, p. 160 (2004).

P. Musumeci, SYa Tochitsky, S. Boucher, A. Doyuran, R. J. England, C. Joshi, C. Pellegrini, J. Ralph, J. B. Rosenzweig, C. Sung, S. Tolmachev, G. Travish, A. Varfolomeev, A. Varfolomeev Jr., T. Yarovoi, and R. Yoder, "Very high energy gain at the Neptune Inverse Free Electron Laser Experiment," AIP Conference Proceedings, vol. 737, p. 160 (2004).

R. J. England, D. Alesini, A. Doyuran, P. Musumeci, J. B. Rosenzweig, "UCLA Neptune Ramped Electron Bunch Experiment," Proceedings of the 11th Advanced Accelerator Concepts Workshop, Stony Brook, NY, p. 414 (2004).

P. Musumeci, SYa Tochitsky, S. Boucher, C. E. Clayton, A. Doyuran, R. J. England, C. Joshi, C. Pellegrini, J. Ralph, J. B. Rosenzweig, C. Sung, S. Tolmachev, G. Travish, A. A. Varfolomeev, A. A. Varfolomeev, T. Yarovoi, and R. B. Yo-

der, "High energy gain of trapped electrons in a tapered, diffraction-dominated inverse-free-electron-laser," Phys. Rev. Lett., **94**, 154801 (2005).

S. G. Anderson, P. Musumeci, J. B. Rosenzweig, W. J. Brown, R. J. England, M. Ferrario, J. S. Jacob, M. C. Thomson, G. Travish, A. M. Tremaine, and R. Yoder, "Velocity bunching of high-brightness electron beams," Phys. Rev. ST-AB, **8**, 014401 (2005).

R. J. England, B. O'Shea, J. B. Rosenzweig, G. Travish, and D. Alesini, "X-Band Dipole Mode Deflecting Cavity for the UCLA Neptune Beamline," Proceedings of the 2005 Particle Accelerator Conference, 2627-2629 (2005).

R. J. England, J. B. Rosenzweig, G. Andonian, P. Musumeci, G. Travish, and R. Yoder, "Sextupole Correction of the Longitudinal Transport of Relativistic Beams in Dispersionless Translating Sections," Phys. Rev. ST-AB, **8**, 12801 (2005).

J. B. Rosenzweig, A. M. Cook, R. J. England, M. Dunning, S. G. Anderson, and M. Ferrario, "Emittance compensation with dynamically optimized photoelectron beam profiles," Nuclear Instruments and Methods in Physics Research A, **557**, 87-93 (2006).

Abstract of the Dissertation

Longitudinal Shaping of Relativistic Bunches of Electrons Generated by an RF Photoinjector

by

Robert Joel England

Doctor of Philosophy in Physics

University of California, Los Angeles, 2007

Professor James B. Rosenzweig, Chair

We propose a mechanism for the generation of ultrashort (sub-ps to a few ps) relativistic electron bunches having a ramp-shaped current profile that rises gradually from the head to the tail, followed by a sharp cutoff. This type of current distribution approximates the idealized profile predicted by linear 1D and nonlinear 2D calculations to be optimal for driving large-amplitude wakefields in a plasma wakefield accelerator (PWFA). The proposed scheme utilizes a dogleg beamline (or dispersionless translating section) as a bunch compressor to impart a linear negative longitudinal dispersion transformation on the longitudinal phase space of a beam that is initially chirped in energy versus longitudinal position within the bunch. A theory to describe this mechanism is derived using first and second-order transport matrix theory. The theoretical results, combined with simulations using the particle transport codes ELEGANT and PARMELA, indicate that sextupole corrector magnets are required in order to cancel out nonlinear chromatic effects which tend to otherwise disrupt the ramped shape of the current distribution.

To provide a venue for a proof-of-principle experiment to test these predic-

tions, a dogleg beamline was designed and built at the UCLA Neptune accelerator laboratory. A standing wave deflecting cavity was designed and built as a temporal diagnostic for measuring the current profiles of the electron bunches after passing through the dogleg. Second-order horizontal dispersion measurements and coherent transition radiation bunch length measurements of the electron beam after passing through the dogleg show good agreement with the predictions of theory and simulation.

Deflecting cavity measurements were conducted to directly measure the current profiles of both compressed and uncompressed electron bunches, with and without sextupole correction. The uncompressed bunch is found to have an asymmetrical (non-Gaussian) shape, presumably inherited from the pulse shape of the photoinjector drive laser. Results for an initially chirped beam show that ramp-shaped bunches can be produced by the proposed method, although due to the asymmetric initial (i.e. pre-compression) current profile of the electron bunches produced by the Neptune photoinjector, it is found to be necessary to overcompensate with the sextupole magnets in order to achieve a ramp-shaped profile.

CHAPTER 1

Introduction

The final distribution of particles within an electron bunch produced by a radio-frequency (RF) photoinjector (or laser-driven electron gun) is the end result of a dynamic evolution under the influence of various forces. The bunch density distribution along the longitudinal axis of the bunch is initially determined by the time structure of the laser pulse that produces the electrons via photoemission at the cathode, as well as by the emission properties of the metal from which the cathode is constructed. The longitudinal bunch distribution is sometimes alternatively referred to as the "time-current profile," since the density distribution is proportional to the beam current passing a stationary point as a function of time. The current profile of the bunch evolves as it passes across the accelerating voltage of the photoinjector cavity due to the influence of various forces, including: (1) the electromagnetic self-forces within the beam (generally referred to as 'space charge' forces), (2) the externally imposed longitudinal accelerating field of the cavity, (3) the force due to the image charge of the beam in the conducting plane of the cathode, and (4) the interaction between the beam and the cavity itself due to the effective impedance of the structure (a process known as "beam loading") and can result in the production of wake-fields at the irises of the structure, which in turn affect the longitudinal dynamics of the beam.

These various forces collectively limit the achievable peak beam current and longitudinal bunch shape. In experiments that require either a higher peak beam

current or a different shape of current profile than what the current photoinjector design produces, one or more longitudinal bunch shaping techniques may be employed. In the present chapter, we discuss several areas of current active research for which relativistic electron bunches of high current and brightness are important (inverse Compton scattering, the free electron laser, and the plasma wakefield accelerator), and review various techniques for manipulating the longitudinal distribution of the beam (velocity bunching, the magnetic chicane, and the dogleg compressor). All of these three techniques have been employed at the UCLA Neptune laboratory in recent years.

The dogleg compressor, in particular, is the technology which underlies the primary experimental work presented in this dissertation. In order to motivate this work, we conclude the chapter with an overview of the technique's most prominent potential application: the generation of an optimized drive beam for the plasma wake-field accelerator (PWFA).

1.1 Definitions of Relevant Beam Parameters

The 6D phase space particle density of a bunched electron beam at some time t may be represented by a distribution function $f(\mathbf{r}, \mathbf{p}, t)$, where $\mathbf{r}$ and $\mathbf{p}$ are vectors in position and momentum space respectively. The charge density ρ of the bunch may be obtained by integrating this function over momenta and multiplying by the total charge Q:

$$\rho(\mathbf{r}, t) = Q \int f(\mathbf{r}, \mathbf{p}, t) d^3p \tag{1.1}$$

Since the distribution function itself is not experimentally measurable, it is common to characterize the beam in terms of various moments of the distribution. For example, the trajectory and momentum of the so-called beam centroid are

given by the first moments:

$$\langle \mathbf{r}(t) \rangle = \int \mathbf{r}\ f(\mathbf{r}, \mathbf{p}, t)\ d^3r\ d^3p \tag{1.2}$$

$$\langle \mathbf{p}(t) \rangle = \int \mathbf{p}\ f(\mathbf{r}, \mathbf{p}, t)\ d^3r\ d^3p \tag{1.3}$$

The averaged values $\langle \mathbf{r} \rangle$ and $\langle \mathbf{p} \rangle$ preferably coincide with the *design trajectory* and the *design momentum* of the beam, meaning the intended trajectory and momentum of the beam. An arbitrary position or momentum may be expressed relative to that of the beam centroid via

$$\mathbf{r} = \langle \mathbf{r} \rangle + \delta\mathbf{r} \tag{1.4}$$

$$\mathbf{p} = \langle \mathbf{p} \rangle + \delta\mathbf{p} \tag{1.5}$$

where $\delta\mathbf{r} = (x, y, z)$ and $\delta\mathbf{p} = (\delta p_x, \delta p_y, \delta p_z)$ are the deviations in position and momentum relative to the centroid, and we have suppressed the explicit time dependence. The distribution function may now be parameterized in terms of the new coordinates, $f(\mathbf{r}, \mathbf{p}) \rightarrow F(\delta\mathbf{r}, \delta\mathbf{p})$, and second moments may be taken:

$$\langle \mu^2 \rangle = \int \mu^2\ F(\delta\mathbf{r}, \delta\mathbf{p})\ d^3\delta r\ d^3\delta p. \tag{1.6}$$

Here μ stands for any one of the coordinates $(x, y, z, \delta p_x, \delta p_y, \delta p_z)$ relative to the centroid. From these second moments we can define the root mean square (RMS) quantities

$$\sigma_\mu = \sqrt{\langle \mu^2 \rangle} \tag{1.7}$$

as well as the transverse and longitudinal normalized emittances:

$$\epsilon_{x,N} = \frac{1}{mc}\sqrt{\langle \delta p_x^2 \rangle \langle x^2 \rangle - \langle \delta p_x x \rangle^2}, \tag{1.8}$$

$$\epsilon_{y,N} = \frac{1}{mc}\sqrt{\langle \delta p_y^2 \rangle \langle y^2 \rangle - \langle \delta p_y y \rangle^2}, \tag{1.9}$$

$$\epsilon_{z,N} = \frac{1}{mc}\sqrt{\langle \delta p_z^2 \rangle \langle z^2 \rangle - \langle \delta p_z z \rangle^2}. \tag{1.10}$$

Note that the normalized emittances have the dimensions of area in each of the three phase planes. Under the influence of a time-independent Hamiltonian and in the absence of coupling between the phase planes they are constants of the motion by virtue of Liouville's Theorem. Their relationships to the unnormalized (or RMS) emittances and to the Courant-Snyder invariants are discussed in Chapter 3. Normalized transverse emittance is a general figure of merit for electron bunches, as the area occupied by the beam distribution in each transverse phase plane limits how tightly the beam can be focused in that dimension. The transverse emittances are related to the transverse beam brightness, defined by

$$\mathcal{B} = \frac{2I}{\epsilon_{x,N}\epsilon_{y,N}} \ , \tag{1.11}$$

where $I = Qv_0/\sigma_z$ is the beam current with v_0 being the bunch velocity. Brightness, a measure of phase space density, is a general figure of merit for electron beams. However, the expression given in Eq. (1.11) poses difficulties in certain circumstances. For example, it contains no information about the longitudinal distribution of the beam. Consequently, various alternative definitions have been formulated for different applications, producing some ambiguity about the meaning of the word brightness. These alternative definitions may, however, introduce additional difficulties in some cases. Averaging over the full 4D distribution in the combined x and y phase space, for example, produces an infinite result for a Kapchinskij-Vladmirskij distribution [1]. The expression presented in Eq. (1.11) is the one most commonly employed.

1.2 Longitudinal Photoinjector Dynamics

The modern electron photoinjector is essentially a multi-cell RF cavity (or iris-loaded waveguide) where the first cell is really a half-cell (or partial-cell) bounded on the upstream side by a conducting plane which serves as a photocathode. The half-cell also serves to give a shorter path for the (initially) nonrelativistic electrons to stay in resonance with the accelerating RF wave. The photocathode is constructed, in whole or in part, out of a metal with a work function near the single-photon energy of the drive laser used to excite the photoemission. The transverse geometry of the cavity is designed in such a way that the electromagnetic field in each cell resembles the TM_{010} mode of a cylindrical pillbox, which has a longitudinal component of electric field along the axis of the structure. If N is the number of cells, then for a given electromagnetic mode of the single-cell geometry there are N coupled modes in the passband of the multi-cell structure. The operating mode is typically identified by the value of the phase shift of the electromagnetic wave between adjacent cells. This cell-to-cell phase shift corresponds with one of the allowed Flouquet phase shifts given by $\phi_n = \pi(n-1)/(N-1)$ where n is an integer from 1 to N. A cartoon drawing of a 1.5 cell photoinjector is shown in Fig. 1.1. Most photoinjectors are operated in the so-called π mode corresponding to $n = N$. Consequently, the fields in adjacent cells are out of phase by 180 degrees. The length d of a full cell (i.e. the distance from the center of one full cell to the center of the next) is then made to be half of the wavelength of the RF source ($d = \lambda/2$). Since the cell-to-cell transit time for a relativistic particle is thereby made equal to the time required for the phase of the field in a given cell to change by 180 degrees, relativistic electrons moving along the axis of a structure operating in the π mode can be made to always experience a longitudinal force in the forward direction.

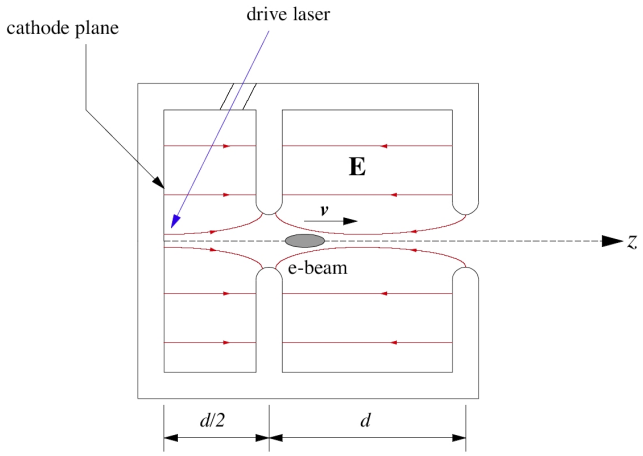

Figure 1.1: Cartoon drawing of 1.5 cell photoinjector.

1.2.1 RF Effects and Longitudinal Phase Space

In describing the longitudinal effects due to the RF acceleration of an electron beam in a photoinjector, we closely follow the theory presented by Kwang-Je Kim [2], with minor typographical changes. The longitudinal force responsible for accelerating the electrons in a photoinjector arises from the longitudinal component of the electric field. For a π mode structure (see Fig. 1.1) we may write the on-axis electric field in the form

$$E_z = E_0 \cos ks \sin(\omega t + \phi_0). \tag{1.12}$$

where s is longitudinal distance from the cathode, ω is the RF frequency, and ϕ_0 is the injection phase.

The electrons are not relativistic at the moment they are emitted from the cathode, as they have not yet experienced any acceleration. The phase of the electric field seen by a given electron changes during the acceleration process, making it necessary to carefully phase the RF in the structure relative to the arrival time of the photocathode laser pulse. At a longitudinal distance s from

the cathode, the phase of the electric field seen by an electron is given by

$$\phi = \phi_0 + k \int_0^s \left(\frac{\gamma(\tilde{s})}{\sqrt{\gamma(\tilde{s})^2 - 1}} - 1\right) d\tilde{s}, \tag{1.13}$$

where ϕ_0 is the injection phase of the electron and γ is its instantaneous energy (normalized by mc^2) at position s. The function $\gamma(s)$ must satisfy the differential equation for energy conservation which takes the form

$$\frac{d\gamma}{ds} = \alpha k[\sin\phi + \sin(\phi + 2ks)], \tag{1.14}$$

where $\alpha = eE_0/2mc^2k$ is the so-called *acceleration factor*, which may also be regarded as a normalized vector potential, or as the fraction of rest energy an electron may receive in one radian of the wave. Equations (1.13) and (1.14) constitute a pair of coupled differential equations for γ and ϕ as functions of longitudinal position s. Kim derives the following approximate analytical solutions [2]:

$$\phi = \frac{1}{2\alpha \sin\phi_0}[\sqrt{\tilde{\gamma}^2 - 1} - (\tilde{\gamma} - 1)] + \phi_0, \tag{1.15}$$

$$\gamma = \gamma_0 + \alpha[ks\sin\phi + \frac{1}{2}(\cos\phi - \cos(\phi + 2ks))], \tag{1.16}$$

where $\tilde{\gamma} = \gamma_0 + 2\alpha\sin(\phi_0)ks$ is the lowest order approximation for γ and γ_0 is the initial energy of the electron. Since the governing equations are controlled by two unitless parameters (the acceleration factor α and the injection phase ϕ_0) this treatment has fairly universal applicability. When considered as a function of s the expression for the phase of the electron asymptotically approaches the value $\phi_\infty = \phi_0 + \frac{1}{2\alpha\sin\phi_0}$. Requiring that this asymptote correspond with the crest of the RF (and the maximum accelerating field) at $\phi_\infty = \pi/2$ produces a simple transcendental equation for the optimal injection phase:

$$(\pi/2 - \phi_{opt})\sin(\phi_{opt}) = 1/(2\alpha). \tag{1.17}$$

For the photoinjector at the UCLA Neptune Laboratory, for example, the value of the acceleration factor is $\alpha = 1.5$, giving an optimal injection phase of 69.1°, or approximately 21° behind the crest of the RF. It should be noted that Kim's theory breaks down for small values of ϕ_0 or α. The conditions for validity of the theory may be stated as: $\alpha \geq 0.9$ and $\phi_0 \geq \pi/4$ [3]. A slightly modified approach valid at smaller values of injection phase has been proposed by Gao [4].

Equations (1.15) and (1.16) provide an approximate analytical description of the effect of the acceleration process on the longitudinal phase space distribution of the electron beam. The process of photoemission is not an instantaneous event, owing to the fact that the drive laser pulse has some nonzero duration, typically on the order of picoseconds. Consequently, electrons are emitted with a distribution in initial phase. This is illustrated in Fig. 1.2, where we plot the phase space distrubutions predicted by Eqs. 1.15 and 1.16 for the Neptune parameters, with a spread in initial phase corresponding to a 10 ps square pulse. In part (a) the central injection phase is $\langle\phi_0\rangle = \phi_{opt} = 69.1°$ and in part (b) it is chosen to be $\langle\phi_0\rangle = 55.3°$. In the case of part (a) the choice of injection phase results in a final distrubution centered about the peak of the RF, while the choice of part (b) results in a distrubtion with maximum energy and minimal energy spread.

In practice, the injection phase is chosen to lie close to ϕ_{opt} as given by Eqn. (1.17), as this choice has been found to minimize the RF contribution to the transverse emittance [2]. With this choice of injection phase the emittances take the following forms for the case of a Gaussian distribution:

$$\epsilon_{x,N}^{rf} = \frac{\alpha k^3 \sigma_x^2 \sigma_z^2}{\sqrt{2}} \quad ; \quad \epsilon_{z,N}^{rf} = \sqrt{3}(\gamma_f - 1) k^2 \sigma_z^3 \tag{1.18}$$

The resulting longitudinal phase space of the beam upon exiting the photoinjector has a chirp in energy, with higher energy particles at the head of the beam and

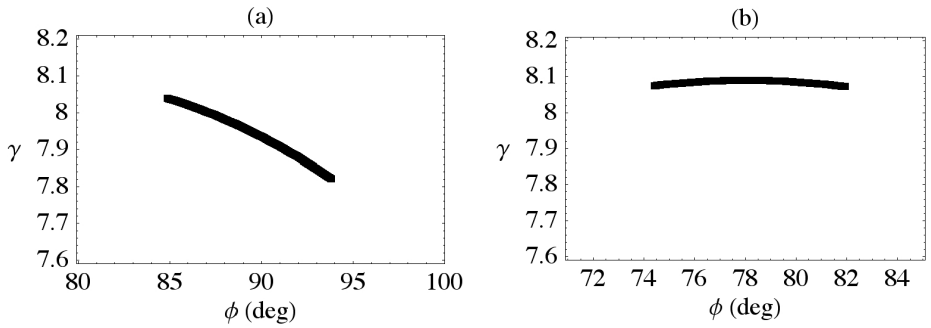

Figure 1.2: Plots of longitudinal phase space.

lower energy particles at the tail, as seen in part (a) of Fig. 1.2. The chirp is not linear but rather possesses a curvature imparted by the sinusoidal variation of the electromagnetic accelerating force. This chirp may be reduced, enhanced, or reversed in sign by appropriate phasing of the electron beam upon injection into whatever standing-wave or travelling-wave structure is used for post-acceleration of the particles following the initial acceleration in the photoinjector. There is also a distribution in initial energy, called the intrinsic (or uncorrelated) energy spread, due to the temperature of the cathode and the spectral width of the laser pulse. The intrinsic energy spread corresponds with the vertical thickness of the curves plotted in Fig. 1.2.

There is also a longitudinal compression produced by the variation in acceleration of the bunch from head to tail. The compression factor is given by differentiating the equation for the asymptotic phase with respect to ϕ_0:

$$\frac{d\phi_\infty}{d\phi_0} = 1 - \frac{\cos\phi_0}{2\alpha \sin^2\phi_0} \tag{1.19}$$

For the Neptune parameters, this gives a compression factor of 0.86. It should be noted that this represents the compression produced solely by RF effects. The expansion of the beam at low energy under the influence of its internal space

charge forces tends to counteract this compression.

1.2.2 Space Charge Effects

The electromagnetic self-forces of the electron beam are generally referred to as space charge, a terminology borrowed from plasma physics. In principle, the action of the internal space charge forces can be accounted for by considering the self-consistent evolution of the beam's distribution function $f(\mathbf{r}, t)$ under the Vlasov equation, in the presence of the externally applied accelerating fields. In practice, a direct analytical solution of this sort is not generally feasible. To properly gauge the effects of space charge on the evolution of the beam inside a photoinjector it is therefore often necessary to resort to one of a variety of photoinjector modeling codes, such as PARMELA or HOMDYN. The qualitative effects in longitudinal phase space include: an expansion of the bunch length during the acceleration process (while the bunch is nonrelativistic and the space charge forces are not yet diminished by the relativistic $1/\gamma^2$ dependence) and an increase in intrinsic (uncorrelated) energy spread, resulting in an increase in the longitudinal emittance.

An approximate analytical treatment of the emittance dilution due to space charge is provided by Kim [2]. The beam is assumed to be cylindrically symmetric with a transverse to longitudinal aspect ratio less than or equal to unity ($\zeta = \sigma_x/\sigma_z \leq 1$). His analysis relies upon deriving the energy scaling of the field components under a quasi-electrostatic assumption in the rest frame of the beam and then separating out the $1/\gamma^2$ dependence of the space charge force $\mathbf{F}_{sc}$ to obtain a geometrical form factor $\mathcal{F}$ that is a slowly varying function of γ. This may be written

$$\mathbf{F}_{sc} = \frac{1}{\gamma^2}\mathcal{F}(\gamma, \delta\mathbf{r}) \tag{1.20}$$

where $\delta\mathbf{r}$ is the position of the particle relative to the bunch centroid. The momentum kick imparted to a test particle in the bunch may then be written

$$\delta\mathbf{p}_{sc} = \int \mathbf{F}_{sc}\, dt = \frac{1}{c}\int \frac{1}{\gamma^2\beta}\mathcal{F}(\gamma, \delta\mathbf{r})\, ds \tag{1.21}$$

Due to the $1/\gamma^2$ scaling, the most significant part of the momentum kick is delivered close to the cathode where the bunch is nonrelativistic. Consequently, the function $\mathcal{F}$ may be evaluated at $\gamma = 1$, and the equation of motion Eq. (1.14) may be evaluated at $s = 0$ and then used to replace the integration over ds by one over $d\gamma$. This produces the result

$$\delta\mathbf{p}_{sc} = \frac{mc\ \mathcal{F}(1)}{eE_0 \sin\phi_0}\int_1^{\gamma_f} \frac{d\gamma}{\gamma^2\beta} \tag{1.22}$$

For large values of γ_f the integral evaluates to $\pi/2$. Defining the normalized field $\mathcal{E}(x, y, z) = (4\pi\epsilon_0/e\lambda_0)\ \mathcal{F}(1, \delta\mathbf{r})$, where λ_0 is the line charge density at the bunch center, the space charge contributions to the emittances as obtained via Eqs. (1.8)-(1.10) are given by

$$\epsilon_{i,N}^{sc} = \frac{\pi I}{4\alpha k \sin\phi_0\ I_A}\mu_i(\zeta) \quad ; \quad i = x, z \tag{1.23}$$

where $\zeta = \sigma_x/\sigma_z$ is the aspect ratio of the beam, I is the beam current, and $I_A = 4\pi\epsilon_0 mc^3/e$ is the *Alvén* current. The quantities μ_i are dimensionless form factors derived from the second moments of the distribution:

$$\mu_x(\zeta) = \sqrt{\langle\mathcal{E}_x^2\rangle\langle x^2\rangle - \langle\mathcal{E}_x x\rangle^2} \tag{1.24}$$

$$\mu_z(\zeta) = \sqrt{\langle\mathcal{E}_z^2\rangle\langle z^2\rangle - \langle\mathcal{E}_z z\rangle^2} \tag{1.25}$$

Kim obtains approximate analytical expressions for the case of a Gaussian:

$$\mu_x(\zeta) \approx \frac{1}{3\zeta + 5}\ ;\ \mu_z(\zeta) \approx \frac{1.1}{1 + 4.5\zeta + 2.9\zeta^2}. \tag{1.26}$$

Due to the variation in space charge force along the bunch the resulting contribution to the intrinsic energy spread for a Gaussian bunch as a function of longitudinal position is given by:

$$\Delta\sigma_\gamma^{sc}(z) = \frac{\pi}{2}\frac{mc^2}{eE_0\sigma_z \sin\phi_0}\frac{I}{I_A}G(z/\sigma_z) \tag{1.27}$$

where G is a complicated integral function, which is defined in Ref. [5]. The longitudinal space-charge expansion of the beam has not been treated analytically except in the case of a large aspect ratio beam (i.e. a *pancake* beam) [6, 7], in which case the above theory fails. And since the emittance growth derived above occurs primarily in the vecinity of the cathode, the values of σ_x and σ_z used can be treated as the RMS dimensions of the drive laser pulse.

1.2.3 Combining the RF and Space Charge Contributions

Since the space-charge and RF contributions to the emittances are not truly decoupled, it is not immediately clear how to combine them in order to obtain the total emittance. It can be shown, however, that the total emittance lies between the direct sum and the root-square sum of the two contributions [2]:

$$\sqrt{(\epsilon_{i,N}^{th})^2 + (\epsilon_{i,N}^{rf})^2 + (\epsilon_{i,N}^{sc})^2} < \epsilon_{i,N} < \epsilon_{i,N}^{th} + \epsilon_{i,N}^{rf} + \epsilon_{i,N}^{sc} \tag{1.28}$$

Note that although it is generally small compared with the RF and space-charge contributions, we have included for completeness the contribution from thermal emittance at the cathode, which may be written

$$\epsilon_{i,N}^{th} = \sqrt{\frac{kT}{mc^2}}\sigma_i \ . \tag{1.29}$$

Comparison of Eqs. (1.23) and (1.18) indicates that for constant bunch charge the space charge contributions to the emittances scale linearly with peak beam current and therefore inversely with the laser pulse length (if the aspect ratio is

scaled accordingly), while the RF contributions scale quadratically or cubically with pulse length for x and z respectively. Consequently, there exists an optimal value for the laser pulse length at which the emittance in one phase plane or the other is minimized (i.e. balanced between the two competing effects). In this regard, the transverse emittance is usually of greater concern, and in practice the optimal pulse length is determined experimentally or by use of photoinjector modeling codes so as to minimize transverse emittance. For a good example of this, see Ref. [8]. Generally the optimal pulse length is on the order of 10 degrees of RF phase. For an S-Band gun operating at 2.856 GHz, this corresponds to 10 ps, which is the approximate (full-width) laser pulse length on the cathode at the UCLA Neptune Laboratory. The transverse space charge emittance can be reduced by using a solenoidal lens to remove linear correlations between the transverse and longitudinal phase planes. This process, called space charge compensation is discussed in the following section.

1.2.4 Space Charge Emittance Compensation

The space charge contribution to the transverse emittance growth in a photoinjector may be regarded as the result of a correlation in phase space which forms between the radial and longitudinal coordinates due to the longitudinal variation of the space charge forces within the beam. When the correlated particle distribution is projected onto the transverse phase plane, the result appears as a growth in transverse emittance. As mentioned previously, when coupling occurs between the phase planes the emittances are no longer invariant quantities. It was proposed by Carlsten that a focusing lens may be used to remove the linear correlation between x and z and thereby undo its contribution to the space charge emittance which, for a space charge dominated beam, is the primary component

of the overall emittance growth in the photoinjector [9]. Consequently, proper employment of this technique can result in a significant improvement in overall transverse emittance.

A simple model which illustrates the basic mechanisms involved is given by Carlsten, who considers the evolution of the edge boundaries of a cylindrical pillbox beam under linear space charge forces combined with a thin lens [9]. This treatment ignores the RF contribution and the acceleration of the beam. The transverse component of the space charge force, Eq. (1.20), is assumed to be linear and invariant along the beam trajectory, taking the form $\mathcal{F}_x = m_e(x/R_0)\lambda(z)$, where m_e is the electron mass, R_0 is the initial radius of the pillbox beam, and λ is the normalized force. We have chosen x as our transverse variable for consistency although due to the cylindrical symmetry we could alternatively have chosen y or the polar coordinate $r = \sqrt{x^2 + y^2}$. The beam is postulated to be initially located at longitudinal position $s = -D$, with its radial edge initially at R_0. The lens, positioned at $s = 0$, has focal length f. At position s downstream of the lens, the radial edge boundary $R(z, s)$ and its derivative $R' = dR/ds$ then have the forms

$$R(z,s) = R_0 + \frac{1}{2}\lambda(z)(D+s)^2 - \frac{1}{f}[R_0 s + \frac{1}{2}D^2\lambda(z)s] \tag{1.30}$$

$$R'(z,s) = \lambda(D+s) - \frac{1}{f}(R_0 + \frac{1}{2}\lambda(z)D^2) \tag{1.31}$$

The quantities R and R' represent the edges of a distribution in the $x - x'$ phase space, with each longitudinal slice of the beam corresponding to a line segment in this phase space. The area of the distribution is nonzero when the slopes of these lines are different for different longitudinal positions within the bunch. That is, if the quantity R'/R is a function of z. Consequently, the distribution is reduced to a single line in phase space (and therefore the linear space charge emittance

is zero) if R'/R is made to be independent of z. This is found to occur at the position $s = s_0$ satisfying

$$\frac{1}{f} = \frac{2(D + s_0)}{s_0^2} \tag{1.32}$$

Substituting Eq. (1.32) back into (1.30), one finds that $R = R' = 0$ when s_0 has the critical value $s_c = \sqrt{D^2 + 2R_0/\lambda}$. For $s_0 \leq s_c$ the analysis fails because the beam edges cross paths and so the assumption that the space charge force is constant cannot hold. For $s_0 > s_c$ a beam waist occurs. The conclusion, then, is that a focusing lens can be used to eliminate the linear space charge emittance, and one expects this to occur immediately following a beam waist (i.e. focus).

While this treatment is very elementary, it helps illuminate the basic mechanism at work. Serafini and Rosenzweig have examined space charge emittance compensation in a more rigorous theoretical framework using the transverse RMS envelope equation, with an extended hard-edged solenoid field as the focusing element [10]. The envelope equation is a differential equation which governs the evolution of the RMS transverse bunch size σ_x in the paraxial limit under the influence of space-charge (κ_s), acceleration (γ'), emittance pressure, and external focusing (K_x^2):

$$\frac{\sigma_x''}{\sigma_x} + \frac{\sigma_x'}{\sigma_x}\left(\frac{\gamma'}{\beta^2\gamma}\right) + K_x^2 - \frac{\kappa_s}{\sigma_x^2\beta^3\gamma^3} - \frac{\epsilon_{x,N}^2}{\sigma_x^4\beta^2\gamma^2} = 0 \tag{1.33}$$

A simplified heuristic version of the Serafini-Rosenzweig model is obtained by dividing the beam into longitudinal slices of width dz and examining the transverse evolution of the slice at longitudinal position z. Equation (1.33) is linearized in the limit of zero acceleration ($\gamma' = 0$), and the solution for the RMS beam size is expanded as a perturbation $\delta\sigma_x$ about the Brillouin equilibrium value $\sigma_{eq}(z) = \sqrt{\kappa_s(z)/[(\beta\gamma)^3 K_x^2]}$, which yields the small-amplitude equation $\delta\sigma_x''(z) = -2K_x^2\delta\sigma_x(z)$. Here, the slice perveance is $\kappa_s(z) = I(z)/2I_A$ where $I(z)$ is the current of the slice at z and I_A is the Alven current. With the initial

conditions $\sigma_x = \sigma_0 < \sigma_{eq}$ and $\sigma_x' = 0$ at the cathode ($s = 0$), the resultant solution for σ_x is

$$\sigma_x(z,s) = \sigma_{eq}(z) + [\sigma_0 - \sigma_{eq}(z)]\cos(\sqrt{2}K_x s) \tag{1.34}$$

This sinusoidal oscillation about the equilibrium value constitutes a transverse plasma oscillation. This oscillatory behavior is reflected also in the transverse emittance which is then given by $\epsilon_{x,N}(s) = \gamma\beta\sqrt{\langle\sigma_x^2\rangle\langle\sigma_x'^2\rangle - \langle\sigma_x\sigma_x'\rangle}$, where the angle brackets denote an average over all slices, weighted by the current density. This yields the result

$$\epsilon_{N,x}(s) \approx \frac{1}{2}\gamma\beta K_x\sigma_0\sigma_{eq}(z_0)\frac{\delta I_{rms}}{I_p}\left|\sin(\sqrt{2}K_x s)\right| \tag{1.35}$$

where δI_{rms} is the averaged RMS deviation from the peak current value I_p which occurs at point z_0. From Eqs. (1.34) and (1.35) we see that the minimum of σ_x occurs at $\sqrt{2}K_x z = 2\pi$ which is also the location of the second null in $\epsilon_{x,N}$. This behavior persists in a qualitative sense even when the acceleration of the beam is properly taken into account, although the oscillation is no longer sinusoidal in nature.

In contrast to the illustrative model just presented, the complete Serafini-Rosenzweig analysis (which utilizes the full RMS envelope equation) successfully explains the major physical features of the emittance compensation process, and can be applied to long integrated photoinjectors (i.e. which are joined to a post-accelerating linac) or to cases where there is a drift region between a small (few cell) photoinjector and a longer (many cell) linac section. In the latter case, which is the scenario at the UCLA Neptune Laboratory, the usual experimental procedure is to place a solenoidal coil immediately after the RF gun and to place the entrance of the linac section immediately after the beam waist so that the space charge emittance growth from the gun is fully compensated and the

beam is well-collimated during post-acceleration, which effectively "locks in" the minimized emittance value by virtue of the $1/\gamma^2$ dilution of the space-charge force. The solenoid is generally positioned such that the magnetostatic field generated by it is zero at the cathode, in order to avoid a longitudinal magnetic field contribution to the transverse emittance. To this end, a secondary (bucking) coil is sometimes placed behind the gun in such a way as to zero the magnetic field in the cathode plane.

1.2.5 Cathode Image Charge Limit

For beams of high charge and/or current density, the force exerted on the beam by its image charge in the conducting plane of the cathode becomes comparable to the RF accelerating force. This results in a lengthening of the bunch due to decceleration of the tail particles and imposes an upper limit on the extractable charge [11]. A simple model which treats the beam as a flat disk of charge with a Gaussian transverse profile yields a maximum surface charge density of $\Sigma_{max} = \epsilon_0 E_0 \sin\phi_0$ and an extracted charge Q of [12]

$$Q = Q_0 \times \begin{cases} \frac{\Sigma_{max}}{\Sigma_0}[1 + \ln(\frac{\Sigma_0}{\Sigma_{max}})] & , \quad \Sigma_0 \geq \Sigma_{max} \\ 1 & , \quad \Sigma_0 < \Sigma_{max} \end{cases} \tag{1.36}$$

where Q_0 and $\Sigma_0 = Q_0/(2\pi\sigma_x^2)$ are the charge and surface charge density which would be extracted in the absence of the image charge effect. The saturation begins when $\Sigma_0 = \Sigma_{max}$ at which point the extracted charge is

$$Q_{sat} = 2\pi\sigma_x^2 \epsilon_0 E_0 \sin\phi_0 \tag{1.37}$$

Although additional charge may be extracted beyond this saturation value by further increasing Q_0, the returns are logarithmically diminished in accordance with Eq. (1.36). A more sophisticated analysis, valid for beams of nonzero

duration, is derived by Travier using the relativistic Child-Langmuir formalism and treating the beam as a voltage gap of width d [3]. This approach yields a saturation charge of

$$Q_{sat} = \frac{2I_A\sigma_x^2\sigma_t}{9}\sqrt{\frac{4\pi}{d}}\left(\frac{eE_0\sin\phi_0}{mc^2}\right)^{3/2} \tag{1.38}$$

where σ_t is the RMS duration of the laser pulse on the cathode. This result reduces to that of Eq. (1.37) in the limit of short pulses, except for a multiplicative constant that is on the order of unity. For typical pulse durations (on the order of 1 to 10 ps) the correction for nonzero duration is small and Eq. (1.37) may be used instead. However, in order to avoid bunch lengthening, Traviers recommends that the bunch charge not exceed one-fifth the saturation value:

$$Q_{max} = \frac{1}{5}Q_{sat} = \frac{2}{5}\pi\sigma_x^2\epsilon_0 E_0\sin\phi_0 \tag{1.39}$$

Rosenzweig derives an expression for the final current density of a pulsed photoinjector in the limit where $Q_0 << Q_{max}$ (or equivalently $\Sigma_0/\Sigma_{max} << 1$) [13]. Let the temporal photon distribution of the drive laser pulse be $\mathcal{E}(t)$. The emitted photocurrent at the cathode as a function of time is then $I_0(t) = e\eta_q\mathcal{E}(t)$, where η_q is the effective *quantum efficiency* (i.e. number of emitted electrons per incident photon). The longitudinal force experienced by an electron emitted at time t_0 is then $F_z = -eE_0\sin\phi_0 + (e\Sigma_0/\epsilon_0 Q_0)\int_{-t_0}^{\infty} I_0(t)dt$. This may be rewritten as $F_z = -eE_0\sin\phi_0[1 - \frac{\Sigma_0}{\Sigma_{max}}G(t_0)]$ where $G(t_0) \equiv \frac{1}{Q_0}\int_{-t_0}^{\infty} I_0(t)dt$. Assuming the lowest-order form $\tilde{\gamma}$ for the acceleration in Eq. (1.16) but replacing the acceleration factor α with the form $\alpha[1 - \frac{\Sigma_0}{\Sigma_{max}}G(t_0)]$, which includes the longitudinal space-charge contribution, the arrival time t of the particle downstream at point s, where the particle is assumed to have attained ultrarelativistic energy, is found to be given by

$$t \approx t_0 + \frac{s}{c} + \frac{1}{2k\alpha c\sin\phi_0}\left[\frac{1}{1 - \frac{\Sigma_0}{\Sigma_{max}}G(t_0)} - 1\right] \tag{1.40}$$

The final beam current is therefore given by

$$I(t) = \frac{I_0}{\partial t/\partial t_0} \approx \frac{I_0(t_0)}{1 + \frac{\Sigma_0/\Sigma_{max}}{Q_0 2k\alpha c \sin\phi_0} I_0(t_0)} \tag{1.41}$$

The denominator represents the expansion factor due to space-charge. In order to obtain the explicit t-dependence on the right-hand side, it is necessary to invert Eq. (1.40) and insert the result for t_0 as a function of t into Eq. (1.41). In the limit of $\Sigma_0/\Sigma_{max} >> 2k\alpha\sigma_z$ the final current in Eq. (1.41) approaches the asymptotic value

$$I_{max} = \frac{Q_0 2k\alpha c \sin\phi_0}{\Sigma_0/\Sigma_{max}} = \frac{e\epsilon_0 E_0^2 \sin^2\phi_0}{mc^2} \int dA \tag{1.42}$$

where $\int dA = Q_0/\Sigma_0$ is the transverse area of the beam. Eq. (1.42) represents the current limit due to space-charge expansion of the beam. The factor $e\epsilon_0 E_0^2 \sin^2\phi_0/mc^2$ is analogous to the Child-Langmuir current density for pulsed sources [13].

1.2.6 Summary and Limits on Transverse Brightness

We may conclude from the preceding analyses that the laser pulse duration and injection phase are somewhat predetermined by an interest in obtaining optimal beam quality. The optimal temporal shape of the laser pulse has also been investigated and has been found to be a square pulse. The end result is that the longitudinal phase space of a beam generated by an RF photoinjector tends to invariably end up resembling that of Fig. 1.2 (a).

One may increase the peak current by scaling the total charge, but in doing so the other photoinjector parameters must also be scaled appropriately in order to prevent blowup of the transverse emittance. In the end, although the peak current increases under such charge scaling, the transverse brightness is diminished by the resulting dilution of the transverse emittance.

Rosenzweig and Colby have derived the general charge scaling laws for an emittance compensated photoinjector [11]. This scaling relies upon keeping the space charge term in the envelope equation $\kappa_s/(\sigma_x^2\beta^3\gamma^3)$ constant. Noting that the beam perveance is given by $\kappa_s = 2I/I_0$ and that the beam current goes as $I \propto Q/\sigma_z$, we see that this can be accomplished by scaling the bunch dimensions as the cube root of charge: $\sigma_{x,z} \propto Q^{1/3}$. It follows from Eqns. (1.29), (1.18) and (1.23) that the thermal, RF, and space charge emittance contributions scale as $\epsilon_{x,N}^{th} \propto Q^{1/3}$, $\epsilon_{x,N}^{rf} \propto Q^{4/3}$, and $\epsilon_{x,N}^{sc} \propto Q^{2/3}$ respectively. If the various contributions are represented by ϵ_0^{th}, ϵ_0^{sc}, and ϵ_0^{rf} for an emittance compensated photoinjector with charge Q_0 and current I_0, then taking the lower limit in Eq. (1.28) gives the following scaling for the transverse emittance:

$$\epsilon_{x,N} = \sqrt{(\epsilon_0^{th})^2\ q^{2/3} + (\epsilon_0^{sc})^2\ q^{4/3} + (\epsilon_0^{rf})^2\ q^{8/3}} \tag{1.43}$$

where $q \equiv Q/Q_0$. This equation may be fitted to data or simulation results of emittance versus charge to extract the parameter values ϵ_0^{th}, ϵ_0^{sc}, and ϵ_0^{rf} for a given photoinjector design. The transverse brightness then scales according to

$$\mathcal{B} = \frac{2I_0}{(\epsilon_0^{th})^2 + (\epsilon_0^{sc})^2\ q^{2/3} + (\epsilon_0^{rf})^2\ q^{4/3}} \tag{1.44}$$

We see immediately that brightness decreases with higher charge. Furthermore, for any reasonable value of the bunch length, the space charge term will dominate, and so the optimal brightness may be written [11]:

$$\mathcal{B} = 16(2\pi)^{9/2}\alpha k_z \frac{I_A(1+\frac{3}{5}\zeta)^2}{\sigma_z\zeta^2} \tag{1.45}$$

This formula provides a rule-of-thumb value for the achievable brightness of a photoinjector. For experiments that require an electron beam with a higher brightness, a shorter bunch length, or a different longitudinal bunch shape than what the photoinjector provides under normal operating conditions, one may

employ one of various techniques to manipulate the longitudinal distribution of particles within the bunch. Several such techniques as well as applications which may benefit from them are discussed in the following two sections.

1.3 Methods of Longitudinal Compression

Attempts to manipulate the longitudinal shape of energetic beams of charged particles date back to the introduction in the 1960's and 1970's of the magnetic chicane, a device which can either separate or compress a beam of electrons along the direction of motion, by utilizing the differences in path-length traversed by particles of different energies. The original proposal for this device came in the form of a U.S. patent, submitted by Leboutet and Pinel in 1959 and approved in 1962 [14]. Although the device was originally intended as a means of increasing the length of electron bunches, the technology has subsequently been adapted as a means of compressing them to short (sub-picosecond) time scales. Other compression mechanisms have also been proposed, including velocity bunching [15] and alternative dispersionless configurations of bending beamlines. In the latter category, the *dogleg* or *dispersionless translating section* can be used as a means of compressing beams or of otherwise manipulating the longitudinal phase space to shape the time-current profile of the beam [16]. All of these methods, however, rely upon taking advantage of strong correlations between energy and longitudinal position in order to shorten the electron bunch.

1.3.1 Magnetic Chicane

An electron beam may be compressed or expanded in the longitudinal dimension by using dispersive magnetic elements to produce trajectories of different total

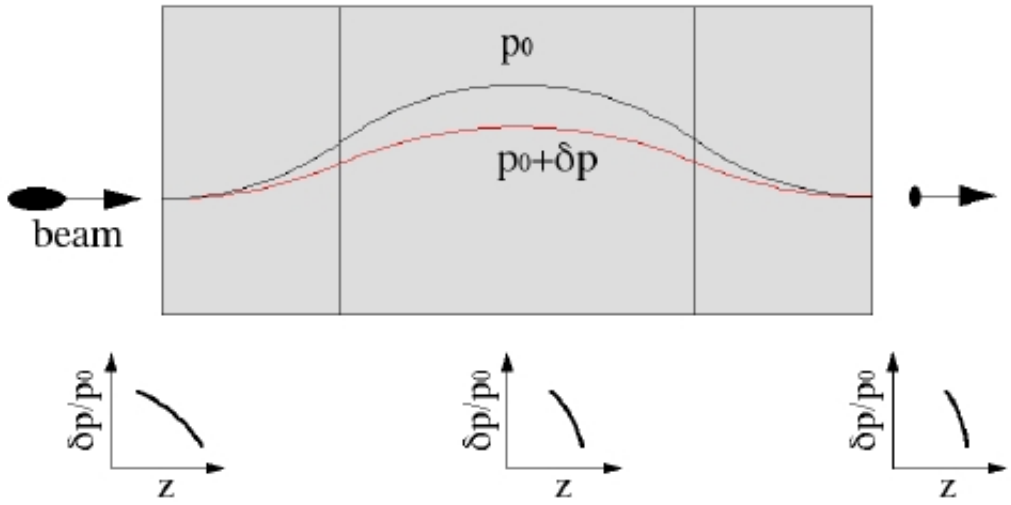

Figure 1.3: Cartoon of a simple chicane compressor.

path-length for particles of different energies. The simplest dispersive magnetic element is one which produces a uniform magnetostatic field over a finite region of space (i.e. a dipole magnet). The trajectory of an electron bunch with average momentum p_0 passing through such a magnet with field strength B_0 will be bent in the plane perpendicular to the magnetic field lines by an angle $\theta = \Delta s/R_0$ where Δs is the arclength traversed along the beam trajectory and $R_0 = p_0/eB_0$ is the bend radius. When applied to a beam which has a strong correlation between energy and longitudinal position, the resultant *longitudinal dispersion* (that is the shift in position of high-energy particles relative to low-energy particles within the bunch due to differences in energy) will cause the beam to either expand or contract in length, depending upon the sign of the correlation.

A single dipole magnet would bend the electron beam's path away from its original trajectory, which is often undesirable. Assuming that one wishes to return the electron beam to a path colinear with its original one, then the simplest configuration for a magnetic compressor of this type is a set of three consecutive

dipole magnets where the first and third magnet are identical, but the field in the middle magnet is reversed, and is either twice as strong or twice the length of the end magnets. This configuration, called a magnetic chicane, is a commonly employed method of bunch compression in linear accelerator systems. A cartoon drawing of a chicane is shown in Fig. 1.3. The trajectory of a particle with the central momentum of the bunch p_0 is shown in black and the trajectory of an off-energy particle with momentum $p_0+\delta p$ is shown in red. Due to the different bend radii, the higher-energy particle will traverse a shorter path through the device and will therefore move forward in longitudinal position z within the bunch. For a bunch that is initially *chirped* such that the higher energy particles lie in the tail of the beam (see the subset plots of momentum error vs. z in Fig. 1.3), the tail particles will move forward and the particles at the head will move backward within the bunch. The result is that the bunch is longitudinally compressed at the exit of the device. The required chirp may be imparted to the beam by choosing the phase of the RF in one of the post-accelerating structures downstream of the photoinjector gun such that the beam is injected forward of the crest of the peak accelerating field. The chirp may alternatively be created in the photoinjector itself, but as discussed in Section 1.2.1, operating the photoinjector away from the optimal phase ϕ_{opt} degrades the emittance of the beam.

The magnitude of the compression is measured by the so-called momentum compaction α_c which is related to the path-length difference ξ between the particle with momentum p_0 and that of momentum $p_0 + \delta p$ by way of

$$\xi = \Delta s \ \alpha_c \ \frac{\delta p}{p_0} \tag{1.46}$$

where $\Delta s = s - s_0$ is the total path-length traversed by the central particle from the entrance to the exit of the device. The quantity $\Delta s \ \alpha_c$ is proportional to the *longitudinal dispersion* η_z, which is defined as $\partial z/\partial\delta$ where z is longitudinal

position within the bunch and $\delta = \delta p/p_0$. The quantity $\partial z/\partial\delta$ is an element of the 6×6 *transport matrix* of partial derivatives of final coordinates with respect to initial ones. This matrix formalism will be presented in Chapter 2, where its use in calculating quantities such as η_x and η_z for compound systems of magnets will be explained. The momentum compaction may be written as an integral over the curvature $k(s)$ of the central trajectory and the horizontal dispersion function $\eta_x(s)$ as

$$\alpha_c = \frac{1}{\Delta s} \int_{s_0}^{s_f} k(s)\ \eta_x(s)\ ds \tag{1.47}$$

The dispersion function η_x may be regarded as the x-coordinate (relative to the bunch centroid), which is chosen to lie in the plane of the bend, of an off-energy particle with a momentum deviation of $\delta p/p_0 = 1$ expressed as a function of longitudinal position s. The dispersion function for a simple chicane of the sort shown in Fig. 1.3 may be derived using the previously mentioned matrix formalism of Chapter 2. Plots of the dispersion function and the curvature (normalized by the magnitude of the bend radius R) as functions of integrated arc-length s traversed along the beam trajectory are superimposed in Fig. 1.4. Their product is highlighted by the solid curve, making clear that for such a system the area under the solid curve [and hence the momentum compaction as defined in Eq. (1.47)] is negative, and therefore the path-length difference ξ is negative for particles with momentum greater than p_0 and positive for particles with momentum less than p_0.

Additional design features may be implemented to improve the performance or versatility of the device, such as splitting the middle magnet into two identical magnets, the use of edge angles on the entrance and exit pole faces to provide vertical focusing, or the introduction of other magnetic elements between the bend magnets to focus or to correct nonlinear effects. Furthermore, although

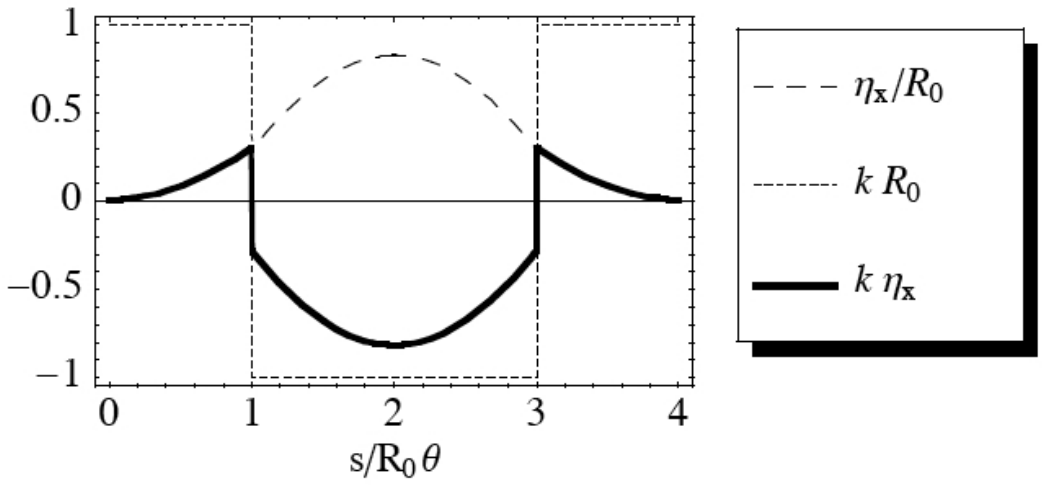

Figure 1.4: Plots of the curvature and dispersion function for a chicane.

the description we have presented illuminates the basic mechanism for compressing the electron beam, various other physical effects may be important, some of which can have a negative impact on beam quality. These include space-charge effects which can cause degradation or bifurcation of the horizontal phase space distribution [17], and emittance increase due to coherent synchrotron radiation [18]. The minimum achievable pulse length obtainable is ultimately limited by the intrinsic energy spread of the beam and by the degree of RF curvature imposed upon the longitudinal phase space. Theoretical limits are in the tens of femtoseconds (RMS), if the beam is sufficiently short to start with, has sufficiently high energy, and the energy-time correlation is quite linear [19]. But to obtain the required (picosecond-level) pre-compression bunch length, an additional prior stage or stages of compression may be needed [20].

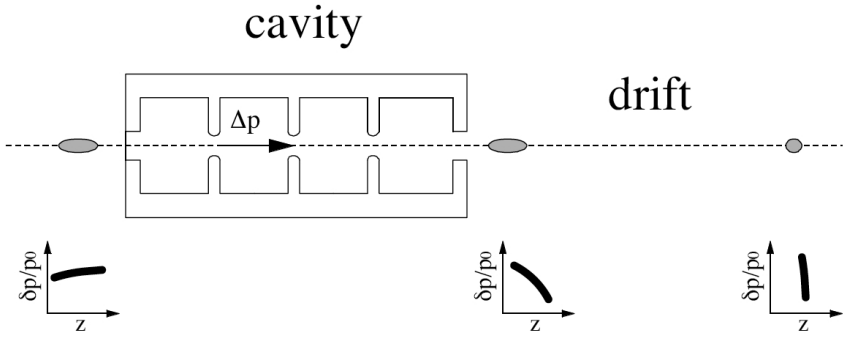

Figure 1.5: Illustration of ballistic bunching compression.

1.3.2 Velocity Bunching

Velocity bunching is a scheme which uses an accelerating RF structure to impart energy correlations onto a moderately relativistic electron bunch in order to produce a longitudinal compression. Two forms of this technique are represented in the literature, which we will refer to respectively as *ballistic bunching* and *phase space rotation* respectively, following the nomenclature of Ref. [21].

In ballistic bunching, the accelerating structure is phased so as to impart a negative chirp on the beam in the longitudinal phase space, with particles at the tail of the beam at higher energy than the head. The compression then occurs in the drift region following the accelerating structure, as differences in velocity permit the trailing high-energy particles to "catch up" to the lower energy particles at the head, thereby producing a net compression of the bunch. This technique requires that the central bunch energy be at most moderately relativistic, since the velocity differences between particles within the bunch will become smaller as the bunch becomes more energetic, thereby requiring longer and longer drifts in order to actualize the compression. The drift length L required to fully compress

the beam is related to the normalized beam energy γ by [21]

$$L = \frac{\gamma^3}{d\delta/dz} \tag{1.48}$$

where $\delta = \delta p/p_0$ is the fractional momentum deviation from the centroid momentum p_0 and z is longitudinal position within the bunch. The derivative in the denominator is intended to represent the slope of the chirp imparted to the beam distribution by the accelerating structure in the trace space of δ and z. This chirp is related to that prior to the accelerating structure used for the velocity bunching by the relation

$$\frac{d\delta}{dz} = \left(\frac{d\delta}{dz}\right)_{init} + k\frac{\Delta p_{max}}{p_0}\left(\frac{\sin\phi}{1+\frac{\Delta p_{max}}{p_0}\cos\phi}\right) \tag{1.49}$$

where k is the RF wavenumber, Δp_{max} is the maximum longitudinal momentum kick the structure imparts, and ϕ is the RF phase relative to the crest (i.e. the phase corresponding to maximum accelerating force).

An alternative method of velocity bunching proposed by Serafini and Ferrario in Ref. [15] relies upon producing a one-quarter rotation of the longitudinal phase space distribution of the electron beam using a traveling wave accelerating cavity with a phase velocity less than the speed of light. Compression is produced by imparting and then smoothly removing an energy-time correlation inside of the structure. The basic mechanism can be illuminated by examining the Hamiltonian for a particle of energy γ in a traveling wave with phase velocity v_r:

$$H(\phi,\gamma) = \gamma - \beta_r\sqrt{\gamma^2-1} - \alpha\ \cos\phi \tag{1.50}$$

Here ϕ is the phase of the particle relative to the crest of the wave, $\beta_r = v_r/c$, and α is the dimensionless acceleration factor defined in Section 1.2.1. Level sets of the Hamiltonian in the phase space of γ and ϕ are plotted in Fig. 1.6, for values of $\alpha = 0.2$ and $\gamma_r = \sqrt{1-\beta_r^2} = 12$. The separatrix is shown in bold and the

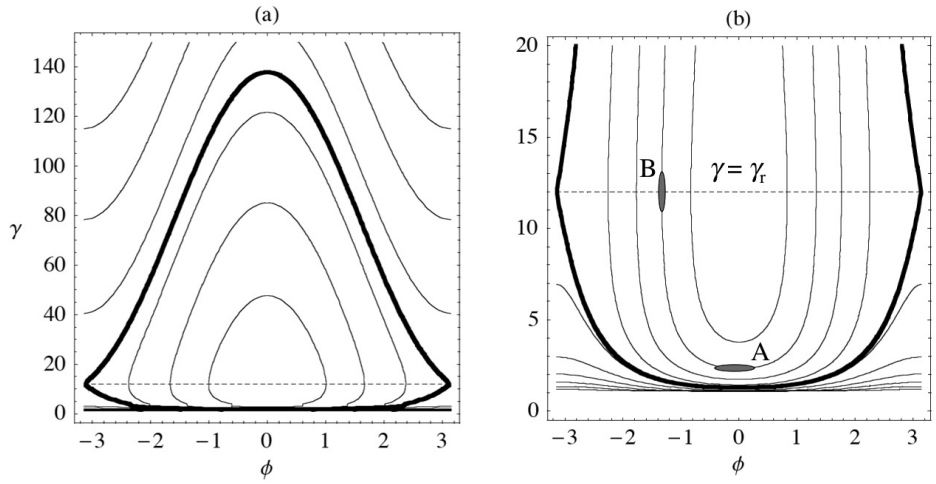

Figure 1.6: Illustration of phase space rotation velocity buching, showing (a) the full separatrix, in bold, and (b) a closeup of the bottom portion.

value of γ_r is marked by a horizontal dashed line. Part (a) of the figure shows the entire separatrix, while (b) is a closeup of the bottom portion of the phase space plot. Orbits lying within the separatrix are closed and represent the trajectories of particles trapped in an accelerating phase of the wave. An unchirped beam (i.e. with zero energy-time correlation and a small energy spread) injected into the wave with a moderately relativistic energy (point A) will slip back in phase as it is accelerated along the closed orbit in phase space and will arrive at point B where the beam energy is equal to the equivalent γ_r of the wave. As seen in the figure, the phase space contours become nearly parallel and vertical, so the movement of the electrons along these contours produces an inherent compression in phase, with the maximum compression occurring at point B.

If the initial energy spread were zero then under this model, the final bunch length would differ from zero only because of nonlinearities in the phase space

transformation imposed upon the bunch as it travels from point A to point B along the contours. Consequently, a reasonable picture of the compression requires inclusion of the intrinsic energy spread $\delta\gamma_0$. If $\delta\phi_0$ is the deviation from zero of the injection phase of a particle in the vecinity of point A and $\phi_r+\delta\phi_r$ is its phase upon extraction in the vecinity of point B, then equating the Hamiltonian at the two locations gives

$$\alpha\cos(\phi_r+\delta\phi_r)=\frac{1}{\gamma_r}-(\gamma_0+\delta\gamma_0)+\beta_r\sqrt{(\gamma_0+\delta\gamma_0)^2-1}+\alpha\cos\delta\phi_0 \qquad (1.51)$$

Expanding the cosines in power series to lowest order produces the result [15]

$$\frac{\delta\phi_r}{\delta\phi_0}=\frac{1}{2\delta\phi_0|\sin\phi_r|}\left[\delta\phi_0^4+\left(\delta\gamma_0/\alpha\gamma_0^2\right)^2\right]^{1/2} \qquad (1.52)$$

from which we see that the fractional compression is ultimately limited by a combination of the phase spread and the initial energy spread $\delta\gamma_0/\gamma_0$. In the limit where the wave phase velocity approaches the speed of light, the top of the separatrix in Fig. 1.6 moves upward and the contours asymptote toward vertical lines extending to infinite γ. In this case, a full quarter rotation in phase space can still be achieved by simply injecting the beam slightly forward in phase.

1.3.3 Dogleg Compressor

As a general rule, any nonisochronous configuration of bending magnets can be used for bunch compression. One such configuration, the dispersionless translating section, known in accelerator jargon as a *dogleg*, is shown in Fig. 1.7. This device consists of two bend magnets (shown as yellow wedges in the figure), whose bend angles are equal in magnitude but opposite in sign, with focusing optics in between (represented here by blue lenses). Its primary use is to switch the beam between two parallel beam lines. At user facilities, arrays of such configurations are used to divert the beam to one of several different experiments being hosted

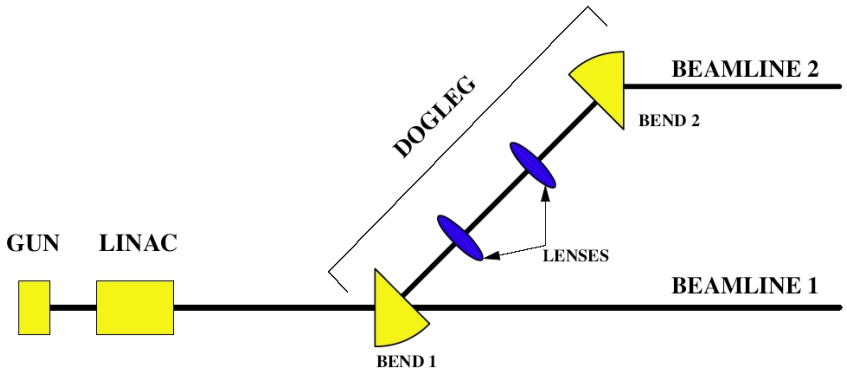

Figure 1.7: Drawing of a dogleg.

on separate beam lines.

The lenses (corresponding to magnetic quadrupole fields) are required in order to force the horizontal dispersion function and its derivative to zero at the exit of the device. This is illustrated in Fig. 1.8, which shows a plot of the dispersion function η_x, the curvature k which is nonzero only inside the bend magnets, and their product, denoted by the thick solid curve. Due to the positive excursions executed by the dispersion function in the bending regions, the total path-length traversed by an off-energy particle of momentum $p_0 + \delta p$ is greater than that of the design particle for positive δp and less than that of the design particle for negative δp. In other words, it has the opposite longitudinal effect to that of a chicane.

It should be noted that although a variety of different lens configurations may be used, the plots shown in Fig. 1.8 correspond with the simple layout of Fig. 1.7. However, regardless of the chosen setup of lenses between the bend magnets, the momentum compaction for a properly compensated dogleg (as will be shown explicitly in Chapter 3) is given by

$$\alpha_c = \frac{R_0}{\Delta s}(\frac{\pi}{2} - \sqrt{2}) = 0.156\frac{R_0}{\Delta s} \tag{1.53}$$

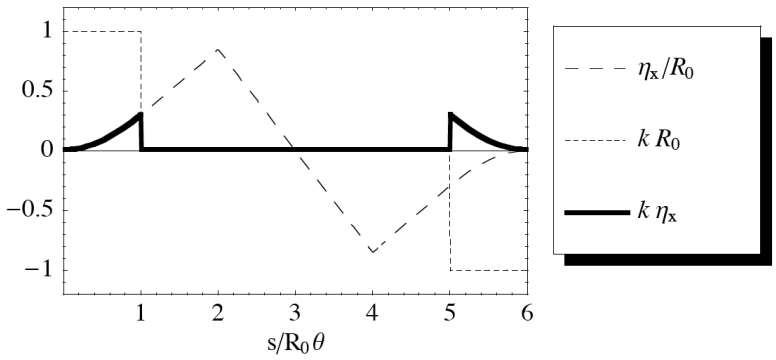

Figure 1.8: Example dispersion function for a dogleg.

Consequently, the value of the momentum compaction is positive in this case, opposite in sign to that of a chicane, as required by the physical description given above. The required energy-time chirp for compression therefore must also be positive ($d\delta/dz > 0$), with higher energy particles at the head of the bunch. This can be accomplished by appropriate phasing of the electron beam upon injection into the accelerator. The positive sign of the momentum compaction (or negative longitudinal dispersion) of the dogleg compressor is what ultimately makes possible the longitudinal bunch shaping technique, discussed in Chapter 3, which forms the core topic of this dissertation.

1.4 Applications of High-Brightness Ultrashort Beams

1.4.1 Inverse Compton Scattering

Pulses of x-rays with durations on the order of a few hundred femtoseconds are of interest in a variety of areas of research, including the probing of sub-molecular chemical and biological processes as well as the development of polarized proton sources for high energy physics applications. Scattering of an intense laser beam

off of a high-brightness bunch of electrons is a promising technique for the generation of ultrashort pulses of short-wavelength and narrow spectrum radiation [22], and has consequently been a subject of various recent experimental efforts [23, 24, 25]. The scattering of photons off of moving electrons is referred to as inverse Compton scattering (ICS). Scattered photons are upshifted in energy by a fractional amount

$$\frac{h\nu'}{h\nu} = \frac{1 - \beta\cos\alpha}{1 - \beta\cos\alpha' + (h\nu/\gamma mc^2)(1 - \cos\psi)} \tag{1.54}$$

where α and α' are the angles between the incoming and outgoing photons and the incident electron, ψ is the angle between the incoming and outgoing photons, ν and ν' are the incident and outgoing photon frequencies, h is Planck's constant, and $\beta = v/c$, $\gamma = U/mc^2$ are the normalized electron velocity and energy [26]. The scattering geometry is shown in Fig. 1.9 (a). If the photon energy is comparable with the relativistic electron energy, then the upshift becomes increasingly small, tending to values less than unity as the photon energy exceeds that of the electron. Therefore, assuming that the incident photon energy is small compared with the relativistic electron energy ($h\nu << \gamma mc^2$), the distribution given by Eq. (1.54) becomes peaked in the vecinity of $\psi \approx \alpha$ with a maximal value of

$$\left(\frac{h\nu'}{h\nu}\right)_{max} = \frac{2}{(1/2\gamma^2) + 2(h\nu/\gamma mc^2)} \tag{1.55}$$

The differential scattering cross-section is proportional to the square of the frequency distribution:

$$\frac{d\sigma}{d\Omega} = \frac{e^2}{mc^2}\left(\frac{h\nu'}{h\nu}\right)^2 \frac{X}{2\gamma^2(1 - \beta\cos\alpha)^2} \tag{1.56}$$

Consequently, the angular distribution is similarly peaked near the forward direction of the incident electron (i.e. $\psi \approx \alpha$). (Note, however, that additional angular dependence is contained in the factor X which also includes the polarization dependence.) The interaction of a short laser pulse with a relativistic

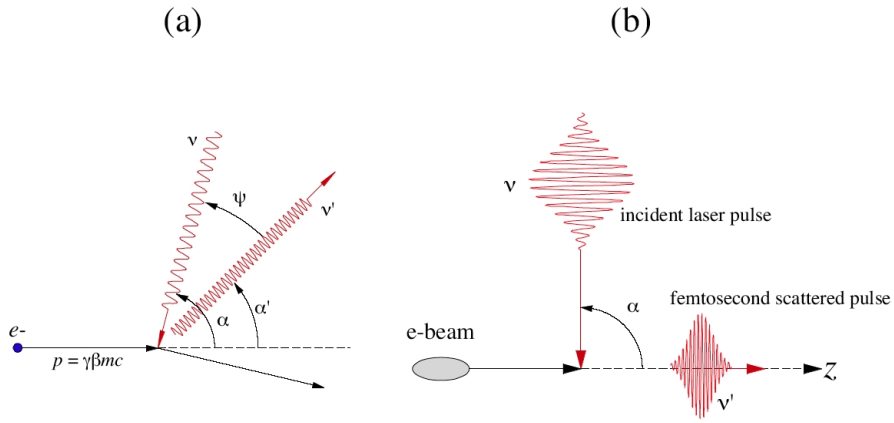

Figure 1.9: Collision geometry for inverse Compton scattering.

electron beam thus produces a pulse of upshifted radiation directed along the path of the electron beam, as illustrated in Fig. 1.9 (b). The interaction angle α between the beam and the laser is generally chosen to be either 90 degrees (right-angle collision) or 0 degrees (head-on collision). The limit ($h\nu << \gamma mc^2$) when observed in the rest frame of the electron beam corresponds to the nonrelativistic limit of ordinary Compton scattering. The total cross-section for ICS in the low-energy photon limit is therefore equal to the (Lorentz invariant) classical Thomson cross-section: $\sigma = \sigma_T = (8\pi/3)(e^2/mc^2)$. This type of scattering is therefore sometimes called Thomson scattering. The total photon count of the scattered pulse is then given by $N_{ph} = \mathcal{L}\ \sigma_T$, where $\mathcal{L}$ is the luminosity of the collision, which is proportional to the number of electrons interacting with the laser field.

The shortness of the duration of the scattered radiation pulse is constrained by the interaction time of the electron bunch and the incident laser. Therefore, in order to obtain sub-picosecond x-ray pulses, the incident laser and electron bunch must be sub-picosecond in duration (in a head-on collision scenario) or else the

electron bunch must be focused to a very tight waist at the interaction point (in the case of a 90-degree scattering geometry). In either scenario, it is desirable to maximize the charge density in the interaction region, requiring electron beams of high current and short bunch length, as well as strong transverse focusing. However, the large energy spreads required for magnetic compression techniques used to obtain high current beams may result in chromatic aberrations in the focusing system. In recent ICS experiments conducted at the PLEIADES x-ray source facility at Lawrence Livermore National Laboratory, very high-gradient (500 T/m) permanent magnet quadrupole magnets were used to overcome these chromatic aberrations and obtain spot sizes on the order of tens of microns [27].

1.4.2 Free Electron Laser

The free electron laser (FEL) is a technique for generating intense coherent radiation over a wide range of frequencies, including those which are too high for the use of traditional optics. The seminal theory was provided by Madey [28]. In a free electron laser an electron beam is injected into a periodic magnetic field (an undulator or wiggler). The transverse oscillation of the electrons in the magnetic field produces coherent radiation at the fundamental resonant wavelength

$$\lambda_0 = \frac{\lambda_u}{2\gamma^2}(1 + K^2) \tag{1.57}$$

where λ_u is the spatial period of the undulator field, γ is the relativistic Lorentz factor of the electron beam, and K is a dimensionless parameter measuring the field strength of the undulator. For a helical undulator, $K = eB_u 2\pi/mc\lambda_u$ where B_u is the peak magnetic field of the undulator. For a planar undulator, B_u is replaced by $B_u/\sqrt{2}$ in this expression. Note the similarity between K and the normalized electric field parameter α used in the photoinjector theory of Section 1.2.1.

Due to poor electron beam quality, early FELs used a seed pulse and mirrors to create an optical cavity with multiple passes of the radiation through the undulator. The advent of the modern photoinjector and the resultant improvement in electron beam brightness has allowed for sufficient improvement in the FEL amplification process that saturation can be reached in a single pass. This has opened the possibility of lasing in the very ultraviolet (VUV) and x-ray regimes where optical mirrors are transparent. However, since traditional lasers do not exist at such frequencies, the FEL in this scenario must either be operated at a higher harmonic of the seed laser pulse (high gain harmonic generation or HGHG) [29] or must start up from noise (self amplified spontaneous emission or SASE) [30, 31, 32].

In the 1-D theory of single-pass FEL operation, the normalized field amplitude A of the produced radiation as a function of distance along the undulator z is a superposition of exponential solutions of the form

$$A = \sum_j A_j e^{ik_j z} \tag{1.58}$$

where $k_j = 4\pi\rho\Lambda_j/\lambda_u$ is the growth rate of the j'th mode, and Λ_j are solutions of the 1D dispersion relation, which in the absence of space charge takes the form [33]

$$(\Lambda + \delta)^2\Lambda + 1 = 0 \tag{1.59}$$

The so-called Pierce parameter ρ and detuning δ are defined by

$$\rho = \left[\frac{K f_c \lambda_u \gamma \Omega_p}{4c\gamma_R^2 2\pi}\right]^{2/3} \quad ; \quad \delta = \frac{\gamma^2 - \gamma_R^2}{2\rho\gamma_R^2} \tag{1.60}$$

where f_c is a coupling factor of order unity, Ω_p is the plasma frequency of the electron beam, and $\gamma_R = k(1 + K^2)\lambda_u/4\pi$ is the resonant energy.

Equation (1.59) produces one real and two complex solutions. Among the latter, the solution which has a negative imaginary part produces a continuous

exponential growth of the radiation field, giving rise to the so-called "high-gain regime." Calling this solution Λ_g, we see that it will begin to dominate Eq. (1.58) for sufficiently large z, particularly if z is greater than the so-called gain length given by $L_g = \lambda_u/(4\pi\rho Re[i\Lambda_g])$. It can be shown that the gain is maximum in the case of zero detuning [i.e. the wavelength of highest gain is the one given by Eq. (1.57)], in which case $\Lambda_g = (1/2) - i(\sqrt{3}/2)$, producing the solution [32]

$$L_g = \frac{\lambda_u}{2\sqrt{3}\pi\rho} \tag{1.61}$$

The gain length is increased above this 1D value by the effects of diffraction, energy spread (σ_γ), and slippage ($S = \lambda N_u$) if the following conditions are not met: $\epsilon_{x,y} \leq \lambda/4\pi$, $\sigma_\gamma/\gamma < \rho$, $S < \sigma_z$, and $Z_R > L_g$, where N_u is the number of undulator periods and Z_R is the coherent FEL radiation Rayleigh range [31]. Physically, the high-gain regime of the FEL corresponds with a collective instability produced by the exchange of energy between the electron beam and the radiation field, producing a ponderomotive microbunching of the electrons [34]. The process saturates when the beam is maximally bunched, typically after about 10 gain lengths.

The ρ parameter provides a figure of merit for the FEL, as maximizing its value reduces the gain length and increases the amplification. Noting that the plasma frequency scales with electron density n_e as $\Omega_p \propto n_e^{1/2}$, we have that $\rho \propto n_e^{1/3}$. So the inverse gain length, and hence the output power, scales directly with the cube root of charge density, making high current and brightness critical to obtaining multiple order of magnitude gain in an undulator of reasonable (a few meters) length. Consequently, photoinjector beams are typically used in conjunction with chicane compression prior to injection into the undulator.

Additionally, particularly in the HGHG scheme, a pre-bunching undulator is used to create an energy modulation of the beam which is then translated into

spatial microbunching with a chicane in order to enhance the amplification of the seed pulse in the primary undulator. In this context, it has recently been proposed that the use of a beam with a triangularly ramped current profile may help to counteract inhomogeneity in the microbunching due to slippage [35]. This proposal requires further study, but is of particular interest here because the primary experimental work of this dissertation revolves around the generation of ramped electron bunches for application to the plasma wake-field accelerator. The latter application is discussed in the following sections.

1.4.3 Plasma Wake-Field Accelerator

Traditional RF accelerators, which rely upon coupling high-peak-power (megawatt) microwave energy into a standing or traveling wave cavity are limited to peak accelerating gradients on the order of 100 MV/m by the electrical breakdown limit of the metallic structures. This limitation means that in order to reach beam energies of interest to the high energy physics community (i.e. hundreds of GeV to TeV) accelerators must be kilometers in length, creating numerous technical and cost issues and requiring years of planning and construction.

Due to their capacity to support large electric fields, plasmas have been considered in recent years as a means for acceleration of charged particles capable of producing field gradients larger than those achievable with traditional radio-frequency linear accelerating cavities by several orders of magnitude. Longitudinal field gradients in excess of 1 GeV/m can be obtained by the excitation of large-amplitude relativistic waves in a plasma. Various acceleration schemes have been proposed which rely upon driving such plasma waves, using either a short intense laser beam (laser wakefield accelerator, LWFA) or a short relativistic electron beam (plasma wakefield accelerator, PWFA) [36, 37, 38, 39, 40]. The

issues of beam quality associated with the drive beam in the PWFA scenario will be found to be relevant to the experimental goals of this dissertation, namely the generation and measurement of ultrashort electron beams with a triangularly ramped current profile.

The 1D fluid theory of longitudinal plasma waves was developed in 1956 by Akhiezer and Polovin [41], and was later reinterpreted for the PWFA by Rosenzweig [42]. Starting from Maxwell's equations and the fluid equation of motion, one obtains a nonlinear differential equation for the normalized plasma fluid velocity $\beta = v_z/c$ as a function of the wave phase $\phi = \omega_p(t - z/v_b)$:

$$\frac{d^2}{d\phi^2}\frac{1-\beta_b\beta}{\sqrt{1-\beta^2}} = \beta_b^2\left(\frac{\beta}{\beta_b-\beta} + \frac{n_b}{n_0}\right) \tag{1.62}$$

Here n_b and n_0 are the drive beam and background (unperturbed) plasma densities respectively, and $\beta_b = v_b/c$ is the normalized beam velocity which is also the phase velocity of the wave. Equation (1.62) can be solved analytically in terms of elliptic integrals for the homogeneous case ($n_b = 0$). The pertubed plasma density n and electric field E_z are then given by

$$\frac{E_z}{E_0} = \frac{1}{\beta_b}\frac{d}{d\phi}\frac{1-\beta_b\beta}{\sqrt{1-\beta^2}} \tag{1.63}$$

$$n = \frac{n_0\beta_b}{\beta_b-\beta} \tag{1.64}$$

where $E_0 \equiv mc\omega_p/e$. The maximum electric field supported by the plasma occurs in the so-called wavebreaking limit, where the plasma fluid velocity β exceeds the phase velocity β_b of the wave resulting in the crossing of fluid element trajectories. This limit therefore also represents the breakdown of the fluid theory, since the fluid variables become multivalued functions. The relativistic electric field amplitude E_m is related to the peak fluid velocity β_m by [41]

$$\frac{E_m}{E_0} = \sqrt{2}\left(\frac{1}{\sqrt{1-\beta_m^2}} - 1\right)^{1/2} \tag{1.65}$$

The wavebreaking electric field E_{WB} is then given by this equation as $\beta_m \to \beta_b$. We can deduce the limiting forms $E_{WB} = \beta_b E_0$ and $E_{WB} = \sqrt{2}E_0(1-\beta_b^2)^{1/4}$ for the small amplitude ($E_m/E_0 << 1$) and large amplitude ($E_m/E_0 >> 1$) cases respectively. In terms of drive beam parameters the maximum achievable field occurs for a delta-function beam with charge density $\rho_b = \sigma_b \delta(\phi)$ where $\sigma_b = Q/\int dA$ is the charge divided by the transverse area of the beam, in which case, the field amplitude is $E_m = 4\pi\sigma_b$. Since the driver is a delta function, the solution for E_z with this amplitude represents the Green's function. In the low-amplitude case, the Green's function is a truncated sinusoid: $G(\phi) = 4\pi\cos(\phi)H(\phi)$, where H is the Heaviside step function. The linear wakefield for an arbitrary 1D drive beam distribution is therefore given by

$$E_z(\phi) = \int_{-\infty}^{\infty} \rho_b(\phi')G(\phi-\phi')d\phi' = 4\pi\int_{\phi}^{\infty} \rho_b(\phi')cos(\phi-\phi')d\phi' \tag{1.66}$$

The shape and amplitude of the wakefield are thus intimately related to the longitudinal shape of the drive beam. For example, for a Gaussian beam with RMS length $\sigma_\phi = k_p\sigma_z$, the wakefield obtained from Eq. (1.66) is

$$E_z(\phi) = \pi\sigma_b e^{-\sigma_\phi^2/2}\left[e^{-i\phi}\mathrm{erf}(w) + e^{i\phi}\mathrm{erf}(w^*) - 2\cos(\phi)\mathrm{erf}(1)\right] \tag{1.67}$$

where $w \equiv (\phi - i\sigma_\phi^2)/\sqrt{2}\sigma_\phi$. This function is plotted for an RMS value of $\sigma_\phi = 1/2$ in Fig. 1.10 (a). For values of $\sigma_\phi < \pi$, the peak amplitude of the accelerating wakefield behind the bunch occurs very close to $\phi = -\pi$, in which case it assumes the form

$$E_+ \approx 4\pi\sigma_b\frac{e^{-\sigma_\phi^2/2}}{4}\left[2\mathrm{erf}(1) + \mathrm{erf}(\frac{\pi - i\sigma_\phi^2}{\sqrt{2}\sigma_\phi}) + \mathrm{erf}(\frac{\pi + i\sigma_\phi^2}{\sqrt{2}\sigma_\phi})\right] \tag{1.68}$$

which is a monotonically decreasing function of σ_ϕ. The naive assumption then would be that the optimal drive beam is one of nearly zero length ($\sigma_\phi \to 0$), in which case E_+ assumes the maximal value of $4\pi\sigma_b$.

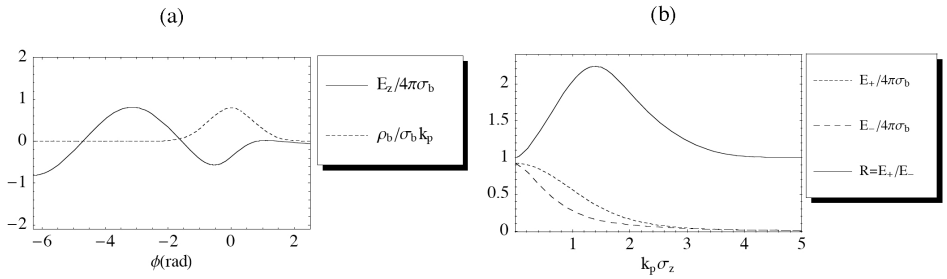

Figure 1.10: Plots of (a) the wakefield for a Gaussian 1D bunch and (b) the accelerating and retarding fields and corresponding transformer ratio.

However, as seen in Fig. 1.10 (a), the peak field E_- inside of the bunch is deccelerating and will tend to deplete the drive bunch energy γ_b after a distance of approximately $\Delta z \approx \gamma_b mc^2/qE_-$. Over the same distance, the increase in energy of a test particle in the accelerating field behind the bunch is $\Delta\gamma \approx qE_+\Delta z/mc^2 = (E_+/E_-)\gamma_b$. So a better figure of merit for the wakefield accelerator is the maximum fractional energy gain which the wakefield can produce as measured by the ratio $R = E_+/E_-$ which is termed the *transformer ratio*. The peak fields E_+ and E_- and their ratio R are plotted in Fig. 1.10 (b) as functions of bunch length $\sigma_\phi = k_p\sigma_z$. We see that the maximum value is $R = 2$, which occurs at $\sigma_\phi = \sqrt{2}$. In fact, it has been shown that for any symmetrical bunch, 2 is the maximal value of the linear 1D transformer ratio [43, 44].

It should be noted that the 1D theory is valid only in the case of a *pancake beam* whose transverse size is much greater than its longitudinal size $\sigma_{x,y} >> \sigma_z$. In fact, the primary operating regime of the PWFA, the so-called *blowout regime*, is one in which this assumption breaks down. In the blowout regime, the beam density is sufficiently larger than the ambient plasma density ($n_b > n_0$) that the plasma electrons are blown radially outward, forming a rarified ion channel behind

the drive bunch, which provides a linear focusing force of strength $K = 2\pi r_e n_0/\gamma_b$. Furthermore, the accelerating wakefield (E_z) is radially uniform across the width of the bunch [45]. These qualities make this regime highly desirable from the perspectives of drive beam stability and uniformity of acceleration.

The mechanics of the blowout process itself is inherently nonlinear and multidimensional and involves wavebreaking. A nonrelativistic radial fluid approximation may be used to describe certain aspects of this regime [45, 46]. This treatment gives an approximate radial equation of motion for the radius r of a 2D fluid element (i.e. a ring of plasma) of initial radius r_0 as a function of wave phase ϕ:

$$\frac{d^2r}{d\phi^2} = -\frac{r}{2} + \frac{1}{r}\left[\frac{r_0^2}{2} + \int_0^r r' \frac{n_b(r',\phi)}{n_0} dr'\right] \tag{1.69}$$

from which the blowout behavior of the ion channel can be calculated (at least up to the point of wavebreaking). This analysis gives a maximum blowout radius of $r_{max} = 2.58\sqrt{\Lambda}$, where $\Lambda = k_p^2 \int_0^\infty r\ n_b(r,0)/n_0\ dr$ is the normalized charge per unit length of the drive bunch. For a bi-Gaussian bunch, $\Lambda = (\hat{n}_b/n_0)k_p^2\sigma_r^2$, where $\hat{n}_b = n_b(0,0)$. For sufficiently large beam density ($\hat{n}_b/n_0 > 10$) almost all electrons are expelled from the region inside this radius. This depletion of the electrons in the ion column results in a saturation of the longitudinal wake-field amplitude, which has the following approximate dependence:

$$\frac{E_{max}}{E_0} \approx 1.3\Lambda\ \ln\frac{1}{\sqrt{\Lambda/10}} \tag{1.70}$$

In the linear regime ($\hat{n}_b/n_0 << 10$) this expression is replaced by

$$\frac{E_{max}}{E_0} \approx 1.3\Lambda\ \ln\frac{1}{\sqrt{\Lambda}} \tag{1.71}$$

An accurate calculation of the transformer ratio in the blowout regime generally requires the use of 2D fluid codes, or particle-in-cell (PIC) simulations.

Values obtained thereby tend to be slightly lower than what is predicted by a linear 1D calculation, such as that shown in Fig. 1.10 for the Gaussian beam. Nevertheless, as the dependence of the transformer ratio on the current distribution is qualitatively similar in these cases, the linear theory provides a useful rule of thumb for both the nonlinear 1D and blowout regimes. As mentioned above, for asymmetric beams the transformer ratio can in principle exceed the usual limit of $R = 2$. Consequently, in the following section we explore the question of what type of current distribution in the drive beam produces the highest possible value for the transformer ratio.

1.5 Motivation for this Dissertation

1.5.1 Optimal Plasma Wake-Field Drive Beam

The theoretical and experimental investigations which will comprise the primary focus of this dissertation initially arose from an interest in discovering methods for tailoring the current profile of a photoinjector beam to make it optimal for use as a plasma wakefield accelerator drive beam. As discussed in Section 1.4.3, the transformer ratio (equal to the maximum energy gain of a witness particle as a fraction of the drive beam energy) is a figure of merit for the PWFA. The amplitude and transformer ratio of the wakefield generated in the PWFA was found to be intimately connected, via Eq. (1.66), to the charge density $\rho_b = en_b$ of particles in the drive beam. The linear 1D wakefield of a Gaussian beam was calculated directly and shown in Fig. 1.10 to have a maximum transformer ratio $R = 2$ for a bunch length of $\sigma_z = \sqrt{2}/k_p$.

For symmetric bunches, $R = 2$ is the maximum achievable transformer ratio [43, 44]. It has also been theoretically predicted that this limit can be exceeded

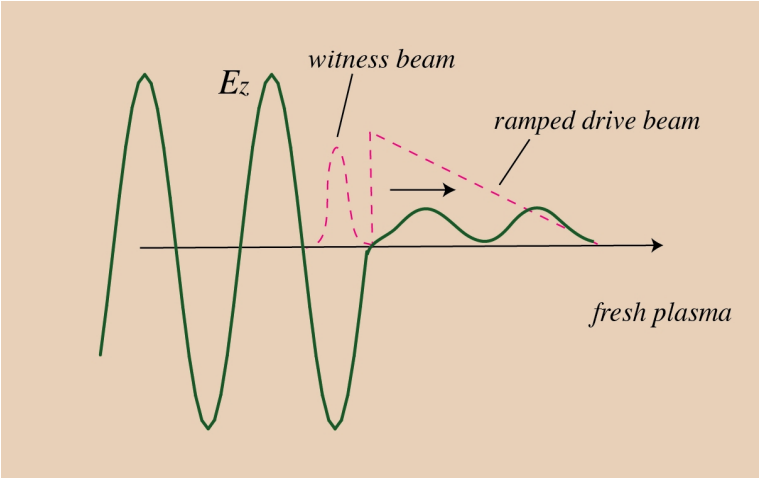

Figure 1.11: PWFA with ramped drive beam and witness bunch.

if the current profile of the drive bunch is asymmetric. In addition, the use of a linearly growing train of bunches has recently been reported at Argonne National Laboratory to produce an enhancement of the transformer ratio [47]. For the case of a single drive bunch, an investigation, using linear 1D theory, of the bunch shape that produces the maximum possible transformer ratio was conducted initially by Bane, Chen, and Wilson [48]. The optimal current distribution was found to be the one which produces a retarding field that is the same for all particles within the drive bunch and vanishes outside of it. Since a retarding field that arises instantaneously from zero at the head of the bunch would be unphysical, a form is proposed with a more gradual exponential rise at the head:

$$E_{ret}(\phi) \propto \begin{cases} (1 - e^{-\alpha\phi}) & , \quad 0 < \phi < \Phi \\ 0 & , \quad \text{otherwise} \end{cases} \tag{1.72}$$

where L is the length of the bunch and $\Phi = k_p L$. Equation (1.66) is then inverted using the Laplace transform $\mathcal{L}$ to solve for the current distribution:

$$\rho_b(\phi) = \frac{1}{2\pi i} \int_{\epsilon - i\infty}^{\epsilon + i\infty} \frac{\mathcal{L}[E_{ret}(\phi)]}{\mathcal{L}[G(\phi)]} e^{s\phi} ds \tag{1.73}$$

yielding the result

$$\rho_b(\phi) = \frac{k_p \sigma_b}{A_\Phi}[(\alpha^2+1)e^{\alpha\phi} - (\alpha\phi - 1)] \quad ; \quad 0 < \phi < \Phi \tag{1.74}$$

where

$$A_\Phi = \Phi - \frac{e^{-\alpha\Phi} - 1}{\alpha} - \alpha\left(e^{-\alpha\Phi} - \frac{\Phi^2}{2} - 1\right) \tag{1.75}$$

is the normalization constant. Equation (1.74) describes a triangular ramp with an exponentially increasing component at the head. The maximum transformer ratio occurs in the limit $\alpha \to \infty$ in which case the wakefield assumes the form

$$E_z(\phi) = \frac{4\pi\sigma_b}{1+\Phi^2/2}\begin{cases} \Phi\sin(\phi+\Phi) - \cos(\phi+\Phi) & ; \quad \phi < -\Phi \\ -1 & ; \quad -\Phi < \phi < 0 \end{cases} \tag{1.76}$$

Dividing the maximum amplitudes of the top and bottom lines gives a transformer ratio of $R = \sqrt{1+\Phi^2} \approx \Phi = k_p L$. Consequently, $R > 2$ if the drive bunch is longer than 2 plasma skin-depths ($L > 2k_p^{-1}$). However, the ideal bunch shape given by Eq. (1.74) is very nonphysical due to the sharp spike at the head. A simple triangular ramp, $\rho_b(\phi) = -(k_p\sigma_b\phi)/(\Phi^2/2)$, gives the following wake-field:

$$E_z(\phi) = \frac{4\pi\sigma_b}{\Phi^2/2}\begin{cases} \cos(\phi) - \cos(\phi+\Phi) - \Phi\sin(\phi+\Phi) & ; \quad \phi < -\Phi \\ \cos(\phi) - 1 & ; \quad -\Phi < \phi < 0 \end{cases} \tag{1.77}$$

The extrema of the top line can be expressed analytically in terms of inverse trig functions, but it is not particularly illuminating to do so. Its maximum value is approximately Φ and that of the lower line is exactly 2, giving a transformer ratio of $R \approx \Phi/2$, which is half that of the ideal case. An alternative distribution considered in Ref. [48] is that of a triangular ramp with a rectangular pulse for the first quarter of a period. This distribution produces a transformer ratio which is almost identical to the ideal one: $R = \sqrt{1+(1-\pi/2+\Phi)^2} \approx \Phi$. The three distributions and their respective transformer ratios are displayed in Fig. 1.12.

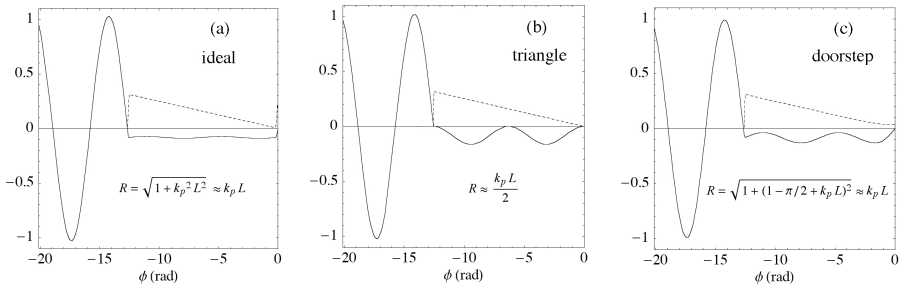

Figure 1.12: Several bunch distributions and their transformer ratios.

These results apply strictly only in the 1D linear regime. However, the use of a truncated Gaussian (which closely resembles a triangular ramp) was investigated in the blowout regime by Rosenzweig [45], who found, for a bunch length of approximately $k_p L = 4\pi$ a transformer ratio of 5.6 in the simulation, as compared with the value $R = 7.85$ predicted by linear theory. And Lotov has recently determined the optimal profile shapes for both the drive and witness bunches in the blowout regime through 2D particle-in-cell simulations using LCODE [49]. The optimal drive bunch current profile obtained in these cases turns out to be close to that predicted by the 1D theory. Consequently, the highest transformer ratio in the various regimes (linear 1D, nonlinear 1D, and blowout) is produced by a drive beam with a ramped current profile. Physically, we can interpret this as an induction problem. The adiabatic rise in current minimizes the electric field inside the beam and maximizes the potential energy stored in the plasma, which is released when the bunch current drops to zero, producing a large-amplitude plasma oscillation. The predicted features of this oscillation (sinusoidal, nonlinear, wavebreaking) depend upon the physical model used, but as the released energy is of similar magnitude in all cases, the various models give similar results for the overall transformer ratio.

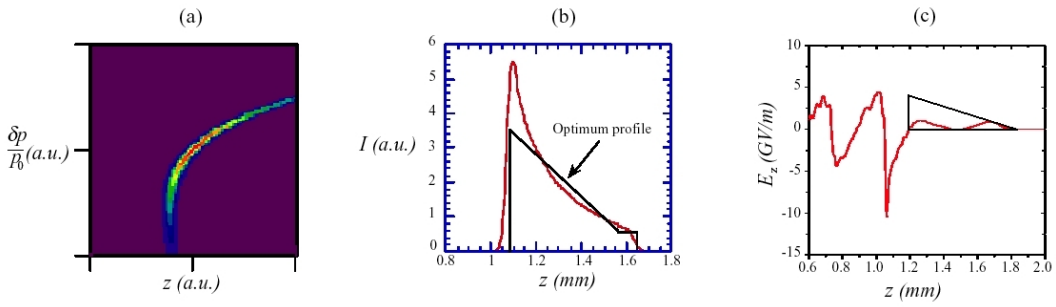

Figure 1.13: Idealized current profile and 2D simulation results.

1.5.2 The Road to Ramped Electron Bunches

An example of a longitudinal trace space distribution which produces a current density that approximates the idealized doorstep profile shown in Fig. 1.12 is shown in Fig. 1.13 (a) below (courtesy of J. B. Rosenzweig). This distribution was artificially created by applying a linear transformation to the set of trace space coordinates produced by a photoinjector simulation using the particle tracking code PARMELA. In part (b) the current profile (in red) corresponding to the distribution of part (a) is superimposed with the idealized *doorstep* profile predicted by the linear 1D theory (in black) to optimize the transformer ratio in a plasma wakefield accelerator scenario. A two-dimensional particle-in-cell (PIC) simulation of the longitudinal wake-field excited by this beam with 4 nC of charge in a plasma of density 10^{16}cm^{-3}, shown in Fig. 1.13(c) predicts a peak field of 10 GV/m with a transformer ratio of 11, which is close to the value $R = 4\pi \approx 12.6$ predicted by the linear theory for the idealized distribution.

The linear transformation used to artificially generate the distribution of Fig. 1.13(a) is of the form $z = z_0 + \eta_z \delta$ where η_z is a negative number. The distribution of particles in z_0 and δ prior to this manipulation had a positive chirp $d\delta/dz_0 > 0$, which was created in the PARMELA simulation by setting the simulated injection

phase back-of-crest in the accelerating section. A linear transformation of this sort is analogous to the compression mechanism of the dogleg, which was discussed in Section 1.3.3, with the association $\eta_z \approx -\alpha_c \Delta s$ where α_c was the (positive-valued) momentum compaction given by Eq. (1.53) and Δs is the total path-length traversed through the device. The quantity η_z, which is termed the *longitudinal dispersion*, will be defined more rigorously in Chapter 2.

Thus, the scheme we propose for generating ramped electron bunches is to use a dogleg compressor to impart a linear transformation upon the longitudinal trace space of a positively chirped photoinjector electron bunch in order to produce a distribution resembling that of Fig. 1.13(a), which is characterized by a gradually rising current density at the head followed by a sharp drop to zero at the tail. As we will see in Chapter 3, the actual z-transformation produced by the dogleg compressor is not truly linear, but possesses higher-order (nonlinear) contributions which tend to distort the longitudinal trace space distribution of the bunch and destroy the ramped shape of the current profile. The dominant nonlinear effect will be found to be second-order in the momentum error, and its removal by the use of sextupole corrector magnets will be seen to eliminate the majority of the undesired distortion of the current profile.

1.5.3 Summary of Experimental Goals

The primary experimental goals of this dissertation are: (1) the design and construction of a dogleg compressor for the UCLA Neptune Laboratory suitable for producing ramped electron bunches, (2) the development and implementation of temporal diagnostics with which to probe the longitudinal structure of these electron bunches on sub-ps time scales, and (3) the experimental generation and temporal measurement of ramped bunches as a proof-of-principle verification of

the mechanism proposed in the previous section. The diagnostics employed are: (1) coherent transition radiation interferometry and (2) a transverse RF deflecting cavity. As the high frequency deflecting cavity is a new technology developed expressly for this experiment, Chapter 4 will be devoted primarily to the details of its design and construction. The experimental results will be presented in Chapter 5. Future efforts using the Neptune dogleg compressor are discussed in Chapter 6.

CHAPTER 2

First and Second Order Beam Optics

The single-particle dynamics of a charged particle beam in a magnetostatic field are referred to as *beam optics*. This naming convention arises from the fact that magnetic fields are used to focus, bend, and otherwise manipulate beams of particles in ways that are similar to the uses of lenses, mirrors, and prisms in traditional optics to focus, reflect, or spectrally separate a beam of light. Also, as in traditional ray optics, matrices may be used to describe the effects of particular optical elements upon a beam particle. The effect of a series of optical elements may be modeled by multiplying together their respective matrices. In beam optics, this matrix formalism operates on rays defined in a 6-dimensional *trace space*, which is a modified version of the usual 6D phase space. The matrices for different types of magnets represent transformations upon this space, and are calculated by casting the single-particle equations of motion into curvilinear coordinates referenced to the design trajectory of the beam, and then linearizing them. Much of the traditional language of accelerator physics derives from this approach. Consequently, in the present chapter, we will present in detail the linear theory of beam optics. Additionally, higher-order (i.e. 2nd, 3rd, etc) tensors, which operate upon the same 6D space as the linear matrices, may be used to describe nonlinear effects. As the primary nonlinear effects relevant to the beam-shaping mechanism outlined in Section 1.5.2 are of second order, we conclude the chapter with an overview of the theory of second-order beam optics.

2.1 Background and Notation

2.1.1 The Curvilinear Coordinate System

Since the manipulation of particle beams is accomplished primarily by the use of static magnetic fields, the beam dynamics are governed by the single particle equations of motion in a magnetic field $\mathbf{B}$:

$$\frac{d\mathbf{p}}{dt} = \frac{q}{c}\mathbf{v} \times \mathbf{B}(\mathbf{r}) \ ; \ \frac{dU}{dt} = 0 \tag{2.1}$$

Here, $\mathbf{p} = \gamma m\mathbf{v}$ is the relativistic momentum, $\mathbf{v}$ is the particle velocity, and $U = \gamma mc^2$ is the energy. The trajectories $\mathbf{r}$(t) of particles in the field $\mathbf{B}$ evolve according to Eqs. (2.1). Presumably, one of these trajectories corresponds to the the *design particle*, whose path $\mathbf{r}_0(t)$ represents the *design trajectory* that the beam is intended to follow. It is customary then to define a set of basis vectors attached to a reference frame moving along the design trajectory and to specify the coordinates of particles in the beam relative to this basis. Let us parametrize $\mathbf{r}_0$ by the arclength parameter s,

$$s = s(t) = \int_{t_0}^{t} |\mathbf{v}_0(\tau)| \ d\tau \tag{2.2}$$

The basis vectors of the coordinate system attached to the design particle are then defined by the Serret-Frenet equations [50]

$$\hat{\mathbf{z}} \equiv \frac{d\mathbf{r}_0/\,\mathrm{ds}}{|d\mathbf{r}_0/\,\mathrm{ds}|} \ ; \ \hat{\mathbf{x}} \equiv -\frac{\mathbf{k}}{k} \ ; \ \hat{\mathbf{y}} \equiv \hat{\mathbf{z}} \times \hat{\mathbf{x}} \tag{2.3}$$

where $\mathbf{k}$ is the *curvature vector*. Its definition in terms of the reference trajectory and its relationship to the radius of curvature of the design trajectory $R(s)$ are given by the following relations:

$$\mathbf{k} \equiv \frac{d\hat{\mathbf{z}}}{ds} \ ; \ R(s) \equiv \frac{1}{k} = \frac{p_0 c}{qB_0(s)} \tag{2.4}$$

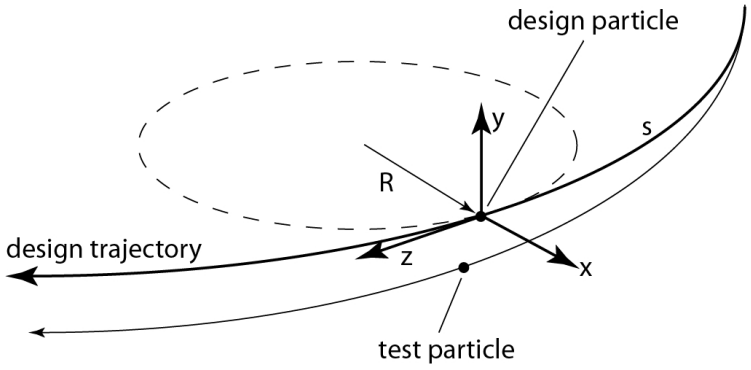

Figure 2.1: The curvilinear coordinate system.

Here q and p_0 are the charge and momentum of the design particle and B_0 is the y-component of the magnetic field along the design trajectory. We will permit R (and k) to assume both positive and negative values, according to the relative signs of q and B_0 in Eq. (2.4). Doing so prevents the coordinate axes, as they are defined in Eq. (2.3), from flipping about the x-z plane in the event that $\mathbf{k}$ changes sign (as would happen if the direction of the vertical component of the magnetic field were reversed). The vector position $\mathbf{r}$ of a given particle relative to a *fixed* coordinate system may now be written:

$$\mathbf{r}(s) = \mathbf{r}_0(s) + \delta\mathbf{r}(s) \tag{2.5}$$

where $\delta\mathbf{r}$ represents the test particle's deviation from the position of the design particle, which in the curvilinear coordinates defined by Equation(2.4) may be written

$$\delta\mathbf{r}(s) = x\ \hat{\mathbf{x}} + y\ \hat{\mathbf{y}} + z\ \hat{\mathbf{z}} \tag{2.6}$$

Here (x, y, z) denote the deviations along the directions of the unit vectors of the test particle position from that of the design particle. These coordinates (and

the unit vectors themselves) are functions of the arclength parameter s, which represents the length traversed by the design particle along the design trajectory (as such it is effectively a temporal parameter). Defining the momenta

$$\mathbf{p} \equiv \gamma \mathrm{m} \dot{\mathbf{r}} \; ; \; \mathbf{p}_0 \equiv \gamma \mathrm{m} \dot{\mathbf{r}}_0 \; ; \; \delta \mathbf{p} \equiv \gamma \mathrm{m} \dot{\delta \mathbf{r}} \tag{2.7}$$

we see that Eq. (2.5) implies that the momentum deviation of the test particle from that of the design particle is given by

$$\delta \mathbf{p} = \mathbf{p} - \mathbf{p}_0. \tag{2.8}$$

However, in the coordinates of Eq. (2.4) the design momentum has only a z-component ($\mathbf{p}_0 = p_0 \hat{\mathbf{z}}$). Hence, Eq. (2.8) reads

$$\delta \mathbf{p} = p_x \hat{\mathbf{x}} + p_y \hat{\mathbf{y}} + \delta \mathrm{p}_z \hat{\mathbf{z}}. \tag{2.9}$$

2.1.2 General Equations of Motion

The next step is to obtain from Eq. (2.1) the general equations of motion in the curvilinear coordinate system defined in Section 2.1.1. From Eqs. (2.3-2.4) we have (assuming that the design trajectory lies in a plane normal to the y-direction),

$$\begin{gathered} \dot{\hat{\mathbf{x}}} = \dot{s} k \hat{\mathbf{z}} \;\; ; \;\; \dot{\hat{\mathbf{y}}} = 0 \;\; ; \;\; \dot{\hat{\mathbf{z}}} = -\dot{s} k \hat{\mathbf{x}} \\ \dot{x} = \dot{s} x' \;\; ; \;\; \dot{y} = \dot{s} y' \;\; ; \;\; \dot{z} = \dot{s} z' \\ \dot{\mathbf{r}}_0 = \dot{s} \hat{\mathbf{z}} \end{gathered} \tag{2.10}$$

Here superscript dots denote time derivatives and $\dot{s} = v_0$ is the velocity of the design particle. Using these identities, we find that

$$\begin{aligned} &\mathbf{r} = \mathbf{r}_0(s) + x \; \hat{\mathbf{x}} + y \; \hat{\mathbf{y}} + z \; \hat{\mathbf{z}}; \\ &\mathbf{v} = v_0 \left(x' - zk\right) \hat{\mathbf{x}} + v_0 y' \hat{\mathbf{y}} + v_0 (z' + x \; k + 1) \hat{\mathbf{z}}; \\ &\dot{\mathbf{p}} = \gamma m \left(\dot{v_x} \hat{\mathbf{x}} + \dot{v_y} \hat{\mathbf{y}} + \dot{v_z} \hat{\mathbf{z}}\right); \end{aligned} \tag{2.11}$$

where

$$\begin{aligned} \dot{v_x} &= v_0^2 \left(x'' - zk' - 2z'k - x\ k^2 - k \right) \ , \\ \dot{v_y} &= v_0^2 y'', \\ \dot{v_z} &= v_0^2 \left(z'' + xk' + 2x'k - zk^2 \right) \ . \end{aligned} \tag{2.12}$$

Combining (2.13) with the first of Eqs. (2.1), which may be cast into the form

$$\begin{aligned} \dot{v}_x &= \frac{q}{\gamma mc}(B_z v_y - B_y v_z); \\ \dot{v}_y &= \frac{q}{\gamma mc}(B_x v_z - B_z v_x); \\ \dot{v}_z &= \frac{q}{\gamma mc}(B_y v_x - B_x v_y); \end{aligned} \tag{2.13}$$

we obtain the following general equations of motion:

$$\begin{aligned} x'' - zk' - 2z'k - x\ k^2 - k &= \frac{q}{\gamma mcv_0} \left\{ B_z y' - B_y \left(z' + x\ k + 1 \right) \right\}; \\ y'' &= \frac{q}{\gamma mcv_0} \left\{ B_x \left(z' + x\ k + 1 \right) - B_z \left(x' - zk \right) \right\}; \\ z'' + xk' + 2x'k - zk^2 &= \frac{q}{\gamma mcv_0} \left\{ B_y \left(x' - zk \right) - B_x y' \right\}. \end{aligned} \tag{2.14}$$

Keep in mind that the field components B_x, B_y, B_z are evaluated at the position of the particle, and are therefore functions of x, y, z, and s. These equations of motion are quite general, the only inherent assumptions being: (i) that the field components are static and obey the symmetries (see Section 1.2.2) necessary to restrict the design trajectory to a plane, (ii) that the electron does not radiate energy, and (iii) that the interparticle interactions are negligible.

2.1.3 The Momentum Deviation

It is customary in beam physics to represent the longitudinal velocity in terms of the momentum deviation $\delta = \delta p_z / p_0$ rather than z'. Using Eqs. (2.8) and (2.12)

we can write

$$\delta = \frac{\delta p_z}{p_0} = \frac{\gamma}{\gamma_0}(z' + xk + 1) - 1 \tag{2.15}$$

The presence of momentum error introduces a difference in total integrated path-length (as opposed to z, the difference in instantaneous longitudinal position) between the test particle and the design particle, due to different radii of curvature in bends. To illuminate this mathematically, define the function $S(p)$ to be the path-length traversed by a particle of momentum p during the time that the design particle travels from s_0 to s. The vector element $d\mathbf{S}$ may then be written

$$d\mathbf{S} = \mathbf{v}\ dt = (v_x\hat{\mathbf{x}} + v_y\hat{\mathbf{y}} + v_z\hat{\mathbf{z}})dt \tag{2.16}$$

Inserting for the components of $\mathbf{v}$ from Eq. (2.12), we find that the integrated path-length difference during the time $t = s/v_0$ that the design particle travels a distance s is

$$S(p) - S(p_0) = \int_0^s [\sqrt{(x' - zk)^2 + y'^2 + (z' + kx + 1)^2} - 1]ds \tag{2.17}$$

where we have used the fact that $dt = ds/v_0$. This difference in distance traveled is due entirely to the disparity in velocity of the two particles, so we can additionally write

$$S(p) - S(p_0) = \frac{\delta v}{v_0}s. \tag{2.18}$$

If we set $z = z' = 0$ in Eq. (2.17), the resulting integral measures the path-length along the test particle trajectory up to the point where it intersects the $x - y$ plane of the curvilinear coordinate system at time $t = s/v_0$. Let us call this integral $\hat{S}(p)$ and write

$$\hat{S}(p) \equiv S(p)|_{z,z'\to 0} = \int_0^s \sqrt{x'^2 + y'^2 + (kx + 1)^2}ds \tag{2.19}$$

The difference in path-length between the two trajectories up to the point s is then

$$\zeta(p) \equiv \hat{S}(p) - \hat{S}(p_0) = \int_0^s [\sqrt{x'^2 + y'^2 + (kx + 1)^2} - 1]ds \tag{2.20}$$

The difference between $S(p) - S(p_0)$ and $\zeta(p)$ is approximately equal to the longitudinal displacement Δz of the test particle. To see this, note that the delay in arrival time at point s between the test particle and the design particle is given by:

$$\Delta t = \frac{\hat{S}(p)}{v} - \frac{\hat{S}(p_0)}{v_0} \ . \tag{2.21}$$

Expanding the right-hand side in powers of $\delta v/v_0$ we obtain

$$v_0 \Delta t = \zeta - (s+\zeta)\frac{\delta v}{v_0} + (s+\zeta)\left(\frac{\delta v}{v_0}\right)^2 + \ldots \tag{2.22}$$

Noting that the time delay times v_0 is the negative of the longitudinal displacement $\Delta z \equiv z - \overset{\circ}{z}$ and invoking Eq. (2.18), we have, to first order in combined powers of ζ and δv, that

$$\Delta z \approx \frac{\delta v}{v_0} - \zeta(p). \tag{2.23}$$

To first order, the velocity is dominated by the longitudinal component, $v \approx v_z$, so the expression for $\zeta(p)$ from Eq. (2.20) becomes

$$\zeta(p) \approx \int_0^s kx \ ds. \tag{2.24}$$

The variable $\zeta(p)$ represents the difference in path-length between the off-momentum particle and the design particle due to the transverse displacement x of the particle, which is also the distance by which its radius of curvature varies locally from that of the design particle. The variable Δz represents the change in longitudinal displacement of the particle relative to the position of the design particle. Here, we give a name to the quantity ζ because some references (see Ref. [51]) refer to ζ as the longitudinal coordinate instead of z (Carey refers to this variable as l). This is justified by noting that in the ultrarelativistic limit, in which case the velocities of both particles are approximately equal to c and so $\delta v/v_0 \to 0$. In this case, we have that $\zeta = -\Delta z$ as $\beta \to 1$.

2.1.4 Vector and Tensor (Transport) Notation

Let $\mathbf{x}$ be a 6-element vector representing the coordinates of a test particle in the curvilinear basis of Section 2.1.1:

$$\mathbf{x}(s) = \begin{pmatrix} x(s) \\ x'(s) \\ y(s) \\ y'(s) \\ z(s) \\ \delta \end{pmatrix} \tag{2.25}$$

Here x, y, and z are the transverse coordinates of a particle relative to the curvilinear coordinate system following the path of the design particle and δ is the fractional longitudinal momentum deviation. The primes denote differentiation with respect to s. The 6-D space in which the vector $\mathbf{x}$ operates we call *trace space*. Let the following denote the trace space vectors of a test particle at two points (s_0 and s) along the design trajectory:

$$\overset{\circ}{\mathbf{x}} = \mathbf{x}(s_0) \; ; \; \mathbf{x} = \mathbf{x}(s) \tag{2.26}$$

The two states are presumed to be related by some transformation $\overset{\circ}{\mathbf{x}} \rightarrow \mathbf{x}$. The nature of this transformation depends upon the configuration of magnetic lenses, bends, and drifts encountered by the particle as it moves from s_0 to s. Assuming that the coordinates represent small perturbations from the design orbit, the final state may be represented to arbitrary precision by taking higher order terms in an expansion in powers of the vector components of the initial state:

$$x_i = Q_i + R_{ij}\overset{\circ}{x}_j + T_{ijk}\overset{\circ}{x}_j\overset{\circ}{x}_k + U_{ijkl}\overset{\circ}{x}_j\overset{\circ}{x}_k\overset{\circ}{x}_l + \ldots \tag{2.27}$$

Note that in Eq. (2.27) there is an implied summation on repeated indices. The transformation from the initial to final state is executed, therefore, by a sequence

of tensors Q, R, T, U, ... of increasing rank which operate upon the initial state $\overset{\circ}{\mathbf{x}}$. These tensors may be defined in component form as follows:

$$\begin{aligned} Q_i &= x_i\big|_{\overset{\circ}{\mathbf{x}}\to 0} \\ R_{ij} &= \left.\frac{\partial x_i}{\partial \overset{\circ}{x}_j}\right|_{\overset{\circ}{\mathbf{x}}\to 0} \\ T_{ijl} &= \frac{1}{2}\left.\frac{\partial^2 x_i}{\partial \overset{\circ}{x}_j \partial \overset{\circ}{x}_k}\right|_{\overset{\circ}{\mathbf{x}}\to 0} \\ U_{ijkl} &= \frac{1}{6}\left.\frac{\partial^3 x_i}{\partial \overset{\circ}{x}_j \partial \overset{\circ}{x}_k \partial \overset{\circ}{x}_l}\right|_{\overset{\circ}{\mathbf{x}}\to 0} \end{aligned} \tag{2.28}$$

Note that the zeroth-order vector Q_i is typically set to zero, as the origin of the curvilinear system generally lies on the design orbit by definition. The components of the first and higher-order tensors are obtained by expanding the equations of motion (2.14) of an arbitrary particle traveling near the design orbit. The 6-vector notation and the corresponding transport matrix formalism was originally developed for use in the particle tracking code TRANSPORT [52]. It has more recently been implemented in the code ELEGANT [53], which will be used extensively in this dissertation. The transport matrix notation has become widely used in the accelerator community as a means of calculating first (and sometimes higher) order analytical expressions for the effects of various configurations of magnets and drifts on the beam dynamics. In order to calculate the elements of the lowest order transformation R_{ij}, it is first necessary to linearize the general equations of motion (2.14) by expanding the static magnetic field $\mathbf{B}$ in powers of the transverse coordinates (and then eliminating the nonlinear contributions). The resulting expansion of the magnetic field into so-called *multipoles* is the topic of the following section.

2.2 Multipole Expansion of the Magnetic Field

In order to obtain explicit analytical forms for the elements of the 6×6 transport matrix R discussed in the previous section, we must linearize the general single-particle equations of motion (2.14). This requires expanding the magnetic field components in powers of the transverse coordinates. The contribution to the magnetic field from products of transverse coordinates of order n is termed the n'th magnetic multipole.

2.2.1 Series Expansions of Some Parameters

Before we linearize the single-particle equations of motion in a static magnetic field, we present some important expansions of the system parameters. We will assume that the velocity is dominated by the longitudinal component, and hence $v \approx v_z$. The Lorentz gamma is then given by

$$\gamma \approx \frac{1}{\sqrt{1 - v_z^2/c^2}} \tag{2.29}$$

where, in accordiance with Eq. (2.12), the longitudinal velocity is $v_z = v_0(z' + xk + 1)$. Expanding γ_0/γ in powers of the coordinates gives us

$$\frac{\gamma_0}{\gamma} \approx \frac{v_z}{v_0}\frac{p_0}{p} = (z' + xk + 1)(1 - \delta + \delta^2 - \delta^3 + \ldots) \tag{2.30}$$

A similar expansion may be performed upon the velocity deviation δv in powers of the fractional momentum deviation δ:

$$\frac{\delta v}{v_0} = \frac{\delta}{\gamma_0^2} - \frac{3}{2}\frac{\beta_0^2}{\gamma_0^2}\delta^2 + \frac{1}{2}(\beta_0^2 - 6\beta_0^4 + 5\beta_0^6)\delta^3 + \ldots \tag{2.31}$$

The utility of these expansions will become apparent when we linearize the single particle equations of motion in Section 2.3.1.

2.2.2 The General Field Expansion

In the current-free region of a magnetic element on a beamline, through which the beam is intended to pass, the magnetic field may be represented by a scalar potential ψ:

$$\mathbf{B} = -\boldsymbol{\nabla}\psi \tag{2.32}$$

The divergencelessness of the magnetic field then requires that ψ satisfy the Laplace equation

$$\nabla^2\psi = 0 \tag{2.33}$$

The transverse plane of the curvilinear coordinate system attached to the design particle will (for some value of s along the design trajectory) intersect any given fixed point $\mathbf{r}$ which we may wish to consider. The potential may therefore be represented by a function of the coordinates x, y, and s:

$$\psi = \psi(x, y, s) \tag{2.34}$$

With respect to these coordinates, the gradient and the Laplacian take the forms

$$\boldsymbol{\nabla} = \frac{\partial}{\partial x}\,\hat{\mathbf{x}} + \frac{\partial}{\partial y}\,\hat{\mathbf{y}} + \frac{1}{1+kx}\frac{\partial}{\partial s}\,\hat{\mathbf{z}}\ ; \tag{2.35}$$

$$\nabla^2 = \left(\frac{1}{1+kx}\frac{\partial}{\partial x}\right)^2 + \frac{\partial^2}{\partial y^2} + \left(\frac{1}{1+kx}\frac{\partial}{\partial s}\right)^2\ ; \tag{2.36}$$

Expanding ψ in powers of x and y gives us

$$\psi(x, y, s) = \sum_{m,\,\ell\,=\,0}^{\infty} A_{m,\ell}(s)\frac{x^\ell y^m}{\ell! m!} \tag{2.37}$$

Substitution of Eq. (2.37) into the Laplace equation results in the following recursion relation among the coefficients [52]

$$\begin{aligned} &A_{m+2,\ell} + A''_{m,\ell} + \ell k A''_{m,\ell-1} - \ell k' A'_{m,\ell-1} + A_{m,\ell+2} + (3\ell+1)kA_{m,\ell+1} \\ &\quad + \ell(3\ell-1)k^2 A_{m,\ell} + \ell(\ell-1)^2 k^3 A_{m,\ell-1} + 3\ell k A_{m+2,\ell-1} \\ &\quad + 3\ell(\ell-1)k^2 A_{m+2,\ell-2} + \ell(\ell-1)(\ell-2)k^3 A_{m+2,\ell-3} = 0 \end{aligned} \tag{2.38}$$

These recurrence relations effectively eliminate the dependence of the field coefficients on the mode number m. Applying the gradient operator to ψ we obtain the magnetic field components

$$\begin{aligned} B_x &= \sum_{m,\,\ell\,=\,0}^{\infty} A_{m,\ell}(s)\frac{x^{\ell-1}y^m}{(\ell-1)!m!}; \\ B_y &= \sum_{m,\,\ell\,=\,0}^{\infty} A_{m,\ell}(s)\frac{x^{\ell}y^{m-1}}{\ell!(m-1)!}; \\ B_z &= \sum_{m,\,\ell\,=\,0}^{\infty} \frac{A'_{m,\ell}(s)}{1+k(s)x}\frac{x^{\ell}y^m}{\ell!m!}; \end{aligned} \tag{2.39}$$

2.2.3 Extraction of the Multipole Moments

The requirement that the reference plane of the design trajectory be normal to the direction of y forces ψ to be an odd function of y: $\psi(x,y,s) = -\psi(x,-y,s)$. If this condition were not satisfied, the design particle could not be constrained to lie in the plane $y = 0$, because $\mathbf{B}$ would have a nonzero component tangential to this plane. In the interest of this symmetry consideration, we therefore require that the coefficients for even values of m vanish

$$A_{m,\ell} = 0 \ ; \ m = 0, 2, 4, 6, ... \tag{2.40}$$

The eliminated terms in the series corresponding to even m are called "skew" terms. Their failure to vanish would violate the symmetry rule imposed above on the magnetic potential, and would permit coupling of the x and y phase planes and deviation of the design trajectory from the $y = 0$ plane. Using (2.38) and (2.40), all coefficients may be expressed solely in terms of those with $m = 1$:

$$\begin{aligned} A_{30} &= -kA_{11} - A_{12} - A''_{10}; \\ A_{31} &= k^2A_{11} - kA_{12} - A_{13} + k'A'_{10} + 2kA''_{10} - A''_{11}; \\ &... \end{aligned} \tag{2.41}$$

We can classify the terms in the field expansion of $\mathbf{B}$ by the combined powers of the transverse coordinates which we shall call n. We see from (2.39) that for the x and y components, $n = \ell + m - 1$, while for the z-component, $n = \ell + m$. We can then write

$$B_x = \sum_{n=0}^{\infty} B_{x,n} \; ; \; B_y = \sum_{n=0}^{\infty} B_{y,n} \; ; \; B_z = \sum_{n=0}^{\infty} B_{z,n} \tag{2.42}$$

where we define

$$B_{x,n} = \sum_{Q} A_{m,\ell}(s) \frac{x^{\ell-1} y^m}{(\ell-1)!m!}; \; Q = \{m, \ell : n = (\ell-1) + m\} \tag{2.43}$$

$$B_{y,n} = \sum_{Q} A_{m,\ell}(s) \frac{x^{\ell} y^{m-1}}{\ell!(m-1)!}; \; Q = \{m, \ell : n = \ell + (m-1)\} \tag{2.44}$$

$$B_{z,n} = \sum_{Q} \frac{A'_{m,\ell}(s)}{1 + k(s)x} \frac{x^{\ell} y^m}{\ell!m!}; \; Q = \{m, \ell : n = \ell + m\} \tag{2.45}$$

The total field contribution from terms of order n,

$$\mathbf{B}_n = B_{x,n}\hat{\mathbf{x}} + B_{y,n}\hat{\mathbf{y}} + B_{z,n}\hat{\mathbf{z}} \tag{2.46}$$

is called the nth magnetic multipole field. Using (2.41) to eliminate the coefficients $A_{m,\ell}$ with m $\neq 1$, the kth contribution to the field can be written solely in terms of the coefficients $A_{1,\ell}$, which we rename

$$a_\ell(s) \equiv A_{1,\ell} = \left(\frac{\partial}{\partial x} \right)^{\ell} \frac{\partial \psi}{\partial y} \bigg|_{x=y=0} \tag{2.47}$$

The first few multipole contributions to the magnetic field are then given by

$$\begin{aligned}
\mathbf{B}_0 &= a_0\hat{\mathbf{y}} && \text{(dipole)} \\
\mathbf{B}_1 &= a_1 y\hat{\mathbf{x}} + a_1 x\hat{\mathbf{y}} + a'_0 \, y\hat{\mathbf{z}} && \text{(quadrupole)} \\
\mathbf{B}_2 &= a_2 xy\hat{\mathbf{x}} + \tfrac{1}{2}a_2 (x^2 - y^2)\,\hat{\mathbf{y}} + (a'_1 - k a'_0)\, xy \; \hat{\mathbf{z}} && \text{(sextupole)}
\end{aligned} \tag{2.48}$$

The "multipoles" derived here are to be distinguished from the usual multipole fields discussed in electrodynamics textbooks, which are obtained by regarding

all current sources as being near the origin and representing the field at a point far away by expanding in powers of $1/r$, where r is the radial distance from the origin. In the present analysis, the field expansion is performed in the smallness of the coordinates, and therefore represents the limit where the current sources producing the field are located away from the origin. Evaluating the vertical (y) component of the total field ($\mathbf{B} = \mathbf{B}_1 + \mathbf{B}_2 + \mathbf{B}_3 + \ldots$) at the midplane ($y = 0$) gives

$$B_y(y=0) \ = a_0 + a_1 x + \frac{1}{2} a_2 x^2 + \frac{1}{6} a_3 x^3 + ... \tag{2.49}$$

The coefficients of this expansion (i.e. a_ℓ) are determined by the physical parameters of the magnetic element which produces the field. The names given to these coefficients vary. Equation (2.49) may alternately be written

$$B_y(y=0) \ = B_0 \left(1 - nkx + \beta k^2 x^2 + \gamma k^3 x^3 + ...\right) \tag{2.50}$$

or

$$B_y(y=0) \ = B_0 R \left(k + K_1 x + K_2 x^2 + K_3 x^3 + ...\right) \tag{2.51}$$

The first form of the expansion is convenient because the coefficients (n, β, γ, ...) are dimensionless, having been normalized to the local radius of curvature $R = 1/k$. However, when considering field configurations that do not possess a dipole component, the curvature radius becomes infinite. In deriving the equations of motion using the general expansion of $\mathbf{B}$, it is then desirable to rewrite the coefficients in the form of (2.51) before taking the limit $k \to 0$.

2.3 Beam Optics

2.3.1 Linearized Equations of Motion

If we assume that the deviation of the particle from the design trajectory is small, then we can expand the equations of motion in the smallness of the coordinates x, y, and z. If we keep only the terms linear in these coordinates (and their derivatives), we obtain a lowest-order representation of the motion. An expansion of this sort was performed upon the magnetic field $\mathbf{B}$ in Section 2.2.3. Retaining only the linear (dipole+quadrupole) terms in this expansion we have

$$B_x = -B_0 kny \ , \ B_y = B_0(1 - nkx) \ , \ B_z = B_0' y. \tag{2.52}$$

The local dipole field B_0 is related to the curvature k by the inverse of the formula for the cyclotron radius applied at the local position of the design particle

$$k = \frac{qB_0}{\gamma_0 mcv_0} \ , \ k' = \frac{qB_0'}{\gamma_0 mcv_0}. \tag{2.53}$$

Now the equations of motion (2.14) read

$$x'' - 2z'k - x\ k^2 - k = \frac{\gamma_0}{\gamma}\left\{k'yy' - k(1 - nkx)\left(z' + x\ k + 1\right)\right\}, \tag{2.54}$$

$$y'' = -\frac{\gamma_0}{\gamma}\left\{nk^2 y\left(z' + x\ k + 1\right) + k'y\left(x' - zk\right)\right\}, \tag{2.55}$$

$$z'' + xk' + 2x'k - zk^2 = k\frac{\gamma_0}{\gamma}\left\{(1 - nkx)\left(x' - zk\right) + nkyy'\right\}. \tag{2.56}$$

Using expansion (2.30) for γ/γ_0 in powers of $(z' + kx)$ and δ, keeping only terms linear in the coordinates, we obtain

$$\begin{aligned} x'' + k^2(1 - n)x &= k\delta, \\ y'' + k^2 ny &= 0, \\ z'' + kx' + xk' &= 0. \end{aligned} \tag{2.57}$$

These equations describe oscillatory motion in x and y, with an added horizontal dispersion due to the momentum deviation δ.

2.3.2 Linear Transverse Solutions

The linearized transverse equations of motion have the general forms

$$x'' + K_x^2(s)x = k\delta \quad , \quad y'' + K_y^2(s)y = 0 \tag{2.58}$$

where

$$K_x^2(s) = k(s)^2[1 - n(s)] \quad , \quad K_y^2(s) = k(s)^2 n(s) \ . \tag{2.59}$$

In the absence of momentum dispersion (δ=0) both equations are homogeneous differential equations of Hill's type, which resemble the equations for a simple harmonic oscillator that is uncoupled in x and y, but with separate s-dependent frequencies $K_{x,y}$. The homogneous solutions are generally oscillatory and periodic in nature. These oscillatory solutions, called *betatron oscillations* have the forms

$$\tilde{x}(s) = C_x(s)\overset{\circ}{x} + S_x(s)\overset{\circ}{x}' \quad , \quad \tilde{y}(s) = C_y(s)\overset{\circ}{y} + S_y(s)\overset{\circ}{y}' \tag{2.60}$$

where $\overset{\circ}{x} = x(s_0)$, $\overset{\circ}{x'} = x'(s_0)$, $\overset{\circ}{y} = y(s_0)$, and $\overset{\circ}{y'} = y'(s_0)$. The C and S functions are called "cosine-like" and "sine-like." In the absence of any field imperfections, the linear motion in y is completely described by the betatron solution. The complete solution for motion in x is the sum of the homogeneous solution in (2.60) and a particular solution $\eta_x(\mathrm{s})\delta$, where η_x is the solution to the first of (2.58) with $\delta = 1$:

$$\eta_x'' + K_x^2(s)\eta_x = k. \qquad \text{(dispersion function)} \tag{2.61}$$

The complete solutions may then be written

$$x(s) = \tilde{x}(s) + \eta_x(s)\delta \quad ; \quad y(s) = \tilde{y}(s) \ . \tag{2.62}$$

The function $\eta_x(\mathrm{s})$ is called the *horizontal dispersion function.* It represents the trajectory followed by an off-momentum particle with unit momentum error that

is initially coincident with the design particle. Equations (2.62) do not include a vertical dispersion function η_y(s) due to the assumption that the design trajectory lies in a plane normal to the y direction. Vertical dispersion may be introduced however in the case of systems with bending in the vertical plane.

2.3.3 Linear Longitudinal Solutions

The third of Eqs. (2.57) is merely a statment of conservation of longitudinal momentum. Multiplying through by ds, it reads

$$dz + (1 + xk)ds = v_z dt \ . \tag{2.63}$$

Integrating and using $dt = ds/v_0$, we obtain

$$z - \overset{\circ}{z} = \int_{s_0}^{s} \left\{ \frac{\delta \mathrm{v}_z}{v_0} - kx \right\} ds \ . \tag{2.64}$$

If we now insert for x the linear solution from Eq. (2.62) and expand $\delta \mathrm{v}_z/v_0$ to lowest order in δ according to Eq. (2.31), we obtain the expression

$$z = \overset{\circ}{z} + C_z \overset{\circ}{x} + S_z \overset{\circ}{x}{}' + \eta_z \delta \tag{2.65}$$

where we have defined the functions

$$C_z \equiv -\int_{s_0}^{s} kC_x ds \ , \tag{2.66}$$

$$S_z \equiv -\int_{s_0}^{s} kS_x ds \ , \tag{2.67}$$

$$\eta_z \equiv (s - s_0) \left\{ \frac{1}{\gamma_0^2} - \alpha_c \right\} . \tag{2.68}$$

The factor α_c which appears in the longitudinal dispersion term is called the "momentum compaction":

$$\alpha_c(s) = \frac{1}{s - s_0} \int_{s_0}^{s} k(s)\eta_x(s) ds \ . \tag{2.69}$$

The function η_z, called the *longitudinal dispersion*, represents the proportionality between the longitudinal momentum deviation δp and the change in the longitudinal position of the test particle over the interval from s_0 to s. The expression for α_c given in Eq. (2.69) is a first-order approximation to the path-length compression in bends defined in Eq. (2.20):

$$\zeta(p) \simeq (s - s_0)\ \alpha_c \frac{\delta \mathrm{p}_z}{p_0}. \tag{2.70}$$

Comparing this with the terms in a Taylor expansion of $\zeta(p)$ in powers of the momentum deviation,

$$\zeta(p) = \frac{\partial \zeta}{\partial p_z}\delta \mathrm{p}_z + \frac{1}{2}\frac{\partial^2 \zeta}{\partial p_z^2}\delta \mathrm{p}_z^2 + ... \tag{2.71}$$

we see that (2.70) is merely the first term in the Taylor series. We can therefore make (to lowest order in the momentum deviation) the following association:

$$\alpha_c \simeq \frac{\partial \zeta}{\partial p_z}\frac{p_0}{s - s_0}. \tag{2.72}$$

This expression illuminates why α_c is called the momentum compaction. It is a dimensionless quanity representing the change in pathlength in a bend $\partial\zeta$ per unit of longitudinal momentum error ∂p_z, normalized to the design particle's path-length-to-momentum ratio over the same interval. From Eq. (2.68) we see that there is a particular design energy, $\gamma_0 = \alpha_c^{-1/2}$, at which the longitudinal dispersion vanishes. We call this value the "transition energy" and denote it by

$$\gamma_t \equiv \frac{1}{\sqrt{\alpha_c}}. \qquad \text{(transition energy)} \tag{2.73}$$

The concept of transition energy relates two competing effects: the longer (shorter) total path-length versus the larger (smaller) velocity of a test particle with a positive (negative) momentum dispersion. When the design energy γ_0 is above the transition energy, particles with a positive momentum deviation

(*i.e.* with a momentum greater than the design momentum) take longer to pass through the system and lag behind the design particle. When the design energy is below transition, these particles pass through the system more quickly and move ahead of the design particle. These statements may be summarized as follows:

$$\begin{array}{lccl} & \delta > 0 & \delta < 0 & \\ & - - -- & - - -- & \\ \gamma_0 < \gamma_t & \Delta z \leq 0 & \Delta z > 0 & \text{(below transition)} \\ \gamma_0 > \gamma_t & \Delta \mathrm{z} > 0 & \Delta \mathrm{z} \leq 0 & \text{(above transition)} \\ \gamma_0 = \gamma_t & \Delta \mathrm{z} = 0 & \Delta \mathrm{z} = 0 & \text{(at transition)} \end{array} \tag{2.74}$$

Here $\Delta \mathrm{z} = z$ - $\overset{\circ}{z}$, and the less than and greater than signs are approximate because we are neglecting the contributions from C_z and S_z.

2.3.4 The Transport Matrix R

To linear order in the coordinates of the initial state, the tensor expansion of Section 2.1.4 reads $\mathbf{x} = \mathbf{Q} + \mathrm{R}\ \overset{\circ}{\mathbf{x}}$. The lowest order tensor $\mathbf{Q}$ is a 6-element vector representing any offset of the beam centroid. If the centroid is assumed to adhere properly to the design trajectory, then $\mathbf{Q}$ may be set to zero. In this case, to lowest nonvanishing order, the transformation is a simple matrix multiplication:

.

$$\mathbf{x} = \mathrm{R}\ \overset{\circ}{\mathbf{x}} \tag{2.75}$$

Typically, the section of beamline extending from s_0 to s may be broken down into a set of N finite components whose individual transport matrices R_n may be calculated separately. The combined transport matrix R is then produced by multiplying together the individual matrices:

$$\mathrm{R} = \mathrm{R}_N \ldots \mathrm{R}_3\ \mathrm{R}_2\ \mathrm{R}_1 \tag{2.76}$$

The matrix R is the Jacobian of a transformation under linear forces. The linearized system it represents has a time-independent Hamiltonian so the phase space area is preserved and its Jacobian has unit determinant. Hence, we can write

$$\det(\mathrm{R}) = 1. \tag{2.77}$$

The components of the matrix R for a particular section of the beamline are obtained by linearizing the equations of motion of an arbitrary particle traveling near the design orbit. This linearization, performed in Sections 2.3.2 and 2.3.3, gives an R of the form

$$\mathrm{R}(s) = \begin{pmatrix} C_x(s) & S_x(s) & 0 & 0 & 0 & \eta_x(s) \\ C_x'(s) & S_x'(s) & 0 & 0 & 0 & \eta_x'(s) \\ 0 & 0 & C_y(s) & S_y(s) & 0 & 0 \\ 0 & 0 & C_y'(s) & S_y'(s) & 0 & 0 \\ C_z(s) & S_z(s) & 0 & 0 & 1 & \eta_z(s) \\ 0 & 0 & 0 & 0 & 0 & 1 \end{pmatrix} \tag{2.78}$$

It is straightforward to obtain the explicit expressions for the various matrix elements for simple beamline components (i.e.where n and k are constants) directly from Eqs. (2.57). The case of a drift corresponds to $k = n = 0$. That of a dipole to $n = 0$. And for a simple quadrupole field, the dispersion term $k\delta$ is omitted. Matrix elements for a drift, a quadrupole magnet, a dipole magnet, and a thin lens thereby obtained are displayed in Table 2.1.

In the case of the quadrupole magnet, due to the fact that the transverse equations of motion differ by a minus sign in front of the linear force term, focusing only occurs in one transverse direction or the other. If $n > 0$ then the magnet is vertically focusing and horizontally defocusing. If $n < 0$ then the magnet is horizontally focusing and vertically defocusing. The quadrupole

Table 2.1: Matrix Elements for Common Beamline Components

Element	Name	Drift	Quad	Dipole	Thin Lens
R_{11}	$C_x(s)$	1	$\cosh[k\sqrt{n}s]$	$\cos(ks)$	1
R_{12}	$S_x(s)$	s	$\frac{1}{k\sqrt{n}}\sinh[k\sqrt{n}s]$	$\frac{1}{k}\sin(ks)$	0
R_{21}	$C'_x(s)$	0	$k\sqrt{n}\sinh[k\sqrt{n}s]$	$-k\sin(ks)$	$-1/f$
R_{22}	$S'_x(s)$	1	$\cosh[k\sqrt{n}s]$	$\cos(ks)$	1
R_{33}	$C_y(s)$	1	$\cos[k\sqrt{n}s]$	1	1
R_{34}	$S_y(s)$	s	$\frac{1}{k\sqrt{n}}\sin[k\sqrt{n}s]$	s	0
R_{43}	$C'_y(s)$	0	$-k\sqrt{n}\sin[k\sqrt{n}s]$	0	$1/f$
R_{44}	$S'_y(s)$	1	$\cos[k\sqrt{n}s]$	1	1
R_{16}	$\eta_x(s)$	0	0	$\frac{1-\cos(ks)}{k}$	0
R_{26}	$\eta'_x(s)$	0	0	$\sin(ks)$	0
R_{51}	$C_z(s)$	0	0	$-\sin(ks)$	0
R_{55}	$S_z(s)$	0	0	$\frac{\cos(ks)-1}{k}$	0
R_{56}	$\eta_z(s)$	$\frac{s}{\gamma_0^2}$	$\frac{s}{\gamma_0^2}$	$\{\frac{s}{\gamma_0^2} - s + \frac{\sin(ks)}{k}\}$	1

matrix elements in Table 2.1 are correct for both cases. If $n < 0$, then $\sqrt{n}$ is pure imaginary and the hyperbolic and sinusoidal functions effectively trade places by virtue of the identities $\cosh(iz) = \cos(z)$ and $\sinh(iz) = i\sin(z)$. There is also a corresponding change in sign in the focusing terms C_x and C_y.

Since the quadrupole produces no bending, the radius of curvature is infinite and hence $k \to 0$. The fact that Eqs. (2.57) contain factors of k^2 is an artifact of the form of the expansion in Eq. (2.50) used for the field. Consequently, the dimensionless quantity n should be regarded as having an effective $1/k^2$ dependence so that in the limit $k \to 0$, the quantity $k^2 n$ does not vanish but kn does. The case of the thin lens is obtained by expanding the quadrupole elements to lowest order in s with the association $k^2 ns = 1/f$. The quantity f is thus the focal length of the thin lens and $1/(k^2 ns)$ is the approximate effective focal length of a quadrupole of length s.

2.3.5 Second Moments of the Beam Distribution

In Section 1.1 we defined a beam distribution function $F(\delta\mathbf{r}, \delta\mathbf{p})$ over the coordinates $(x, y, z, \delta p_x, \delta p_y, \delta p_z)$ relative to the beam centroid, and used this distrubution to obtain second moments and to define the normalized emittances. If we express the beam distribution instead in the trace space coordinates of the 6-vector $\mathbf{x}$ defined in Eq. (2.25), we can then use it to obtain a 6×6 matrix of second moments whose evolution (to linear order) is given by way of a simple matrix multiplication with the transport matrix R. Let this new distribution function be denoted $f(\mathbf{x}, s)$. If the beam is properly centered about its design position and momentum then the first moments vanish:

$$\langle x_j \rangle = \int x_i f(\mathbf{x}, s) d^6 x = 0. \tag{2.79}$$

We can define a 6×6 matrix Σ of second moments of the distribution:

$$\Sigma_{ij}(s) = \int x_j x_k f(\mathbf{x}, s) d^6x = \langle x_j x_k \rangle. \tag{2.80}$$

By Liouville's theorem, a distribution function, when followed under the equations of motion generated by a Hamiltonian, is invariant. Hence, the value of the distribution function at point $\mathbf{x}$ when the design particle is at s may be obtained from an earlier known functional form of the distribution, when the design particle was at s_0, by evaluating it at the point $\overset{\circ}{\mathbf{x}}$, which is the inverse of a linear transformation of the form in Eq. (2.75). That is,

$$f(\mathbf{x}, s) = f(\overset{\circ}{\mathbf{x}}, s_0), \quad \text{where } \mathbf{x} = \mathrm{R}\overset{\circ}{\mathbf{x}} \text{ or } \overset{\circ}{\mathbf{x}} = \mathrm{R}^{-1}\mathbf{x}. \tag{2.81}$$

Due to the fact that the transport matrix has unit determinant [Eq. (2.77)] we can write

$$d^6x = \det(\mathrm{R})\ d^6\overset{\circ}{x} = d^6\overset{\circ}{x}. \tag{2.82}$$

Using Eqs. (2.81) and (2.82), Eq. (2.80) becomes

$$\Sigma_{jk} = \int R_{ij}\ \overset{\circ}{x}_i\ R_{kl}\ \overset{\circ}{x}_l f(\overset{\circ}{\mathbf{x}}, s_0)\ d^6\overset{\circ}{x}. \tag{2.83}$$

Defining the beam matrix at the earlier position s_0 by

$$\overset{\circ}{\Sigma} \equiv \int \overset{\circ}{x}_j\ \overset{\circ}{x}_k\ f(\overset{\circ}{\mathbf{x}}, s_0)\ d^6\overset{\circ}{x}, \tag{2.84}$$

we see that Eq. (2.83) is the component form of the following matrix relationship between the sigma matrices at the two points on the beamline:

$$\Sigma = \mathrm{R}\ \overset{\circ}{\Sigma}\ \mathrm{R}^T. \tag{2.85}$$

The off-diagonal elements of the Σ matrix are symmetric under an exchange of indices: $\Sigma_{ij} = \Sigma_{ji}$. This is clearly seen by interchanging x_i and x_j in Eq. (2.80) and observing that the integral is unaltered. The diagonal elements represent the

variances in each of the 6 trace space coordinates. Taking their square roots then gives us the RMS values for each of these quantities. We typically denote these as follows:

$$\sigma_{x_j} \equiv \sqrt{\Sigma_{\rm jj}} = \sqrt{\langle x_j^2 \rangle}, \tag{2.86}$$

where the index j takes the values {1,2,3,4,5,6} corresponding to the trace space coodinates $(x, x', y, y', z, \delta)$. Because of their application to the examination of the transverse dynamics, it is also customary to define the following transverse submatrices:

$$\Sigma_x \equiv \begin{pmatrix} \Sigma_{11} & \Sigma_{12} \\ \Sigma_{21} & \Sigma_{22} \end{pmatrix} \; ; \; \Sigma_y \equiv \begin{pmatrix} \Sigma_{33} & \Sigma_{34} \\ \Sigma_{43} & \Sigma_{44} \end{pmatrix} \tag{2.87}$$

and the corresponding 2×2 transport matrices

$$M_x \equiv \begin{pmatrix} R_{11} & R_{12} \\ R_{21} & R_{22} \end{pmatrix} \; ; \; M_y \equiv \begin{pmatrix} R_{33} & R_{34} \\ R_{43} & R_{44} \end{pmatrix} . \tag{2.88}$$

The transverse RMS emittances are then defined by

$$\epsilon_x \equiv \sqrt{\det \Sigma_x} \; ; \; \epsilon_y \equiv \sqrt{\det \Sigma_y} \tag{2.89}$$

These quantites measure the areas occupied by the beam's distributions in the transverse trace space. They can be connected to the normalized emittances $\epsilon_{x,N}$, $\epsilon_{y,N}$ previously defined in Eqs. (1.8) and (1.9) by noting that $\delta p_x = \gamma_0 m v_0 x'$ and $\delta p_y = \gamma_0 m v_0 y'$. Hence,

$$\epsilon_{x,N} = \gamma_0 \beta_0 \epsilon_x \quad , \quad \epsilon_{y,N} = \gamma_0 \beta_0 \epsilon_y \; . \tag{2.90}$$

Under a linear matrix transformation R which has no dispersion terms $\eta_x = \eta_x' = 0$, the RMS emittances as defined defined by Eq. (2.89) are invariant. The

presence of dispersion and/or nonlinear effects, however, will tend to produce emittance growth. The contribution to the emittance from the linear dispersion can be seen by transporting the matrix of second moments according to Eq. (2.85) and then calculating the emittances $\epsilon_{x,0}$ and $\epsilon_{x,f}$ before and after respectively. Because the y (vertical) elements of the matrices do not contribute to the final result for x, we can write the matrix transport in an abbreviated 3×3 form

$$\overset{=}{\Sigma}_x = \begin{pmatrix} M_x & \boldsymbol{d} \\ 0 & 1 \end{pmatrix} \begin{pmatrix} \overset{\circ}{\Sigma}_x & 0 \\ 0 & \sigma_\delta^2 \end{pmatrix} \begin{pmatrix} M_x & \boldsymbol{d} \\ 0 & 1 \end{pmatrix}^T \tag{2.91}$$

where $\boldsymbol{d}$ is the dispersion vector

$$\boldsymbol{d} = \begin{pmatrix} \eta_x \\ \eta_x' \end{pmatrix} \tag{2.92}$$

and $\sigma_\delta = \sqrt{\Sigma_{66}}$ is the rms momentum spread. Evaluating Eq. (2.91) gives

$$\overset{=}{\Sigma}_x = \begin{pmatrix} \Sigma_x & \boldsymbol{d}\sigma_\delta^2 \\ \boldsymbol{d}^T\sigma_\delta^2 & \sigma_\delta^2 \end{pmatrix}, \text{ where } \quad \Sigma_x \equiv M_x \overset{\circ}{\Sigma}_x M_x^T + \sigma_\delta^2 \, \boldsymbol{d}\boldsymbol{d}^T. \tag{2.93}$$

The final rms emittance is then obtained by taking the determinant of the upper left 2×2 portion of the matrix. This gives

$$\epsilon_{x,f} = \sqrt{\det \Sigma_x} = \left\{ \det \left[M_x \overset{\circ}{\Sigma}_x M_x^T + \sigma_\delta^2 \boldsymbol{d}\boldsymbol{d}^T \right] \right\}^{1/2} \tag{2.94}$$

In the case where the dispersion is zero ($\boldsymbol{d} = 0$) the above reduces, by utilizing the identity $\det(AB) = \det(A)\,\det(B)$ and the fact that the transport matrix M_x has unit determinant, to the expression for the initial emittance:

$$\epsilon_{x,f} = \left(\det \overset{\circ}{\Sigma}_x \right)^{1/2} = \epsilon_{x,0} \ ; \ (\boldsymbol{d} \to 0) \tag{2.95}$$

It should be noted that the equality is valid only to linear order, and to the extent that space charge effects on the emittance growth can be neglected.

2.3.6 Betatron Motion

The betatron motion was the name given earlier to the homogeneous parts ($\tilde{x}$, $\tilde{y}$) of the solutions to the linear transverse equations of motion, which satisfy differential equations of the type:

$$\mu'' + K_\mu^2(s)\mu = 0 \; ; \tag{2.96}$$

where μ stands for either $\tilde{x}$ or $\tilde{y}$. For a periodic function $K_\mu(s)$, this equation is of Hill's type. However, even if the system under investigation is not periodic but is of finite length, the periodic Hill's solution is still useful as a means of reparametrizing the equations of motion. In terms of 2×2 transport matrices the betatron solutions satisfy the transport relation

$$\boldsymbol{\chi}_\mu = M_\mu \overset{\circ}{\boldsymbol{\chi}}_\mu, \tag{2.97}$$

where we have defined the 2-vector $\boldsymbol{\chi}_\mu = (\mu, \mu')$. An alternate parametrization of the solution to this equation, originally proposed by Courant and Snyder [54], gives rise to much of the traditional terminology of beam optics. Periodic solutions to Hill's equation may be written as cosine functions with an s-dependent phase and amplitude:

$$\mu = w_\mu(s) \cos\left[\psi_\mu(s) + \phi_\mu\right]. \tag{2.98}$$

Substitution of Eq. (2.98) into (2.96) produces a pair of differential equations for w_μ and ψ_μ,

$$\left(w_\mu'' + K_\mu^2 w_\mu\right) = \frac{e_\mu^2}{w_\mu^3} \tag{2.99}$$

$$\psi_\mu' = \frac{e_\mu}{w_\mu^2} \tag{2.100}$$

where e_μ is a constant of integration called the *Courant-Snyder invariant*. Using the amplitude function w_μ, we can define the following parameters of the test

particle:

$$\beta_\mu \equiv \frac{w_\mu^2}{e_\mu} \; ; \; \alpha_\mu \equiv -\frac{1}{2}\beta'_\mu \; ; \; \gamma_\mu \equiv \frac{1+\alpha_\mu^2}{\beta_\mu}. \tag{2.101}$$

The parameters $\alpha_\mu, \beta_\mu, \gamma_\mu$ are referred to as *Twiss parameters*, after R. Q. Twiss [55]. For reasons which will become clear later, let us also define a matrix of these parameters

$$W_\mu \equiv e_\mu \begin{pmatrix} \beta_\mu & -\alpha_\mu \\ -\alpha_\mu & \gamma_\mu \end{pmatrix}. \tag{2.102}$$

Utilizing the definitions above and various matrix identities, it is straightforward to show that W_μ satisfies the following matrix equations:

$$\det(W_\mu) = e_\mu^2 \; , \tag{2.103}$$

$$\boldsymbol{\chi}_\mu^T W_\mu^{-1} \boldsymbol{\chi}_\mu, = 1 \tag{2.104}$$

$$W_\mu = M_\mu \overset{\circ}{W}_\mu M_\mu^T \; . \tag{2.105}$$

Equation (2.103) follows directly from the third of Eqs. (2.101). Equation (2.104) may be verified by combining (2.98) with (2.101) and employing various trigonometric identities. Equation (2.105) then follows from (2.104) and (2.97), with use of the identity $(ABA^T)^{-1} = (A^T)^{-1}B^{-1}A^{-1}$.

Since e_μ is a constant, Eq. (2.103) represents an invariance relationship between the elements of the W matrix. The second equation describes an ellipse of area πe_μ in the phase plane of μ and μ'. We can see this more clearly by multiplying out the matrices and writing it in the form,

$$\gamma_\mu \mu^2 + 2\alpha_\mu \mu\mu' + \beta_\mu \mu'^2 = e_\mu \; . \tag{2.106}$$

We conclude that the betatron motion is represented by an elliptical trajectory in the transverse trace space plane. There are an infinite number of such trajectories, which describe at a given point s along the beamline a set of concentric

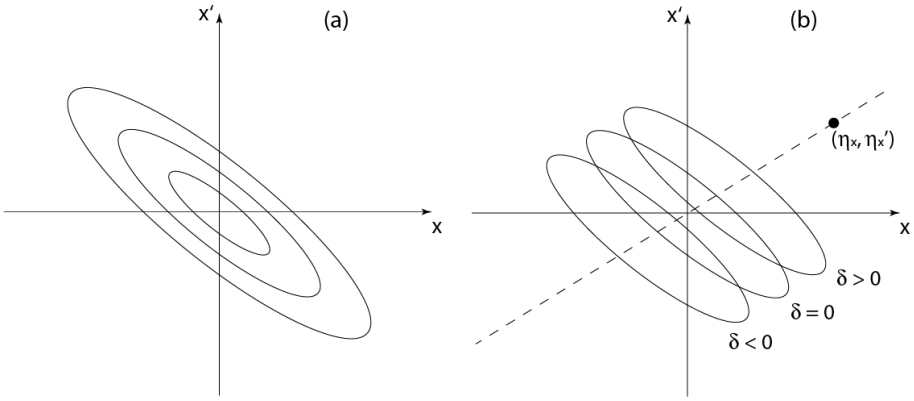

Figure 2.2: Trace space ellipses for (a) three trajectories with different invariants and (b) three trajectories with the same invariant but different momenta.

ellipses. All of these ellipses have the same Twiss parameters but vary according to the areas which they enclose in the trace space plane of μ and μ'. This is illustrated in Fig. 2.2(a) which shows three ellipses in the (x, x') plane with the same Twiss parameters $(\alpha_x, \beta_x, \gamma_x)$ but with different values of the Courant-Snyder invariant e_x. Consequently γ_μ, α_μ, β_μ are functions of s which are determined by the curvature function K_μ(s) of the lattice and by their initial values. It should also be noted that since γ_μ, α_μ, β_μ are all functions of s, the orientation of the trace space ellipse upon which a particle's betatron motion is constrained to lie changes as the particle travels through the lattice. However, the area πe_μ of this ellipse does not change.

Recall that the horizontal dispersion function η_x(s) describes the trajectory of an off-energy particle having unit momentum error and initially coincident with the design particle. A particle that is initially displaced from the design trajectory and having the arbitrary momentum error δ will then execute betatron oscillations about this trajectory.

Consequently, the trace space ellipses in the plane of x and x' (as opposed to $\tilde{x}$ and $\tilde{x}'$ are those of Eq. (2.106) but offset from the origin by amounts $\eta_x\delta$ and $\eta'_x\delta$ along the horizontal and vertical axes respectively. In this representation then the set of all possible trace space trajectories consists of the set of concentric ellipses described by (2.106) plus the set of all possible translations of them along a line in the phase plane which extends from the origin through the point (x, x')=(η_x,η'_x). Figure 2.2(b) illustrates three trace space ellipses in the (x, x') plane corresponding to the same value of e_x but with different values of δ. Since there is generally some spread in momentum σ_δ the phase ellipses are essentially "smeared out" along this line in a way consistent with the momentum distribution of the particles in the beam.

2.3.7 Definition of the RMS Ellipse

Since a nonzero dispersion function η_x is produced by the interaction of the beam with a dipole field, it is reasonable to assume that during some initial interval after the beam's generation and before it has encountered such a field, the dispersion is equal to zero or is at least very nearly zero. Consequently, the phase space ellipses at this initial point are concentric and so if one chooses a sufficiently large phase space ellipse, it can be expected to contain most of the particles in the beam and therefore some proportional relationship may be expected to exist between the area of this ellipse and the emittance of the beam. Let us therefore suppose that the beam at some initial point s_0 has zero dispersion ($\mathring{\eta}_x$=$\mathring{\eta}_y$=$\mathring{\eta}'_x$=$\mathring{\eta}'_y$=0).

The ellipses described by Eq. (2.106) represent an infinity of mathematically allowed trajectories which particles may follow in transverse trace space as they propagate along the beamline. Let us choose from among these the ellipse whose

W-matrix and Courant-Snyder invariant satisfies

$$\overset{\circ}{W}_{\mu} = \overset{\circ}{\Sigma}_{\mu} \quad \text{and} \quad \overset{\circ}{e}_{\mu} = \overset{\circ}{\epsilon}_{\mu}, \tag{2.107}$$

where $\overset{\circ}{\Sigma}_{\mu}$ is the actual RMS matrix of second moments of the beam. We call the corresponding ellipse the *RMS ellipse*. After propagating both matrices ($\overset{\circ}{W}_{\mu}$ and $\overset{\circ}{\Sigma}_{\mu}$) via the usual linear transport relations (2.91) and (2.105), they are found at a later position s along the beamline to be related by way of

$$\Sigma_x(s) = W_x(s) + \sigma_\delta^2 \boldsymbol{d}\boldsymbol{d}^T \ ; \ \Sigma_y(s) = W_y(s). \tag{2.108}$$

If there is horizontal dispersion present in the section of beamline separating the points s_0 and s, then in the horizontal direction the equality of the RMS emittance ϵ_x and the Courant-Snyder invariant e_x is destroyed. From Eqs. (2.89) and (2.108) it follows that the relationships connecting these quantities at point s are given by

$$\epsilon_x = \sqrt{\det\left[W_x + \sigma_\delta^2 \boldsymbol{d}\boldsymbol{d}^T\right]} \ , \ \epsilon_y = \sqrt{\det W_y} = e_y \ . \tag{2.109}$$

Similarly, the RMS beam sizes in x and y are given by

$$\sigma_x = \sqrt{\beta_x e_x + \eta_x^2 \sigma_\delta^2} \ , \ \sigma_y = \sqrt{\beta_y e_y} \ . \tag{2.110}$$

In the limit of zero dispersion the foregoing results are much simplified. In a dispersionless beamline, the RMS emittance (to linear order and neglecting space-charge forces) is preserved and the envelope equations have the same form for both transverse directions. To see the truth of these statements, we need merely to set $\boldsymbol{d} = 0$ in Eq. (2.108). We then have that the matrix of second moments and the matrix of Courant-Snyder parameters are equal at all points. This statement may be written

$$\Sigma_\mu\left(s_0\right) = W_\mu\left(s_0\right), \ \boldsymbol{d} = 0 \implies \Sigma_\mu(s) = W_\mu(s). \tag{2.111}$$

The RMS ellipse is a useful concept because it transforms under linear focusing forces according to the same matrix transport relation as the matrix of second moments. The Courant-Snyder parameters of the RMS ellipse therefore provide information about the size of the beam (β_μ), the angular divergence or convergence (γ_μ), the position-to-angle correlation (α_μ), and the phase space area (e_μ). It follows that under these conditions the RMS beam size σ_μ is equal to the betatron amplitude function w_μ for *both* transverse directions. Consequently, Eq. (2.99) takes the form

$$\frac{\sigma_\mu''}{\sigma_\mu} + K_\mu^2 - \frac{\epsilon_\mu^2}{\sigma_\mu^4} = 0 \ , \ (\boldsymbol{d} \to 0). \tag{2.112}$$

The RMS emittance appears on the right-hand side now, since ϵ_μ=e_μ for both x and y. Note that this is identical to the RMS envelope equation, Eq. (1.33), in the absence of the space charge and acceleration terms ($\kappa_s = \gamma' = 0$).

2.3.8 Second Order Optics

As a first approximation for the preliminary design of a linear beamline, the first order matrix approach discussed in Section 2.3.4 is sufficient. A more accurate description of the single-particle beam dynamics can be obtained by inclusion of higher-order terms in the matrix expansion in Eq. (2.28). In circular machines, where minor discrepancies in the theory can accumulate over many passes through the machine to create significant errors, it may be necessary to include terms up to 5th order. For linear devices, the inclusion of the 2nd order $6 \times 6 \times 6$ tensor elements T_{ijk} is often sufficient, although under some circumstances (such as a large energy spread), 3rd order terms may be required to explain observed beam dynamics.

Calculating higher order matrix elements is a tedious process. Second order matrix elements are obtained by expanding the general equations of motion (2.14)

but keeping terms to second order in products of the coordinates. This produces a set of coupled nonlinear differential equations. To second order, the transverse equations of motion read

$$\begin{aligned} x'' + (1-n)k^2 x - k\delta &= (2n-1-\beta)k^3x^2 + k'xx' + \frac{1}{2}kx'^2 \\ &\quad + (2-n)k^2x\delta + \frac{1}{2}(k'' - nk^3 + 2\beta k^3)y^2 + k'yy' - \frac{1}{2}ky'^2 - k\delta^2, \\ y'' + nk^2 y &= 2(\beta - n)k^3xy + k'xy' - k'x'y + kx'y' + nk^2y\delta. \end{aligned} \tag{2.113}$$

Although these equations cannot be solved through direct analytical means, as in the linear case, the required matrix elements can be extracted by the use of driving terms. Consequently, their solutions are subsequently transformed into the sort of Cartesian basis used in our linear evaluation, by way of the tranformation. This is done by substituting the following form for the solutions

$$x_i = R_{ij}\overset{\circ}{x}_j + \tilde{T}_{ijk}\overset{\circ}{x}_j\overset{\circ}{x}_k \quad ; \quad i = 1,2,3,4 \tag{2.114}$$

into Eqs. (2.113) and then equating coefficients of like products of the initial coordinates ($\overset{\circ}{x}_j\overset{\circ}{x}_k$). This produces a set of differential equations of the form

$$\tilde{T}''_{ijk}(s) + K_\mu^2(s)\tilde{T}_{ijk}(s) = f_{ijk}(s) \quad ; \quad i = 1,2,3,4. \tag{2.115}$$

where μ stands for either x or y and the form $K_x^2 = (n-1)k^2$ or $K_y^2 = nk^2$ that appears depends upon which of Eqs. (2.113) the particular element originated from, and the so-called *driving terms* $f_{ijk}(s)$ are functions of n, β, k, $C_{x,y}$, $S_{x,y}$, and their derivatives. The second order matrix elements are then obtained by individually solving each of Eq. (2.115) by integrating the driving term over the Green's function G_μ for each term:

$$\tilde{T}_{ijk} = \int_0^s G_\mu(s,\tau)f_{ijk}(\tau)d\tau \quad ; \quad i = 1,2,3,4. \tag{2.116}$$

The Green's function is given by $G_\mu(s,\tau) = S_\mu(t)C_\mu(\tau) - S_\mu(\tau)C_\mu(s)$. It should further be noted that to maintain continuity in the second order across field boundaries, which may change abruptly, it is appropriate to employ a change from derivatives d/ds with respect to path-length along the reference trajectory to derivatives d/dz with respect to the longitudinal cartesian coordinate z. That is, we implement the transformations

$$x' = \frac{dx}{ds} \rightarrow \frac{dx}{dz} = \frac{dx/ds}{1+kx}, \tag{2.117}$$

$$y' = \frac{dy}{ds} \rightarrow \frac{dy}{dz} = \frac{dy/ds}{1+kx}. \tag{2.118}$$

This change of variable effectively adds an additional term $F_{ijk}(s)$, which is a function of the first-order matrix elements, to the solution for $\tilde{T}_{ijk}$ in Eq. (2.116), so that the final matrix elements T_{ijk} are given by

$$T_{ijk} = \int_0^s G_\mu(s,\tau) f_{ijk}(\tau) d\tau + F_{ijk}(s) \quad ; \quad i = 1,2,3,4. \tag{2.119}$$

Explicit general forms for the matrix elements are derived at length in Refs. [52, 56]. The transverse second order matrix elements extracted from these results for a drift, a quadrupole, a dipole, and a sextupole are shown in Table 2.2. It should be noted that in this table, we have used the abbreviations $K_1 = -k^2 n$ and $K_2 = k^3\beta$ for the quadrupole and sextupole field strengths respectively. This is consistent with the notation of Eqs. (2.50) and (2.51).

The longitudinal ($i = 5$) matrix elements T_{5jk} are obtained by expanding the expression for the time delay Δt in Eq. (2.21) but keeping terms to second order in ζ and $\delta v/v_0$. Consequently, in place of Eq. (2.23) we have

$$z = \overset{\circ}{z} - \zeta + (s+\zeta)\frac{\delta v}{v_0} - s\left(\frac{\delta v}{v_0}\right)^2. \tag{2.120}$$

The velocity deviation $\delta v/v_0$ can then be expanded in powers of momentum deviation δ in accordance with Eq. (2.31). Keeping only terms that are up to

Table 2.2: Second-order (relativistic) matrix elements for common optical beamline components.

Element	Drift	Quad	Dipole	Sextupole
T_{111}	0	0	$-k\frac{\sin^2(ks)}{2}$	$-\frac{K_2 s^2}{4}$
T_{121}	0	0	$\sin[ks]\cos(ks)$	$-\frac{K_2 s^3}{6}$
T_{122}	0	0	$\frac{1}{k}\cos[ks]\sin^2(ks/2)$	$-\frac{K_2 s^4}{24}$
T_{133}	0	0	0	$\frac{K_2 s^2}{4}$
T_{143}	0	0	0	$\frac{K_2 s^3}{6}$
T_{144}	0	0	$-\frac{1}{2k}(1-\cos(ks))$	$\frac{K_2 s^4}{24}$
T_{161}	0	$\frac{1}{2}\sqrt{K_1}s\sin(\sqrt{K_1}s)$	$\sin^2(ks)$	0
T_{162}	0	$\frac{-3K_1^2 s\cos(\sqrt{K_1}s)+3K_1^{3/2}\sin(\sqrt{K_1}s)}{6K_1^2}$	$\frac{1}{k}\sin(ks)[1-\cos(ks)]$	0
T_{166}	0	0	$-\frac{1}{2k}\sin^2(ks)$	0
T_{211}	0	0	0	$-\frac{K_2 s}{2}$
T_{221}	0	0	0	$-\frac{K_2 s^2}{2}$
T_{222}	0	0	$-\frac{\sin(ks)}{2}$	$-\frac{K_2 s^3}{6}$
T_{233}	0	0	0	$\frac{K_2 s}{2}$
T_{243}	0	0	0	$\frac{K_2 s^2}{2}$
T_{244}	0	0	$-\frac{\sin(ks)}{2}$	$\frac{K_2 s^2}{2}$
T_{261}	0	$\frac{3K_1^2 s\cos(\sqrt{K_1}s)+3K_1^{3/2}\sin(\sqrt{K_1}s)}{6K1}$	$k\sin(ks)$	0
T_{262}	0	$\frac{1}{2}\sqrt{K_1}s\sin(\sqrt{K_1}s)$	0	0
T_{266}	0	0	$-\sin(ks)$	0
T_{331}	0	0	0	$\frac{K_2 s^2}{2}$
T_{332}	0	0	0	$\frac{K_2 s^3}{6}$
T_{341}	0	0	$\sin(ks)$	$\frac{K_2 s^3}{6}$
T_{342}	0	0	$\frac{1}{k}(1-\cos(ks))$	$\frac{K_2 s^4}{12}$
T_{363}	0	$-\frac{1}{2}\sqrt{K_1}s\sinh(\sqrt{K_1}s)$	0	0
T_{364}	0	$\frac{-K_1 s\cosh(\sqrt{K_1}s)+\sqrt{K_1}\sinh(\sqrt{K_1}s)}{2K_1}$	$s-\frac{1}{k}\sin(ks)$	0
T_{431}	0	0	0	$K_2 s$
T_{432}	0	0	0	$\frac{K_2 s^2}{2}$
T_{441}	0	0	0	$\frac{K_2 s^2}{2}$
T_{442}	0	0	0	$\frac{K_2 s^3}{3}$
T_{463}	0	$-\frac{1}{2}[K_1 s\cosh(\sqrt{K_1}s)+\sqrt{K_1}\sinh(\sqrt{K_1}s)]$	0	0
T_{464}	0	$-\frac{1}{2}\sqrt{K_1}s\sinh(\sqrt{K_1}s)$	0	0
T_{511}	0	$-\frac{1}{4}K_1(s-\frac{\cos(\sqrt{K_1}s)\sin(\sqrt{K_1}s)}{\sqrt{K_1}})$	0	0
T_{521}	0	$\frac{1}{2}\sin^2(\sqrt{K_1}s)$	0	0
T_{522}	$-\frac{s}{2}$	$-\frac{1}{4}(s+\frac{\cos(\sqrt{K_1}s)\sin(\sqrt{K_1}s)}{\sqrt{K_1}})$	$-\frac{1}{2k}\sin(ks)$	$-\frac{s}{2}$
T_{533}	0	$\frac{1}{4}K_1(s-\frac{\cosh(\sqrt{K_1}s)\sinh(\sqrt{K_1}s)}{\sqrt{K_1}})$	0	0
T_{543}	0	$-\frac{1}{2}\sinh^2(\sqrt{K_1}s)$	0	0
T_{544}	$-\frac{s}{2}$	$-\frac{1}{4}(s+\frac{\cosh(\sqrt{K_1}s)\sinh(\sqrt{K_1}s)}{\sqrt{K_1}})$	$-\frac{1}{2k}\sin(ks)$	$-\frac{s}{2}$
T_{561}	0	0	0	0
T_{562}	0	0	$\frac{1}{k}[\cos(ks)-1]$	0
T_{566}	0	0	0	0

second order in ζ and δ this yields

$$z = \overset{\circ}{z} - \zeta + \frac{\delta}{\gamma_0^2}(\zeta + s) - s\left[\frac{1}{\gamma_0^4} + \frac{3}{2}\left(\frac{\beta_0}{\gamma_0}\right)^2\right]\delta^2. \tag{2.121}$$

For an ultrarelativistic beam, only the first two terms contribute ($z = \overset{\circ}{z} - \zeta$). The remaining terms containing powers of $1/\gamma_0$ contribute nonrelativistic corrections to the second order matrix elements involving the momentum error δ, namely the nonvanishing T_{5jk} where j and/or k is equal to 6. These correction terms are derived in [51]. The relativistic terms are then obtained from the expression $z = \overset{\circ}{z} - \zeta$, which is the same expression used in the linear case except that the integral for ζ from Eq. (2.20) is expanded to second order in the transverse coordinates:

$$z \approx \overset{\circ}{z} + \int_0^s \left[kx + \frac{1}{2}(x'^2 + y'^2)\right] ds. \tag{2.122}$$

The matrix elements are then obtained by substituting the form $z = R_{5j}\overset{\circ}{x}_j + T_{5jk}\overset{\circ}{x}_j\overset{\circ}{x}_k$ into the left-hand side and the form of Eq. (2.114) for the transverse coordinates on the right-hand side and then equating coefficients of like powers of the initial coordinates $\overset{\circ}{x}_i$. General forms for the nonvanishing relativistic matrix elements T_{5jk} are given in Refs. [52, 57]. The explicit forms for a drift, quadrupole, dipole, and sextupole obtained therefrom are displayed in Table 2.2.

CHAPTER 3

Dogleg Compression and Bunch Shaping

The technique for generating ramped electron bunches proposed in Section 1.5.2 relies upon the use of a dogleg as a bunch compressor. We will derive in the present chapter the general beam optics theory of this device. We then apply this theory specifically to the dogleg design implemented at the UCLA Neptune Laboratory, including discussion of the optimal Twiss parameters for matching the electron beam into the device and conditions for killing the horizontal dispersion and its derivative. Additionally, we describe in detail the bunch-shaping mechanism in the language of first- and second-order beam optics. The resulting analytical predictions are supported with simulations of the Neptune beamline.

3.1 Theory of the Dogleg Compressor

3.1.1 General Conditions on the System Optics

Examples of three dogleg beamlines found at different facilities are shown in Fig. 3.1: (a) the Accelerator Test Facility (ATF) at Brookhaven National Laboratory, (b) the UCLA Neptune Laboratory, and (c) the Stanford Linear Accelerator Laboratory (SLAC) ORION test beamline. The drawings are cartoons drawn to different scales, but the actual physical lengths are shown on the figure. Wedges, blue lenses, and red rectangles represent dipoles, quadrupoles, and sextupoles,

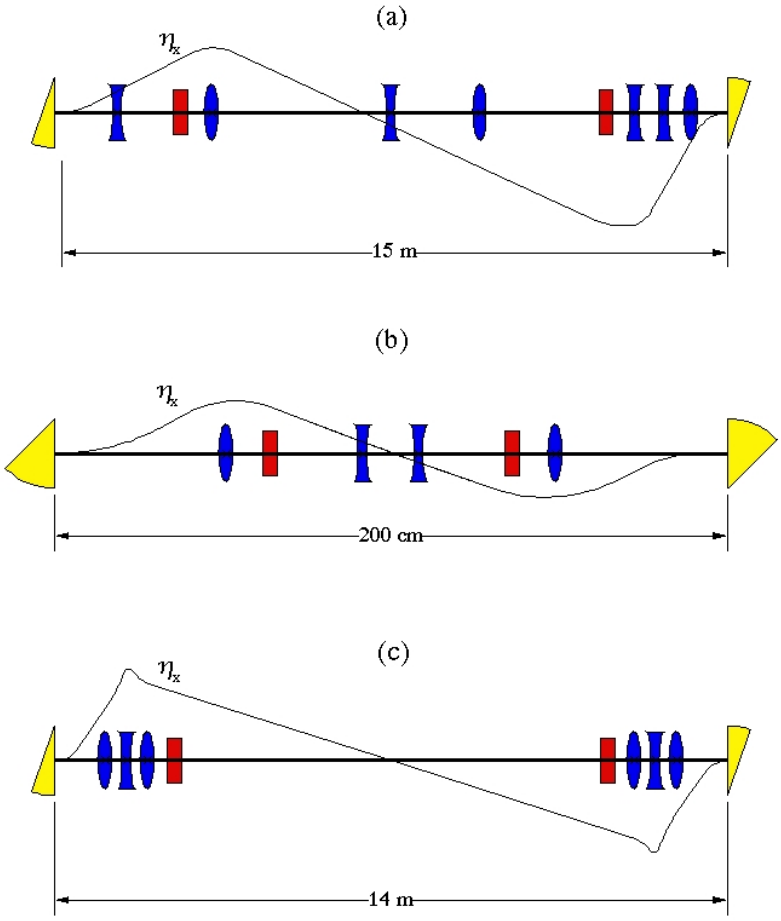

Figure 3.1: Cartoon drawings of doglegs at (a) ATF-VISA, (b) UCLA-Neptune, and (c) ORION-SLAC. Each drawing is scaled to fit the figure.

respectively. In the drawing an approximate representation of the horizontal dispersion function η_x is superimposed. We observe that the arrangement of magnets has a mirror symmetry in the beamlines of Fig. 3.1(b) and (c), but not (a). Although it is not strictly necessary to implement this sort of optical symmetry, doing so simplifies both the analytical description and experimental operation of the device as a compressor. Optimal operation of the dogleg as a bunch compressor, under an optically symmetric geometry, relies upon the horizontal dispersion function η_x passing through zero at the midpoint between the bends. This ensures that the final dispersion function and its derivative with respect to the path length parameter s are both zero at the exit of the device. In order to further utilize the symmetry of the beamline in controlling the beam size and eliminating net emittance growth, we additionally require that a waist be formed at the midpoint. This ensures that the beta functions have mirror symmetry and therefore return to their original values at the exit of the beamline. In summary, then, the contraints we will impose upon the system are that it

$$\begin{aligned} &\text{(i) be optically symmetric,} \\ &\text{(ii) be nondispersive } (\eta_x = \eta_x' = 0 \text{ at the exit}), \\ &\text{(iii) have a waist at the midpoint } (\alpha_x = \alpha_y = 0). \end{aligned} \tag{3.1}$$

For the optical analysis we will represent the trace space coordinates of a test particle in the beam distribution using the transport 6-vector notation $\mathbf{x} = (x, x', y, y', z, \delta)$ described in Section 2.1.4. Let $R(s_0, s)$ denote the transport matrix between the points s_0 and s, with $s = 0$ denoting the entrance of the first bend magnet of the dogleg, and let $\Sigma(s)$ denote the 6×6 matrix of second moments of the beam distribution at the point s. Since we are concerned with the values of the various system parameters primarily at three points (the en-

trance $s = 0$, the midpoint $s = \hat{s}$, and the exit $s = \Delta s$), we adopt the following simplified notation:

$$\hat{R} \equiv R(0, \hat{s}), \quad R \equiv R(0, \Delta s), \quad \overset{\circ}{\Sigma} \equiv \Sigma(0), \quad \hat{\Sigma} \equiv \Sigma(\hat{s}), \quad \Sigma \equiv \Sigma(\Delta s). \tag{3.2}$$

The linear analysis then proceeds straightforwardly, and is further simplified by the symmetry condition (i) which effectively reduces the problem to that of the half-lattice, containing only a compound bend radius ρ, quadrupoles, and drifts. The free parameters are then the quadrupole focal lengths and the initial Twiss parameters of the beam (which can be adjusted using the upstream optics on the main beamline). Under the assumption of optical symmetry, the remaining conditions, which we may write as

$$\hat{R}_{16} = 0 \tag{3.3}$$

$$\hat{\Sigma}_{12} = \hat{\Sigma}_{21} = \hat{\Sigma}_{34} = \hat{\Sigma}_{43} = 0 \tag{3.4}$$

form contraints upon the system which effectively reduce the number of free parameters. Equations (3.3) and (3.4) produce a set of simultaneous algebraic equations for the values of the focal lengths f_i (or equivalently, the field strengths K_i) of the quadrupoles and the initial Twiss parameters $\overset{\circ}{\alpha}$ and $\overset{\circ}{\beta}$, which are connected to the midpoint sigma-matrix elements by the linear transport relation

$$\hat{\Sigma} = \hat{R}^T \overset{\circ}{\Sigma} \hat{R}. \tag{3.5}$$

For a given initial beam, Eqs. (3.3) and (3.4) provide the values of the quadrupole strengths which optimize the lattice, to linear oder.

3.1.2 Transformation Equation for the Longitudinal Coordinate

For considerations of beam shaping, we are concerned with the longitudinal (or $i = 5$) component of the general transport relation Eq. (2.27) from the entrance

$s = 0$ to the exit of the final bend at $s = \Delta s$ which is given by

$$z = \overset{\circ}{z} + R_{51}\overset{\circ}{x} + R_{52}\overset{\circ}{x}' + R_{56}\delta + T_{561}\overset{\circ}{x}\delta + T_{562}\delta\overset{\circ}{x}' + \ldots \tag{3.6}$$

Here we have included nonlinear terms dependent only on the second-order coupling between the momentum error and the motion in x. For beams of small transverse emittances but with a large energy spread, the chromatic terms in the transformation will tend to dominate the final form of the longitudinal profile. Among these the strongest contributors are the longitudinal dispersion terms, which are dependent on the momentum; the coupling of final longitudinal position to the initial transverse coordinates is relatively quite small. Hence, we may formulate the following approximation, including terms up to thrid order in the momentum error δ:

$$z \approx \overset{\circ}{z} + R_{56}\delta + T_{566}\delta^2 + U_{5666}\delta^3 + \ldots \tag{3.7}$$

The first order coefficient $R_{56} = (\partial z/\partial\delta)_{\delta\to 0}$ represents the longitudinal dispersion function η_x. The remaining elements, $T_{566}, U_{5666}, \ldots$, are higher-order momentum error contributions to the longitudinal dispersion. We may consider Eq. (3.7) to apply to a beam of small transverse emittances and large energy spread. Of course, it is conceivable to have a beam of very small emittance, but which is either large in its transverse dimensions and very well collimated, or which is very small in transverse size but with large angles. In either of these cases, the assumption of small emittance is insufficient, so we additionally stipulate that the beam size is well controlled and does not undergo a sharp focus. It is also presumed that the beam is sufficiently relativistic that space charge may be neglected. The point at which higher-order terms in Eq. (3.7) may be truncated depends upon the energy spread of the beam. In practice it is rarely necessary to consider higher than third-order contributions for single-pass transport. For

the Neptune dogleg compressor, the third-order effects are negligible. General relations for the first- and second-order contributions (R_{56} and T_{566}) are derived explicitly in the following section.

3.1.3 Derivation of the Longitudinal Dispersion Terms

Explicit first-order matrix elements for various common beamline components were provided in Table 2.2. We may write generic matrices for a bend B of angle $\theta = k\Delta s$ and bend radius $\rho = 1/k$, a thin-lens quadrupole of focal length f and a drift of length l as follows:

$$B(\theta,\rho) = \begin{pmatrix} \cos\theta & \rho\sin\theta & 0 & 0 & 0 & \rho(1-\cos\theta) \\ -(\sin\theta)/\rho & \cos\theta & 0 & 0 & 0 & \sin\theta \\ 0 & 0 & 1 & \rho\theta & 0 & 0 \\ 0 & 0 & 0 & 1 & 0 & 0 \\ -\sin\theta & \rho(\cos\theta-1) & 0 & 0 & 1 & \left(\frac{\rho\theta}{\gamma_0^2} - \rho\theta + \rho\sin\theta\right) \\ 0 & 0 & 0 & 0 & 0 & 1 \end{pmatrix} \tag{3.8}$$

$$Q(f) = \begin{pmatrix} 1 & 0 & 0 & 0 & 0 & 0 \\ -1/f & 1 & 0 & 0 & 0 & 0 \\ 0 & 0 & 1 & 0 & 0 & 0 \\ 0 & 0 & 1/f & 1 & 0 & 0 \\ 0 & 0 & 0 & 0 & 1 & 0 \\ 0 & 0 & 0 & 0 & 0 & 1 \end{pmatrix}; \tag{3.9}$$

$$D(l) = \begin{pmatrix} 1 & l & 0 & 0 & 0 & 0 \\ 0 & 1 & 0 & 0 & 0 & 0 \\ 0 & 0 & 1 & l & 0 & 0 \\ 0 & 0 & 0 & 1 & 0 & 0 \\ 0 & 0 & 0 & 0 & 1 & l/\gamma_0^2 \\ 0 & 0 & 0 & 0 & 0 & 1 \end{pmatrix}; \tag{3.10}$$

Let Y represent the linear matrix for a combination of quadrupoles and drifts. The total first order transport matrix for a dogleg can then be written $R = BY\tilde{B}$, where $B = B(\theta, \rho)$, $\tilde{B} = B(-\theta, -\rho)$ and Y has the form

$$Y = \begin{pmatrix} Y_{11} & Y_{12} & 0 & 0 & 0 & 0 \\ Y_{21} & Y_{22} & 0 & 0 & 0 & 0 \\ 0 & 0 & Y_{33} & Y_{34} & 0 & 0 \\ 0 & 0 & Y_{43} & Y_{44} & 0 & 0 \\ 0 & 0 & 0 & 0 & 1 & Y_{56} \\ 0 & 0 & 0 & 0 & 0 & 1 \end{pmatrix}; \tag{3.11}$$

The resultant horizontal dispersion function and its derivative (elements R_{16} and R_{26} of the total transport matrix) obtained by matrix multiplication are then given by

$$\begin{aligned} R_{16} &= \rho - \rho\cos\theta + \rho(\cos\theta - 1)(Y_{11}\cos\theta + \rho Y_{21}\sin\theta) \\ &\quad - \sin\theta(Y_{12}\cos\theta + \rho Y_{22}\sin\theta), \\ R_{26} &= \sin\theta + (\cos\theta - 1)(\rho Y_{21}\cos\theta - Y_{11}\sin\theta) \\ &\quad + \sin\theta(Y_{12}\sin\theta - \rho Y_{22}\cos\theta)/\rho. \end{aligned} \tag{3.12}$$

The longitudinal dispersion element may then be written in terms of these functions as follows:

$$R_{56} = Y_{56} + \frac{2\theta\rho}{\gamma_0^2} - 2\theta\rho + (2\rho - R_{16})\sin\theta + R_{26}\rho(1 - \cos\theta). \tag{3.13}$$

Noting that $Y_{56}+2\rho\theta/\gamma_0^2 = \Delta s/\gamma_0^2$, where Δs is the total path length, we see that if the quadrupoles are effectively utilized to eliminate the horizontal dispersion terms ($R_{16}, R_{26} \rightarrow 0$) then Eq. (3.13) reduces to

$$R_{56} = \frac{\Delta s}{\gamma_0^2} - 2\rho(\theta - \sin\theta) \tag{3.14}$$

Noting that according to Eq. (2.69), the longitudinal dispersion element is related to the momentum compaction via $R_{56} = \eta_x = \Delta s[(1/\gamma_0^2) - \alpha_c]$ we see that Eq. (3.14) is consistent with the example of Eq. (1.53) given earlier under the replacements $\rho \rightarrow R_0$ and $\theta \rightarrow \pi/4$. Furthermore, we see that for a relativistic beam the drift dispersion term $\Delta s/\gamma_0^2$ is close to zero and so the value of R_{56} is inherently negative and that of α_c is positive.

To obtain an analytical expression for the second-order longitudinal dispersion (element T_{566} of the total transformation) we required the assistance of the commercial software package Mathematica 5.1. Because of the cumbersome algebraic manipulations involved, we will merely outline the steps used to arrive at our results. Tabulations of the various second-order matrix elements were given in Table 2.2. For simplicity, we will represend the second-order counterparts to the linear matrices B_{ij}, Y_{ij}, and $\tilde{B}_{ij}$ by denoting them in component form using the same symbols but with three indices instead of two (i.e. B_{ijk}, Y_{ijk}, and $\tilde{B}_{ijk}$). For B_{ijk} and $\tilde{B}_{ijk}$ we use the analytical forms of Table 2.2 with the replacements $ks \rightarrow \theta$ and $1/k \rightarrow \rho$. For Y_{ijk} we use a generic form equivalent to Eq. (3.11), where we set to zero all elements which would naturally vanish for a system composed only of drifts, quads, and sextupoles. We then produce the total second-order matrix T by successive multiplication of the matrices for the individual components, which we can write as

$$T_{ijk} = B_{il}[Y\tilde{B}]_{ljk} + B_{ilm}[Y\tilde{B}]_{lj}[Y\tilde{B}]_{mk} \tag{3.15}$$

where $[Y\tilde{B}]_{ijk} = Y_{il}\tilde{B}_{ljk} + Y_{ilm}\tilde{B}_{lj}\tilde{B}_{mk}$ denotes the second-order matrix for the first two successive elements $\tilde{B}$ and Y and there are implied sums on repeated indices. This produces a set of equations for the elements T_{ijk} in terms of ρ, θ, Y_{ij}, and Y_{ijk}. Using these expressions, which are algebraically cumbersome and which we will therefore neglect to write out explicitly, the equation for the longitudinal dispersion element T_{566} may be expressed as a linear combination of the expressions for the other matrix elements as follows:

$$T_{566} = 4\rho\sin^2(\theta/2)\cos(\theta/2) + a_{16}R_{16} + a_{26}R_{26} + \sum_W a_{i6k}T_{i6k}, \tag{3.16}$$

where W is the set of values

$$W = \{(i,k) : (i,k) = (1,1),(1,2),(1,6),(2,1),(2,2),(2,6),(5,1),(5,2)\} \tag{3.17}$$

and

$$\begin{aligned}
&a_{16} = -\cos\theta\sin\theta, \quad a_{26} = \rho(1+2\cos\theta)\sin^2(\theta/2),\\
&a_{161} = 2\rho\cos(\theta/2)\sin^3(\theta/2), \quad a_{162} = -\frac{1}{2}\sin^2\theta,\\
&a_{166} = \sin\theta, \quad a_{261} = -2\rho^2\sin^4(\theta/2),\\
&a_{262} = 2\rho\cos(\theta/2)\sin^3(\theta/2), \quad a_{266} = \rho(\cos\theta - 1),\\
&a_{561} = -\rho\sin^2(\theta/2), \quad a_{562} = \frac{1}{2}\sin\theta
\end{aligned} \tag{3.18}$$

In the limits where $R_{16}, R_{26} \to 0$, we find that Eq. (3.16) reduces to

$$T_{566} = 4\rho\sin^2(\theta/2)\cos(\theta/2) + \sum_W a_{i6k}T_{i6k} \tag{3.19}$$

Recall from Table 2.2 that the T_{566} element is zero (at least in the relativistic limit) for all of the constituent components (i.e. quads, drifts, bends, sextupoles). It therefore arises in this system by virtue of the interaction of other nonlinear correlations which form between the transverse and longitudinal coordinates and

the momentum error. These correlations are embodied by the nonlinear dispersion terms T_{i6k} which appear in Eq. (3.19). For a chirped electron beam, such as that proposed in Section 1.5.2 as being necessary for the ramped beam mechanism, the beam has a pre-existing correlation between z and δ. Consequently, the correlations between the transverse coordinates and δ are inherently coupled to z as well. The importance of the term T_{566} in the general longitudinal transformation of Eq. (3.6) will be made clear in the following sections, where it is found to produce a profound distortion of the longitudinal phase space. This distortion, if left uncorrected, effectively destroys the ramped shape of the electron bunches that is predicted by the linear theory. As will be seen, the implementation of sextupoles can be used to remedy this situation.

3.1.4 Bunch Shaping Mechanism

The basic mechanism proposed in Section 1.5.2 for generating ramped electron bunches required an electron bunch that is initially positively chirped in energy with higher-energy particles at the head of the bunch. A plot of the longitudinal trace space distribution of such a beam is shown in Fig. 3.2(a). This distribution was produced by a simulation of the UCLA Neptune photoinjector and linac, using the particle tracking code PARMELA, with a simulated beam charge of 600 pC and a beam energy of 11.8 MeV. The energy chirp was produced by setting the simulated injection phase in the linac to 22 degrees behind the phase which corresponds to the peak acceleration. In Fig. 3.2(b) we impose a simple linear transformation of the form $z \rightarrow z + \frac{\partial z}{\partial \delta}\delta$ upon the longitudinal coordinate, where we have chosen $\partial z/\partial \delta = -5$ cm. Since the transformative term is negative (i.e. $\partial z/\partial \delta < 0$) particles at the head of the bunch, for which $\delta > 0$, are transported backward within the bunch and particles in the tail, for which $\delta < 0$, are

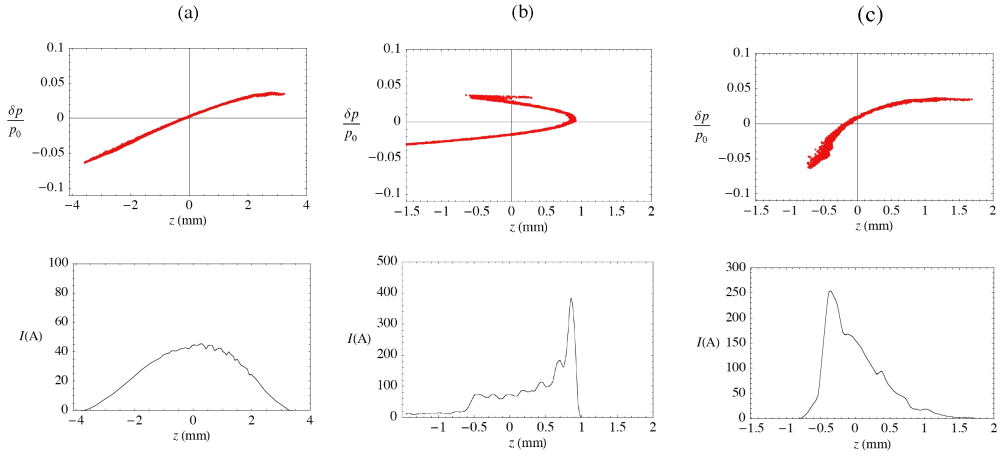

Figure 3.2: Artificial manipulation of a chirped energy distribution (a) by a linear transformation with $\partial z/\partial\delta < 0$ to generate a ramped bunch (c). In (b) a quadratic term has been added to the transformation.

transported forward.

As seen in Fig. 3.2(c), this linear transformation produces a "hook-shaped" distribution in the longitudinal trace space, which has a distinctly triangle-like current profile. The pronounced curvature of the distribution exhibited by this "hook" is a reflection of the *RF curvature* of the chirped distribution in Fig. 3.2(a). The RF curvature (or nonlinearity of the δ-z correlation) is an artifact of the acceleration process, owing to the fact that the accelerating field has a sinusoidal variation in time. This curvature is in fact critical to the bunch-shaping mechanism we are proposing. If the initial chirp were perfectly linear then the transformation used to produce Fig. 3.2(c) would result in a compression of the pulse, but it would not alter its *shape*.

As we found in Section 3.1.3, the transformation imposed upon the longitudinal trace space by a dogleg with properly controlled horizontal dispersion is (to lowest order) of the same form as that which we have artificially imposed

in Fig. 3.2. That is, the longitudinal transformation for a dogleg compressor is dominated by the dispersion term $R_{56} = (\partial z/\partial\delta)_{\delta\to 0}$, which is inherently negative according to Eq. (3.14). However, with significant energy spread, the presence of the higher-order longitudinal dispersion terms in the transformation of Eq. (3.7) for a dogleg must be taken into consideration. Including a term that is quadratic in the momentum error in the transformation, corresponding to the second-order term T_{566} in Eq. (3.7), produces the plot shown in Fig. 3.2(b). The longitudinal phase space in this plot is severely distorted by the quadratic correlation between z and δ, destroying the ramped profile. As we will see in Section 3.2.4 the value T_{566} = - 2 m used in Fig. 3.2(b) is close to the actual second-order longitudinal dispersion of the UCLA Neptune dogleg. Consquently, the second-order term T_{566} is of particular concern, and thus its elimination by the use of sextupole magnets will be considered in the next section.

3.1.5 Sextupole Correction

In order to linearize the longitudinal transport of the dogleg and thereby mimmic the mathematical transformation of Fig. 3.2, we must eliminate the second-order longitudinal dispersion term T_{566} in Eq. 3.7. The obvious method for doing this is to use sextupole magnets, which are inherently second-order in their effects, and have no first-order (linear) matrix elements. They may thereby be employed to manipulate the second-order properties of the beamline with no effect upon its optics to linear order. Higher than second-order corrections may in principle be implemented (to eliminate U_{5666} for example), by use of octupole or higher multipole magnets, but for single-pass transport this is rarely necessary.

To determine the dependence of T_{566} on the sextupole field strength, let us assume that the sextupoles lie just inside the bends and are separated from

each other only by quads and drifts. Although the same final result may be obtained without them, these assumptions will greatly simplify our calculation. Let the two sextupoles, of strengths κ and $\alpha\kappa$, respectively, and of equal length d, be denoted by the symbols S and $\tilde{S}$ and the intervening system of quads and drifts by H. We then decompose the first- and second-order representations of Y as $Y_{ij} = S_{ik}H_{kl}\tilde{S}_{lj}$ and $Y_{ijk} = S_{il}[H\tilde{S}]_{ljk} + S_{ilm}[H\tilde{S}]_{lj}[H\tilde{S}]_{mk}$, where $[H\tilde{S}]_{ijk} \equiv H_{il}\tilde{S}_{ljk} + H_{ilm}\tilde{S}_{lj}\tilde{S}_{mk}$. Multiplying the linear matrices out explicitly and imposing the requirements

$$R_{16} = 0, \quad R_{26} = 0, \quad \det \begin{pmatrix} H_{11} & H_{12} \\ H_{21} & H_{22} \end{pmatrix} = 1, \tag{3.20}$$

we arrive at the following conditions on H:

$$\begin{aligned} H_{12} &= -(1 + H_{22})(d + \rho \tan[\theta/2]), \\ H_{21} &= (1 - H_{22})/(d + \rho \tan[\theta/2]), \\ H_{11} &= H_{22}. \end{aligned} \tag{3.21}$$

Applying these conditions in the calculation of the second-order matrix, we arrive at the following result for the element T_{566} expressed in powers of κ:

$$\begin{aligned} T_{566} = {} & 2\sin^2(\theta/2)(A_0\rho\sin\theta + A_+ + A_-\cos\theta) - \frac{d}{4}\sin^2\frac{\theta}{2} \\ & \times \left[4|C_0|^2\left(2\mathrm{Re}C_0 - d\cos\frac{\theta}{2}\right)\sin\frac{\theta}{2} + 8\rho^3\cos\theta(1-\sin\theta)\right](1-\alpha)\kappa, \end{aligned} \tag{3.22}$$

where for the sake of compactness we have defined the functions

$$\begin{aligned} A_\pm &\equiv H_{162} + H_{522} + d[H_{161} + H_{262} + H_{521} + d(H_{261} + H_{511}) - 1] \\ &\quad \pm \rho^2(H_{261} + H_{511}), \\ A_0 &\equiv 1 + H_{161} + H_{262} + H_{521} + 2d(H_{261} + H_{511}) - \cos\theta, \\ C_0 &\equiv d\cos(\theta/2) + (1+i)\rho\sin(\theta/2). \end{aligned} \tag{3.23}$$

With the additional associations

$$A \equiv 2\sin^2(\theta/2)(A_0\rho\sin\theta + A_+ + A_-\cos\theta) \tag{3.24}$$
$$C \equiv \left[4|C_0|^2\left(2\mathrm{Re}C_0 - d\cos\frac{\theta}{2}\right)\sin\frac{\theta}{2} + 8\rho^3\cos\theta(1-\sin\theta)\right] \times \frac{d}{4}\sin^2\frac{\theta}{2},$$

we find that Eq. (3.22) takes the form

$$T_{566} = A - C(1-\alpha)\kappa \tag{3.25}$$

The linear dependence on κ is a reflection of the fact that the second-order matrix elements for a sextupole are proportional to the field strength. The quantities A and C are algebraic functions of θ and ρ, as well as the drift lengths and quadrupole focal lengths. The general form of Eq. (3.25) is valid for any dogleg with 2 symmetrically placed sextupoles, although the exact functional dependences of A and C may vary with sextupole placement.

If the goal is to eliminate T_{566} altogether, then (i) to avoid asymptotic behavior, the value of α (the ratio of the two sextupole field strengths) should not approach unity, and (ii) in order to minimize κ the quantity $C(1-\alpha)$ should be large and therefore α should be negative. A simple choice in agreement with these requirements is $\alpha = -1$, corresponding to sextupole fields equal in magnitude but of opposite polarity. As a rule, the minimum number of sextupoles needed is equal to the number of second-order matrix elements one wishes to eliminate. Therefore $\alpha = 0$ is also a possibility, although the elimination of one sextupole would disrupt the optical symmetry and require the remaining one to have double the field strength. Minimization of the required sextupole fields, through appropriate placement of the correcting magnets, is desirable from the standpoint of preventing the inadvertent introduction of strong second-order geometrical effects as well

as third-order chromatic effects. From a heuristic perspective, the sextupole manipulation of the T_{566} amounts to a correction of chromatic errors introduced by the horizontally focusing lenses. This connection is made in greater detail in Section 3.2.4.

3.1.6 Emittance Growth

The sextupole correction of T_{566} in this system often has the added effect of minimizing the horizontal emittance growth, due to the coupling of T_{566} to the second-order horizontal dispersion discussed above. For a beam of large energy spread and small transverse emittance, the nonlinear emittance growth is dominated by the second-order horizontal dispersion elements T_{166} and T_{266}. To demonstrate this, note that to second order, the matrix of second moments Σ transforms according to

$$\Sigma_{jk} = \int (R_{jl}\mathring{x}_l + T_{jlm}\mathring{x}_l\mathring{x}_m)(R_{kn}\mathring{x}_n + T_{knp}\mathring{x}_n\mathring{x}_p) f(\mathring{\mathbf{x}})\det(J) d^6\mathring{x}, \tag{3.26}$$

where the Jacobian of this transformation is

$$J_{ij} = \frac{\partial x_i}{\partial \mathring{x}_j} = R_{ij} + \sum_k T_{ijk}\mathring{x}_k(1+\delta_{jk}), \tag{3.27}$$

with δ_{jk} representing the Kronecker delta. Writing Eq. (3.26) in the bracket notation, we have

$$\Sigma_{jk} = R_{jl}R_{kn}\langle \mathring{x}_l\mathring{x}_n\rangle + 2T_{knp}R_{jl}\langle \mathring{x}_l\mathring{x}_n\mathring{x}_p\rangle + T_{jlm}T_{knp}\langle \mathring{x}_l\mathring{x}_m\mathring{x}_n\mathring{x}_p\rangle, \tag{3.28}$$

where there is an implied sum on repeated indices and $\langle \ldots \rangle \equiv \int \ldots f(\mathring{\mathbf{x}})\det(J) d^6\mathring{x}$. Now assume the beam distribution function to be uncoupled between the three trace space planes, to have vanishing third moments, and unit Jacobian determinant. Then the upper left 2×2 submatrix of Eq. (3.28) takes the form

$$\Sigma_x = M_x \mathring{\Sigma}_x M_x^T + \sigma_\delta^2 \boldsymbol{d}\boldsymbol{d}^T + \langle \delta^4 \rangle \boldsymbol{D}\boldsymbol{D}^T + \Sigma_{geo}, \tag{3.29}$$

where $\boldsymbol{D} = (T_{166}, T_{266})$ is the second-order dispersion vector, and $\boldsymbol{d}$, M_x, and $\overset{\circ}{\Sigma}_x$ are the first-order horizontal dispersion vector, the 2×2 linear transpor matrix for the (x, x') trace plane, and the initial 2×2 matrix of second moments, respectively, as they were defined in Eqs. (2.87), (2.88), and (2.92). The matrix Σ_{geo} is the contribution from second-order geometrical terms. Equation (3.29) may be regarded as a second-order extension of Eq. (2.108). For a beam of small intitial emittance (with well-controlled beam sizes and angles) and large energy spread, Eq. (3.29) is dominated by the dispersion terms, and we can set $\Sigma_{geo} << \langle\delta^4\rangle \boldsymbol{D}\boldsymbol{D}^T$. Furthermore, if the beam distribution in the z trace space plane can be approximated by a rotated bi-Gaussian in z and δ, then $\langle\delta^4\rangle = 3\sigma_\delta^4$. With these approximations, insertion of Eq. (3.29) into the definition of the transverse emittance, Eq. (2.89), we have that the final emittance $\epsilon_{x,f}$ is given by

$$\epsilon_{x,f} \approx \sqrt{\det(M_x \overset{\circ}{\Sigma}_x M_x^T + \sigma_\delta^2 \boldsymbol{d}\boldsymbol{d}^T + 3\sigma_\delta^4 \boldsymbol{D}\boldsymbol{D}^T)}. \tag{3.30}$$

The first of the three terms inside the determinant in Eq. (3.30) is the contribution from the initial emittance, which would be invariant if the transformation were governed solely by the linear matrix M_x. Consequently, if the first-order horizontal dispersion and its derivative are eliminated in accordance with the discussion surrounding Eqs. (3.14) and (3.19), then $\boldsymbol{d} \rightarrow 0$ and the emittance growth described by Eq. (3.30) is dominated by the third term inside the parentheses. The coupling of longitudinal to horizontal dispersion is such that for the sextupole configuration described in Section 3.1.5 the values of T_{166} and T_{266} tend to be reduced under the sextupole correction of T_{566}. Consequently, in many cases sextupole correction of the longitudinal dispersion also has a reducing effect upon the transverse emittance.

3.2 The UCLA Neptune Dogleg Compressor

Having derived a general theoretical treatment of the dominant first- and second-order optics pertinent to the shaping of the longitudinal trace space using a dogleg, we proceed to apply these results to the specific design of the UCLA Neptune dogleg compressor. In particular, we will derive the matching conditions on the initial transverse Twiss parameters of the beam, as a function of the quadrupole focal lengths, which are additionally constrained to produce a horizontally dispersionless beamline (to first order). We then use particle tracking codes to simulate the compressor and verify our analytical predictions.

3.2.1 A Simple Model of the Compressor

The layout of the UCLA Neptune dogleg compressor, which has been dubbed the "S-Bahn" after a train system in Germany, is shown in Fig. 3.3 using the same iconography as Fig. 3.1, but with labels indicating the quadrupole spacings L_1, L_2, L_3, the quadrupole focal lengths f_1, f_2, and the sextupole field strengths κ and $\alpha\kappa$. A more detailed description of the actual beamline hardware will be provided in Chapter 5. Furthermore, details such as the finite lengths of the quadrupole magnets and the fact that each of the 45 degree bends is actually composed of two successive dipole magnets will be taken into account in the simulations, but will be ignored for the purposes of the simplified linear analytical treatment which we will now undertake. For our present purpose (namely, describing the linear beam optics and parameter space of this compressor) the simple representation of Fig. 3.3 is sufficient. For the sake of consistency with the notation of Eq. (3.2), the initial, midpoint, and final s-positions are labeled ($s = 0$, $s = \hat{s}$, and $s = \Delta s$). The bend angle is 45 degrees, or $\theta = \pi/4$, with an effective bend radius of approximately $\rho = 32$ cm. The quad spacing lengths are $L_1 = 50$ cm, $L_2 = 40$

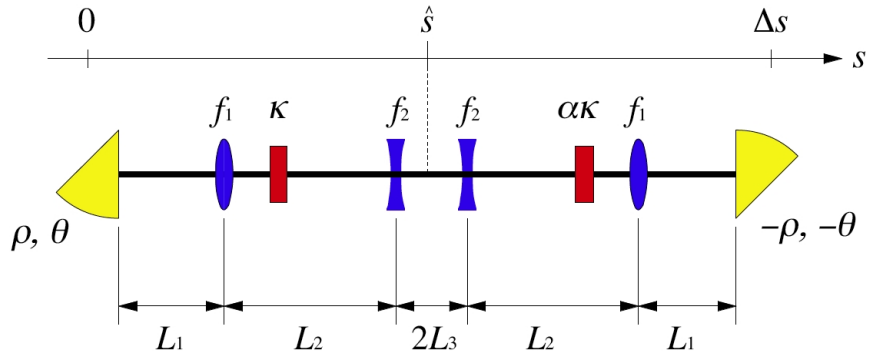

Figure 3.3: Cartoon drawing of Neptune "S-Bahn" dogleg.

cm, and $L_3 = 7.54$ cm.

The configuration of quadrupoles shown in Fig. 3.3 is similar to that of the simple example considered in Section 1.3.3, but with the addition of two horizontally defocusing (vertically focusing) quadrupole magnets symmetrically placed near the midpoint. The addition of these two magnets helps to control the vertical beam size. However, since the beam has a sharp horizontal waist at the midpoint and the dispersion is small there, the vertically focusing quads are nearly free in their strength. Without them, in order to obtain a vertical waist at the midpoint, condition (iii) of Eq. (3.1), the beam size at the entrance of the S-Bahn would have to be larger and more sharply convergent in the vertical dimension than in the horizontal (i.e. we would require that the initial Twiss parameters satisfy $\mathring{\alpha}_y >> \mathring{\alpha}_x$ and $\mathring{\beta}_y >> \mathring{\beta}_x$ at $s = 0$). This would be difficult to accomplish considering that the photoinjector produces a nearly *round beam* (that is, the horizontal and vertical Twiss parameters and emittances are nearly equal). The two sextupoles are present in order to provide a knob for manipulating the second-order horizontal dispersion (T_{566}) in accordance with the discussion of

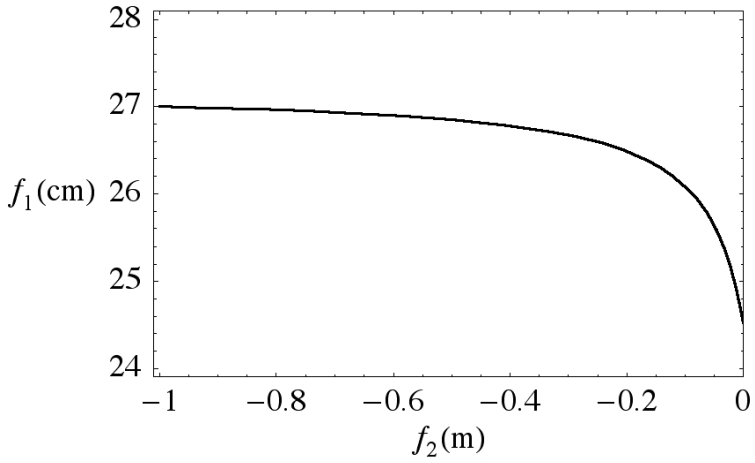

Figure 3.4: Plot of the equation $\hat{R}_{16}(f_1, f_2) = 0$.

Section 3.1.5.

3.2.2 Dispersion-Killing Conditions

Under the assumption of optical symmetry, the requirement that the beamline be nondispersive [condition (ii) of Eq. (3.1)] was found in Section 3.1.1 to reduce to Eq. (3.3), namely $\hat{R}_{16} = \eta_x(\hat{s}) = 0$. The transport matrix from the entrance of the first bend to the midpoint of the S-Bahn, written in terms of the linear matrices for a bend, a thin lens, and a drift as given by Eqs. (3.8) - (3.10), reads

$$\hat{R} = D(L_3)Q(f_2)D(L_2)Q(f_1)D(L_1)B(\theta, \rho) \tag{3.31}$$

Setting element (1,6) of this matrix to zero produces an algebraic equation relating the parameters L_1, L_2, L_3, f_1, f_2, θ, and ρ. Among these, the focal lengths f_1 and f_2 are the obvious free parameters, the others having the fixed values given in the previous section. The condition $\hat{R}_{16} = 0$ thus describes a curve in the space of the free parameters f_1 and f_2. The plot of this curve is shown in Fig. 3.4.

Note that the values on the horizontal axis are negative because f_2 represents

the focal length of the horizontally *defocusing* lens. Each point on the curve in Fig. 3.4 represents a possible operating point. However, the choice of (f_1, f_2) affects the values of the initial Twiss parameters which are needed in order to produce a waist at the midpoint, and thereby symmetrize the beam envelope. Since large initial Twiss parameter values are actually more difficult to produce out of the photoinjector, we will search for a point on the f_1-f_2 curve which minimizes the initial Twiss parameter values. This analysis is performed in the following section.

3.2.3 Beam Matching Requirements

The last of the three conditions in Eq. (3.1) requires a beam waist at the midpoint of the dogleg. This condition, in conjunction with the optical symmetry requirement, symmetrizes the beam envelopes $\sigma_x(s)$ and $\sigma_y(s)$ about the midpoint $(s = \hat{s})$. While this is not strictly necessary for the beam-ramping mechanism to work, it is important from the standpoint of controlling the transverse beam size. The corresponding mathematical relation written in terms of the midpoint Σ matrices, Eq. (3.4), amounts to a constraint upon the initial Twiss parameters of the beam at the dogleg entrance, which are in turn related to the midpoint sigma matrix via the usual linear transport relation, Eq. (3.5).

Since the dogleg has been constrained to have zero horizontal dispersion at the midpoint, we can equate the Σ-matrices with the Twiss parameter W-matrices for the RMS ellipse at both the entrance and midpoint. That is, $\overset{\circ}{\Sigma} = \overset{\circ}{W}$ and $\hat{\Sigma} = \hat{W}$. Combining these with the midpoint waist condition of Eq. (3.4) we have

that

$$\mathring{\Sigma}_x = \epsilon_x \begin{pmatrix} \mathring{\beta}_x & -\mathring{\alpha}_x \\ -\mathring{\alpha}_x & \mathring{\gamma}_x \end{pmatrix}, \quad \mathring{\Sigma}_y = \epsilon_y \begin{pmatrix} \mathring{\beta}_y & -\mathring{\alpha}_y \\ -\mathring{\alpha}_y & \mathring{\gamma}_y \end{pmatrix}, \tag{3.32}$$

$$\hat{\Sigma}_x = \epsilon_x \begin{pmatrix} \hat{\beta}_x & 0 \\ 0 & 1/\hat{\beta}_x \end{pmatrix}, \quad \hat{\Sigma}_y = \epsilon_y \begin{pmatrix} \hat{\beta}_y & 0 \\ 0 & 1/\hat{\beta}_y \end{pmatrix}. \tag{3.33}$$

Relating (3.32) and (3.33) via $\hat{\Sigma}_\mu = \hat{M}_\mu \mathring{\Sigma}_\mu \hat{M}_\mu^T$ produces 8 separate relations, although half of them are not linearly independent. Eliminating the redundant equations leaves the following:

$$\begin{aligned}
&\mathring{\beta}_x \hat{R}_{11}^2 - 2\mathring{\alpha}_x \hat{R}_{11}\hat{R}_{12} + \mathring{\gamma}_x \hat{R}_{12}^2 = \hat{\beta}_x, \\
&\mathring{\beta}_y \hat{R}_{33}^2 - 2\mathring{\alpha}_y \hat{R}_{33}\hat{R}_{34} + \mathring{\gamma}_y \hat{R}_{34}^2 = \hat{\beta}_y, \\
&\hat{R}_{11}(\mathring{\beta}_x \hat{R}_{21} - \mathring{\alpha}_x \hat{R}_{22}) + \hat{R}_{12}(\mathring{\gamma}_x \hat{R}_{22} - \mathring{\alpha}_x \hat{R}_{21}) = 0, \\
&\hat{R}_{33}(\mathring{\beta}_y \hat{R}_{43} - \mathring{\alpha}_y \hat{R}_{44}) + \hat{R}_{34}(\mathring{\gamma}_y \hat{R}_{44} - \mathring{\alpha}_y \hat{R}_{43}) = 0.
\end{aligned} \tag{3.34}$$

These constitute four equations in six unknowns, the unknowns being $\mathring{\alpha}_{x,y}$, $\mathring{\beta}_{x,y}$, and $\hat{\beta}_{x,y}$. Furthermore, the equations are uncoupled between x and y, so $\mathring{\alpha}_x$ and $\mathring{\beta}_x$ can separately be expressed as functions only of $\hat{\beta}_x$; and $\mathring{\alpha}_y$ and $\mathring{\beta}_y$ can separately be expressed as functions only of $\hat{\beta}_y$. Due to the dependence of the matrix $\hat{R}$ on the focal lengths of the quadrupoles, a different set of such solutions exists for every point (f_1, f_2) on the curve in Fig. 3.4. Solutions corresponding to three such points are shown in Fig. 3.5(a), (b), and (c).

In Fig. 3.5, the initial x Twiss parameters are plotted against $\hat{\beta}_x$ in the first column and the initial y Twiss parameters are plotted against $\hat{\beta}_y$ in the second column. The beta functions are in units of meters. The plots in the third column show a reproduction of Fig. 3.4 with a dot marking the coordinates of the point along the f_1-f_2 curve for which the Twiss parameter equations were solved. Note

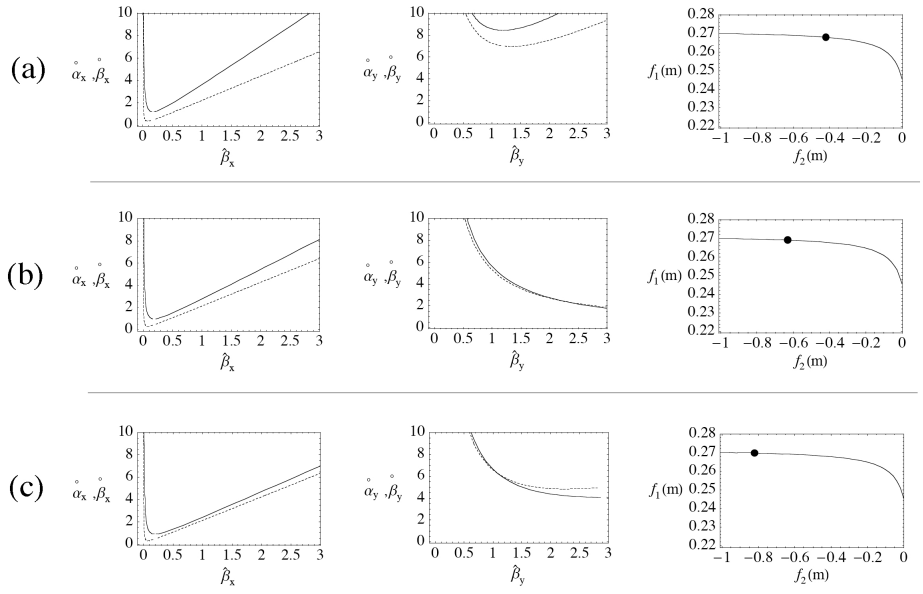

Figure 3.5: Allowed Twiss parameters for three different values of (f_1, f_2) corresponding to points on the curve in Fig 3.4: (a) f_1 = 0.267 m, f_2 = -0.42 m; (b) f_1 = 0.269 m, f_2 = -0.63 m; (c) f_1 = 0.267 m, f_2 = -0.82 m.

that the x-parameters in the first column are relatively insensitive to the choice of f_1 and f_2 as compared with the y-parameters. Thus, it is good that these quads are relatively unconstrained.

Also, all solutions for the Twiss parameters $\mathring{\alpha}_{x,y}$ are positive, and therefore the incoming beam must be convergent in both dimensions. To minimize the vertical spot size at the midpoint of the compressor and to keep the initial Twiss parameters near the values achievable with the Neptune photoinjector and linac (which tend to be on the order of $\alpha \approx 1$, $\beta \approx 1$ m, we pick the solution for (f_1, f_2) which brings the $\mathring{\alpha}_y$, $\mathring{\beta}_y$ curves as close to the origin as possible. This solution corresponds, in fact, to the plot in part (b) of Fig. 3.5, for which $f_2 = -0.63$ m and $f_1 = 0.269$ m. Optimal coupling of the electron beam into the compressor then requires matching its Twiss parameters to a set of values which lie on the first two plots of Fig. 3.5(b). The experimental procedure for accomplishing this matching will be discussed in Chapter 5.

3.2.4 Analytical Calculations

For the choice of parameter values corresponding to the point (f_1, f_2) in Fig. 3.5(b), we can determine various quantities of interest analytically by using transport matrix theory. The linear R_{56} as given by Eq. (3.14), for example, is

$$R_{56} = \eta_x(\Delta s) = -5.04 \text{ cm} \tag{3.35}$$

For a given location of the sextupole magnets, we can also obtain an explicit form of the second-order longitudinal dispersion corresponding to Eq. (3.25). For the dogleg layout shown in Fig. 3.3, with the sextupoles positioned a distance h = 10 cm inside the outermost pair of lenses and having lengths of 5 cm, the T_{566}

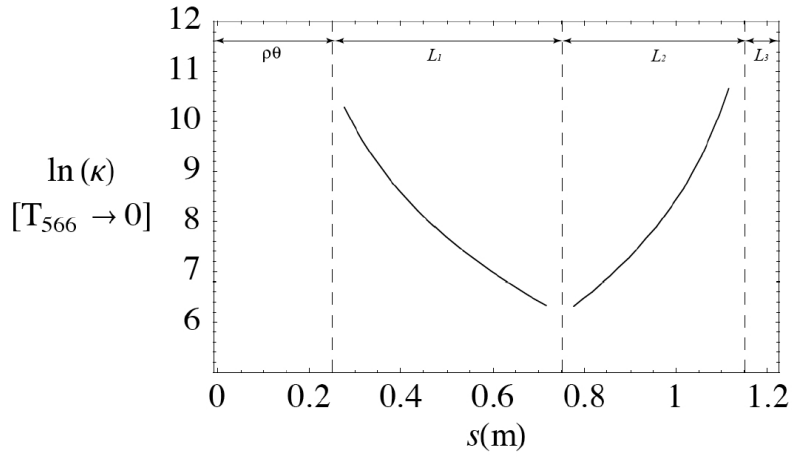

Figure 3.6: Values of κ required to eliminate T_{566} as a function of sextupole position s up to the midpoint.

takes the form

$$T_{566} = -2.11 \text{ m} + (0.00175 \text{ m}^4)\ \kappa \tag{3.36}$$

Here we have assumed $\alpha = -1$, so that the two sextupole magnets have equal field strengths but opposite polarities.

For this configuration, the T_{566} therefore has a value of -2.11 m in the absence of sextupole correction, but can be forced to zero at a sextupole field strength of $\kappa = 1204 \text{ m}^{-3}$. Our choice of location for the sextupole magnets is informed by the observation that the nonlinear horizontal chromaticity (i.e. T_{261}) of the horizontally focusing lenses amplifies the second-order longitudinal dispersion by coupling it to the linear horizontal dispersion of the dipoles. The T_{566} then grows linearly in the drift section after each lens, due to the inherent nonlinear x-z correlation introduced by the drifts. This correlation is due to deviation from the paraxial approximation, which is a second-order effect. Consequently the sextupole correctors should be located close to the horizontally focusing lenses, so that the chromatic couplings produced by them can be counteracted before

they have a chance to grow in the subsequent drift sections. This is demonstrated in Fig. 3.6 where the value of κ needed to cancel the T_{566} as a function of the position s of the sextupole magnet from the entrance of the first dipole up to the midpoint of the compressor. The other sextupole is assumed to be symmetrically located with field strength $-\kappa$. Values of κ are plotted only in regions where a sextupole 5 cm long (since this is the actual physical length of the sextupoles used on the Neptune dogleg) could reasonably be placed. Note that the vertical scale is logarithmic, so the plot indicates that the required field strength grows by orders of magnitude as the sexupole position moves further from the vecinity of the outermost lens (marked by the second dashed vertical line).

The location for the sextupoles previously assumed (10 cm inside the outermost quads) therefore reflects a compromise between the desire to locate them as close to the quadrupoles as possible and the spatial constraints imposed by the hardware and vacuum system. For this choice of sextupole location, the choice of values of T_{566} as well as the *horizontal* second-order dispersion terms T_{166} and T_{266} are plotted against κ in Fig. 3.7. We see that at the sextupole field strength where the T_{566} vanishes (around 1200 m^{-3}), the nonlinear horizontal dispersion terms are simultaneously inverted in sign and reduced in magnitude by nearly a factor of 3. Consequently, in accordance with the nonlinear emittance formula, Eq. (3.30), the sextupole correction should also have a reducing effect on the horizontal emittance growth in the compressor. This prediction is confirmed by the simulation results presented in the following section.

3.2.5 Simulation Results

The primary codes used in this dissertation for simulating the electron beam dynamics in the Neptune beamline and dogleg compressor are PARMELA (ver-

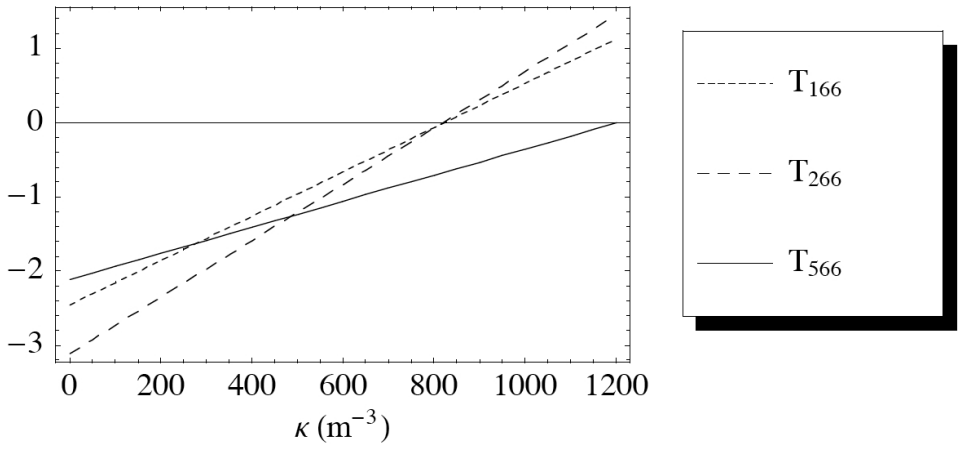

Figure 3.7: Second-order dispersion terms as functions of sextupole field strength.

sion UCLA-PARMELA 2.1) and ELEGANT (version 15.1.1) [58, 53]. Both of these are particle tracking codes, which treat the beam as a collection of particles, whose position and momentum are calculated individually at various points along the beamline. In order to reduce computation time, only a small number N, typically much less than the number of actual particles $N_b = Q/e$ being simulated are tracked. Thus for purposes of space-charge calculations, each of these N *macroparticles* has a charge of Q/N.

PARMELA generates the macroparticles at the photocathode based upon specified drive laser parameters and then transports them through a user-specified system by numerically integrating the forces in a series of discrete time-steps. Space-charge effects are included by calculating the electrostatic force "kicks" in the beam frame at successive time steps either between aggregate clumps of particles on a user-defined 2D mesh or in a point-to-point fashion between all of the individual macroparticles. The mesh technique is much faster than the point-to-point calculation, but because it is 2D it is less accurate if the beam is not

azimuthally symmetric. ELEGANT, on the other hand, uses transport matrices (up to third order) to track the macroparticle coordinates in trace space and propagate them through a series of user-specified beamline components. Since this approach neglects the space-charge forces, it is valid only at ultrarelativistic energies (since the space-charge force in the lab frame scales as $1/\gamma_0^2$). In the simulations conducted for this thesis, a combination of PARMELA and ELEGANT was employed in most cases. PARMELA was used to model the beam dynamics in the photoinjector and linear accelerator. The macroparticle coordinates of the beam were then extracted and used as input for an ELEGANT simulation of the dogleg compressor. In addition, the PARMELA model was extended to include the dogleg as well, so that the effects of space-charge could be gauged separately.

The longitudinal trace space distributions at the exit of the compressor, predicted from simulations using PARMELA with 10,000 macroparticles, are shown without and with sextupole correction in Figs. 3.8(b) and 3.8(c), respectively. The S-shaped distribution in Fig. 3.8(b) is evidence of the quadratic momentum dependence of the z transformation produced by the second-order T_{566} contribution in Eq. (3.7). Note the similarity between Figs. 3.8 and 3.2. When sextupole fields are utilized in accordance with the description of Section 3.1.5 to eliminate this contribution, the resulting distribution [Fig. 3.8(c)] is found to correspond very closely to that produced by a purely linear R_{56} transformation, such as that shown in Fig. 3.2. The resulting current profile exhibits a sharp drop in current at the back of the bunch, where the distribution begins to turn over on itself, preceded by an approximately linear ramp of the sort described in Section 1.5.1 as being ideal for generating large-amplitude transformer ratios in a wakefield accelerator.

It has been observed recently [17] that space-charge driven transverse phase

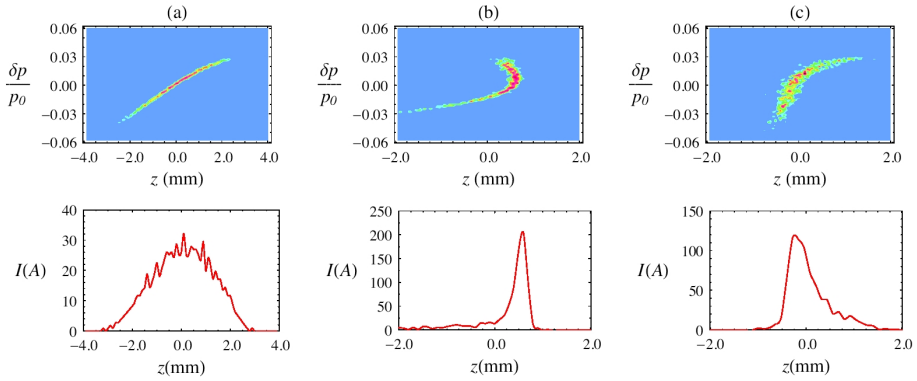

Figure 3.8: Plots of the z trace space and current profile from PARMELA simulations showing (a) the beam at the entrance of the dogleg compressor, and the same beam at the end (b) without sextupole correction and (c) with sextupole correction.

space bifurcation and accompanying emittance growth are potential hazards encountered in low-energy (12-14 MeV) compression at Neptune. To gauge the tranverse effects arising separately from non-linearities and space-charge forces, ELEGANT and PARMELA simulations were employed to calculate the normalized transverse emittance $\epsilon_{x,N} = \gamma_0\beta_0\epsilon_x$ of the beam. The ELEGANT simulation, with sextupoles turned off, predicts an emittance growth in the Neptune dogleg due to nonlinear effects of $\Delta\epsilon_{x,N} = 13$ mm mrad over the initial value of 5 mm mrad at the entrance. This is consistent with the approximation of Eq. (3.30) which gives $\Delta\epsilon_{x,N} \approx 12$ mm mrad.

With sextupoles turned on, ELEGANT predicts a much improved $\Delta\epsilon_{x,N} = 1.7$ mm mrad, due to partial cancellation of the T_{166} and T_{266}, as discussed above. To gauge the effect of space-charge velocity field forces in the dogleg compressor, a calculational model for sextupoles was introduced into the PARMELA source code and simulations were run using PARMELA's point-to-point space charge routine. With the space-charge routine turned off, the PARMELA results match

the ELEGANT prediction of $\Delta\epsilon_{x,N} = 1.7$ mm mrad. With the space-charge routine turned on, PARMELA predicts a total emittance growth of $\Delta\epsilon_{x,N} = 11.6$ mm mrad, for a 300 pC beam, indicating a significant additional contribution from space-charge forces. These results lie in the intermediate range of $\Delta\epsilon_{x,N}$ values measured in Ref. [17] and do not show evidence of the sort of phase space bifurcation reported there. The predicted growth in transverse emittance, however, imposes restrictions upon the focusability of the beam, requiring sharper focusing angles and higher gradient quadrupole to match the beam into a PWFA. A planned future experiment at the Neptune Laboratory to focus the beam using high-gradient permanent magnet quadrupoles will be discussed in Chapter 6.

CHAPTER 4

Design of Deflecting Cavity for Subpicosecond Beam Profile Measurements

4.1 Introduction

Experimental verification of the technique proposed in Section 1.5.2 for generating ramped electron bunches that are one to several picoseconds in duration using a dogleg compressor, requires a diagnostic that is capable of measuring the current profile of such bunches with sub-picosecond resolution. The most commonly employed beam current monitors have rise times in the nanosecond range, making them unsuitable.

Another possibility is to use the electron beam to generate, via interaction with a refractive or conducting material, a pulse of radiation [e.g. coherent Čerenkov radiation or coherent transition radiation (CTR)] which reproduces the time profile of the bunch intensity, and then use interferometric optical techniques to extract the temporal profile of the emitted pulse. However, such interferometric techniques suffer from the so-called *phase retrieval problem*. Since the quantity measured by the interferogram is an autocorrelated intensity, the phase information is lost, making it impossible to reconstruct the original profile, without making some assumption about its shape (e.g. Gaussian, Lorentzian, exponential, etc.) or about the phase distribution (e.g. that it's equal to the

minimal Kramers-Kroenig phase).

The intensity profile of the radiation pulse could alternately be measured directly with a *streak camera*. This is a device that uses a photocathode to convert the radiation into electrons by photoemission, accelerates the electrons in a cathode ray tube, and then "streaks" them transversely by deflecting them with a DC electric field. The deflected electrons then impinge upon a phosphorescent surface or detector. There is currently an operational streak camera in the Neptune laboratory, but its resolution is on the order of 1 to 2 ps, which is inadequate for our purposes.

A more direct and sophisticated technique for measuring the time-structure of an electron beam is to use a radio-frequency (RF) cavity to directly manipulate the beam's distribution in phase space so as to create a linear (or nearly linear) correlation between the longitudinal coordinate z and either (i) the energy, or (ii) one of the transverse coordinates. In the case of (i) the time structure can be extracted from the projection of the energy distribution onto one of the transverse coordinates (e.g. by using a dipole spectrometer magnet). In the case of (ii) the time structure is immediately obtained from projections of the transverse coordinate space onto a phosphorescent screen placed in the beam path.

The type of RF cavity employed for application (i) is an accelerating structure operated at the zero-crossing of the RF (i.e. at the RF phase where the beam centroid experiences no acceleration). The head and tail of the beam then experience accelerating forces of opposite sign, thereby producing a strong correlation between longitudinal position and energy. For application (ii), the device employed is a so-called *deflecting cavity*. This is an RF structure that operates in an electromagnetic mode similar to the TM_{110} mode of a cylindrical pillbox, and delivers a transverse momentum kick to the electron beam. Such structures are

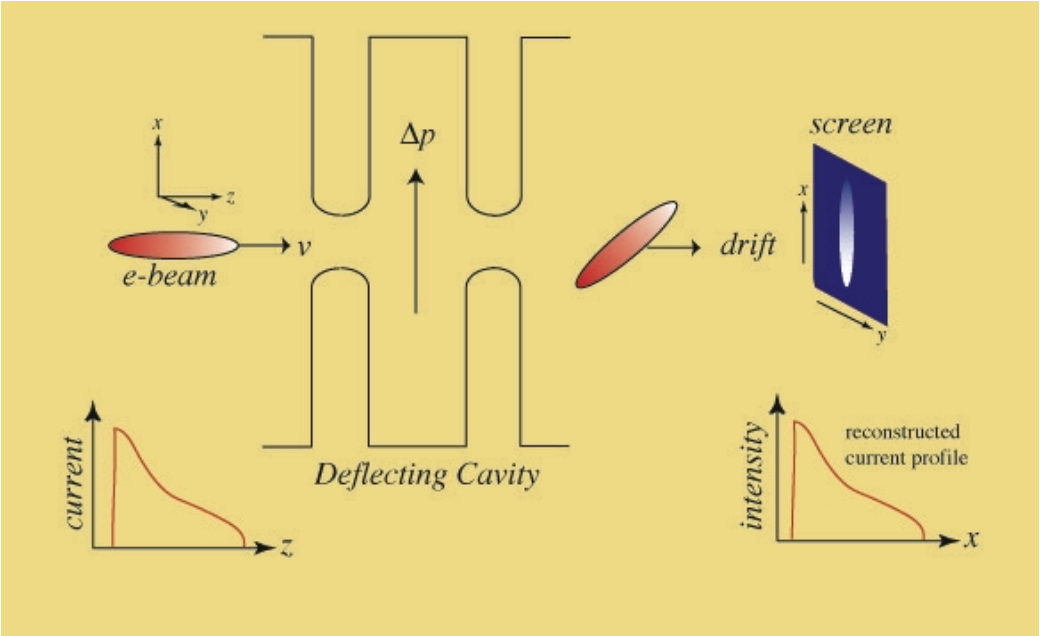

Figure 4.1: Illustration of current profile measurement using a deflecting cavity.

also generally operated at or near the zero-crossing of the RF so that the momentum kick imparted to the beam varies linearly with time and the transverse kicks imparted to the head and tail of the beam are of opposite sign. Consequently, in the drift following the deflecting cavity, the beam gradually elongates along the coordinate corresponding to the deflection axis of the cavity. The temporal structure of the beam thus becomes correlated with one of its transverse coordinates and can be imaged on a simple phosphorescent screen inserted in the beam path. This procedure is illustrated in Fig. 4.1.

A multi-cell RF deflecting cavity was chosen as the temporal diagnostic for measuring the current profiles of ramped electron bunches generated by the photoinjector and dogleg compressor at the Neptune laboratory. Note that deflecting mode cavities were originally invented in the early 1960s as a way to separate different species of particles in an accelerator [59, 60]. Their potential as a bunch

length diagnostic was noted soon after [61]. So, the deflecting cavity is a relatively old technology. However, the design of the structure built for the UCLA Neptune beamline incorporates a number of unique features, including a modular o-ring-based assembly, high operating RF frequency, and low input power requirements. In the present chapter we will describe the design process for this cavity using a bottom-up approach, starting with the basic design parameters and the analytical formulas for a single-cell pillbox cavity, and then extending these results to describe multi-cell structures. We then discuss the use of computer simulations to finalize the geometry of the cavity design, as well as the hardware details associated with its construction, testing, and installation.

4.2 Instantaneous Transverse Deflection

In order to obtain a few important rule-of-thumb relationships which will be useful later for developing the first-order cavity design parameters, we consider an instantaneous sinusoidal transverse voltage $V_0 \sin\psi$ imparted to the beam, followed by a drift of length L. The amplitude V_0 of the deflection is a standard design parameter for a deflecting cavity, as it ultimately limits the resolution of the device, as we will demonstrate shortly. (Note that for a physical cavity, which has nonzero length, the deflecting voltage is obtained by integrating the net transverse momentum kick imparted to be beam along the length of the structure.) The y-z correlation imparted by the deflection and the drift may be written as a matrix equation,

$$\begin{pmatrix} y \\ z \end{pmatrix} = \begin{pmatrix} \hat{Q} \\ 0 \end{pmatrix} + \begin{pmatrix} 1 & \hat{M} \\ 0 & 1 \end{pmatrix} \begin{pmatrix} y_0 \\ z_0 \end{pmatrix}, \tag{4.1}$$

where [62]

$$\hat{Q} = \frac{eV_0}{p_0 c}\sqrt{\beta_d \beta_s}\sin\psi_0 \ \sin\Delta \quad ; \quad \hat{M} = \frac{eV_0}{p_0 c}\sqrt{\beta_d \beta_s}\frac{2\pi}{\lambda}\cos\psi_0 \sin\Delta. \tag{4.2}$$

and y_0 and z_0 denote the coordinates of the particle at the location of the final screen when the deflecting voltage is zero. Here, β_d is the beta function at the deflector, β_s is the beta function at the screen, Δ is the betatron phase advance from deflector to screen, ψ_0 is the injection RF phase (i.e. the phase of the bunch centroid), and λ is the RF wavelength. The quantity $\hat{Q}$ represents a vertical deflection of the beam centroid. If the beam is phased at the so-called RF zero crossing ($\psi_0 = 0$) then the bunch centroid sees zero net deflection and $\hat{Q} \to 0$. The quantity $\hat{M}$ represents the vertical expansion coefficient of the beam following the drift. Thus, the contribution to the vertical RMS beam size due to the deflection is $\sigma_{def} = \hat{M}\sigma_z$. The total RMS beam size at the screen is then

$$\sigma_y = \sqrt{\sigma_0^2 + \sigma_{def}^2}, \tag{4.3}$$

where σ_0 is the RMS spot size at the screen when the cavity is turned off. In order to resolve the time structure of the bunch from the vertical streak of the beam as seen at the screen, we require that the contribution to the vertical spot size due to the z-correlated deflection exceed the nominal spot size of the beam with the deflecting voltage turned off by about a factor of two: $\sigma_{def} > 2\sigma_0$. This translates into a condition on the transverse voltage V_0 required to resolve the time structure of the beam, which we may write as

$$V_0 > V_{min} = \frac{cU/e}{\sigma_z L \pi f}\sigma_0 \ , \tag{4.4}$$

where we have used the fact that the quantity $\sqrt{\beta_d \beta_s}\sin\Delta$ is equal to the drift length L between the deflector and the screen, and have denoted the relativistic beam energy by $U = \gamma_0 mc^2 \approx p_0 c$. The rule-of-thumb expression in Eq. (4.4)

for the minimum deflecting voltage will be useful in developing the basic design parameters of the deflecting cavity. We can see immediately from Eq. (4.4) that in order to minimize the needed deflecting voltage, it is beneficial to have a small initial spot size σ_0 as well as a high RF frequency. To achieve the former, it is customary to locate the screen at a minimum of the beta function (i.e. at a focus). To take advantage of the inverse relation between V_{min} and f we will choose a high-frequency (X-band) RF power source for the Neptune deflecting cavity.

4.3 The Single-Cell Pillbox Approximation

We begin our discussion of deflecting cavity design by considering the simplest example of such a cavity, which is a cylindrical pillbox. We can then utilize these results to make rule-of-thumb estimates of the design parameters for a multi-cell structure, such as the required input power and quality factor.

4.3.1 Fields in a Cylindrical Pillbox Cavity

Let us begin by deriving the equations for the electromagnetic fields in a cylindrical waveguide of radius b. Under the assumption of a travelling-wave z-dependence to the fields:

$$\left\{ \begin{array}{c} \mathbf{E}(\mathbf{r}) \\ \mathbf{B}(\mathbf{r}) \end{array} \right\} = \left\{ \begin{array}{c} \mathbf{E}(r,\phi) \\ \mathbf{B}(r,\phi) \end{array} \right\} e^{i(kz-\omega t)} \tag{4.5}$$

The wave-equation reduces to the eigenvalue (Helmholtz) equation

$$\left(\nabla_t^2 + \kappa^2\right) \left\{ \begin{array}{c} \mathbf{E} \\ \mathbf{B} \end{array} \right\} = 0 \tag{4.6}$$

where

$$\kappa^2 = k_0^2 - k^2 \ ; \ k_0 = \sqrt{\mu\epsilon}\frac{\omega}{c} \tag{4.7}$$

Applying Maxwell's equations, it is found that the transverse components of the fields can be obtained directly from the solutions for the longitudinal components. Since the boundary conditions on E_z and B_z are different, the eigenvalues are in general different. The fields thus naturally divide themselves into two distinct categories, with the longitudinal component of either the magnetic or electric field being identically zero. The former case is called transverse magnetic (TM) and the latter transverse electric (TE):

$$\begin{aligned} B_z = 0 \ ; \ E_z(r=b) = 0 \quad &; \quad \text{TM} \\ E_z = 0 \ ; \ \partial_r B_z(r=b) = 0 \quad &; \quad \text{TE.} \end{aligned} \tag{4.8}$$

The longitudinal wave equation is then of the form

$$\left(\nabla_t^2 + \kappa^2\right)\Psi = 0 \tag{4.9}$$

which for cylindrical symmetry has the solution

$$\Psi_{mn}(r,\phi) = \left\{ \begin{array}{c} E_0 \\ B_0 \end{array} \right\} J_m\left(\kappa_{mn} r\right) e^{\pm im\phi} \left\{ \begin{array}{l} \text{TM modes} \\ \text{TE modes} \end{array} \right. \tag{4.10}$$

where

$$\kappa_{mn} = \frac{1}{b} \left\{ \begin{array}{l} x_{mn} \\ x'_{mn} \end{array} \right. \equiv \sqrt{\mu\epsilon}\omega_{mn} \tag{4.11}$$

with the upper (lower) line corresponding to TM (TE) modes. Here ω_{mn} is the resonance frequency corresponding to the eigenvalue κ_{mn} of the Helmholtz equation. For each value of κ_{mn} (and therefore of ω_{mn}) one obtains a normal mode solution for the longitudinal wave-number k,

$$k = \sqrt{k_0^2 - \kappa_{mn}^2} = \sqrt{\mu\epsilon\left(\omega^2 - \omega_{mn}^2\right)} \tag{4.12}$$

Consequently, if the driving frequency is above the cutoff ($\omega > \omega_{mn}$), then k is real and waves of mode (m, n) can propagate in the waveguide. Otherwise, k is imaginary and so waves in that mode are damped. The case of a resonant cavity of length ℓ corresponds to a waveguide with transverse conducting plates introduced at its ends. Imposing this restriction, the z-dependences of the fields become those appropriate for a standing wave. Applying the boundary conditions at $z = 0, \ell$ we have that

$$\left\{ \begin{array}{c} E_z \\ B_z \end{array} \right\} = \Psi(r, \phi) \left\{ \begin{array}{ll} \cos(k_p z) & \text{(TM)} \\ \sin(k_p z) & \text{(TE)} \end{array} \right\} \tag{4.13}$$

where Ψ is the corresponding solution for the infinite waveguide of the same cross-section, and k_p is the (now quantized) longitudinal wave-number, with p being the longitudinal mode number:

$$k_p = \frac{p\pi}{\ell} \tag{4.14}$$

The oscillation freqency ω is now restricted to the discrete set of normal mode frequencies $\omega_{\rm mnp}$:

$$\omega_{\rm mnp} = \frac{1}{\sqrt{\mu\epsilon}} \sqrt{\kappa_{\rm mn}^2 + k_p^2} \tag{4.15}$$

The transverse fields are obtained from the longitudinal solutions via (for TM modes),

$$\mathbf{E}_t = -\frac{k_p}{\kappa_{\rm mn}^2} \sin(k_p z) \boldsymbol{\nabla}_t \Psi \quad , \quad \mathbf{B}_t = \frac{i\epsilon\omega_{\rm mnp}}{c\kappa_{\rm mn}^2} \cos(k_p z) \ \hat{\boldsymbol{z}} \times \boldsymbol{\nabla}_t \Psi \ , \tag{4.16}$$

and (for TE modes),

$$\mathbf{E}_t = -\frac{i\mu\omega_{\rm mnp}}{c\kappa_{\rm mn}^2} \sin(k_p z) \ \hat{\boldsymbol{z}} \times \boldsymbol{\nabla}_t \Psi \quad , \quad \mathbf{B}_t = \frac{k_p}{\kappa_{\rm mn}^2} \cos(k_p z) \boldsymbol{\nabla}_t \Psi \ . \tag{4.17}$$

For a cylindrical cavity, these expressions yield, for the TM modes,

$$
\begin{aligned}
E_r &= -\frac{E_0 k_p}{\kappa_{\mathrm{mn}}} J'_m\left(\kappa_{\mathrm{mn}} r\right) e^{im\phi} \sin\left(k_p z\right) \ , \\
E_\phi &= -\frac{iE_0 k_p}{\kappa_{\mathrm{mn}}^2} \ \frac{m}{r} J_m\left(\kappa_{\mathrm{mn}} r\right) e^{im\phi} \sin\left(k_p z\right) \ , \\
E_z &= E_0 J_m\left(\kappa_{\mathrm{mn}} r\right) e^{im\phi} \cos\left(k_p z\right), \\
B_r &= \frac{E_0 \epsilon \omega_{\mathrm{mnp}}}{c\kappa_{\mathrm{mn}}^2} \frac{m}{r} J_m\left(\kappa_{\mathrm{mn}} r\right) e^{im\phi} \cos\left(k_p z\right) \ , \\
B_\phi &= \frac{iE_0 \epsilon \omega_{\mathrm{mnp}}}{c\kappa_{\mathrm{mn}}} J'_m\left(\kappa_{\mathrm{mn}} r\right) e^{im\phi} \cos\left(k_p z\right), \\
B_z &= 0 \ ;
\end{aligned}
\tag{4.18}
$$

and for TE modes,

$$
\begin{aligned}
E_r &= -\frac{B_0 \mu \omega_{\mathrm{mnp}}}{c\kappa_{\mathrm{mn}}^2} \frac{m}{r} J_m\left(\kappa_{\mathrm{mn}} r\right) e^{im\phi} \sin\left(k_p z\right), \\
E_\phi &= -\frac{i\mu B_0 \omega_{\mathrm{mnp}}}{c\kappa_{\mathrm{mn}}} J'_m\left(\kappa_{\mathrm{mn}} r\right) e^{im\phi} \sin\left(k_p z\right), \\
E_z &= 0, \\
B_r &= \frac{B_0 k_p}{\kappa_{\mathrm{mn}}} J'_m\left(\kappa_{\mathrm{mn}} r\right) e^{im\phi} \cos\left(k_p z\right), \\
B_\phi &= \frac{iB_0 k_p}{\kappa_{\mathrm{mn}}^2} \frac{m}{r} J_m\left(\kappa_{\mathrm{mn}} r\right) e^{im\phi} \cos\left(k_p z\right), \\
B_z &= B_0 J_m\left(\kappa_{\mathrm{mn}} r\right) e^{im\phi} \sin\left(k_p z\right).
\end{aligned}
\tag{4.19}
$$

The general solution for the fields in a cylindrical pillbox cavity can be represented by a superposition of the TE and TM modes in the usual way. The lowest-order mode with transverse fields capable of imparting a net transverse deflection to an electron traveling along the axis of the structure is the TM mode with $m = 1$, $n = 1$, and $p = 0$, which we denote TM_{110}. The fields near the center of the cells in a multi-cell deflecting structure closely resemble those of the TM_{110} mode. In the next section, we therefore derive the fields of this mode explicitly and obtain the limiting forms near the axis.

4.3.2 On-Axis Fields for the Deflecting Mode

For acceleration, RF cavities are operated in the TM_{010} mode. In this mode, the only surviving field components are

$$E_z = E_0 J_0(\kappa_{01} r) \quad , \quad B_\phi = i E_0 \sqrt{\frac{\epsilon}{\mu}} J_0'(\kappa_{01} r) \,. \tag{4.20}$$

For a deflecting cavity, we would like to have zero longitudinal electric field and transverse fields on-axis which tend to produce a net transverse momentum kick. The lowest-order TM dipole mode for this purpose is TM_{110}. From the results of the previous section, the fields for this mode have the forms

$$\begin{aligned} E_z &= E_0 J_1(\kappa_{11} r)\, e^{i\phi} \;; \\ B_r &= \frac{E_0 \epsilon \omega_{110}}{c\kappa_{11}^2} \frac{1}{r} J_1(\kappa_{11} r)\, e^{i\phi}; \\ B_\phi &= \frac{i E_0 \epsilon \omega}{c\kappa_{11}} J_1'(\kappa_{11} r)\, e^{i\phi}; \end{aligned} \tag{4.21}$$

Dropping the subscripted indices on κ and ω for convenience and defining $\mathcal{E} \equiv E_0 \epsilon \omega / c\kappa$, we have

$$E_z = E_0 J_1(\kappa r) e^{i\phi} \;\; , \;\; B_r = \mathcal{E} \frac{J_1(\kappa r)}{\kappa r} e^{i\phi} \;\; , \;\; B_\phi = i\mathcal{E} J_1'(\kappa r) e^{i\phi}. \tag{4.22}$$

All other field components vanish. Note that there is no transverse electric field in this mode. Therefore any transverse deflection of the beam would have to be due entirely to magnetic forces. (Note that in the multi-cell structure this is not the case, as there is a nonzero transverse electric field in the iris region between cells). For small values of the argument, we can expand the 1st Bessel function and its derivative as follows:

$$\frac{J_1(\xi)}{\xi} = \frac{1}{2} - \frac{\xi^2}{16} + \frac{\xi^4}{384} + ... \;\; ; J_1'(\xi) = \frac{1}{2} - \frac{3\xi^2}{16} + \frac{5\xi^4}{384} + ... \tag{4.23}$$

We then have (near the axis) the expressions

$$E_z = \frac{E_0}{2}\kappa r e^{i\phi} \ , \ B_r = \frac{\mathcal{E}}{2}e^{i\phi}; \ B_\phi = i\frac{\mathcal{E}}{2}e^{i\phi}. \tag{4.24}$$

Converting to cartesian coordinates, we have

$$\begin{aligned} B_x &= B_r\cos\phi - B_\phi\sin\phi \ ; \ B_y = B_r\sin\phi + B_\phi\cos\phi \\ E_x &= E_r\cos\phi - E_\phi\sin\phi \ ; \ E_y = E_r\sin\phi + E_\phi\cos\phi. \end{aligned} \tag{4.25}$$

or

$$E_z = \frac{E_0}{2}\kappa r e^{i\phi} \ ; \ B_x = \frac{\mathcal{E}}{2} \ ; \ B_y = i\frac{\mathcal{E}}{2}. \tag{4.26}$$

So at $r = 0$, the electric field vanishes and we have only the x and y magnetic field components, which are out of phase by 90 degrees. Consequently, the on-axis magnetic field vector is circularly polarized (i.e. rotates about the z axis in time). This is to be expected from the cylindrical symmetry of the structure, which prefers no particular transverse direction. In practice, a small asymmetry may be introduced which couples more strongly to one transverse direction or the other. This produces a mode-splitting whereby the two linear polarizations (x and y) have different resonant frequencies. The desired polarization direction is then selected by setting the driving RF frequency to match the correct resonant value. The resulting fields of the separated polarizations (for deflections along the x and y axes respectively) read:

$$x: \quad E_z = \frac{E_0}{2}\kappa r\cos\phi \ ; \ B_x = 0 \ ; \ B_y = \frac{\mathcal{E}}{2} \tag{4.27}$$

$$y: \quad E_z = \frac{E_0}{2}\kappa r\sin\phi \ ; \ B_x = \frac{\mathcal{E}}{2} \ ; \ B_y = 0. \tag{4.28}$$

As we will see in Section 4.4, the technique used to separate the two polarizations in the multi-cell deflecting cavity design for the Neptune laboratory will consist of a pair of small holes penetrating the wall between adjacent cells.

4.3.3 The Transverse Cavity Voltage

The transverse momentum kick imparted to a relativistic electron traversing a pillbox cavity is approximately given by simply integrating the transverse force along a linear trajectory $z = z_0 + ct$ at a distance r and angle ϕ relative to the cylindrical coordinate system:

$$\Delta \mathbf{p}_t \simeq -\frac{e}{c}\int_0^{\ell} \{\mathbf{E}_t + (\mathbf{v}\times\mathbf{B})_t\}\, dz = -i\frac{e}{\omega}\int_0^{\ell} \boldsymbol{\nabla}_t E_z\, dz \tag{4.29}$$

where ℓ is the length of the cell and $\boldsymbol{\nabla}_t$ denotes the transverse gradient operator. Equation (4.29) is known as the Panofsky-Wenzel theorem [63]. For a vertical (y) deflection in the TM_{110} dipole mode, we have that the longitudinal electric field is given by Eq. (4.28). Taking the transverse gradient of that expression gives us

$$\boldsymbol{\nabla}_t E_z = \frac{E_0\kappa}{2} e^{i\omega t}\hat{\mathbf{y}} \tag{4.30}$$

where we have reinserted the explicit harmonic time dependence. Inserting this into Eq. (4.29) and taking the real part, the transverse momentum kick reads

$$\Delta \mathbf{p}_t = \mathrm{Re}\left[-i\frac{e}{\omega}\int_{-\ell/2}^{\ell/2} \boldsymbol{\nabla}_t E_z\, dz\right] = \frac{e}{\omega}\frac{E_0\kappa}{2}\hat{\mathbf{y}}\int_{-\ell/2}^{\ell/2} \sin\left[\frac{\omega\,(z-z_0)}{c}\right] dz \tag{4.31}$$

Making the substitution of variables

$$\psi_0 = -\frac{z_0\omega}{c},\ \Delta\psi = \frac{\ell\omega}{c} \tag{4.32}$$

the integral yields

$$\Delta \mathbf{p}_t = \frac{eE_0}{\omega}\sin(\psi_0)\sin(\Delta\psi/2)\ \hat{\mathbf{y}}. \tag{4.33}$$

Here we have used the fact that (for the TM_{110} mode) $\kappa = k_0 = \omega/\mathrm{c}$. Note that the value of $\Delta\psi$ is determined by the frequency and length of the cavity. However, the value of ψ_0 represents the phase arrival time of the particle at the center of the cavity. If the design particle arrives at the phase ψ_0=0 then it

experiences no momentum kick and hence there is no offset of the beam centroid. Particles which arrive before or after the design particle, however will experience a transverse momentum kick that is approximately proportional to the z-position of the particle within the bunch (since for small arguments $\sin\psi_0 \simeq \psi_0$).

Let us define the voltage V_T to be the voltage over which a particle would acquire the transverse momentum whose magnitude was determined above:

$$\Delta \mathrm{p}_t = \frac{e}{c} V_T. \tag{4.34}$$

Hence,

$$V_T = \frac{cE_0}{\omega} \sin(\psi_0) \sin(\Delta\psi/2). \tag{4.35}$$

This may alternately be considered the real part of the voltage phasor

$$\tilde{V}_T = V_0 \; e^{i\,\psi_0}, \tag{4.36}$$

which has the magnitude

$$V_0 = \left|\tilde{V}_T\right| = \frac{cE_0}{\omega} \sin(\Delta\psi/2). \tag{4.37}$$

The quantity V_0 is typically referred to as the transverse cavity voltage. Note that for the voltage to be maximized, we would like $\Delta\psi$ to be equal to an odd multiple of π. This is equivalent to requiring that the overall cavity length ℓ be equal to an odd multiple of half the RF wavelength:

$$\ell = \frac{\lambda}{2}, \frac{3\lambda}{2}, \frac{5\lambda}{2}, ... \tag{4.38}$$

Note that Eq. (4.37) may alternately be written (see e.g. Ref. [64])

$$V_0 = \frac{E_0 \ell}{2} T \;;\; \text{where } T \equiv \frac{\lambda}{\pi\ell} \sin(\Delta\psi/2),$$

where the quantity T is referred to as the *time transit factor*.

Power Coupling to the Cavity

Suppose we have a cavity that is initially driven by an external RF generator, which is coupled to the cavity by a waveguide and a coupling slot. If the source is suddenly switched off, then the energy stored in the cavity will dissipate due to losses. The total power being lost is then given by

$$P_{\text{tot}} = P_w + P_c \tag{4.39}$$

where P_w is the power lost in the wall of the cavity and P_c is the power that escapes by returning out through the coupling slot. We can define the external, resonant, and loaded quality factors:

$$Q_e = \frac{\omega_0 U}{P_c} \; ; \; Q_0 = \frac{\omega_0 U}{P_w} \; ; \; Q_L = \frac{\omega_0 U}{P_{\text{tot}}} \tag{4.40}$$

From these relations we then see that the quality factors satisfy the reciprocal addition rule

$$\frac{1}{Q_L} = \frac{1}{Q_0} + \frac{1}{Q_e} \tag{4.41}$$

The coupling of the power into the cavity may then be characterized by a coupling parameter β_c which is defined by

$$\beta_c = \frac{Q_e}{Q_0} = \frac{P_w}{P_c} \tag{4.42}$$

Consequently, β_c=1 corresponds to the case P_c=P_w. This indicates that the stored energy is emitted by the coupler at the same rate that it is absorbed by the cavity walls. If the cavity is instead driven in a steady state at its resonance frequency, then a fraction $|\Gamma|^2$ of the power P_{in} that is incident upon the input coupler from the external waveguide is reflected, where Γ is the complex reflectance. The power P_w transmitted into the cavity is then

$$P_w = P_{in}(1 - |\Gamma|^2) \quad , \quad \text{where } |\Gamma| = \begin{cases} (1-\beta_c)/(1+\beta_c) & , \quad \beta_c \leq 1 \\ (\beta_c - 1)/(\beta_c + 1) & , \quad \beta_c \geq 1 \end{cases} . \tag{4.43}$$

The above relation between Γ and β_c is derived in Ref. [65], among others. Consequently, with a coupling β_c of unity, when the cavity is driven in steady state all input power is transmitted into the cavity with zero reflections. It can be shown that under these conditions the stored energy in the cavity is maximized and the cavity acts like a perfectly matched load. In microwave circuit theory, the load mismatch of a terminated line is measured by the so-called *voltage standing wave ratio* or VSWR, which is related to the magnitude of the reflectance Γ by VSWR $= (1+|\Gamma|)/(1-|\Gamma|)$ [66]. Hence, the coupling parameter may be expressed as

$$\beta_c = \begin{cases} 1/\text{VSWR} & , \quad (undercoupled) \\ \text{VSWR} & , \quad (overcoupled) \\ 1 & , \quad (matched) \end{cases} . \tag{4.44}$$

This expression is useful, because it is common practice in the accelerator community to express the coupling in terms of β_c, but the VSWR is what is generally measured empirically.

4.3.4 Calculation of the Q and Power Loss

We wish to relate the power requirement for the TM_{110} mode of a pillbox cavity to the quality factor Q_0 and the deflecting voltage V_0. The square of the deflecting voltage and the power are generally expressed relative to each other by defining a *shunt impedance* $\tilde{R}_s$ in analogy with circuit theory. The quality factor and shunt impedance are given by

$$Q_0 = \omega_0 \frac{U}{P_w} \quad , \quad \tilde{R}_s = \frac{V_0^2}{P_w}, \tag{4.45}$$

where ω_0 is the resonant frequency of the given mode, U is the time-averaged energy stored in the cavity, and P_w is the power loss in the walls of the cavity.

For a pillbox cavity of length ℓ, the stored energy of a TM mode is given by

[67]

$$U = \frac{\epsilon \ell}{4} \left\{ 1 + \left(\frac{p\pi}{\kappa_{\rm mn} \ell} \right)^2 \right\} \int_S |\Psi|^2 dS \times \begin{cases} 1 & p \neq 0 \\ 2 & p = 0 \end{cases} \tag{4.46}$$

where S is the cross-section of the cavity and Ψ is the solution to the Eq. (4.6). For the TM_{110} mode, the solution is given by

$$\Psi = E_0 J_1(\kappa r) \cos(\phi). \tag{4.47}$$

Hence,

$$\begin{aligned} \int_S |\Psi|^2 dS &= E_0^2 \int_0^{2\pi} \int_0^b J_1^2(\kappa r) r \cos^2(\phi) dr \; d\phi \\ &= \frac{E_0^2 a^2 \pi}{2} \left\{ J_1^2(\kappa b) - J_0(\kappa b) J_2(\kappa b) \right\} \end{aligned} \tag{4.48}$$

Noting that $\kappa b = x_{11} = 3.832$ is the first zero of J_1 and that $J_2(x_{11})$=-$J_0(x_{11})$=0.403 we have that the stored energy is given by

$$U = E_0^2 \pi b^2 \frac{\epsilon \ell}{4} J_2^2(\kappa b). \tag{4.49}$$

The power loss for TM modes is given by [67]

$$P_w = \frac{\epsilon}{\sigma \delta \mu} \left\{ 1 + \left(\frac{p\pi}{\kappa_{\rm mn} \ell} \right)^2 \right\} \left(1 + \begin{Bmatrix} \xi \\ 2\xi \end{Bmatrix} \frac{C\ell}{4A} \right) \int_S |\Psi|^2 dS \tag{4.50}$$

where the upper (lower) line is for $p \neq 0$ ($p = 0$), ϵ and μ are the dielectric constant and magnetic permeability, ξ is a geometrical factor of order unity, and δ and σ are the skin depth and conductivity of the conducting boundary. So for the TM_{110} mode, we have (ξ=1 for TM modes in a circular cavity)

$$P_w = \frac{\epsilon}{2\sigma \delta \mu} \left(1 + \frac{\ell}{a} \right) E_0^2 \pi b^2 \; J_2^2(\kappa b) \tag{4.51}$$

This expression for the power may be recast in terms of the deflecting voltage V_0 by using Eq. (4.37) to replace E_0:

$$P_w = \frac{\epsilon \omega^2}{2\sigma \delta \mu \; c^2} \pi \frac{a^2 (1 + \ell/b)}{\sin^2[\Delta\psi/2]} \; J_2^2 \left(x_{11} \right) V_0^2. \tag{4.52}$$

Table 4.1: Comparison of Pillbox Parameters for Different Frequencies

Parameter	Units	S-Band	X-Band	X-Band
f	GHz	2.856	11.424	9.6
λ	cm	10.4	2.62	3.1
ℓ	cm	5.2	1.31	1.56
b	cm	6.4	1.6	1.9
δ	μm	1.22	0.614	0.670
Q_0	-	23473	11735	12803
$\tilde{R}_s$	kΩ	1505	752	821
V_{min}	kV	593	148	176
V_0	kV	1780	444	529
P_w	kW	2103	263	341

Using the relations for the power loss and stored energy, Eqs. (4.49), (4.51) and (4.52), we can now write explicit expressions for the quality factor and the shunt impedance:

$$Q_0 = \frac{\mu}{\mu_c}\frac{\ell}{\delta}\frac{1}{\left(1+\frac{\ell}{b}\right)} \tag{4.53}$$

$$\tilde{R}_s = \frac{2\sigma\delta\mu\ c^2}{\epsilon\omega^2}\frac{\sin^2[\Delta\psi/2]}{\pi a^2(1+\ell/b)\ J_2^2\left(x_{11}\right)} \tag{4.54}$$

where $\mu_c = \delta^2\omega\sigma/2$ is the magnetic permeability of the conducting boundary. In Table 4.1 we use these formulas, combined with Eq. (4.4) for the minimum cavity voltage V_{min} to calculate the quality factor and input power for three different frequencies. The assumed drift length is $L = 43.3$ cm, and the beam energy is taken to be 12 MeV (both of these being reasonable values for the Neptune beamline). The voltage V_0 is taken to be three times the minimum voltage ($V_0 = 3V_{min}$), implying the minimum deflecting voltage can be achieved

with a power level a factor of 9 below those given in Table 4.1. Note that in this regard one must consider losses in the waveguides when specifying the needed power levels from the RF sources.

The RF frequencies considered in Table 4.1 correspond to three possible sources of high power RF which were under consideration at the time the UCLA deflecting cavity was in the preliminary design stages. The value of 2.856 GHz is the standard high-power RF frequency used at the Stanford Linear Accelerator Center (SLAC) and is the resonant frequency of the UCLA Neptune photoinjector gun and linac. The second value of 11.424 GHz represents the standard X-Band SLAC frequency. The third value (9.6 GHz) represents the approximate frequency of a commercially available 50 kW (peak power) refurbished military klystron from Radio Research Instruments. The first two options would have required (respectively) either siphoning off RF power from the 20 MW S-Band klystron used to drive the gun and linac at the Neptune laboratory, or acquiring an X-band klystron from SLAC. As the first of these options would have entailed difficult and costly modifications to the Neptune high-power RF waveguide system, and the second was not feasible, it was decided to purchase the 9.6 GHz klystron and to design the deflecting cavity to match its output frequency and power capability. Therefore, henceforth we will use f =9.6 GHz and P_{max} = 50 kW as our rule-of-thumb operating frequency and peak power level.

4.4 The Multi-Cell Design

By combining multiple cells in series, the overall impedance of the deflecting structure can be increased, thereby reducing the input power required to achieve the same net deflecting voltage. The cells are electromagnetically coupled by holes or gaps in the walls separating them, which include, at the minimum, a

central iris through which the electron beam may pass.

A structure of this type may also be regarded as a waveguide loaded with periodically spaced disks (hence it is sometimes referred to as a *disk-loaded waveguide*). A traveling wave propagating in a simple waveguide (i.e. in the absence of loaded disks) must have a frequency above the cutoff, and therefore its phase velocity $v_\phi = \omega/k$ is greater than c, as required by Eq. (4.12). This would make it impossible for an ultrarelativistic beam to remain in phase with the wave. The inclusion of the periodic disks effectively slows the phase velocity of the propagating wave to that of light.

Due to the periodicity of the structure the electromagnetic fields can be made to satisfy the Flouquet condition, whereby the field at the center of one cell is equal to that at the center of another cell located an integer number of cell-spacings downstream. This may be written $\mathbf{E}(z) = \mathbf{E}(z + jd)$ where j is an integer and d is the distance from the center of one cell to the next. For a finite number N of cells, the allowed Flouquet phase shifts are then given by $\Delta\phi_n = \pi(n-1)/(N-1)$ where $n = 1, 2, 3, \ldots, N$. These discrete values for the cell-to-cell phase shift correspond to an N-fold degeneracy of the single-cell cavity mode produced by the coupling of the cells, with a resultant splitting of the single-cell resonant frequency into a set of N distinct mode frequencies. These modes are analogous to the normal modes of a chain of coupled oscillators. In fact, the mode behavior and dispersion relation of a multi-cell cavity can be calculated using a lumped-element circuit model of the structure as a chain of coupled resonators. This methodology is outlined in the following section.

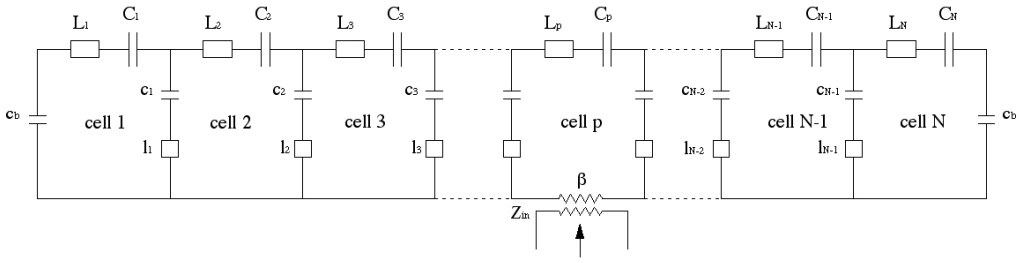

Figure 4.2: Equivalent circuit diagram for a chain of coupled cavities.

4.4.1 Circuit Theory of a Chain of Coupled Cavities

A fairly general circuit model for multicell cavities is given by Nagle, et al. [68]. This model is generalized by Yi, et al. [69], who also provide a block diagram of a possible C+ algorithm for solving the equations. In this model, a multicell RF cavity is represented by a circuit of the form shown in Fig. 4.2. The figure is shown with the input power coupler located on the p'th cell, although additional couplers could be included as well.

The quantities L_n and C_n denote the inductance and capacitance of each oscillator, and $2\kappa_n$ is the coupling between cell n and cell $n+1$. For inductive coupling, κ_n is negative and for capacitive coupling it is positive. The resultant circuit equations relating the voltage V_n and current I_n of cell n are

$$\begin{aligned}
V_1 &= I_1\left(i\omega L_1 + R_1 + \frac{1}{i\omega C_1}\right) + i\omega\kappa_1\sqrt{L_1L_2}I_2, \\
V_n &= I_n\left(i\omega L_n + R_n + \frac{1}{i\omega C_n}\right) \\
&\quad + i\omega\sqrt{L_n}\left(\kappa_{n-1}I_{n-1}\sqrt{L_{n-1}} + \kappa_n I_{n+1}\sqrt{L_{n+1}}\right), \\
V_N &= I_n\left(i\omega L_N + R_N + \frac{1}{i\omega C_N}\right) + i\omega\kappa_{N-1}\sqrt{L_N}\left(I_{N-1}\sqrt{L_{N-1}}\right).
\end{aligned} \tag{4.55}$$

Defining the quantities

$$X_n = \sqrt{L_n} I_n \ , \ Q_n = \omega_n \frac{L_n}{R_n} \ , \ \omega_n = \frac{1}{2\pi\sqrt{L_n C_n}}, \tag{4.56}$$

Eqs. (4.55) may be cast into the form of a matrix equation,

$$\mathrm{A} \cdot \mathbf{X} = \mathbf{V}, \tag{4.57}$$

where

$$\mathrm{A} = \begin{pmatrix} a_1 & \kappa_1 & 0 & \cdots & 0 \\ \kappa_1 & a_2 & \kappa_2 & \cdots & 0 \\ 0 & \kappa_2 & a_3 & \cdots & 0 \\ \vdots & \vdots & \vdots & \ddots & \vdots \\ 0 & 0 & 0 & \kappa_{N-1} & a_N \end{pmatrix} \ , \ \mathbf{X} = \begin{pmatrix} X_1 \\ X_2 \\ X_3 \\ \vdots \\ X_N \end{pmatrix} \ , \ \mathbf{V} = \begin{pmatrix} V_1 \\ V_2 \\ V_3 \\ \vdots \\ V_N \end{pmatrix}. \tag{4.58}$$

The diagonal elements of A are given by

$$a_n = 1 - \frac{\omega_n^2}{\omega^2} - i\frac{\omega_n \left(1 + \beta_n\right)}{\omega Q_n}. \tag{4.59}$$

where β_n is a measure of the local coupling in cell n to the excitation voltage V_n. If, as is shown in the example circuit of Fig. 4.2, there is a single input coupler located on the p'th cell, then β_n would be zero except for $n = p$. The Q_n and ω_n values represent the monocell quality factor and resonant frequency respectively. The quantity X_n is the normalized current in circuit n, representing the complex field amplitude in the n'th cell. If the quantities ω_n, V_n, Q_n, X_n, β_n, κ_n are known for all N cells, then Eqn. (4.57) may be solved to obtain both the complex fields X_n and the eigenfrequencies. The fields as a function of ω are obtained by simply inverting the matrix A:

$$\mathbf{X}(\omega) = \mathrm{A}^{-1}(\omega) \cdot \mathbf{V} \tag{4.60}$$

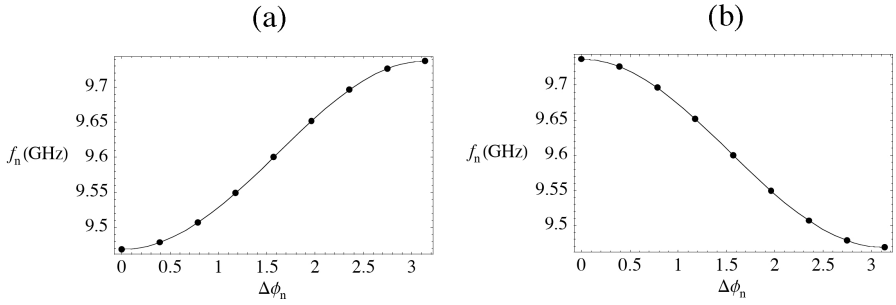

Figure 4.3: Example plots of the dispersion relations for (a) a forward-wave and (b) and backward-wave 9-cell structure.

The eigenfrequencies can be obtained by solving the homogeneous equation $\mathrm{A} \cdot \mathbf{X} = \mathbf{0}$. This produces the requirement $\det(\mathrm{A}) = 0$, which forms a polynomial equation for ω, with N distinct solutions, which we will denote $2\pi f_n$ where $n = 1, 2, 3, \ldots, N$. These solutions correspond to the allowed Flouquet phase shifts $\Delta\phi_n = \pi(n-1)/(N-1)$. For the case where all of the cells are identical, having the same single-cell frequency and inter-cell couplings (i.e. $\omega_n = 2\pi f_0$ and $\kappa_n = \kappa$ for all n) then the dispersion relation takes the simple form [68]

$$f_n = \frac{f_0}{\sqrt{1 + 2\kappa\cos(\Delta\phi_n)}} \quad ; \quad n = 1, 2, 3, \ldots, N. \tag{4.61}$$

The width of the passband and the frequency of the π-mode are then given by

$$\Delta f = f_0 \left| \frac{1}{\sqrt{1-2\kappa}} - \frac{1}{\sqrt{1+2\kappa}} \right| \quad , \quad f_N = \frac{f_0}{\sqrt{1-2\kappa}}. \tag{4.62}$$

In Fig. 4.3, Eq. (4.61) is plotted for a single-cell frequency of $f_0 = 9.6$ GHz and a coupling coefficient of magnitude $|\kappa| = 0.014$. The plot in part (a) corresponds to the case where $\kappa > 0$ and the cell-to-cell coupling is primarily capacitive. The group velocity in this case is positive and the structure is called a *forward-wave* structure. The plot in part (b) for $\kappa < 0$ corresponds to a primarily inductive cell-to-cell coupling, which results in a negative group velocity.

A multi-cell cavity with a dispersion relation of this form is therefore called a *backward-wave* structure. We make this distinction because the strong magnetic component to the deflecting voltage in a multi-cell deflecting cavity tends to produce a predominantly inductive cell-to-cell coupling. And in fact our final design for the 9.6 GHz cavity will be a backward-wave device.

4.4.2 Traveling vs. Standing Wave Cavities

The multi-cell cavity, or disk-loaded waveguide, may be classified as either a traveling or standing wave device, depending upon whether the fields excited in the structure have only an e^{ikz} or e^{-ikz} dependence, or a superposition of the two. The distinction is largely dependent upon the manner in which power is coupled into and out of the cavity. If all of the cells are fed by a single central coupler as in Fig. 4.4(a) then the power is reflected at the ends of the cavity and a standing-wave is formed. On the other hand, if the power is coupled in at one end of the structure and then coupled out at the other, as in Fig. 4.4(b) then no such reflection occurs and the device is called a traveling wave cavity. It should be noted, however, that a traveling wave structure can also be constructed with no net power flow along the device by powering each cell separately.

Generalizing from the usual results for multi-cell accelerating cavities (see for example Ref. [70]), the transverse deflecting voltage is related to the input power by a relation of the form

$$V_0 = K\sqrt{P_0 \tilde{r}_s L} \tag{4.63}$$

where L is the total length of the structure, $\tilde{r}_s$ is the shunt impedance per unit length, and K has the following forms for traveling waves (TW) and standing

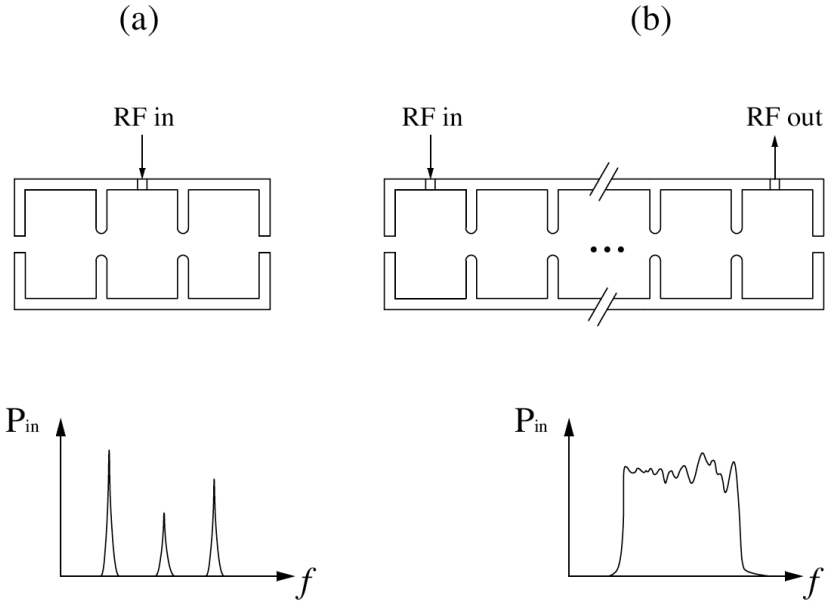

Figure 4.4: Examples of a standing-wave (a) and a traveling-wave (b) multi-cell structure with power vs. frequency plots.

waves (SW) respectively:

$$K = \begin{cases} \sqrt{2\tau}\,[(1-e^{-\tau})/\,\tau] & ;\ \text{TW} \\ \left[(\tanh\tau/2)\,/\tfrac{1}{2}\,\tau\right]^{1/2}(1+e^{-2\tau})^{-1/2} & ;\ \text{SW} \end{cases} \tag{4.64}$$

and τ is the attenuation factor for traveling waves in the structure, given by

$$\tau = \frac{L\omega}{v_g Q_0} = \frac{L}{\delta}\ ;\ \text{where}\ \delta = \frac{v_g Q_0}{\omega} \tag{4.65}$$

Here v_g is the traveling wave group velocity. Below we plot K for both cases as functions of τ. We see that for $\tau < 1$ the standing wave structure produces a stronger deflection. The value for τ which maximizes the value of K for the traveling wave case is approximately τ=1.26. At this value of τ, we can see from the plot that the two curves are fairly close together and are approximately $K_{\max}\simeq$0.9.

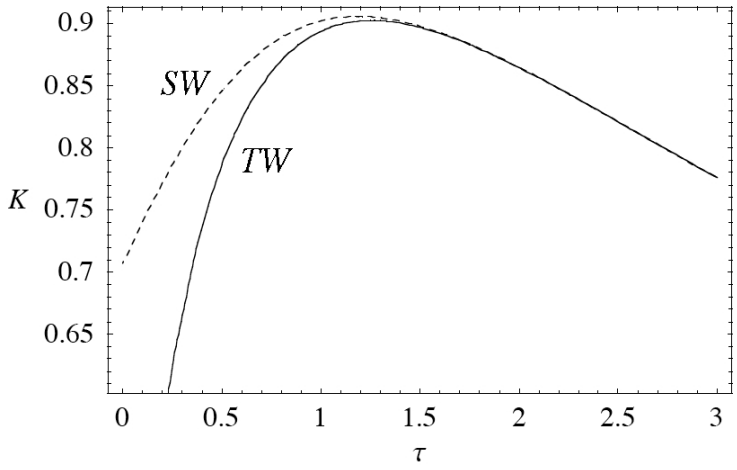

Figure 4.5: Plot of K vs. τ for standing wave (dashed) and traveling wave structures (solid).

If we assume a constant impedance structure, then $\tilde{r}_s L = n\tilde{R}_s$ where $\tilde{R}_s$ is the shunt impedance for one cell and n the number of cells. Then for τ near the optimal value of 1.26, $K \approx 1$ and we have

$$V_0 \simeq \sqrt{P_{cav} n \tilde{R}_s} \implies P_{cav} \simeq \frac{V_0^2}{n\tilde{R}_s} = \frac{P_{\rm w}}{n} \tag{4.66}$$

The required input power P_{cav} is therefore approximately the single-cell value divided by the number of cells. The primary benefit of the TW over the SW structure is that a TW structure can maintain a larger mode separation for a longer cavity length. So, for very long cavities (> 10 cells), a TW structure is preferred. However, fewer cells are generally desirable in order to improve the field flatness and avoid trapped modes. Since standing wave cavities tend to have only a few cells, power can be coupled into them only at a few discrete frequency values, corresponding to the normal mode frequencies in Eq. (4.61), as shown in Fig. 4.4(a). For traveling wave structures, with tens (or hundreds) of cells, these discrete resonances begin to overlap and thereby create a semi-continuous

passband, which is illustrated in Fig. 4.4(b). The presence of this continuous passband for the traveling wave case is also aided by the fact that the output coupler is generally terminated with a matched load, which causes the structure to appear infinitely long with respect to the power coupling at the input. Since the single-cell power requirement (341 kW) for the 9.6 GHz case, as indicated in Table 4.1, exceeds the peak power of the available source (50 kW) by only a factor of 7, a standing wave cavity is feasible for this design.

4.4.3 Estimated Power and Resolution

The achievable temporal resolution of a deflecting cavity is ultimately limited, in accordance with Eq. (4.3), by the minimum spot size σ_0 that can be achieved on the downstream imaging screen when the deflecting cavity is turned off. This can be seen by noting that according to Eq. (4.1) the relation between a particle's arrival time $t = -z/c$ and its vertical position y on the deflector screen is given by

$$t = \frac{y_0 - y}{c\hat{M}}, \tag{4.67}$$

where we have taken the phase to be $\psi_0 = 0$. However, in reconstructing the time-distribution from the image on the deflecting screen, the initial and deflected positions y_0 and y of individual particles are not known. What is measured instead is a projection of the phase space distribution onto the vertical coordinate. Therefore, in reconstructing the longitudinal profile of the beam using Eq. (4.67) the value y_0 must be neglected. There is then, on average, an ambiguity of $\langle y_0 \rangle = \sigma_0$ in the reconstructed longitudinal position of the portion of the beam located at the deflected position y.

If the initial spot size is neglected then the time resolution is limited by the deflecting voltage and the resolution of the screen and camera optics used to

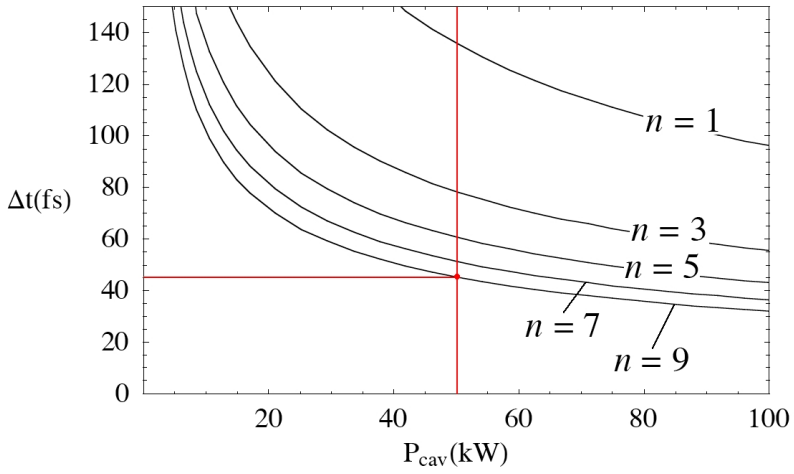

Figure 4.6: Time resolution vs. power for n pillbox cells in series.

digitize the final y-distribution. Taking the cavity to consist of n identical pillbox cells in series, we will approximate the total shunt impedance by $n\tilde{R}_s$ where $\tilde{R}_s$ is the shunt impedance per cell as given by Eq. (4.54). The total deflecting voltage is thus approximately

$$V_0 \approx \sqrt{n\tilde{R}_s P_{cav}} \tag{4.68}$$

where P_{cav} is the total input power required. Thus, for a fixed value of the deflecting voltage, the input power scales as $P_{cav} \approx P_w/n$ where P_w is the single-cell input power as given by Eq. (4.52). Now, let Δx represent the distance on the final deflector screen corresponding to a single pixel in the digitized image, as viewed using a camera and whatever collecting optics are present. The smallest beam size $\Delta z = c\Delta t$ which can be resolved then is the value which results in a deflection $\Delta y = \hat{M}\Delta z$. Hence, the best achievable time resolution in this case is

$$\Delta t = \frac{\Delta y U/d}{L\pi f\sqrt{\tilde{R}_s n P_{cav}}}. \tag{4.69}$$

Equation (4.69) is plotted in Fig. 4.6 as a function of total power P_{cav} for dif-

ferent numbers n of cells, for an RF frequency of 9.6 GHz and a screen resolution of $\Delta y = 30$ μm (a typical value for the camera and screen setups in the Neptune lab). Only odd values of n are considered because a standing-wave center-fed cavity can by definition have only an odd number of cells. As was noted in Section 4.3.4, the maximum power available from the X-band power source is 50 kW. Furthermore, from Table 4.1 we see that the single-cell power required at 9.6 GHz to obtain a suitable deflecting voltage was approximately 7 times the available peak power, suggesting that the cavity should be designed to incorporate at least 7 cells. However, in order to further reduce the power requirements of the cavity and to ensure that there would be sufficient deflecting voltage to make the desired measurements, a 9-cell design was decided upon. The commercial RF modeling code HFSS 9.2 was then used to finalize the design, and the particle tracking code ELEGANT was used to simulate the effect of the cavity on the electron beam.

4.5 Simulations of the 9-Cell Cavity

The computer-aided design of the UCLA Neptune deflecting cavity was a three-year endeavor, which proceeded simultaneously with the construction and testing of two prototypes (as well as the final cavity), included two changes in the design frequency of the structure (due to unexpected hardware limitations of the RF power source), and involved experimentation with a number of design features that were later abandoned or significantly modified.

However, our goal here is to present the basic methodology of the computer-aided design process in a compact and thematically (rather than chronologically) organized fashion. We will therefore overview the computer modeling of the final cavity design in a bottom-up approach, neglecting to mention a variety of interceding design changes and modifications that would likely serve only to

Table 4.2: Basic Design Parameters for Deflecting Cavity

Frequency	9.59616 GHz
Flouquet mode	π-mode
Number of cells	9
Peak input power	50 kW
Coupler type	central coupler
Deflecting Voltage	529 kV

distract the reader. We will begin with a description of the eigenmode design and definition of the main geometrical parameters, and then proceed to the simulation of more advanced design features, such as the input coupler and the inclusion of holes in the walls between cells to separate the orthogonal polarization modes discussed at the end of Section 4.3.2.

For the purposes of the following discussions, we will take as our starting design parameters those which are shown in Table 4.2. These are in fact the basic design characteristics of the UCLA Neptune deflecting cavity, and are consistent with the discussions and justifications provided by our comments in Section 4.4. The deflecting voltage is that given in Table 4.1. The frequency shown (which differs slightly from the previously assumed 9.6 GHz) is derived from the 252nd harmonic of the drive laser oscillator frequency (38.08 MHz) since this was used as the reference RF signal. The reasoning for this frequency choice will be explained in more detail in Section 4.6.1.

4.5.1 Description of the Modeling Code: HFSS 9.2

The code used to design the 9-cell deflecting cavity for the Neptune Laboratory was the commercial RF modeling software package HFSS version 9.2 by Ansoft

Corporation. This software uses the finite element method (FEM) to calculate harmonic electric and magnetic fields in a high-frequency electromagnetic structure. The geometry of the electromagnetic structure to be modeled is created using a computer-aided design or CAD-like graphical user interface. The adaptive grid on which the solution is performed is then generated automatically based upon the user-specified geometry, although the fineness of the mesh may be specified by the user on any or all of the surfaces in the model. Solutions may be performed using an *eigenvalue solver*, which computes the eigenfrequencies and associated eigenmode fields in the structure, or using a excitation-based *driven modal solver* whereby the user defines an excitation on one or more port boundaries and then the resulting fields are calculated inside the structure.

Both solution methods are highly valuable in the design process. The first permits a quick way of tracking the behavior of the eigenmode frequencies under modifications of the cavity geometry, while the second provides a more complete but computationally intensive solution of the fields and impedance properties of the structure, including the transmittance and reflectance at the port(s). In addition, idealized boundary conditions (perfect electric, perfect magnetic) may be imposed on surfaces, different materials can be specified for the composition of the cavity and its interior volume, and symmetry planes may be introduced to reduce the computation time.

4.5.2 Eigenmode Solutions

Prior to designing the input power coupler, the basic mode structure of the cavity was explored using the eigenmode solver. The cavity geometry is shown in Fig. 4.7, which depicts a cross-section of the half-cavity in the x-z plane. Only a quarter of the structure is modeled in the simulation, as symmetry planes have

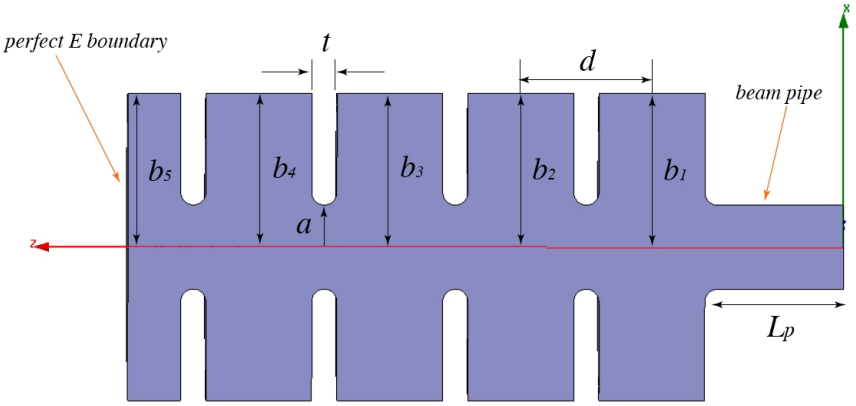

Figure 4.7: Geometry of the half-structure for the eigenmode solver.

been defined to reduce the computational volume. A perfect electric boundary is defined on the downstream x-y cross-section which defines the midplane of the center cell, and a perfect magnetic boundary is defined on the surface which bisects the cavity in the x-z plane (i.e. the plane of the page).

Note that a beam pipe of length L_p has been included, as well as circular irises of radius a and width t connecting the individual cells. The radii on the edges of the irises are set to $t/2$ so that the surface has no sharp edges. The iris radii were chosen to be sufficiently large to provide an adequate aperture for the electron beam. The value of the cell-to-cell spacing d is constrained by the RF wavelength of the design frequency and the Flouquet phase shift of $\Delta\phi = \pi$ to satisfy $d = \lambda/2 = 15.62$ mm (for a π-mode frequency of 9.59616 GHz). With all of the cell radii set to the same value $b_1 = b_2 = b_3 = b_4 = b_5 = b$, the simulated eigenmode frequencies should be approximated by the dispersion relation given in Eq. (4.61). This comparison is made in Fig. 4.8. The cavity dimensions used in this simulation are shown in Table 4.3, where the simulated eigenmodes are plotted in superposition with the dispersion curve for a cell-to-cell coupling of

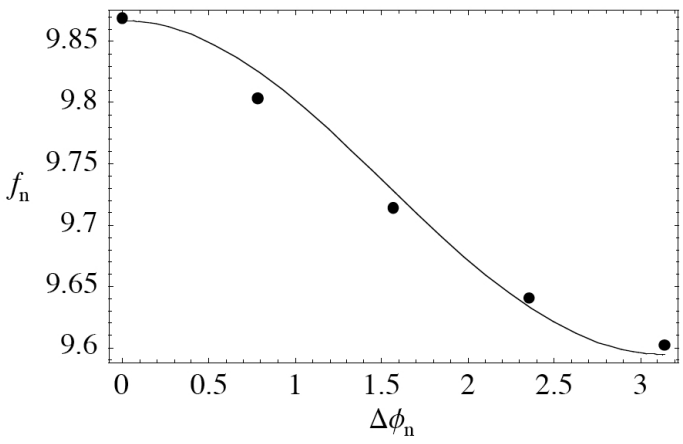

Figure 4.8: Comparison of simulated eigenfrequencies (dots) with the curve predicted by Eq. (4.61).

$\kappa = -0.014$. The value of the cell radius b has been chosen so that the π-mode frequency is equal to the desired 9.6 GHz.

For a 9-cell deflecting cavity, there should in principle be 9 eigenmodes corresponding to the TM_{110}-like mode of the single-cell geometry. However, in Fig. 4.8 we see that only 5 eigenmodes appear. This is due to the perfect electric boundary condition imposed at the midplane, which supresses any modes having a field-null at the midplane of the cavity. Recalling that, for a 9-cell structure, the allowed

Table 4.3: Dimension values corresponding to the plot of Fig. 4.8

Dimension	Value	Units
b	18.27	mm
a	5	mm
t	3	mm
d	15.62	mm
L_p	15	mm

Flouquet modes are $\Delta\phi_n = \pi(n-1)/8$, we have then that the supressed modes are those corresponding to $n = 2, 4, 6,$ and 8 or $\Delta\phi = \pi/8, 3\pi/8, 5\pi/8,$ and $7\pi/8$. The mode suppression imposed by the boundary condition on the midplane is not unphysical, however, because the eventual inclusion of a central power coupler on the middle cell of the cavity will produce the identical form of mode supression, as we will see in Section 4.6.3.

Note also from Fig. 4.8 that the dispersion curve corresponds to that of a backward-wave structure, as the group velocity is negative (except at $\Delta\phi = 0, \pi$ where it is zero). It may therefore be compared with the plot of Fig. 4.3(b). However, there is a relative offset in frequency between the two plots due to the fact that the monocell frequency was set to 9.6 GHz in Fig. 4.3. In the present simulation, the monocell frequency has been effectively increased by reducing the cell diameter b, in order to match the lowest-frequency (π) mode to the desired 9.6 GHz.

4.5.3 Input Coupler Design

Power is coupled into the cavity by way of a coupling aperture introduced into one or more cells, which connects the interior volume of the cavity to that of an external waveguide which carries RF power from the generator. For a 9-cell standing-wave structure, a single coupling iris on the center cell is the simplest solution. In principle, the coupler could be located elsewhere but this would disrupt the cavity symmetry, making the design and simulation of the structure unnecessarily difficult. Figure 4.9 shows the simulation geometry for a coupling iris of width $2w$, length $2l$, corner radius r, and depth db located on the center cell of the cavity. Note that because of the symmetry boundaries in the simulation, only a quarter of the structure is shown. Consequently, the dimensions l and w

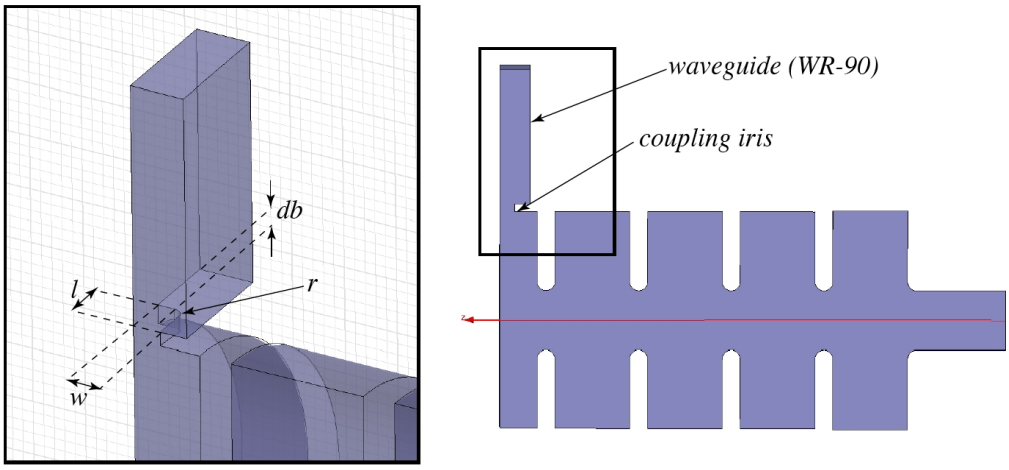

Figure 4.9: Geometry of the input coupler design for the HFSS simulation.

shown in Fig. 4.9 correspond to the half-length and half-width of the coupling iris respectively. The cross-sectional dimensions of the rectangular waveguide section are set to correspond to those of the standard size of waveguide (WR-90) for this frequency range: 0.4"×0.9", or 10.16 mm×22.86 mm.

The geometry of the coupling iris affects the electromagnetic properties of the structure in several ways: (1) it determines the coupling parameter β_c of the cavity, (2) it alters the monocell frequency of the center cell and thus changes the π-mode frequency of the structure, and (3) it affects the relative amplitudes of the fields in adjacent cells (i.e. the *field balance*). Consequently, simultaneously optimizing the coupling ($\beta_c = 1$), and maintaining both the field balance and the correct π-mode frequency in the simulation requires a series of iterations over the size of the coupling iris and the radii (b_1, b_2, ..., b_5) of the cells.

If only the diameter of the center cell (cell 5) is reduced in order to compensate for the lowering of the resonant π-mode frequency produced by the introduction of the coupling iris, there is a marked fall-off in the field strength progressing

Table 4.4: Cavity and coupling iris dimensions for the field-balanced driven modal simulation.

Dimension	Value	Units
b_1	18.4774	mm
b_2	18.25	mm
b_3	18.3462	mm
b_4	18.25	mm
b_5	18.25	mm
a	5	mm
t	3	mm
d	15.62	mm
L_p	15	mm
w	2.54	mm
l	4.22	mm
db	1.283	mm
r	0	mm

from the central cell out towards the end-cells. In order to create a more uniform field balance, the impedances of the cells must be gradually increased as one progresses from cell 5 towards cell 1 (and likewise from cell 5 towards cell 9). This may be accomplished by increasing the cell diameters in a tapered fashion from the central cell outward. However, in order to simplify the design process, the radii of all cells were reduced (with the same values) and then the radii of cells 1 and 3 were varied to balance out the fields. This process was iterated many times with small adjustments in the width of the coupling iris l to eventually produce the values shown in Table 4.4.

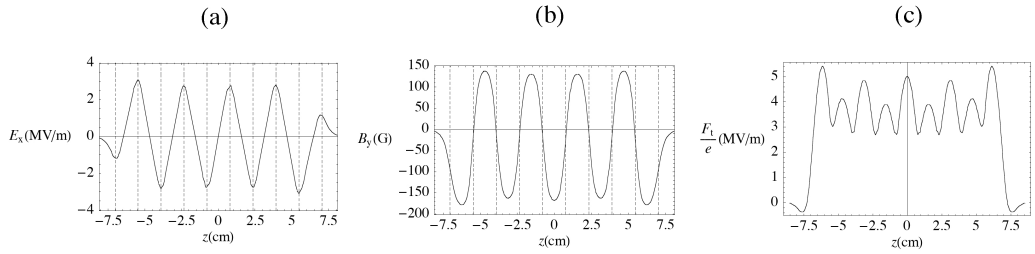

Figure 4.10: Plots of axial (a) electric field, (b) magnetic field, and (c) field gradient as functions of position along the cavity axis.

The simulated transverse electric and magnetic field components along the axis of the structure, corresponding with the cavity and iris dimensions of Table 4.4 and an input power of 50 kW, are shown in Fig. 4.10(a) and (b) respectively. Note that the on-axis fields $E_x(z)$ and $B_y(z)$ in these plots are out of phase by $\pi/2$. Thus, the transverse force experienced by an electron traveling along the axis of the structure is given by

$$F_t = \mathrm{Re}\left\{[E_x(z)e^{-i\pi/2} - vB_y(z)]e^{-i\omega z/c}\right\}. \tag{4.70}$$

This force is plotted in Fig. 4.10(c). Note that because of the $\pi/2$ phase difference between the electric and magnetic fields the electric fields in the iris actually contribute to the transverse deflection. Integrating under the curve in Fig. 4.10(c) gives us the simulated transverse deflecting voltage. The resulting value of V_0, as well as the simulated coupling β_c, π-mode frequency, and total shunt impedance are shown in Table 4.5. Note that the corner radius of the coupling iris slot in these studies was taken to be zero. The case of a nonzero corner radius is considered in the next section.

Table 4.5: Simulated cavity parameters for optimimized cavity and coupling iris dimensions.

Parameter	Value	Units
P_{in}	50	kW
V_0	528	kV
$\tilde{R}_{tot}$	5.6	MΩ
β_c	1.028	
Q_0	13710	
f_π	9.5977	GHz

4.5.4 Polarization Holes and Coupling Iris Corner Radius

In principle, the presence of the central coupler breaks the azimuthal symmetry of the cavity and thereby creates a preferred polarization of the deflecting fields (the direction of the deflecting force being along the transverse symmetry line of the coupler). However, the presence of small asymmetrical machining errors in the construction of the cavity can cause a rotation of the polarization vector from cell-to-cell. Such a rotation would cause the direction of the transverse deflecting force seen by the beam to change as it travels through the cavity, thereby producing a distortion of the streaked image on the downstream profile monitor.

One solution to this problem is to try to eliminate any asymmetric machining errors, guided by measurements made using a pair of sampling couplers built into the cavity, each of which couples only to one polarization mode or the other. Another possibility is to introduce into the structure an intentional asymmetric feature which couples strongly to the undesired polarization mode but not to the

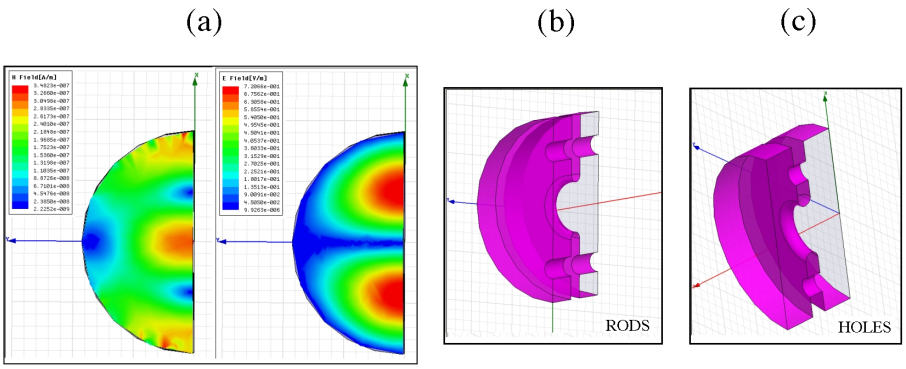

Figure 4.11: Plots (a) electric and magnetic field magnitudes in the transverse center plane of a cell, (b) the rod geometry at a junction between cells, and (c) the hole geometry.

desired one. The resonant frequency of the undesired mode is thereby shifted so that it is no longer excited by the driving RF. Commonly employed techniques for this include the introduction of carefully placed rods, holes, or grooves into the interior of the structure, in locations where the resulting perturbation of the conducting boundary is strongly coupled to the fields of the undesired polarization mode, but not to the desired one.

For the present case, we studied the use of both rods and holes, symmetrically placed on either side of the irises between adjacent cells at a distance R_p from the axis and having radius r_p. The HFSS model geometries for a single monocell with holes and rods respectively are depicted in Fig. 4.11(b) and (c). The placement of the holes and rods as shown in Fig. 4.11 corresponds to a perturbation of the undesired mode. This is seen by observing the field intensity plots in part (a) of Fig. 4.11, which shows that the depicted hole/rod positions are close to magnetic field maxima, and therefore their presence will strongly perturb the monocell frequency. Rotating the the azimuthal positions of the holes or rods by 90 degrees about the z-axis would place them on a magnetic field null, where the

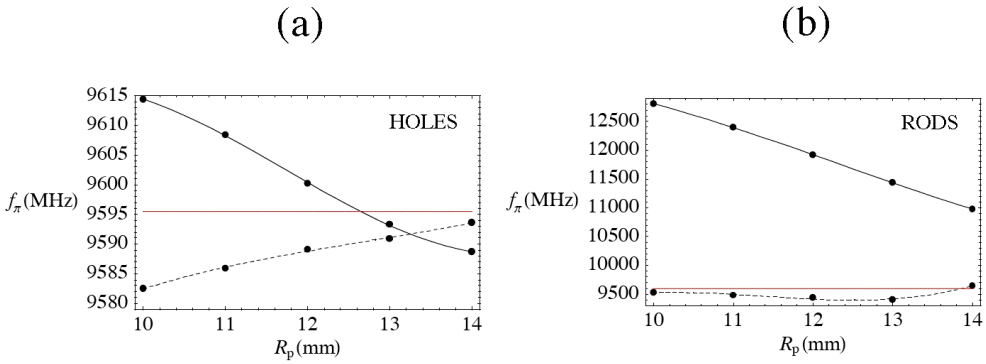

Figure 4.12: Plots of resonant pi-mode frequency for a pair of (a) holes and (b) rods of radius 2 mm, as a function of radial position. The curves are polynomial fits, with the dashed curves representing the desired polarization mode, and the solid curves the undesired mode.

frequency perturbation would be less. This scenario would then represent the effect of the holes or rods on the *desired* polarization mode.

The π-mode frequencies for the two polarizations were simulated in this manner using the eigenmode solver for both holes and rods of a fixed diameter of r_p = 2 mm, as the radial position R_p was varied from 10 to 14 mm. The results are shown in Fig. 4.12 for (a) holes and (b) rods. From these plots we can see that the perturbative effect of the rods on the monocell frequency is greater than that of the holes by 2 orders of magnitude (i.e. on the order of hundreds of MHz as opposed to a few MHz).

For a standing wave cavity with discrete resonances, it is sufficient to separate the two polarization mode frequencies by an amount that is on the order of the width of the resonance, or about 1 MHz. The holes are therefore adequate for our purposes as well as being less difficult to manufacture than the rods. From Fig. 4.12(a) we see that the desired mode (dashed curve) is less strongly perturbed as the holes become more distant from the center of the structure. Hence, we

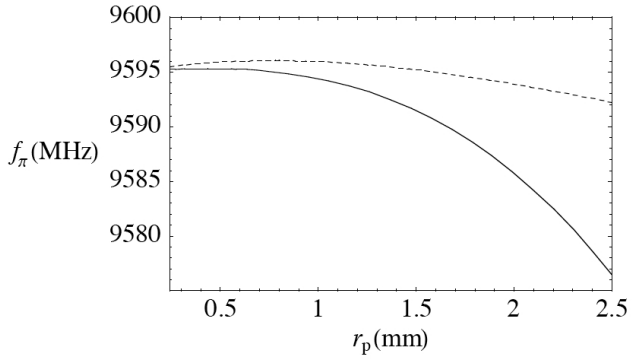

Figure 4.13: Plots of resonant pi-mode frequency for a pair of holes located a distance 14 mm from the axis as a function of hole radius. The dashed (solid) curve is for the desired (undesired) polarization mode.

choose the outermost position (R_p = 14 mm) and examine variations in mode frequency as the hole diameter r_p is varied. The resulting eigenmode simulation results are shown in Fig. 4.13.

Note that the curves in Fig. 4.13 are interpolations of the simulation data. For a pair of 2 mm diameter holes (i.e. $r_p = 1$ mm) the simulated mode separation is 0.94 MHz, which is the approximate width of the π-mode resonance. We therefore chose this as the design value for the polarization separation holes. Note that the simulations which produced the plots in Figs. 4.12 and 4.13 were conducted for a single monocell using the eigenvalue solver.

The polarization holes as well as the effect of nonzero corner radii on the coupling iris were then incorporated into the full 3D model using the driven modal solver with an excitation on the input waveguide port. The iris corners were given nonzero radii because it was decided that sharp corners on the input coupler should be avoided to prevent electrical breakdown in the actual cavity, and because it would simplify the process of tuning the input coupling of the

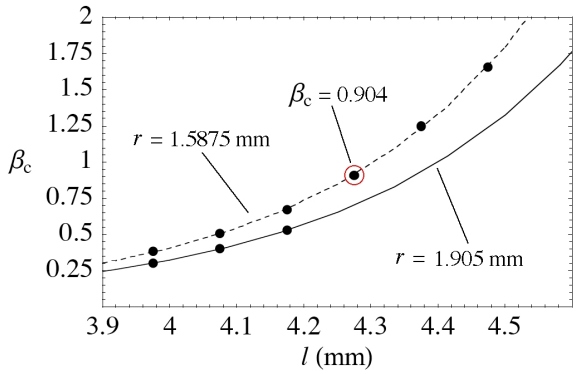

Figure 4.14: Plots of simulated coupling beta for two different coupling iris radii vs the half-width of the coupler.

cavity. Simulations were conducted for two different corner radius values r = 0.075" = 1.905 mm and r = 0.0625" = 1.5875 mm as the half-width l of the iris was varied. The simulated coupling beta values are shown in Fig.4.14. The point corresponding to the final design model is marked by a circle, corresponding to r = 1.5875 mm and l = 4.2754 mm. The simulated resonant frequency for these dimensions was found to be 9.6006 GHz. The cavity was intentionally undercoupled by design, because the tolerances specified on the machining of the cavity cell diameters was always set to negative values so that their frequencies would come out slightly high (by a few MHz). This way, the final frequency tuning could be accomplished by raising and regulating the temperature of the cavity. However, the increase in cavity temperature would also increase the coupling beta by a few percent. Thus the nominal beta value was set by design to slightly less than unity.

4.6 Hardware and Construction

The UCLA Neptune deflecting cavity was constructed with the goal of providing a robust, functional diagnostic for the Neptune laboratory which could be easily moved to other locations (either on the Neptune beamline or elsewhere) and which would be simple to tune, assemble, and install. The goals of simplicity of installation and transportation are aided by the choice of a high frequency (and hence small wavelength) compact portable power source. In the following sections we outline the layout of the RF system used to drive the cavity, its mechanical construction, and the experimental results of its testing and tuning.

4.6.1 RF Power and Hardware Layout

The ultimate source of the RF for all of the cavities on the UCLA Neptune beamline (gun, linac, deflector) is a 38.08 MHz signal generated by the crystal oscillator in the mode-locker driver for the Nd:YAG photocathode drive laser (model Antares 76-S by Coherent). Phase-locked dielectric resonating oscillators (PLDRO's) are used to frequency multiply this base signal by 75 and 252 to generate the 2.856 GHz and 9.59616 GHz low-level reference signals that ultimately drive the gun/linac and deflecting cavities respectively. The layout of the RF system is shown as a block diagram in Fig. 4.15.

The output of the drive laser is modulated at twice the 38.08 MHz oscillator frequency, producing a 76.16 MHz pulse train of 1064 nm infrared laser light. Every 1/5 second, one of these pulses is selected by a regenerative amplifier to be amplified (by 10^6) and upshifted twice in frequency, eventually producing a 75 μJ pulse of (266 nm) UV energy that is used to drive the photocathode. The laser pulse train (and hence the photoinjector beam) phase is maintained relative

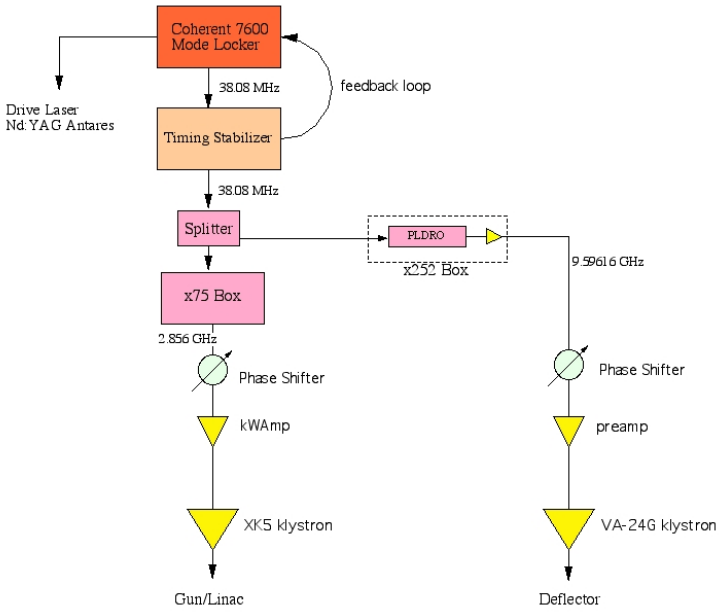

Figure 4.15: Block diagram of the RF system layout for the UCLA Neptune photoinjector, linac, and deflecting cavity.

to the mode-locker RF by a timing stabilizer box. The timing stabilizer monitors the laser output signal from a photodiode and then creates a feedback loop which matches the zero-crossing of the RF reference to the measured zero-crossing of the laser pulse train. The resultant timing stability is on the order of 1 ps.

Since the low-level RF signals for the various cavities are harmonics of the base frequency of 38.08 MHz, they are phase-locked with respect to the laser oscillator and therefore with respect to the electron beam. The low-level 9.59616 GHz RF signal produced by the PLDRO (and phase-locked to the 38.08 MHz reference) is then transported on low-loss Heliax coaxial RF cable to a phase shifter and attenuator (which can be manipulated in the control room) and then to a 28 dB preamplifier which can provide up to 500 mW for the input of a VA-24G klystron. The klystron unit is a turn-key rebuilt military device provided by Radio Research Instruments. It has a built-in high-voltage power supply and

pulse-forming network and contains all the necessary electronics to produce up to a 50 kW (peak power) output pulse of 1 μm duration which is synched to an externally provided trigger pulse. The klystron can be operated at repetition rates up to 1 kHz.

The 50 kW pulse from the VA-24G klystron is transported to the input coupler of the deflecting cavity by a system of WR-90 waveguide. The output waveguide port of the klystron is attached to an isolator made by Wenteq Corporation, which acts like an RF "diode" to allow the flow of RF power only in the forward direction and thereby prevent any reflected power from damaging the klystron. The trigger pulse for the klystron is derived from the same chain of timing boxes that is used to trigger the high-power RF system for the gun and linac. Hence, both the timing of the 1 μm pulse and the phase of the 9.59616 GHz RF power it carries are synchronized with the gun/linac RF system and with the electron beam itself.

4.6.2 The Mechanical Design

The final cavity design incorporates a knife-edge vacuum seal machined directly into the mating faces of the cells. The knife-edge seal can accommodate either a copper gasket or Viton o-ring. This design allows the cavity to be easily disassembled, and negates the need for brazing, welding, or diffusion bonding of the structure, which could warp and detune the cells. This design feature is unusual, but is made feasible in this case by the low peak power required (50 kW) and by the less-than-stringent vacuum tolerances (on the order of 10^{-6} torr). A computer-aided design (CAD) drawing of the structure is shown in Fig. 4.16. A quarter of the structure is cut away to show the interior.

The cells and their interior cavities were machined on a lathe in the UCLA

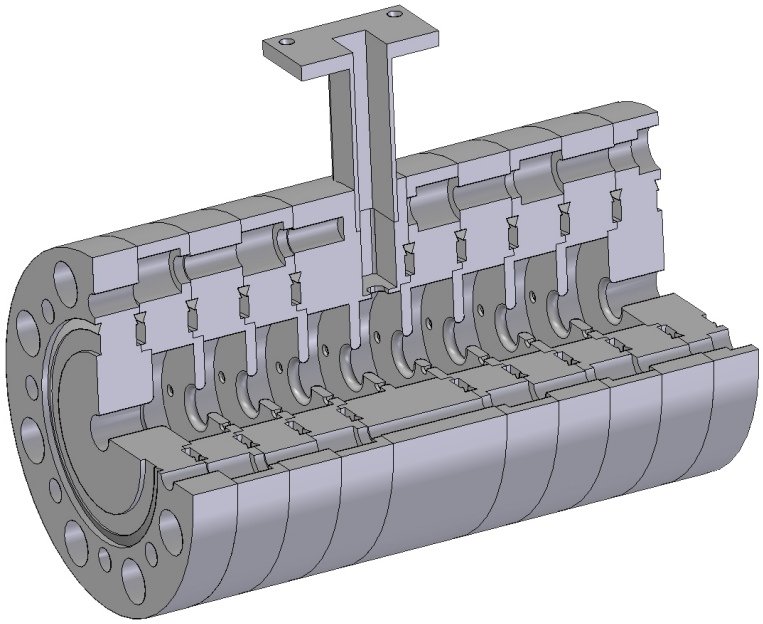

Figure 4.16: CAD drawing of the Neptune deflector with 1/4 section cutaway.

Physics Department machine shop. Tolerances on the inner cell diameters was met to within approximately 0.0002" of the design values. A rectangular slot in the top of the center cell and the polarization mode-splitting holes were machined using electric discharge machining (EDM) by WireCut Co. of Los Angeles. A custom-made waveguide section (shown at top in the figure) was constructed using wire-EDM at the UCLA Department of Electrical Engineering machine shop. This waveguide piece was brazed into the rectangular slot on the center cell by a local brazing company. This was the only permanent bonding that was performed on the structure.

Since the knife-edge seal design is an experimental and untested method of assembling a high-power RF cavity, the structure shown in Fig. 4.16 was designed in such a way that all of its parts could (in principle) be brazed or diffusion bonded together in the event that the vacuum-seal design resulted in deleterious effects

such as extensive RF breakdown. As we will see, no such deleterious effects were observed and therefore no permanent bonding of the cavity was attempted. The material for the structure was chosen to be GlidCop AL-15, an industrial material which has the electrical properties of copper but a tensile strength near that of stainless steel. It consists of copper suspended in a matrix of aluminum oxide. This material was chosen so that copper gaskets could (in principle) be used to join the cells, and because it was hoped that the higher tensile strength would help prevent deformation of the structure in the event that it needed to be permanently bonded.

4.6.3 Field Flatness and Resonant Frequency Measurements

The electromagnetic properties of the deflecting cavity were tested using a network analyzer (model HP 8719D) which is essentially a frequency sweeper that can measure the forward, reflected, and transmitted amplitude and phase of the RF wave on one or two ports, and can thereby calculate the complex transmittances and reflectances between the ports of a passive RF device. In Fig. 4.17(a) the square magnitude of the complex reflectance Γ (also known in transmission matrix theory as the S_{11}) at the input coupling port of the deflecting cavity is plotted in decibels over the full frequency range of the passband of the structure, showing all five of the resonances. As predicted by the simulation results of Section 4.5.2, the π-mode corresponds to the first resonance, which occurs at the lowest eigenfrequency. A closeup of the resonance for this mode is shown in part (b). In part (c) the complex reflectance values corresponding to the frequency range of part (b) are transposed onto the complex plane. This type of plot is known in microwave circuit theory as a *Smith Chart*. The circle traced by the resonance in this plot measures the impedance matching of the structure and

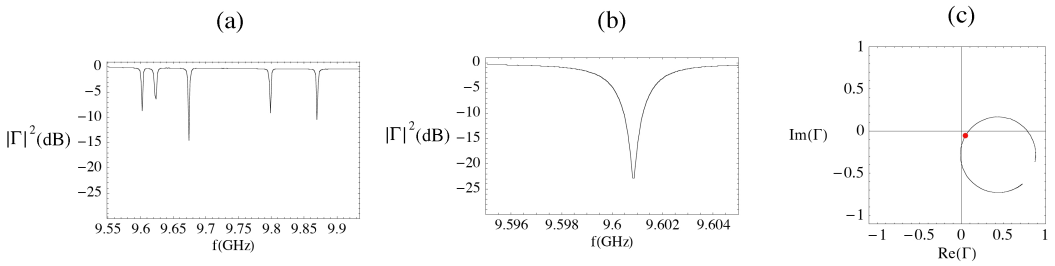

Figure 4.17: Plots of reflectance at the input coupler showing (a) all five modes of the passband, (b) a closeup of the π mode, and (c) the reflectance plot in the complex plane (i.e. Smith Chart) for the π mode.

thereby provides an indication of the efficiency of the coupling. Since the radius of the circle is less than unity, we deduce that the structure is *undercoupled* in the sense defined by Eq. (4.44).

In Table 4.6 we list the various cavity parameters extracted from the resonance plot of the π-mode shown in Fig. 4.17(b) and (c), including the resonant frequency and the full-width at half-max (FWHM) of the resonance. Since the cavity is slightly undercoupled (as it was intended to be, pursuant to the discussion of Section 4.5.4) the coupling beta is inversely related to the VSWR. The resonant, loaded, and external quality factors as defined in Section 4.3.3 are also listed.

To measure the field balance of the structure, a *bead pull* was performed. This is a technique whereby a metallic or dielectric bead, whose dimensions are small compared to the RF wavelength, is suspended on a wire and then pulled along the axis of the cavity. The presence of the bead at a given location z along the axis of the structure produces a perturbation Δf of the resonant frequency given by Slater's theorem: $\Delta f/f = (\alpha_m|H|^2 - \alpha_e|E|^2)/W_0$, where f is the unperturbed frequency, W_0 is the stored energy in the unperturbed cavity, H and E are the magnetic and electric fields at the location of the bead (in the unperturbed

Table 4.6: Measured parameters of the π resonance in air at room temperature.

Parameter	Value	Units
f_π	9.60084	GHz
FWHM	1.51	MHz
VSWR	1.15	
β_c	0.870	
Q_0	11889	
Q_L	6359	
Q_e	13672	

cavity), and α_m, α_e are factors which depend upon the geometry and material properties of the bead.

Consequently, a measurement of Δf as a function of longitudinal position produces a plot which is a sum of the square amplitudes of the axial electric and magnetic fields, as shown in Fig. 4.18(a). Note that due to the minus sign between terms in the Slater equation and the fact that the magnetic field is a maximum in the cell centers and the electric field is maximum at the irises, the resulting plot oscillates between positive and negative peaks. The positive-going peaks corresponds to maxima in $|H|^2$ and the negative-going peaks correspond to maxima in $|E|^2$. To obtain a plot that represents the field amplitudes (rather than their squares) we take the positive square root for positive values and the negative square root of the magnitude of the negative values, producing the result in Fig. 4.18(b). Now the positive-going peaks are proportional to $|H|$ and the negative-going peaks are proportional to $|E|$ at the given axial locations. We see that the resultant field balance is good to within 10%.

The plots in Figs. 4.17 and 4.18 and the corresponding parameter values in

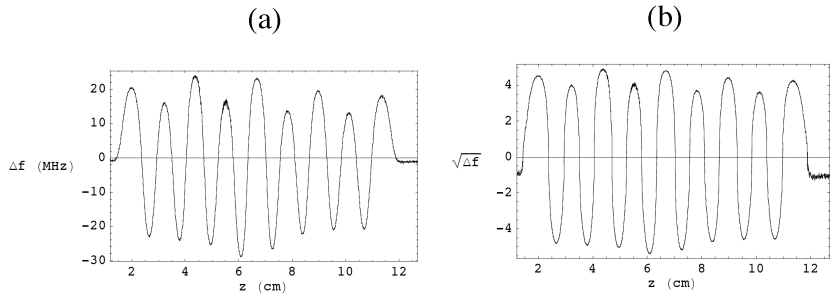

Figure 4.18: Aluminum bead pull results showing (a) frequency shift and (b) the square root of the frequency shift vs. position along the cavity axis.

Table 4.6 were taken in air at room temperature. The frequency and coupling were then measured as the temperature of the cavity was increased. Cavity temperature was regulated using a heater tape with a temperature controller. The controller was connected to a thermocouple measuring the cavity temperature and was set to regulate the current in the heater tape in order to stabilize the cavity at a preset temperature value. The feedback mechanism for this temperature control was PID (proportional, integral, derivative) with the PID parameters set automatically by the controller's "autotune" feature. The cavity with heater tape and thermocouple attached was then wrapped in several layers of aluminum foil to help thermally isolate the cavity from the environment and thereby permit it to reach thermal equilibrium more quickly. The resonant frequency of the cavity π-mode is plotted as a function of the thermocouple temperature reading in Fig. 4.19(a) for both in-air (red line) and in-vacuum (blue line) operation of the cavity. For the vacuum measurements the cavity was evacuated on a test-stand to a pressure of 1.8×10^{-6} torr using a turbo-molecular pump. The vertical offset of approximately 2 MHz between the red and blue curves is consistent with a simple estimate obtained by noting that the monocell resonant frequency varies

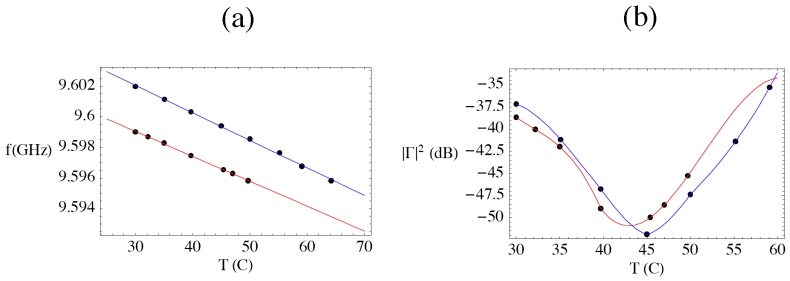

Figure 4.19: Plots of (a) resonant frequency and (b) reflectance as functions of cavity temperature in air (red curves) and in vacuum (blue curves).

with dielectric contant as $1/\sqrt{\epsilon}$. Substituting the value for air ($\epsilon = 1.00059$) gives a shift of 0.3 % or 2.8 MHz for air vs. vacuum.

The plot in Fig. 4.19 (b) shows the corresponding reflectance values (in dB) for both air and vacuum. The curves shown are interpolations of the data points. They are not intended as a theoretical fit to the data, but merely as an aid in visualization. From the linear fit to the vacuum plot in part (a) we find that the resonant frequency matches the design value of 9.59616 GHz at a temperature of 65 C. We see from the plots in part (b) that the cavity passes through the optimal coupling point at a temperature near 45 C. After this point, it becomes slightly overcoupled. Consequently, at the projected resonant temperature of 65 C we find that the reflectance value is -35 dB which corresponds to a coupling of $\beta_c = 1.036$.

After installing the deflecting cavity on the UCLA Neptune beamline, high-power testing was performed to verify that it was operating normally and would accept high-power RF without experiencing significant breakdown. The forward and reflected power levels were measured on a 49 dB cross-waveguide coupler located just before the input waveguide flange of the cavity, using a calibrated

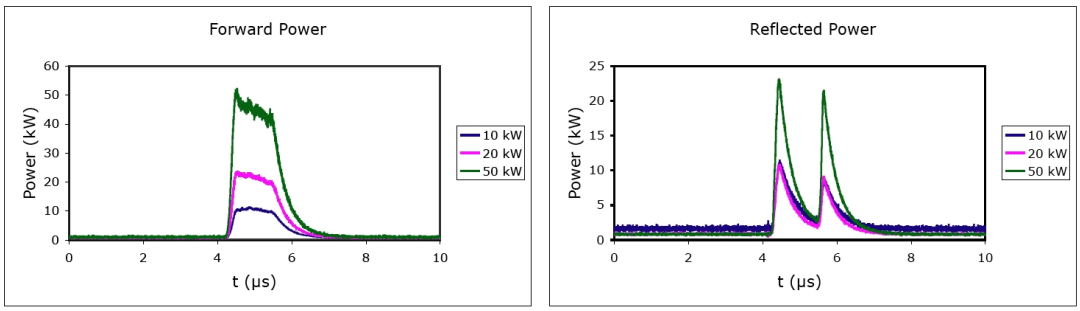

Figure 4.20: Plots of deflecting cavity forward and reverse power vs time at several different output levels of the klystron.

crystal detector. The waveforms on the forward and reverse couplers were observed on an oscilloscope terminated at 1 MΩ. The captured oscilloscope traces are reproduced in Fig. 4.20. The vertical scales have been converted into units of kilowatts using the measured calibrations of the forward and reverse couplers and the crystal detector. Traces are shown for three different settings of the input attenuation on the X-band klystron. The sharp spikes in the reflected power trace are typical of a resonant standing wave structure. The first spike is an initial reflection due to the nonzero fill time of the cavity, and the second represents the exponential leakage of stored power in the cavity through the coupler following the sudden termination of the drive pulse.

The maximum peak power output of the klystron was found to be approximately 50 kW, which is consistent with the nominal output power quoted by the vendor. One of the primary concerns in any high-power test of a metallic cavity is electrical breakdown due to the strong electromagnetic fields in the structure. The electrical plasma discharge characteristic of a breakdown event causes all of the input power to be reflected after the point in time when the breakdown occurs, resulting in an obvious distortion of the reflected power trace. During the high-power testing (and subsequent operation) of the deflecting cavity no

breakdown events were observed even at the highest achievable power levels.

CHAPTER 5

Experiment and Results

5.1 The Neptune Laboratory

The UCLA Neptune Laboratory is a state-of-the-art facility devoted to the study of the dynamics of and the interactions between relativistic electron beams, high-power lasers, and plasmas. The lab is jointly operated by the Laser-Plasma Group, under the direction of Professor Chan Joshi of the UCLA Department of Electrical Engineering, and the Particle Beam Physics Laboratory (PBPL), headed by Professors James Rosenzweig and Claudio Pellegrini of the UCLA Department of Physics and Astronomy. The two primary systems which comprise the lab are a high-power CO_2 laser system and a photoinjector beamline. The CO_2 laser is designed to generate up to 600 GW of peak laser power in a 200 ps pulse, thereby delivering as much as 120 Joules of directed laser energy to an experimental target. The photoinjector produces a low-emittance (4 mm mrad) beam of electrons at energies up to 14.5 MeV. In the present section we describe the layout of the accelerator and the details of its various subsystems. In the sections which follow, we describe the specific layout of the ramped electron bunch experiment and the experimental results obtained from it.

5.1.1 Beamline

The RF gun at Neptune is a product of the BNL-SLAC-UCLA collaboration on high-brightness beam development and is similar to guns that have been operated at BNL and SLAC. It is a 1.625 cell π-mode standing wave cavity, cell-to-cell on-axis coupled. The nominal on-axis peak field is 100 MV/m, although it is possible to obtain 115 MV/m with the available power; the central launch phase of the laser beam is 30 degrees (where 90 degrees corresponds to maximum field). The nominal energy of the beam at gun exit is 4.6 MeV; in practice, energies from 3.5 to 5 MeV have been obtained. The gun is coupled to the waveguide in the full cell only, with a symmetrizing port located opposite the coupling slot to cancel dipole components of the field which can lead to emittance growth. Several different cathode types have been employed. Initially, the cathode was a disk of solid copper, and subsequently a single copper crystal was embedded in the cathode center; currently, a magnesium cathode is in use, which has raised quantum efficiencies by a factor of 2 to 3. Emittance compensation during injection is accomplished by a yoked magnetic solenoid mounted around the gun exit port. Measured normalized beam emittances have ranged from 4 to 10 mm mrad, with nominal value near 5 mm mrad.

The linac is a 7+2/2 cell π-mode standing wave structure and the first fully operational version of a plane-wave transformer (PWT). Under normal operating conditions, roughly 9 MeV of acceleration is produced in the linac (45 MV/m peak field), but more acceleration is possible. The design of this novel device is discussed in Ref. [71] and summarized here. The structure is similar to a disc-loaded linac, except that the outer wall is moved to a large radius, leaving a gap between the disks and the wall. This gap serves as a coaxial, plane-wave transmission line, which provides extremely strong cell-to-cell coupling and

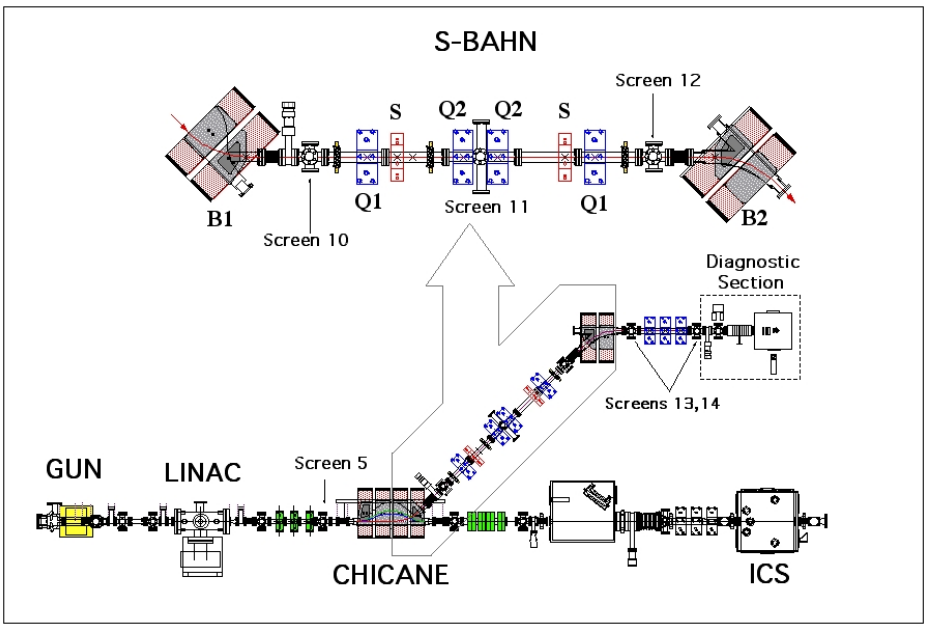

Figure 5.1: Schematic of the Neptune beamline and the S-Bahn dogleg compressor.

excellent mode separation. In the absence of support rods (which are needed to hold the disks in place), this structure also has a very high shunt impedance R_s and high unloaded Q, with the ratio R_s/Q approximately the same as a more standard structure. The introduction of the four support (and water-cooling) rods into the cavity causes enhanced RF power losses, and R_s is actually smaller in this case than that found in a standard structure. Even so, Q is enhanced, and the PWT has a long fill time. Both the gun and PWT are approximately critically coupled, and the PWT barely fills during the 3.5 μs RF pulse.

The PWT was designed at UCLA and built in the Physics Deptartment machine shop. Engineering issues to be solved included effective internal cooling, incorporating all-metal sealing surfaces, and optimization of the iris apertures to reduce the maximum surface gradient. The continued successful operation of the PWT, despite its unusual mode and frequency spectrum, demonstrates its

usefulness as an RF linac.

5.1.2 RF System

The RF system at Neptune operates at the SLAC frequency of 2.856 GHz and relies on standard S-band technology. Synchronization with the drive laser is ensured by using the laser modelocker output (at 38.08 MHz) as the RF clock, after frequency multiplication by 75. About one watt of continuous low-level RF is delivered to a pulsed ($<$12 μs) solid state amplifier, which in turn drives the input of the XK-5 klystron. The klystron is pulsed using a custom modulator with pulse length variable between 3.5 and 7 usec, achievable by varying the number of capacitors in the modulator circuit. For normal (short-pulse) operation, a PFN composed of 10 capacitors is charged to 41 kV and discharged using a thyratron switch into the klystron pulse transformer, where the pulse is voltage-multiplied by 12.

Up to 20 MW of output power is supplied by the klystron and delivered to the beamline through a waveguide system pressurized to 28 psi with sulfur hexafluoride. Power is divided in a 2:1 ratio between the linac and gun, with typical values of 4-5 MW in the gun and 10-12 MW in the linac. Both gun and linac are equipped with high-power variable attenuators, and there is also a phase shifter on the linac input waveguide, which allows the operation of the linac at any desired phase relative to the gun. The injection phase of the drive laser at the gun can also be varied with a phase shifter on the low-level RF line.

Forward and reflected power levels in the system are measured using directional couplers in different portions of the waveguide and calibrated crystal detectors. RF power values can be calculated from oscilloscope traces of the crystal detector voltages and displayed automatically in the control room.

5.1.3 Photoinjector Drive Laser

The photocathode drive laser illuminates the gun cathode with a pulse of ultraviolet (266 nm) light having a minimum temporal length of about 1 psec (FWHM), at an energy up to 100 microjoule/pulse. This is accomplished using chirped pulse amplification and compression of a 1.064 μm pulsed mode-locked Nd:YAG laser (using the 38.08 MHz master RF signal) amplified by a Nd:glass regenerative amplifier (regen) at 5 Hz. To amplify the pulse in the regen the laser is first matched into a 500 m long optical fiber to produce pulse lengthening and a frequency chirp. The chirped pulse is then amplified by a factor of 1 million in the regen and sent to a grating pair where it is compressed by removing the chirp correlation. The pulse length can be arbitrarily lengthened by detuning the grating compressor, allowing a choice of pulse lengths for emittance optimization. The resulting picosecond pulse is frequency up-converted using two stages of BBO doubling crystals. The conversion efficiency is typically 10%. Because of the many nonlinear stages in this laser configuration the pulse-to-pulse fluctuation amplitude is at best 10% RMS. There are also pulse length fluctuations associated with these effects, but they are not of great consequence operationally. The time of arrival of the laser with respect to the RF wave is controlled by a phase-shifters (manual and electronic) in the low level 2.856 GHz RF system. The fluctuations in the arrival time of the laser pulse on the cathode with respect to this RF signal are suppressed by use of a Lightwave electronics feedback system on the oscillator. The fluctuations have been measured to be below one picosecond.

5.1.4 Video and Trigger System

Along the beamline there is a system of CCD cameras for imaging the beam on various insertable profile monitors. The cameras are all *gen-locked* to a master video signal which originates from a master camera located in the control room, and is then repeatedly amplified by a series of distribution amplifiers, which provide gen-lock reference signals for the cameras. This ensures that the video signals from all of the cameras are synchronized. The video signal from the master camera is also the source of the 5 Hz master trigger for the regenerative amplifier and high-power RF systems. This 5 Hz trigger is derived from the 60 Hz sync pulse of the master video signal, which is extracted by a video sync box and is then used as the reference for a Stanford Research Systems delay generator, which outputs a 5 Hz pulse train to trigger the lamps and Pockel's cells of the regenerative amplifier.

A homemade box located in the control room reduces the repetition rate of the master trigger from 5 Hz to 1 Hz. The output of this box is the trigger source for the S-Band and X-Band klystrons as well as the freeze-frame which is used to capture images from the cameras. Therefore, although the rep rate of the drive laser is fixed at 5 Hz, that of the high-power RF system can be set to either 5 Hz or 1 Hz, depending upon whether the homemade box is turned on or off. Under most conditions the RF system is triggered at 1 Hz repetition, as this is sufficient for most experimental efforts and it gives the beam operator sufficient time to interrupt the trigger to the high-power RF in the event of a series of breakdown events.

5.1.5 Control System

The photoinjector is operated through a mixture of computer and manual controls. Beamline magnet and actuator control, data acquisition, and video manipulation are accomplished using LabView 5.1 running on a Macintosh G4 computer. Magnets and actuators are switched and controlled via CAMAC modules, with readback of signals and diagnostics primarily through digitizing oscilloscopes which communicate via GPIB with the control computer. Sixteen channels of video are switched in the control room and may be digitized via a frame grabber for online, shot-by-shot analysis of beam spots or emittance slits. RF power levels are monitored on various oscilloscopes in the control room, and the RF phases of the gun, linac, and deflecting cavity are controlled by manual phase shifters. The beam charge and the UV drive laser energy are read automatically on every shot and their values are updated on the computer control display.

5.2 Preliminary Diagnostic Measurements

5.2.1 Horizontal Dispersion Measurements

Prior to the construction and installation of the deflecting cavity, measurements were done of the beam sizes at various locations along the beamline in order to benchmark them against the simulation results. Since these measurements were done at low charge, they are suitable for approximate comparison with ELEGANT which does not include space-charge effects. Recall that the various conditions on the optics of the S-Bahn compressor discussed in Section 3.2.3 constrain the allowed transverse Twiss parameters and emittance of the beam entering the dogleg section. In particular, the normalized emittance should be less than about 10 mm mrad, the beta function should be relatively large (at

Table 5.1: Beam Parameters

Parameter	Measured Value	Location
Q	35.4±3.8 pC	Faraday Cup
U	11.5 MeV	Screen 10
σ_δ	<0.5%	Screen 10
α_x	-0.94±0.43	Prefocus Quads
β_x	0.77±0.43 m	Prefocus Quads
ϵ_N	6.03±1.8 mm mrad	Prefocus Quads

least 1 meter) and the beam should be highly convergent at the entrance to the first dipole.

However, technical and spatial constraints required that the photoinjector and upstream optics be operated in a mode with somewhat smaller beta functions and a larger emittance. It was observed that when the beamline is operated in accordance with the emittance compensation scheme described in Section 1.2.4, the beam which it produces tends to be transversely small and well-collimated (i.e. $\beta_{x,y} < 1$ m and $\alpha_{x,y} \approx 0$). In order to increase the beta functions and make the beam more convergent, the photoinjector was operated in a somewhat non-optimal regime (from the perspective of emittance compensation) by increasing the solenoid field by about 20% above the value corresponding to minimum emittance, and moving the first set of quadrupole magnets shown in Fig. 5.1 (dubbed the *prefocus quads*) as close to the first dipole magnet as spatial constraints would allow. The empirical values for the Twiss parameters and normalized emittance obtained from quadrupole scans are shown in Table 5.1.

Since these measurements were made prior to the installation of a diagnostic for measuring beam compression, the linac phase was set to minimize energy

spread rather than to produce a chirped beam. Previous measurements have indicated an energy spread of less than 0.5% under these operating conditions. A stable nondispersive operating point was determined empirically by observing the beam on the six profile monitors (Screens 5, 10, 11, 12, 13, and 14 in Fig. 5.1). The horizontal dispersion function η_x (or R_{16}) was minimized by observing the beam centroid position at the S-Bahn midpoint (Screen 11) under a variation of the fields of all magnetic elements on the dogleg (B1, B2, Q1, Q2) by a fractional offset ζ from the values corresponding to the desired operating configuration. For a beam of constant central energy, the resultant shift in the centroid position is the same as that which would be observed due to a change in the central momentum by a fractional amount $\delta = -\zeta$, and is therefore given by

$$\Delta x_{cen} = -R_{16}\zeta + T_{166}\zeta^2 + O(\zeta^3) \tag{5.1}$$

Consequently, the first- and second-order horizontal dispersion terms R_{16} and T_{166} can be obtained by fitting the measured centroid position data to a quadratic in ζ. The values of T_{166} at the exit of the S-Bahn (Screen 13) obtained by this method are shown in Table 5.2 for three different settings of the sextupole field strength. Simulation values from the transport code ELEGANT are provided for comparison. The geometrical field strength κ and ratio α correspond with the quantities in Eq. (3.25).

Experimental errors in Table 5.2 correspond to a 95% confidence level. Since the quadrupoles were set to eliminate the linear dispersion, R_{16} in all three cases was found to be zero to within the experimental error. Measurements of the RMS beam beam size on Screens 5, 10, 11, 12, 13, and 14 agree with the ELEGANT simulation results to within 20%.

Table 5.2: Comparison of experimental and simulated second-order dispersion values for various sextupole field settings

$\kappa(\mathrm{m}^{-3})$	α	$T_{166,\mathrm{exp}}(\mathrm{m})$	$T_{166,\mathrm{sim}}(\mathrm{m})$
0	0.00	2.56±0.59	2.54
537	-2.13	0.22±0.77	0.26
995	-1.55	-1.27±0.93	-1.69

5.2.2 Coherent Transition Radiation Interferometry Measurements

Since the horizontal dispersion does not provide a diagnostic of the longitudinal trace space, the measurements of Table 5.2 were performed using a beam with no momentum chirp and a relatively small (<0.5%) energy spread. To obtain information about the effect of the sextupoles on the longitudinal distribution of the beam, the beam was then chirped in momentum by injecting it with an RF phase offset of -28 degrees relative to the crest of the accelerating field in the standing wave linac cavity. The bunch length was then measured at different sextupole settings using coherent transition radiation (CTR) autocorrelation. Transition radiation emitted by the beam at a metal foil on Screen 14 of Fig. 5.1, oriented at 45 degrees incidence, was autocorrelated using a Martin-Puplett-type interferometer with wire grid polarizing beam splitters [72]. The bunch length σ_t was extracted from the interferograms using the time-domain fitting procedure of Ref. [73]. The extracted values are plotted in Fig. 5.2 as a function of sextupole strength κ. The ratio of the two sextupole fields was set to $\alpha = -1$. The data show the dependence of bunch length upon the magnitude of the sextupole correction, with an approximately twofold compression occuring near the field value $\kappa = 1094\ \mathrm{m}^{-3}$.

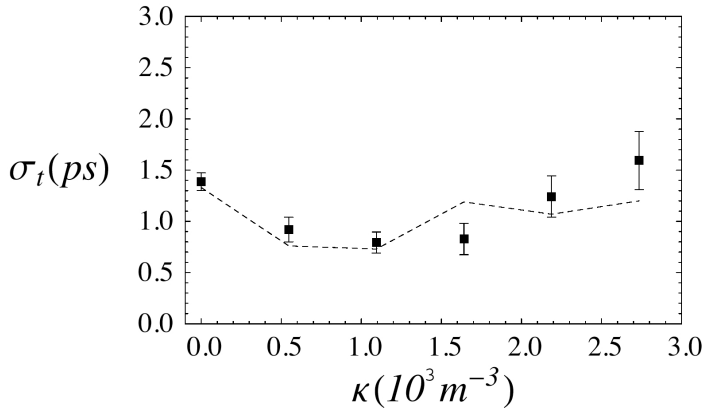

Figure 5.2: CTR autocorrelator measurements of electron bunch length as a function of sextupole field strength, with superimposed theoretical result (dashed line) obtained from PARMELA/ELEGANT simulation combined with an autocorrelation algorithm.

It should be noted that, due to both the limited frequency bandwidth of the autocorrelator apparatus and the nature of the fitting procedure used to extract the pulse length from the data (which assumes a Gaussian current profile), for a beam whose temporal profile is asymmetric, the value of σ_t obtained from the interferogram is more closely connected with the FWHM than with the RMS width of the distribution. Consequently, we have found that obtaining a theoretical prediction to complement the data of Fig. 5.2 involves a somewhat complicated computational procedure, the result of which is superimposed as a dashed curve.

To produce this theoretical curve, first the creation and transport of the beam in the accelerating sectio were simulated using the tracking code PARMELA. This detailed simulation employed 5000 macroparticles, whose initial temporal profile (inherited from the laser pulse) was modulated in a way consistent with observations of the energy modulation of the beam, and a -28 degree phase offset in the linac, producing a chirped beam. The set of output 6D trace space coordinates

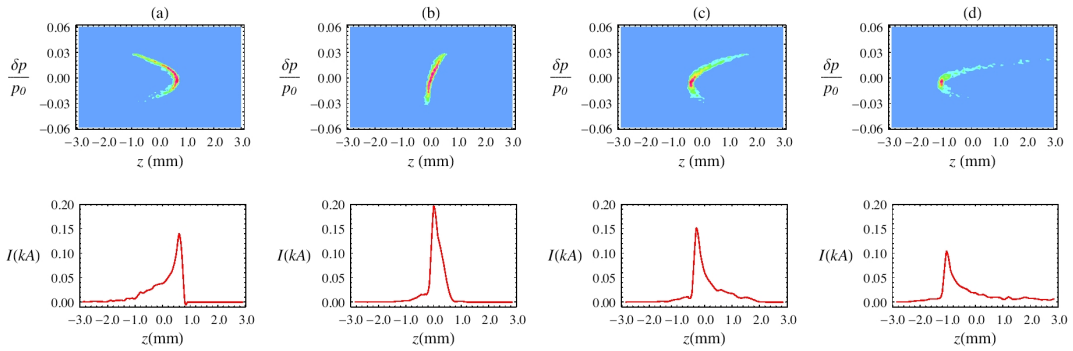

Figure 5.3: Longitudinal phase space plots and density profiles obtained from ELEGANT results corresponding to the sextupole settings of the (a) first, (b) third, (c) fourth, and (d) sixth data points in Fig. 5.2 respectively, illustrating the progression of the phase space compression and decompression.

obtained from PARMELA was then used as the input beam for an ELEGANT simulation of the dogleg section, including a truncation of outlying particles consistent with the observed 60% electron transmission efficiency through the device. The longitudinal (z) coordinates of the particles were extracted from the ELEGANT simulation at the location corresponding to Screen 14, where the CTR foil was inserted. An algorithm was used to reconstruct from the extracted z coordinates the predicted autocorrelation function, including appropriate filtering of the frequency content due to diffraction, collection, and transport efficiency effects.

The simulated autocorrelation function was then subjected to the same fitting procedure that was used to extract σ_t from the empirical interferograms, yielding values which produce the dashed curve in Fig. 5.2. These simulation results suggest that the observed compression and decompression results from a "folding over" of the longitudinal trace space due to the quadratic T_{566} dependence in Eq. (3.7), where particles of both high and low energy begin to occupy the

same longitudinal position within the bunch. This scenario is illustrated by the trace space plots in Fig. 5.3. The maximum compression [Fig. 5.3(b)] occurs at the sextupole field value where this folding over begins to change direction in z, corresponding to the point at which the second-order term T_{566} changes sign. The discrepancy between theory and data near the fourth data point in Fig. 5.2 appears to be due to the sensitivity of the theoretical autocorrelation algorithm to the sharp spikes in the temporal distribution displayed in Figs. 5.3(c) and 5.3(d).

Although the temporal RMS of the distribution is smaller in 5.3(c) than in 5.3(d), the spike is more pronounced in 5.3(c). That the physical data appears less sensitive to this effect may be related to the additional frequency filtering produced by the interferometer in the short wavelength components of the spectrum. These effects may arise from the poor high frequency performance of the wire grid beam splitters in the Martin-Puplett device. Of course, one cannot rule out the possibility that the beam performance is not completely consistent with the predictions of simulations.

These sorts of uncertainties highlight the limited utility of CTR interferometry in this context and point to the need for more sophisticated measurements of the longitudinal phase space. The diagnostic constructed for this purpose, as discussed in Chapter 4, was a 9-cell deflecting mode cavity driven at an X-band frequency of 9.59616 GHz. In the following section we present the results of measurements of the longitudinal profile in the Neptune experiment using this device.

5.3 Deflecing Cavity Longitudinal Profile Measurements

5.3.1 Experimental Setup

As was seen in Fig. 5.1, the dogleg section is followed by a triplet of quadrupole magnets (dubbed the *final focus quads*) which are used to help transport the emerging electron beam through the 1 cm aperture of the deflecting cavity and focus it on a profile monitor located 28 cm from the exit of the deflecting cavity. A cartoon diagram of the setup is shown in Fig. 5.4 for reference. The screen on which the final beam profile is imaged (Screen 15) consists of a 1"-diameter Cesium-doped yttrium-aluminum garnet (YAG) crystal, which is mounted perpendicular to the beam path and followed by a 45 degree mirror. This is the same basic configuration used for all of the profile monitors on the Neptune beamline except that a larger diameter crystal was used in this case, to provide an adequate aperture for the deflected (i.e. streaked) electron beam. A CCD camera was used to capture the reflected image of the beam profile from the back side of the YAG crystal.

The mount for the YAG crystal incorporates a built-in Faraday cup for measuring the final beam charge. The center of the Faraday cup is vertically displaced by 2 inches from the center of the YAG screen, as seen in Fig. 5.5. The entire mount is then attached to a pneumatic actuator with a 2" stroke, so that either the YAG or the Farday cup can be selectively inserted into the beam path.

Alignment of the beam through the deflector was accomplished by sending a red diode laser down the final section of beamline and marking its position on the two profile monitors along the way (Screens 13, 14 in Fig. 5.1). To check that the alignment laser trajectory was coincident with the axis of the deflecting cavity, the final pop-in screen was temporarily removed and the circular aperture of the

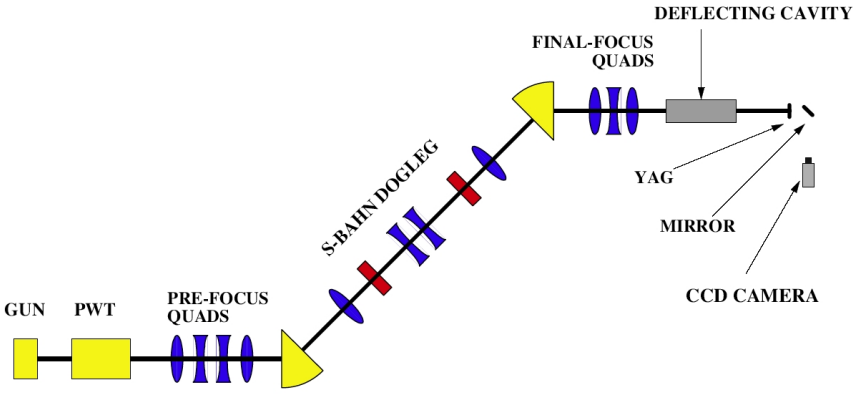

Figure 5.4: Block diagram of the experimental setup for the deflecting cavity measurements.

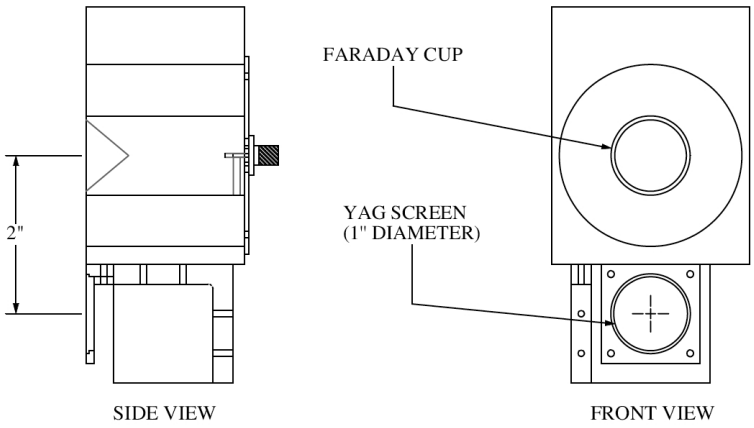

Figure 5.5: Schematic of the combined beam dump and YAG profile monitor built as a final diagnostic device.

deflecting cavity was traced onto a sheet of paper placed on the wall past the end of the beamline. In addition, the laser position was checked at two locations on the final vacuum chamber to verify that it coincided with the center of the beam pipe. Due to small variations in the actuator assemblies for Screens 13 and 14 (such as minor differences in the lengths of the custom-made extension pieces for the actuator arms and issues such as whether copper or viton o-rings were used) it was found that the centers of the YAG crystals deviated from the center of the beamline by as much as 2 to 3 mm. Thus, the vector trajectory of the electron beam was adjusted, using steering magnets and the trim coils on the final pair of dipole magnets, to coincide on these screens with the measured position of the alignment laser rather than with the geometrical centers of the screens.

5.3.2 Deflection vs. RF Phase

In order to verify the sinusoidal dependence of the deflecting field on RF phase and to provide a direct measure of the deflecting voltage of the cavity, the position of the beam centroid was measured as a function of RF phase at a fixed input power of approximately 10 kW as measured on the forward power coupler with a crystal detector. The resulting data are plotted in Fig. 5.6 alongside two captured images taken at different phase values. A sinusoidal function has been fitted to the data, indicating very good agreement. Note that the scale on the horizontal axis has been offset in order to match the zero-crossing of the sinusoidal fit, and the vertical axis has been offset so that the centroid position of the streak corresponding to the zero-phase point has a nominal vertical position of $y = 0$.

Recalling that the $y - z$ correlation was given by Eq. (4.1), we see that the position of the centroid is described by $y = \hat{Q}$ where $\hat{Q}$ is the centroid offset in Eq. (4.2), which varies sinusoidally with phase ψ_0. The maximum deflection is

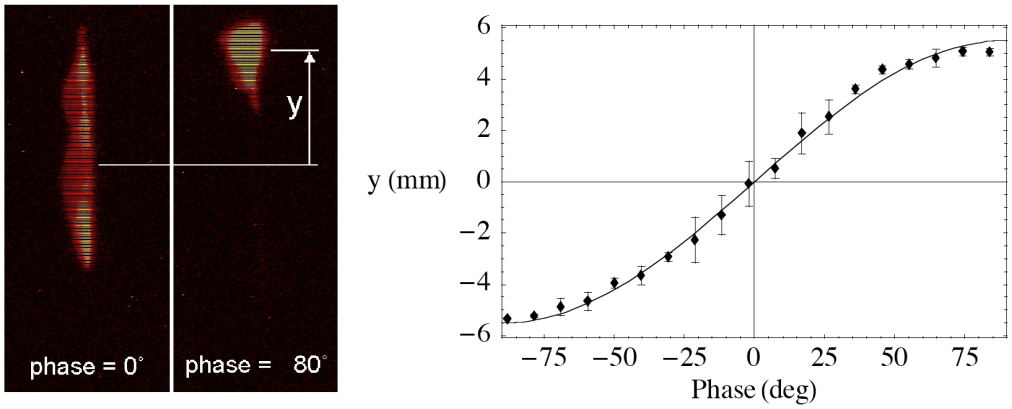

Figure 5.6: Images of the deflected beam at two different phases and measured on-screen deflection distance y plotted against the RF phase. A sinusoidal function is fitted to the data (solid curve).

given by the amplitude $\hat{Q}_{max} = eV_0L/p_0c$. The sinusoidal fit in Fig. 5.6 gives an amplitude value of $\hat{Q}_{max} = 5.51 \pm 0.21$ mm. Hence, at the measured beam energy of 11.73 MeV and a drift length of 27.9 cm, the predicted deflecting voltage is $V_0 = 232 \pm 9.6$ kV. This value is compared with those calculated from the RF power levels measured at two different internal oscilloscope impedance settings (50 Ω vs 1 MΩ) in Table 5.3. The RF power going into the cavity was measured on the oscilloscope using a crystal detector attached to the forward power coupler on the deflecting cavity. Since the impedance of the oscilloscope alters the amplitude of the power signal, separate power-to-signal calibrations were performed for the two impedance settings. The deflecting voltage was then calculated using the formula $V_0 = \sqrt{P_{cav}\tilde{R}_s}$ where we take the shunt impedance value $\tilde{R}_s = 5.6$ MΩ predicted by the HFSS simulations.

Note that the deflecting voltage values obtained from the RF measurements are consistent with each other but differ from the phase scan result by about 14%. Since the phase scan is a more direct method and has fewer potential sources of

Table 5.3: Comparison of deflecting voltage calculated from phase scan and RF power measurements.

Method	Forward Power (kW)	V_0 (kV)
Phase Scan	9.6±0.8	232±9.6
RF (50 Ω termination)	12.8±6.8	267±71
RF (1 MΩ termination)	12.1±4.7	261±51

measurement and systematic error, this value is more reliable. The magnitude of this discrepancy lies within the random errors in the RF measurements, which are large because of the large (49 dB) attenuation of the forward power coupler, which makes power values calculated from the coupled signal extremely sensitive to any measurement error in the attenuation value of the coupler itself. Some additional systematic error may also be present due to the fact that the simulated value of the shunt impedance was used in the RF calculations.

The deflecting voltage in this measurement is approximately half of the design value specified in Table 4.2, because at full voltage, the maximum deflection begins to exceed the width of the screen. But recall that the design voltage was somewhat overspecified by setting it to be three times the minimum voltage of Eq. 4.4. Consequently, in practice, the cavity was rarely operated at full power.

5.3.3 Deflector Results with Unchirped Beam

Prior to running a chirped beam through the dogleg and the deflector, the beam was run near the optimal linac phase for minumum energy spread in order to optimize the transport and measure the longitudinal structure of the uncompressed pulse. An example trace of the deflector streak produced by such a beam is shown

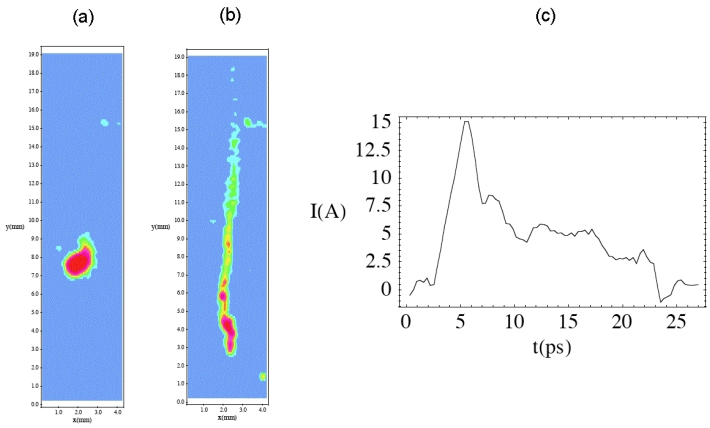

Figure 5.7: False color plots of uncompressed electron beam with (a) deflecting cavity turned off, (b) deflecting cavity turned on, as well as (c) the current profile reconstruction of the image in part (b).

in Fig. 5.7. In this case, the beam energy was 13.14 MeV and the final beam charge measured on the Faraday cup was 270 pC.

The image in Fig. 5.7(a) shows the focused beam with the deflecting cavity turned off. When the deflecting cavity is turned on at an input power of 40.6 kW the beam is streaked along the vertical axis producing the image in Fig. 5.7(b). The contour plots in parts (a) and (b) of Fig. 5.7 are false-color reconstructions of the captured black-and-white CCD camera images on the final large-aperture YAG screen located after the deflecting cavity (i.e. Screen 15). The bit count on each pixel of the captured CCD image was assumed to be proportional to the number of electrons hitting the YAG within the geometrical area corresponding to the size of one pixel. Then 5×5 blocks of neighboring pixels were averaged together and interpolated in order to smooth over the noise in the video signal. The background has been subtracted out by sampling a region well outside the area where the beam is located and then subtracting the average bit count per pixel from the whole image. The horizontal and vertical axes have been scaled to

units of mm based upon the calibrated pixel count per unit length of the imaged object for the camera and optical setup used.

The plot in Fig. 5.7(c) shows the reconstructed current profile based upon the streaked image in part (b) and the measured charge of the beam. To produce this reconstruction, the bit counts per averaged 5×5 block used to produce the interpolated (i.e. smoothed) false-color plot in part (b) were projected on the vertical (y)axis by summing over horizontal rows. The vertical axis was then rescaled to units of time by virtue of Eq. (4.67). Note that there is some ambiguity as to which end of the plot corresponds to the head of the beam as opposed to the tail. This is due to the fact that there are two zero-crossings of the RF per period, separated in phase by 180 degrees, and with the sign of the deflection correspondingly reversed for the head relative to the tail. However, based upon the results for the chirped beam, which will be presented in Section 5.3.4, the locations of the head and tail have been inferred here and the directionality of the horizontal scale on the current profile plot has been adjusted appropriately. Thus the plot indicates an uncompressed beam profile with a sharp initial spike followed by a gradually decaying tail.

To gauge the reasonableness of these results in terms of the temporal bunch length and bunch shape, we can compare with independent measurements of the temporal structure of the autocorrelated drive laser pulse in the infrared (1064 nm), following its amplification in the regenerative amplifier and compression in the grating compressor. The diagnostic employed for this purpose was a home-made multi-shot second-harmonic-generation (SHG) autocorrelator [74]. The resulting interferogram, shown in Fig. 5.8(b), provides an indirect measure of the drive laser pulse length immediately after the compressor gratings. The FWHM of this interferogram is found to be 28.8 ps. For comparison, the autocorrelation

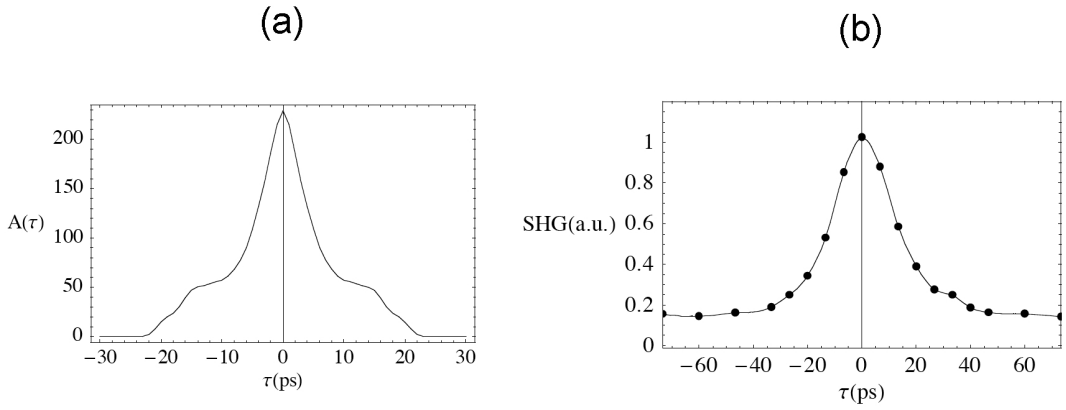

Figure 5.8: Plots showing (a) the autocorrelation function of the reconstructed electron bunch profile in Fig. 5.7(c) and (b) the normalized autocorrelation of the drive laser obtained by second-harmonic-generation interferometry.

function of the reconstructed profile of the electron bunch from Fig. 5.7(c) is shown in Fig. 5.8(a), having a FWHM of 10 ps. The discrepancy is partially resolved by noting that the laser autocorrelation measurement is taken prior to two stages of frequency up-conversion by colinear SHG in a pair of nonlinear crystals. Since the SHG pulse varies with the square of the intensity of the input laser pulse there is an approximate $\sqrt{2}$ reduction in pulse length corresponding to each stage of frequency conversion. Consequently, the drive laser pulse is expected to be shortened by approximately a factor of 2 by the time it reaches the photoinjector cathode. Note that there is also additional structure in the wings of the autocorrelation in Fig. 5.8(a) as compared with (b), which is due to the highly structured tail seen in Fig. 5.7.

The profile of Fig. 5.7 is typical of streaks taken of the uncompressed beam, including the large degree of structure in the tail. In some streaks, this structure is more pronounced, as seen in Fig. 5.9. The origin of this structure is not fully

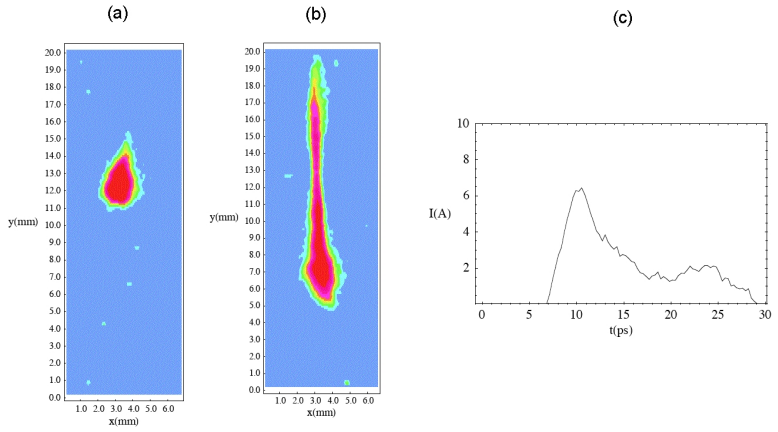

Figure 5.9: False color streak images with (a) deflecting cavity turned off, (b) deflecting cavity turned on, as well as (c) the current profile reconstruction of the image in part (b) showing structure in the tail region.

understood. One possibility is that there is additional structure in the tail of the drive laser pulse in the IR which varies from shot-to-shot, and is not apparent in the wings of the laser autocorrelation of Fig. 5.8(b) because the data has been averaged over many shots. Any such structure in the tail of the laser pulse could subsequently be amplified by the frequency doubling mechanism in the nonlinear crystals due to the previously mentioned dependence of the SHG on the square amplitude of the input pulse.

Additional verification of the electron bunch length can be obtained by a scan of beam charge versus the RF phase in the gun. The theoretical relationship between the two may be written in the form

$$Q(\psi_0) = A \int_{-\infty}^{\infty} I(\psi - \psi_0)\eta_q(\psi_0)d\psi \; \frac{e^{-(\psi_0 - \alpha\pi/2)/\tau}}{1 + e^{-(\psi_0 - \alpha\pi/2)/\tau}}, \tag{5.2}$$

where A is an amplitude constant, $I(\psi_0)$ is the laser intensity on the cathode as a function of gun phase. The peak field is assumed to occur at a phase of $\psi_0 = \pi/2$. Note that we have appended to the integral in Eq. 5.2 an exponentially decaying

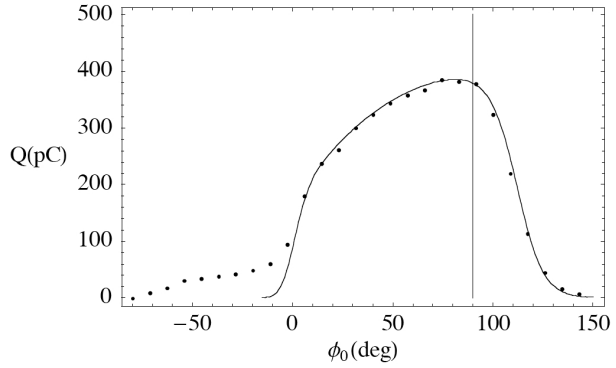

Parameter	Value
σ_ℓ	5 ps
β	0.9
A	$3.64\times10^5\ C^2/J$
τ	6.5 °
α	1.25

Figure 5.10: Measured electron beam charge vs gun RF phase with superimposed theory curve from Eq. 5.2 and corresponding fitting parameters.

component for phases exceeding this value, in order to account for the loss of charge resulting from radial blowout of the beam at large phase values. This decay has associated fitting parameters α and τ which represent the fractional phase offset of the falloff region from $\pi/2$ and the exponential decay rate respectively. The quantity η_q is the effective quantum efficiency of the cathode, given by

$$\eta_q(\psi_0) = \left[\frac{h\nu}{e} - \frac{W}{e} + \sqrt{\frac{e}{4\pi\epsilon_0}\beta E_0 \sin\psi_0}\right]^2 \tag{5.3}$$

where $h\nu$ is the drive laser photon energy, W is the cathode work function, β is an empirical field enhancement factor, and E_0 is the electric field amplitude at the cathode.

Data of beam charge, measured using an integrated current transformer (ICT) located at the photoinjector gun exit, plotted against RF phase is presented in Fig. 5.10. Note that there is a pedestal at negative phase values, indicating the presence of a secondary beam of lower charge that arrives 50 degrees earlier in phase than the primary pulse. Eq. 5.2 is fitted to the data of the primary pulse only, assuming for $I(\psi_0)$ a Gaussian laser pulse distribution with RMS width σ_ℓ.

The resulting fit is superimposed as a solid curve on the plot in Fig. 5.10 alongside the corresponding fit parameters. The fitted σ_ℓ value of 5 ps is consistent with the RMS width of the pulse in Fig. 5.7, which was 5.9 ps. However, it should be noted that the region of the theoretical curve in Fig. 5.10 that is most sensitive to the laser pulse width is the rising edge near zero phase, where the data is distorted by the presence of the secondary pulse, making the fitted value of this parameter less reliable than the others. Nevertheless, the same fit parameters are found to produce a good fit to the pedestal as well with a simple offset in phase and an adjustment of the amplitude factor A. This suggests that the secondary beam responsible for the pedestal is a ghost image of the primary pulse but offset in phase by 50 degrees. The most likely explanation for the presence of the pedestal is that there is a pre- or post-pulse from the regenerative amplifier due to the nonzero *contrast ratio* of the optical cavity. This pulse is would then be separated from the main one by about 7 ns and would therefore be injected many RF cycles later and at a different RF phase relative to the peak of the RF. The relative amplitudes of the main pulse and the pedestal in Fig. 5.10 are consistent with the typical 1:10 contrast ratio for the regenerative amplifier.

5.3.4 Deflector Results with Chirped Beam

Deflecting cavity data for an electron beam that was chirped in energy by running the RF phase in the linac backward of crest by approximately 20 degrees is shown in Fig. 5.11. Experimental parameters corresponding to the data of Fig. 5.11 are shown in Table 5.4. The sextupole magnets were set to have opposite polarities, corresponding to $\alpha = -1$ where α is the field ratio parameter appearing in Eq. (3.25).

As seen in Fig. 5.11(a), when the sextupoles are turned off the current profile

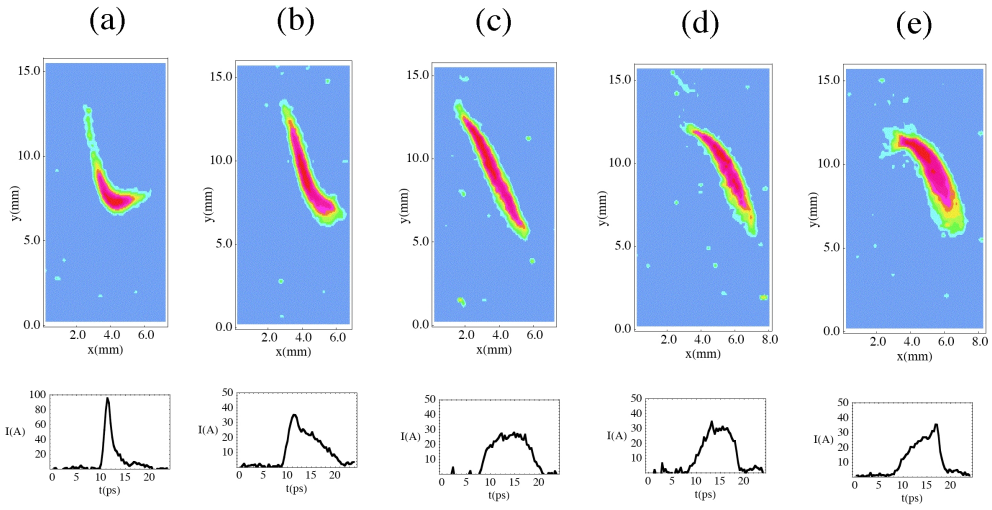

Figure 5.11: Deflecting cavity streaks and current profile reconstructions of an (initially) chirped electron beam for five different sextupole field values, with a sextupole field ratio $\alpha = -1$: (a) $\kappa = 0$, (b) $\kappa = 547$ $\mathbf{m}^{-3}$, (c) $\kappa = 1094$ $\mathbf{m}^{-3}$, (d) $\kappa = 1641$ $\mathbf{m}^{-3}$, and (e) $\kappa = 2188$ $\mathbf{m}^{-3}$.

Table 5.4: Experimental parameters corresponding to the data of Fig. 5.11.

Parameter	Symbol	Value	Units
Final Charge	Q	234	pC
Energy	U	11.86	MeV
Forward Power	P_{cav}	28.7	kW
Deflecting Voltage	V_0	401	kV
Gun Phase	ψ_0	60	degrees
PWT Phase	ψ_{pwt}	70	degrees

is characterized by a sharp narrow spike at the head, followed by a shallow tail, as was seen in the simulation predictions of Figs. 3.8(b) and 5.3(a). (Note that since the horizontal coordinate in Fig. 5.11 is arrival time t, whereas in Figs. 3.8, 5.3 it is longitudinal position z there is a reversal of direction due to the convention $z = -ct$). As the sextupole field strength is increased, the hard edge at the head of the beam gives way to a gradual ramp followed by a sharp drop at the tail, as seen in Fig. 5.11(e). The intermediate stages shown in (b) through (d) demonstrate the progression of this process.

Several significant features in Fig. 5.11 should be remarked upon. One is the significant energy correlation on the horizontal axis, producing the obvious tilt of the streak profiles. This energy correlation was produced by slightly detuning the first horizontally focusing quadrupole magnet on the dogleg section by approximately 2%. The resulting effect is a combination of the usual residual second-order horizontal dispersion (T_{166}), which was discussed in Section 5.2.1, combined with an induced linear dispersion due to the detuning. The resulting effect upon the streak data is that the vertical (y) dependence on arrival time is complemented by a horizontal (x) dependence on energy, which results in a reconstruction of the longitudinal phase space distribution of the beam. This permits a direct visualization of the turning over of the phase space as the nonlinear correction is implemented by the sextupole magnets. Simulations of the beamline using ELEGANT predict that a detuning of the first quadrupole by 2% should produce a residual horizontal dispersion of R_{16} = -1.1 cm and a slightly increased longitudinal dispersion value of R_{56} = -5.7 cm.

The sextupole field strength ($\kappa = 2188$ m^{-3}) required to produce the ramp-shaped beam in Fig. 5.11(e) is 80% higher than what was predicted by the simulations of Section 3.2.5 and by the empirical measurements of Section 5.2.1 to

be necessary in order to cancel the T_{566} of the dogleg. Consequently, the ramped beam of Fig. 5.11(e) is characterized by a significant overcorrection of the second-order longitudinal dispersion, similar to the simulated result of Fig. 5.3(d). This overcorrection is most likely required by the fact that the uncompressed electron bunches are not Gaussian but are asymmetrical in shape, as was seen in Figs. 5.7 and 5.9, and have a significant amount of charge concentrated at the head of the beam.

Reproducing the results of Fig. 5.11 in simulation therefore required imposing a similar asymmetry on the temporal distribution of the simulated beam prior to the entrance of the dogleg. Since the UCLA version of PARMELA does not currently support the ability to specify an asymmetric temporal shape for the photocathode drive laser, we instead ran PARMELA simulations of the photoinjector using a flat-top temporal distribution at the cathode and 10,000 macroparticles. The simulated distribution of 6-D phase space coordinates of the particles at the exit of the linac was then filtered to selectively eliminate particles in the tail of the distribution, thereby creating an artificially asymmetric temporal structure characterized by a sharp rise in current at the head of the bunch followed by a gradually decaying tail. The longitudinal phase space distribution and current profile of the simulated electron beam thereby produced are shown in Fig. 5.12. The 6-D phase space coordinates of this bunch (containing approximately 5000 macroparticles) were then used as input for an ELEGANT simulation of the dogleg and the deflecting cavity. These results are shown in Fig. 5.13, which displays the predicted deflecting cavity streak image, longitudinal trace space, and current profile for four different sextupole field values, corresponding to those of Fig. 5.11(a), (c), (d), and (e) respectively.

The ELEGANT simulations of Fig. 5.13 successfully reproduce the primary

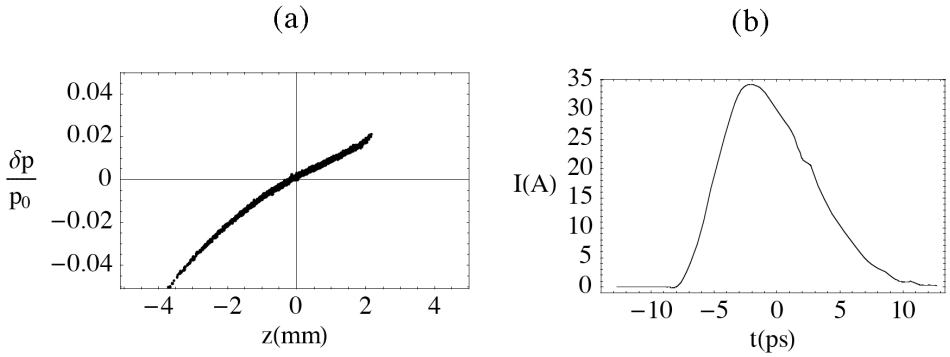

Figure 5.12: Plots of the simulated asymmetric bunch used as input for the ELEGANT results of Fig. 5.13 showing (a) longitudinal trace space and (b) current profile.

qualitative features of the data in Fig. 5.11, including the shape of the streak images and the higher sextupole field strength required in order to achieve a ramp-shaped bunch. When an initially symmetric Gaussian bunch is used as the input for these simulations (with all other simulation parameters unaltered), the results are found to be consistent with the previously shown PARMELA results of Section 3.2.5, which predicted that the ramp-shaped current profile should occur at a sextupole field strength of $\kappa = 1204$ m^{-3}. This suggests that the sextupole overcorrection required in the experimental run to produce ramped beams can be largely explained by the temporal asymmetry of the initial bunch. It also indicates that the bunch-ramping mechanism is somewhat forgiving of such asymmetries, since ramped bunches can be obtained in spite of them simply by adjusting the strength of the sextupoles.

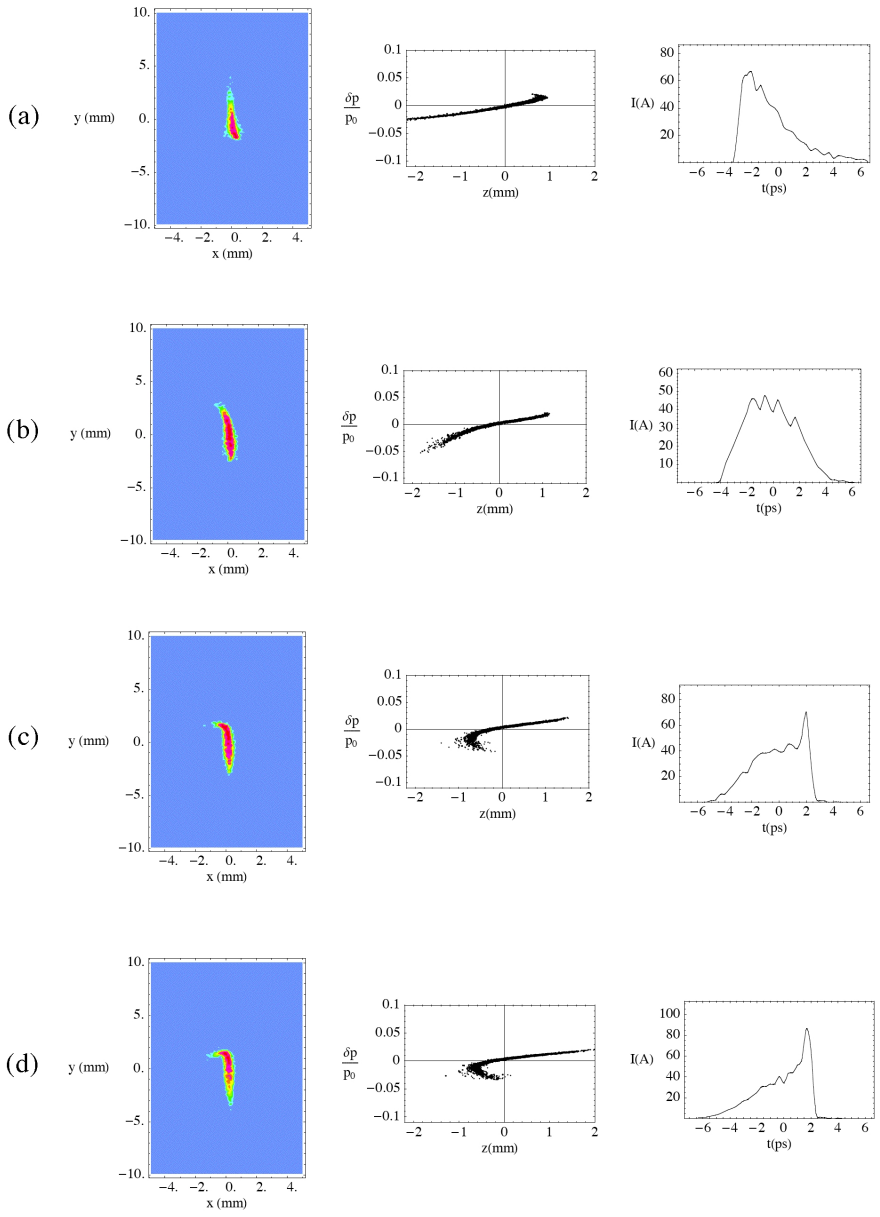

Figure 5.13: Simulated deflecting cavity streaks and current profiles (using ELEGANT with 10,000 macroparticles) of an (initially) chirped Gaussian electron beam for four different sextupole field values, with a sextupole field ratio $\alpha = -1$: (a) $\kappa = 0$, (b) $\kappa = 1094$ $\mathbf{m}^{-3}$, (c) $\kappa = 1641$ $\mathbf{m}^{-3}$, (d) $\kappa = 2188$ $\mathbf{m}^{-3}$.

5.4 Summary of Findings

We have reported on an experiment at the UCLA Neptune Laboratory to generate ramped electron bunches for potential application as a drive beam for plasma wakefield studies, using a dispersionless translating section or dogleg as a bunch compressor. Experimental results have indicated successful operation of the beamline in a regime predicted by particle tracking simulations as being suitable for compression and ramped bunch generation, as well as the use of sextupole correctors to manipulate the nonlinear *horizontal* dispersion. Results using coherent transition radiation (CTR) interferometry provide direct evidence that the sextupole magnets can also be used to manipulate the longitudinal shape of the electron bunch in a way that is qualitatively consistent with theoretical predictions. To obtain a more complete experimental picture of the longitudinal dynamics, a deflecting mode cavity was used as a diagnostic to reconstruct the current profiles of the electron bunches after passing through the compressor.

Deflector studies with uncompressed bunches indicate that the beam has an asymmetrical (non-Gaussian) shape with a sharp peak at the head of the beam followed by a decaying tail, and an RMS duration of approximately 6 ps. The measured bunch length is compared with autocorrelation measurements of the drive laser and with the bunch length extracted from fitting to a charge vs. RF phase scan of the photoinjector, and is found to be reasonably consistent with those results. Studies with chirped bunches indicate that ramp-shaped current profiles can be produced. The resulting deflector streak images and reconstructed current profiles for the compressed beam are found to be qualitatively consistent with ELEGANT simulations, so long as the initial temporal asymmetry of the beam is included in the simulation. However, as a result of the asymmetric initial current profile of the beam, the sextupole field strength required to produce

a ramped current profile is found (in both simulation and experiment) to be 80% higher than what was predicted by simulations of beams with an initially Gaussian current profile.

CHAPTER 6

Future Directions

The experimental results presented in Chapter 5 provide a proof-of-principle demonstration of the effectiveness of the proposed mechanism for generating ramp-shaped electron bunches. However, in order to make such a scheme practicable for reliably and efficiently driving a plasma wake-field accelerator, a variety of additional experimental issues must be addressed. The longitudinal bunch shape is not the only characteristic of beam quality which is relevant to the successful operation of a PWFA. To properly match such a beam into a plasma, we require that the betatron matching condition $\beta_r = \beta_{eq} = \sqrt{\gamma/(2\pi r_e n_0)}$ be satisfied, where γ is the normalized bunch energy, n_0 is the ambient plasma density, and r_e is the classical electron radius. From this requirement, combined with the condition on the bunch length $L > 2k_p^{-1}$ imposed by requiring that the transformer ratio $R = k_p L$ be greater than 2, and the condition for the blowout regime $n_b >> n_0$ (which we will interpret as $n_b > 4n_0$), we obtain a set of constraints on the plasma density, the drive beam RMS size σ_r, and the normalized emittance ϵ_N:

$$n_0 > n_{0,min} = \frac{mc^2}{\pi e^2 L}, \tag{6.1}$$

$$\sigma_r < \sigma_{max} = \sqrt{\frac{Q/e}{4\pi n_0 \sigma_z}}, \tag{6.2}$$

$$\epsilon_N < \epsilon_{N,max} = \gamma\beta\frac{\sigma_{max}^2}{\beta_{eq}}. \tag{6.3}$$

In these relations, we have approximated the beam density by $n_b = Q/(e\pi\sigma_r^2\sigma_z)$ and have used the definition of the normalized emittance $\epsilon_N = \gamma\beta(\sigma_r^2/\beta_r)$, where β is the bunch velocity normalized by the speed of light, β_{eq} is the equilibrium beta function given above, σ_z is the RMS bunch length, and Q is the bunch charge. We can use these constraints to obtain the following expression for the minimum required beam brightness:

$$\mathcal{B} > \mathcal{B}_{min} = \frac{2cQ}{\epsilon_{N,max}^2\sigma_z}. \tag{6.4}$$

Here we have used the definition for the transverse brightness $\mathcal{B} = 2I/\epsilon_N^2$, where $I = en_b\beta c\pi\sigma_r^2$ is the beam current. These relations provide us with an estimate of the required beam parameters for successfully applying the bunch shaping technique to create an adequate drive beam for a PWFA. In the present chapter, we discuss several future experiments planned at the Neptune laboratory as an extension of the work comprising this dissertation, which are aimed at addressing these issues of beam quality. We also propose a simple technique for creating a witness bunch.

6.1 High-Gradient Quadrupole Focusing

6.1.1 Experimental Overview

For the next stage of experiments on the Neptune dogleg beamline, an alternative diagnostic setup will be employed, as shown in the inset in Fig. 6.1. Setup 1 corresponds with the previously conducted bunch profile measurements and longitudinal phase space reconstruction which was discussed in Section 5.3.4. Setup 2 will consist of a triplet of permanent magnet quadrupoles followed by a Ce:YAG profile monitor, which will be used to obtain a high-brightness focus.

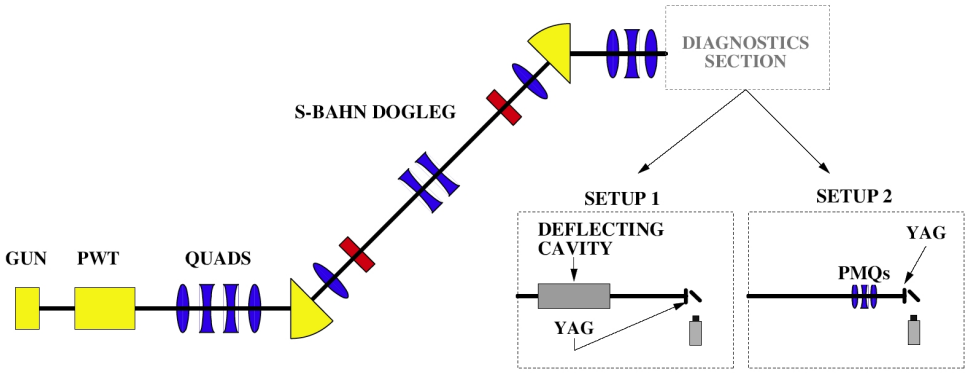

Figure 6.1: Cartoon graphic of the experimental beamline (not to scale). Blue lenses, red rectangles, and yellow wedges represent quadrupoles, sextupoles, and dipole magnets respectively. Two alternate setups are shown for the final diagnostics section.

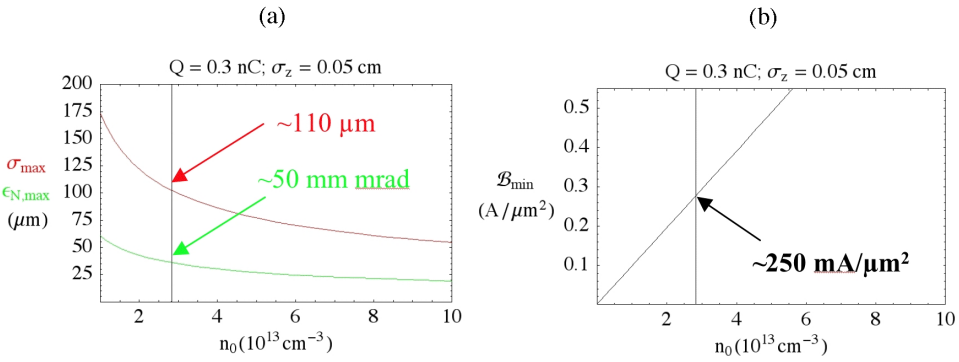

Figure 6.2: Plot of the constraints as given by Eqs. (6.1)-(6.4), with approximate maximal values for beam size and emittance, and minimum brightness.

Using the constraints on the beam parameters imposed by Eqs. (6.2)-(6.3), we can construct plots showing the maximum allowable beam size and emittance as a function of plasma density n_0 for a 0.5 mm long 300 pC beam. This is shown in Fig. 6.2(a). Combining this with the minimum density of $n_0 = 2.8 \times 10^{13} cm^{-3}$ required by Eq. (6.1) gives us estimated upper limits on RMS beam size and normalized emittance of 110 μm and 50 mm mrad respectively. A corresponding plot of minimum brightness using Eq. (6.4), shown in Fig. 6.2(b), gives a lower limit of 250 $mA/\mu m^2$. These limits are compared with simulation results in Section 6.1.3.

6.1.2 Permanent Magnet Quadrupoles

The permanent magnet quadrupoles (PMQs) to be used for the S-Bahn final focus shown in Setup 2 of Fig. 6.1 are compact, with a high magnetic field gradient, making them useful for focusing of high-brightness space-charge dominated beams such as those produced at the Neptune laboratory. The magnets incorporate a hybrid iron and permanent magnet design originally developed for the nonlinear inverse Compton scattering experiment that is currently in progress at the Neptune laboratory [75]. The magnets, shown in Fig. 6.3, contain cubes of NdFeB, surrounded by an iron yoke which serves to close the magnetic circuit. Four hyperbolic pole faces constructed by wire electric discharge machining (EDM) are held against the NdFeB cubes in a quadrupole array around the geometric center by an aluminum keeper.

Magnets of 1 cm and 2 cm lengths have been constructed, incorporating 4 and 8 NdFeB cubes respectively. The measured field strengths of the two types are similar (109 and 110 T/m respectively). The proposed configuration for the triplet is a single 1 cm length defocusing PMQ, followed by a focusing and then a

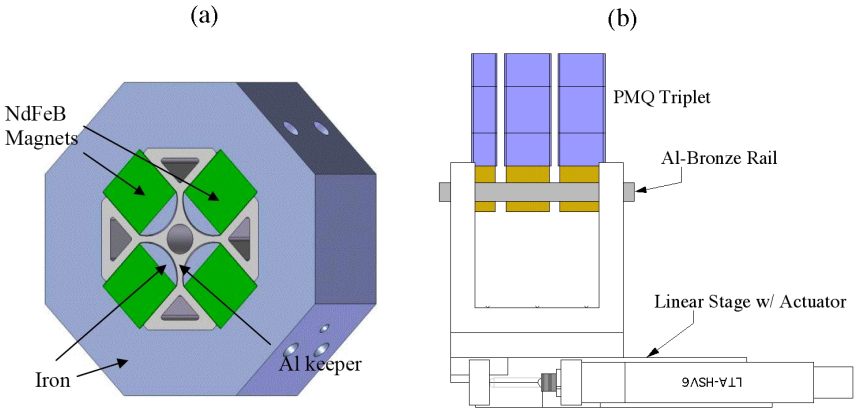

Figure 6.3: Drawing of hybrid permanent magnet quadrupole design (a), courtesy of A. Doyuran, and schematic of assembled triplet and stand (b).

defocusing 2 cm long PMQ. A side view of the assembly is shown in Fig. 6.3(b) at a reduced scale.

6.1.3 Simulations of the Focusing Experiment

The PMQ focusing system described in Section 6.1.2 was simulated initially using the matrix-based beam envelope code PowerTrace. Further studies were then done using the particle tracking code ELEGANT to model the dogleg and final focus sections [53]. The phase space coordinates for the particles used as the input for the ELEGANT simulation were generated by a PARMELA simulation of the photoinjector and linac.

Simulated experimental values for energy E, charge Q, normalized emittances $\epsilon_{x,N}$ and $\epsilon_{y,N}$, RMS bunch length and transverse dimensions σ_t, σ_x, σ_y, and brightness $\mathcal{B}$ are given in Table 6.1. Initial values correspond to the beam parameters immediately after the accelerating section, and final values correspond to the

Table 6.1: Simulated Experimental Parameters

Parameter	*Initial*	*Final*	*Units*
E	13	13	MeV
Q	300	240	pC
$\epsilon_{x,N}$	5	41	mm mrad
$\epsilon_{y,N}$	5	15	mm mrad
σ_t	2.5	1.8	ps
σ_x	1	0.130	mm
σ_y	1	0.057	mm
$\mathcal{B}$	7600	433	mA/μm^2

final focus location of the permanent magnet quadrupole triplet of Setup 2. Final values represent design goals based upon the PARMELA and ELEGANT simulation results. The reduction in charge is a prediction based upon observed transportation losses in the beamline, and the emittance growth is due primarily to transverse nonlinear effects in the dogleg. Note that the predicted beam sizes, emittance values, and brightness fall roughly within the limits set by Eqs. (6.1)-(6.4), for applicability to plasma wake-field studies with large transformer ratios.

6.2 Creation of a Witness Beam

In order for the ramped bunch mechanism presented in this dissertation to represent a useful technology for the wake-field accelerator, it must be compatible with some feasible scheme for creating a witness bunch. The witness bunch would ideally be a bunch of much lower charge which trails behind the main drive bunch,

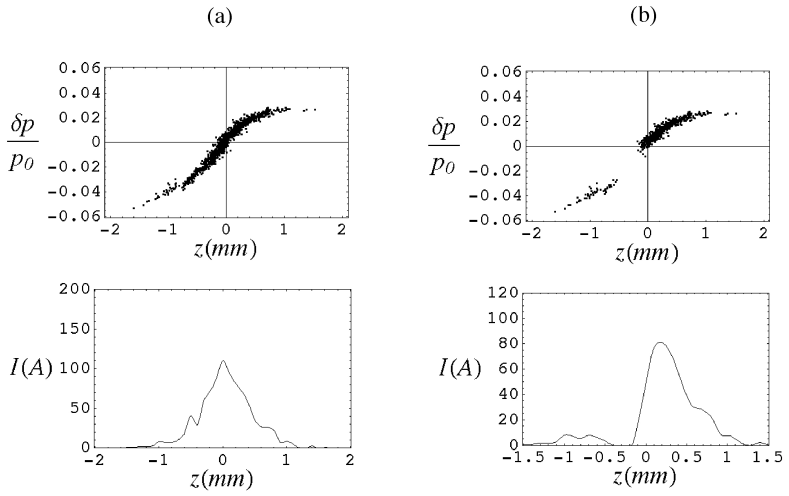

Figure 6.4: Simulation of undercorrected beam at exit of dogleg with collimator removed in (a) and inserted in (b), thereby producing a ramped drive beam followed by a low-charge witness bunch.

and can therefore be accelerated by the wake-fields which are generated by it. One technique used in the past has been to accelerate the tail of the drive bunch itself. However, a ramped drive bunch is intended by design to have a sharp cutoff at the tail end. We saw, however, in Fig. 3.8(b), that with the sextupole correctors turned off, the nonlinear effects produce a significant lower-energy tail behind the bunch, though the ramped shape is lost. A potential solution would be to operate in a regime intermediate between the conditions represented in Fig.3.8(b) and 3.8(c), where the sextupole magnets are turned on but at a lower field strength, producing a beam with a ramp at the front followed by a more tapered fall-off at the back. This situation is seen in Fig.6.4(a), which shows the results of an ELEGANT simulation of the dogleg compressor. By inserting a 1 cm wide collimator in the x-direction, at a location in the dogleg (corresponding to the position of the quadrupole before the final dipole in Fig. 6.1) where the

horizontal dispersion is large and therefore there is a strong correlation between x and z, the tail of the beam can be truncated from the main body. As shown in Fig. 6.4(b) this results in a ramp-shaped primary bunch followed by a separate trailing bunch of lower charge. This scheme has the benefit of being relatively simple, requiring only the insertion of a collimator into the beamline. However, the resultant reduction in charge and horizontal truncation of the beam must be taken into consideration in the design of the downstream focusing optics.

6.3 Scaling to Higher Charge

Future upgrades to the Neptune laboratory, including a new drive laser oscillator, replacement of the photoinjector, photocathode laser cleaning, and higher RF power levels in the gun are expected to increase the bunch charge to as high as 4 nC. It is therefore of interest to consider how the bunch shaping mechanism described previously scales to higher charge. Preservation of the beam envelope under the emittance compensation mechanism in the gun and linac requires that the bunch dimensions at the cathode scale with charge as $Q^{1/3}$. This scaling is accomplished by stretching the pulse length of the photocathode drive laser and expanding its transverse dimensions accordingly. Simulations of the Neptune photoinjector under this scaling in UCLA-PARMELA indicate a normalized emittance of $\epsilon_{x,N} = \epsilon_{y,N} = 25$ mm mrad at the exit of the linac with 4% transportation losses for an initial charge of 4 nC. Since the dogleg compression mechanism requires a chirped beam, the bunch was chirped in energy by setting the RF phase of the linac in the simulation to a value corresponding to an injection phase of 22 degrees back of crest. This chirp, and the increase in bunch length due to the charge scaling, result in a predicted 4.5% RMS energy spread, compared with 1.8% energy spread for the 300 pC case.

Table 6.2: Simulated Parameters Corresponding to Fig. 6.5 (a), (b), and (c)

Parameter	(*a*)	(*b*)	(*c*)	*Units*
$\epsilon_{x,N}$	742	96	46	mm mrad
$\epsilon_{y,N}$	456	141	68	mm mrad
T_{166}	-0.26	0.00	-0.26	m
T_{266}	-7.9	0.00	-7.9	rad
T_{566}	-0.04	0.623	-0.04	m
U_{5666}	-2.44	-1.02	-2.44	m

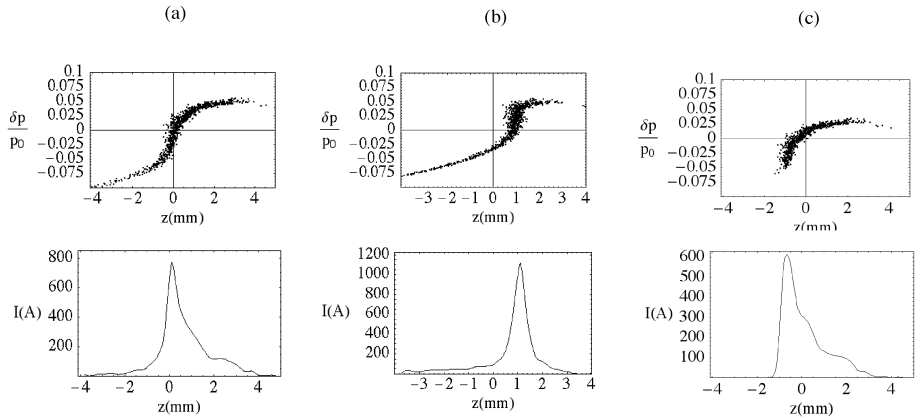

Figure 6.5: Simulation of longitudinal phase space and current profiles of 4nC beam at exit of dogleg compressor with (a) with sextupoles set to eliminate second-order longitudinal dispersion (T_{566}), (b) with sextupoles set to eliminate second-order horizontal dispersion (T_{166}), and (c) with sextupoles set as in part (a) but with a collimator inserted to remove low-energy tail.

The final phase space coordinates of the particles in the PARMELA simulation were then used as the input for an ELEGANT simulation of the dogleg compressor. The results of these simulations indicated that due to the larger energy spread of the 4 nC beam, two undesirable effects became more pronounced: (1) distortion of the longitudinal phase space by third-order longitudinal dispersion (U_{5666} in transport notation) and (2) emittance growth due to horizontal second-order dispersion (T_{166} and T_{266}). The first effect results in the formation of a low-energy tail behind the beam. This is seen in Fig.6.5(a). The tail can, in principle, be corrected by the use of octupole magnets. The second effect requires the use of sextupole magnets and is somewhat more difficult to remedy, due to the fact that, at least for the particular optical configuration of the Neptune dogleg, it is impossible to simultaneously eliminate both the horizontal and longitudinal second order dispersion (T_{166} and T_{566} respectively). Consequently, the sextupole magnets may be used to eliminate the second order horizontal dispersion, thereby improving the final emittance, but as a result the longitudinal dispersion becomes nonzero and so the shape of the ramped profile is destroyed. This scenario is illustrated in Fig. 6.5(b). A solution which appears to solve both problems is to simply eliminate the tail in part (a) by collimating the beam. As it turns out, much of the emittance growth is due to the low-energy particles contained in this tail, and their removal improves the final emittance by a factor of two and restores the ramped profile, as seen in Fig. 6.5(c). By using a collimator of finite width, a small subset of the tail particles could be left as a witness bunch, making this technique compatible with the results of the previous section. To clarify these results, the simulated emittance and corresponding matrix element values are provided in Table 6.2.

It should be noted that the simulations above do not include transmission losses due to ordinary apertures of the beamline. And in fact, the simulated

RMS beam sizes in the dogleg for the high-charge case are found to exceed the radius of the beam pipe. Consequently, although scaling the compressor to higher charge appears theoretically feasible, it would, in practice, be necessary to expand the apertures of the beamline, which would require a significant redesign of the beamline hardware.

References

[1] M. J. Rhee. Refined definition of beam brightness. *Phys. Fluids B*, 4:1674–1676, 1992.

[2] K. J. Kim. RF and Space-Charge Effects in Laser-Driven RF Electron Guns. *Nuclear Instruments and Methods in Physics Research*, A287:201–218, 1989.

[3] C. Travier. An introduction to photo-injector design. *Nuclear Instruments and Methods in Physics Research A*, 340:26–39, 1994.

[4] J. Gao. Theoretical investigation of traveling wave rf gun. In *EPAC92. Third European Particle Accelerator Conference*, pages 584–586, 1992.

[5] Z. Huang, D. Dowell, P. Emma, C. Limborg-Deprey, G. Stupakov, and J. Wu. Uncorrelated Energy Spread and Longitudinal Emittance of a Photoinjector Beam. Technical Report SLAC-PUB-11240, Stanford Linear Accelerator Center, Stanford, CA, 2005.

[6] O. J. Luiten, S. B. van der Geer, M. J. de Loos, F. B. Kiewiet, and M. J. van der Wiel. How to Realize Uniform Three-Dimensional Ellipsoidal Electron Bunches. *Physical Review Letters*, 93:0948021–4, 2004.

[7] L. Serafini. The short bunch blow-out regime in rf photoinjectors. In *AIP Conference Proceedings*, number 413, pages 321–334, 1997.

[8] K. T. McDonald. Design of the Laser-Driven RF Electron Gun for the BNL Accelerator Test Facility. *IEEE Transactions on Electron Devices*, 35(11):2052–2059, 1988.

[9] B. E. Carlsten. New Photoelectric Injector Design for the Los Alamos National Laboratory XUV FEL Accelerator. *Nuclear Instruments and Methods in Physics Research A*, 285:313–319, 1989.

[10] L. Serafini and J. B. Rosenzweig. Envelope analysis of intense relativistic quasilaminar beams in rf photoinjectors: A theory of emittance compensation. *Physical Review E*, 55:7565–7590, 1996.

[11] J. B. Rosenzweig and E. Colby. Charge and wavelength scaling of rf photoinjector designs. In *AIP Conference Proceedings*, number 335, pages 724–737, 1995.

[12] J. Rosenzweig, N. Barov, S. Hartman, M. Hogan, S. Park, C. Pellegrini, G. Travish, R. Zhang, P. David, G. Hairapetian, and C. Joshi. Initial measurements of the UCLA RF photoinjector. *Nuclear Instruments and Methods in Physics Research A*, 341:379–385, 1994.

[13] J. B. Rosenzeig. personal communication, 2007.

[14] H. P. Leboutet. A device for separating electrons in accordance with their energy levels. *U.S. Patent*, 3031596, 1962.

[15] M. Ferrario and L. Serafini. Velocity bunching in photo-injectors. In *AIP Conference Proceedings*, number 505, pages 87–106, 2001.

[16] R. J. England, P. Musumeci, R. Yoder, and J. B. Rosenzweig. Beam shaping and compression scheme for the ucla neptune laboratory. In *Proceedings of the 2003 Particle Accelerator Conference*, IEEE, page 3258, Portland, OR, 2003.

[17] S. G. Anderson, J. B. Rosenzweig, P. Musumeci, and M. C. Thompson. Horizontal Phase-Space Distortions Arising from Magnetic Pulse Compression of an Intense Relativistic Electron Beam. *Physical Review Letters*, 91(7):074803, 2003.

[18] P. Emma, F-J Decker, P. Krejcik, C. L. O'Connell, M. Woodley, H. Schlarb, and F. Stulle. Measurements of transverse emittance growth due to coherent synchrotron radiation in the slac spps bunch compressor chicane. In *Proceedings of the 2003 Particle Accelerator Conference*, pages 3129–3131, 2003.

[19] S. H. Shin and M. Yoon. Femto-second electron pulses from an rf linear accelerator as a far-infrared radiation source. *Journal of Physics D*, 39:1584–1593, 2006.

[20] P. Emma, R. Iverson, P. Krejcik, P. Raimondi, and J. Safranek. Femtosecond electron bunch lengths in the slac fftb beamline. In *Proceedings of the 2001 Particle Accelerator Conference*, pages 4038–4040, 2001.

[21] S. G. Anderson, P. Musumeci, J. B. Rosenzweig, W. J. Brown, R. J. England, M. Ferrario, J. S. Jacob, M. C. Thompson, G. Travish, A. M. Tremaine, and R. Yoder. Velocity bunching of high-brightness electron beams. *Physical Review Special Topics - Accelerators and Beams*, 8:014401, 2005.

[22] R. W. Shoenlein, W. P. Leemans, A. H. Chin, P. Volfbeyn, T. E. Glover, P. Balling, M. Zolotorev, K-J Kim, S. Chattopadhyay, and C. V. Shank.

Femtosecond X-Ray Pulses at 0.4 Angstrom Generated by 90 Degree Thomson Scattering: A Tool for Probing the Structural Dynamics of Materials. *Science*, 274:236–238, 1996.

[23] A. Doyuran, R. J. England, C. Joshi, P. Musumeci, J. B. Rosenzweig, S. Tochitsky, G. Travish, and O. Williams. Study of x-ray harmonics of the polarized inverse compton scattering experiment at ucla. In *AIP Conference Proceedings*, number 737, pages 750–756, 2004.

[24] T. Oshima, Y. Hama, H. Ishikawa, S. Kashiwagi, R. Kuroda, M. Washio, A. Yada, H. Hayano, and J. Urakawa. All-solid-state picosecond laser system for photo cathode rf-gun and x-ray generation at waseda university. In *Proceedings of the 2001 Particle Accelerator Conference*, pages 2400–2402, 2001.

[25] M. Babzien, I Ben-Zvi, K. Kusche, I. V. Pavlishin, I. V. Pogorelski, , D. P. Siddons, V. Yakimenko, D. Cline, F. Zhou, T. Hirose, Y. Kamiya, T. Kumita, T. Omori, J. Urakawa, and K. Yokoya. Observation of the Second Harmonic in Thomson Scattering from Relativistic Electrons. *Physical Review Letters*, 96:054802, 2006.

[26] F. R. Arutyunian and V. A. Tumanian. The Compton Effect on Relativistic Electrons and the Possibility of Obtaining High Energy Beams. *Physics Letters*, 4(3):176–178, 1963.

[27] J. Lim, P. Frigola, J. B. Rosenzweig, S. Telfer, G. Travish, W. Brown, and A. Tremaine. An adjustable permanent magnet quadrupole (pmq) final focus system for low energy experiments. In *Proceedings of the 2003 Particle Accelerator Conference*, pages 2192–2194, 2003.

[28] J. M. Madey. Stimulated Emission of Bremsstrahlung in a Periodic Magnetic Field. *Journal of Applied Physics*, 42(5):1906–1913, 1971.

[29] L. H. Yu and et al. High-Gain Harmonic-Generation Free Electron Laser. *Science*, 289:932–934, 2000.

[30] T. J. Orzechowski and et al. Microwave Radiation from a High-gain Free-Electron Laser Amplifier. *Physical Review Letters*, 54(9):889–892, 1985.

[31] M. J. Hogan and et al. Measurements of Gain Larger than 10^5 at 12 μm in a Self-Amplified Spontaneous-Emission Free-Electron Laser. *Physical Review Letters*, 81(22):4867–4871, 1998.

[32] S. V. Milton and et al. Exponential Gain and Saturation of a Self-Amplified Spontaneous Emission Free-Electron Laser. *Science*, 292:2037–2041, 2001.

[33] R. Bonifacio, C. Pellegrini, and L.M. Narducci. Collective Instabilities and High-Gain Regime in a Free Electron Laser. *Optics Communications*, 50(6):373–378, 1984.

[34] N. M. Kroll and W. A. McMullin. Stimulated emission from relativistic electrons passing through a spatially periodic transverse magnetic field. *Physical Review A*, 17(1):300–308, 1978.

[35] C. Sung, S. Ya. Tochitsky, S. Reiche, J. B. Rosenzweig, C. Pellegrini, and C. Joshi. Seeded free-electron and inverse free-electron laser techniques for radiation amplificiation and electron microbunching in the terahertz range. *Physical Review Special Topics - Accelerators and Beams*, 9:120703, 2006.

[36] C. E. Clayton, K. A. Marsh, A. Dyson, M. Everett, A. Lal, W. P. Leemans, R. Williams, and C. Joshi. Ultrahigh-gradient acceleration of injected electrons by laser-excited relativistic electron plasma waves. *Phys. Rev. Lett.*, 70:37–40, 1993.

[37] K. Nakajima and et al. Observation of Ultrahigh Gradient Electron Acceleration by a Self-Modulated Intense Short Laser Pulse. *Phys. Rev. Lett.*, 74:4428–4431, 1995.

[38] C. W. Siders, S. P. Le Blanc, D. Fisher, T. Tajima, M. C. Downer, A. Babine, A. Stepanov, and A. Sergeev. Laser Wakefield Excitation and Measurement by Femtosecond Longitudinal Interferometry. *Phys. Rev. Lett.*, 76:3570–3573, 1996.

[39] F. Amiranoff and et al. Observation of Laser Wakefield Acceleration of Electrons. *Phys. Rev. Lett.*, 81:995–998, 1998.

[40] P. Muggli and et al. Meter-Scale Plasma-Wakefield Accelerator Driven by a Matched Electron Beam. *Phys. Rev. Lett.*, 93:014802, 2004.

[41] A. I. Akhiezer and R. V. Polovin. Theory of Wave Motio of an Electron Plasma. *Soviet Physics, JETP*, 3(5):696–705, December 1956.

[42] J. B. Rosenzweig. Nonlinear Plasma Dynamics in the Plasma Wake-Field Accelerator. *Physical Review Letters*, 58(6):555–558, 1987.

[43] J. T. Seeman. Collective Electron Driven Linac for High Energy Physics. *IEEE Trans. Nucl. Sci.*, NS-30:3180–3182, August 1983.

[44] K. L. F. Bane and P. B. Wilson. Wake fields and wake field acceleration. In *Physics of High Energy Particle Acceleration*, number 127 in AIP Conference Proceedings, pages 875–928, 1983.

[45] J. B. Rosenzweig. Acceleration and focusing of electrons in two-dimensional nonlinear plasma wake fields. *Phys. Rev. A*, 44:R6189–6192, November 1991.

[46] W. Lu, C. Huang, M. Zhou, M. Tzoufras, F. S. Tsung, W. B. Mori, and T. Katsouleas. A nonlinear theory for multidimensional relativistic plasma wave wakefields. *Physics of Plasmas*, 13:056709, 2006.

[47] C. Jing, A. Kanareykin, J. G. Power, M. Conde, Z. Yusof, P. Schoessow, and W. Gai. Observation of Enhanced Transformer Ratio in Collinear Wakefield Acceleration. *Physical Review Letters*, 98:114801, 2007.

[48] K. L. F. Bane, Pisin Chen, and P. B. Wilson. On Collinear Wake Field Acceleration. Technical Report SLAC PUB-3662, Stanford Linear Accelerator Center, Stanford, CA 94305, April 1985.

[49] K. V. Lotov. Efficient operating mode of the plasma wakefield accelerator. *Physics of Plasmas*, 12:053105, 2005.

[50] D. Zwillinger, editor. *CRC Standard Mathematical Tables and Formulae, 30th Edition*, page 322. CRC Press, New York, 1996.

[51] D. C. Carey. *The Optics of Charged Particle Beams*, pages 142–143. Harwood Academic Publishers, New York, 1987.

[52] K. L. Brown. A First and Second Order Matrix Theory for the Design of Beam Transport Systems and Charged Particle Spectrometers. Technical Report SLAC-75, Stanford Linear Accelerator Center, Stanford, CA, 1982.

[53] M. Borland. ELEGANT: A Flexible SDDS-Compliant Code for Accelerator Simulation. Technical Report LS-287, Argonne National Laboratory Advanced Photon Source, Argonne, IL, September 2000.

[54] E. D. Courant and H. S. Snyder. Theory of the alternating gradient synchrotron. *Annals of Physics*, 3:1–48, 1958.

[55] R. Q. Twiss and N. H. Frank. Orbital Stability in a Proton Synchrotron. *Review of Scientific Instruments*, 20:1–17, 1949.

[56] D. C. Carey. *The Optics of Charged Particle Beams*, pages 135–138. Harwood Academic Publishers, New York, 1987.

[57] D. C. Carey. *The Optics of Charged Particle Beams*, pages 139–141. Harwood Academic Publishers, New York, 1987.

[58] L. Young and J. Billen. PARMELA. Technical Report LA-UR-96-1835, Los Alamos National Laboratory, Los Alamos, NM, 1996.

[59] P. R. Phillips. *The Separation of High-Energy Particle Beams by Microwave Techniques*. PhD thesis, Stanford University, Stanford, CA 94305, November 1960.

[60] O. A. Altenmueller, R. R. Larsen, and G. A. Loew. Investigations of Travelling-Wave Separators for the Stanford Two-Mile Linear Accelerator. Technical Report PUB-R-017, Stanford Linear Accelerator Center, Stanford, CA, 1963.

[61] G. A. Loew and O. H. Altenmueller. Design and Application of RF Separator Structures at SLAC. Technical Report PUB-135, Stanford Linear Accelerator Center, Stanford, CA, 1965.

[62] R. Akre, L. Bentson, P. Emma, and P. Krejcik. Bunch length measurements using a transverse rf deflecting structure in the slac linac. In *Eighth European Particle Accelerator Conference*, pages 1882–1884, 2002.

[63] W. K. H. Panofky and W. A. Wenzel. Some Considerations Concerning the Transverse Deflection of Charged Particles in Radio-Frequency Fields. *Review of Scientific Instruments*, 27:967, 1956.

[64] J. D. Fuerst, M. S. McAshan, and et al. An RF Separated Kaon Beam from the Main Injector: Superconducting Aspects. Technical Report CDR98, Fermi National Accelerator Laboratory, Batavia, IL, 1998.

[65] H. Padamsee, Jens Knobloch, and Tom Hays. *RF Superconductivity for Accelerators*, pages 148–156. John Wiley and Sons, Inc., New York, 1998.

[66] M. L. Sisodia and G. S. Raghuvanshi. *Microwave Circuits and Passive Devices*, pages 29–31. John Wiley and Sons, Inc., New York, 1987.

[67] J. D. Jackson. *Classical Electrodynamics, 2nd Edition*, page 358. John Wiley and Sons Inc., New York, 1975.

[68] D. E. Nagle, E. A. Knapp, and B. C. Knapp. Coupled Resonator Model for Standing Wave Accelerator Tanks. *Review of Scientific Instruments*, 38:1583, 1967.

[69] N. Yi, X. Liling, T. Dechun, and L. Yuzheng. Diagnosis of Individual Cell Frequencies in a Coupled Cavity Chain Without Introducing Objects into the Cavity. *IEEE Transactions on Nuclear Science*, 48:1623, 2001.

[70] P. M. Lapostolle and A. L. Septier, editors. *Linear Accelerators*, pages 212–213. American Elsevier Publishing Company, New York, 1970.

[71] R. Zhang, S. Hartman, and C. Pellegrini. The plane wave transformer linac development at UCLA. In *Proceedings of the 1993 Particle Accelerator Conference*, pages 575–577, 1993.

[72] D. H. Martin. *Infrared and Millimeter Waves*, pages 65–148. Academic Press, New York, 1982.

[73] A. Murokh, J. B. Rosenzweig, M. Hogan, H. Suk, G. Travish, and U. Happek. Bunch length measurement of picosecond electron beams from a photoinjector using coherent transition radiation. *Nucl. Instr. Meth. Phys. Res. A*, 410:452–460, June 1998.

[74] R. J. England. Neptune Second Harmonic Generation Autocorrelator. Technical report, University of California Los Angeles, Particle Beam Physics Laboratory, April 2005.

[75] A. Doyuran, O. Williams, R. J. England, C. Joshi, J. Lim, J. B. Rosenzweig, S. Tochitsky, and G. Travish. Investigation of x-ray harmonics of the polarized inverse compton scattering experiment at UCLA. In *Proceedings of the 2005 Particle Accelerator Conference*, IEEE, pages 2303–2305, 2005.